MODELS OF X-RAY BRIGHT POINTS AND CONCELLING MAGNETIC FEATURES

Clare E. Parnell

A Thesis Submitted for the Degree of PhD
at the
University of St Andrews

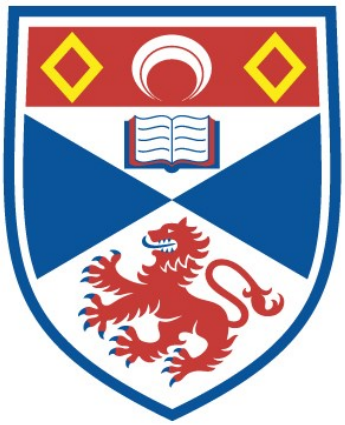

1995

MODELS OF X-RAY BRIGHT POINTS AND CANCELLING MAGNETIC FEATURES

CLARE E. PARNELL

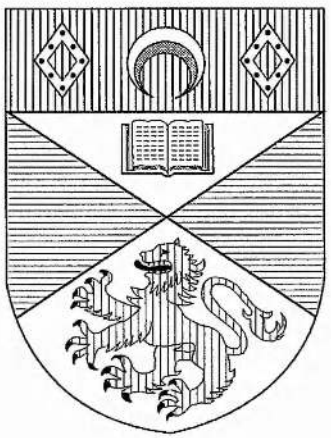

Thesis Submitted for the Degree of Doctor of Philosophy
of the University of St. Andrews.

ProQuest LLC.
789 East Eisenhower Parkway
P.O. Box 1346
Ann Arbor, MI 48106 – 1346

In Memory of Matthew Walsh

Declaration

In accordance with the regulations of the University of St Andrews as of December 1993,

1. I, Clare Elizabeth Parnell, hereby certify that this thesis has been composed by myself, that it is a record of my own work, and that it has not been accepted in partial or complete fulfilment for any other degree or professional qualification.

Signed: ... . Date: ....12.12.94.....

2. I was admitted to the Faculty of Science of the University of St Andrews under Ordinance General No 12 in October 1991 and as a candidate for the degree of PhD on the same date.

Signed: .... Date: ....12.12.94.....

3. I hereby certify that the candidate has fulfilled the conditions of the Resolution and Regulations appropriate to the degree of PhD.

Signed: .... Date: 12.12.94

4. In submitting this thesis to the University of St Andrews I understand that I am giving permission for it to be made available for use in accordance with the regulations of the University Library for the time being in force, subject to any copyright vested in the work not being affected thereby. I also understand that the title and abstract will be published, and that a copy of the work may be made and supplied to any bona fide library or research worker.

Abstract

Small brightenings called x-ray bright points (Golub *et al.*, 1974) occur in the solar corona. They are observed with the soft x-ray telescope on Skylab to be approximately 22 Mm in diameter with a brighter inner core of width 4 - 7 Mm although with the Normal Incidence X-ray Telescope their dimensions are observed to be typically 6 Mm × 9 Mm. By comparison with magnetograms of the photosphere it has been noticed recently that there is a high correlation between the occurrence of x-ray bright points and the mutual reduction of flux between two opposite polarity magnetic fragments. These fragments are originally unconnected magnetically, but move towards each other and simultaneously lose equal amounts of flux (cancel): they are called *cancelling magnetic features* (Martin *et al.*, 1984). The observations relating to these features were reviewed by Priest *et al.* (1994) who suggested that they naturally evolve through three phases: the *pre-interaction*, *interaction* and *cancellation* phases. From this evidence qualitative pictures of the magnetic field structure for an x-ray bright point and associated cancelling magnetic feature were established.

The aim of this thesis has been to build on the ideas of Priest *et al.* (1994) to produce a detailed theoretical model of an x-ray bright point and a cancelling magnetic feature. The magnetic field structures are estimated, and the position and lifetime of the bright point are calculated, as is the total amount of energy released during the bright point. This work is also extended to study more complex cancelling configurations representing the main basic types of cancelling magnetic feature. The results of these models determine the factors that affect the lifetime and position of a bright point and indicate which types of cancelling magnetic features are most likely to produce bright points that are long-lived, lie directly above the cancellation site and occur simultaneously with the cancellation phase.

The complex structure of a bright point cannot be explained from the above two-dimensional models: thus two recently observed bright points were studied to see if the above model could be extended into three dimensions to explain the structure seen in soft x-ray images. The available observational data was used and leads to reasonable explanations for the complex shapes of both bright points.

Finally, a more realistic model for the overlying field was set up involving a model of the field above a supergranule cell field with fragments of finite width. The interaction of an ephemeral region within this field was then studied and led to five different scenarios. The results obtained reaffirmed those found in the previous simpler models and suggest where bright points may appear in a cell relative to the cancelling magnetic feature and for how long the bright points might last. Predictions for the lifetimes of cancelling magnetic features are also made, indicating when the cancelling magnetic feature occurs relative to the bright point.

Acknowledgements

I wish to record my thanks to:

Eric Priest, my supervisor, whose advice and encouragement has been invaluable to my work;

Mum and Dad for their support and excellent supply of chocolate cake;

all members of the solar group with whom I have had interesting and stimulating discussions especially Gordon Inverarity who's proved continually willing to listen and help and Tim Bungey who was brave enough to read through this thesis;

Tricia Heggie, Craig Anderson and others in the solar group for their welcome supply of computing hints and tips;

Pete Hurst for volunteering to read this thesis;

the SERC for their financial support;

and last, but certainly not least, the wonderful companionship of Simon in the completion of not only my PhD, but also all the Munros (mountains over 3000ft in Scotland) which have been an immensely important part of my 3 years in St Andrews and are recorded in Appendix E.

Contents

Chapter 1

Introduction

1.1 The Sun

As an object central to our existence, the Sun is both beautiful and interesting. It has been studied for many thousands of years, but it is only in this century that the existence and importance of the Sun's magnetic field has been appreciated. It is widely believed that this magnetic environment is responsible for most of the coronal structures that are observed (e.g solar flares, prominences and x-ray bright points).

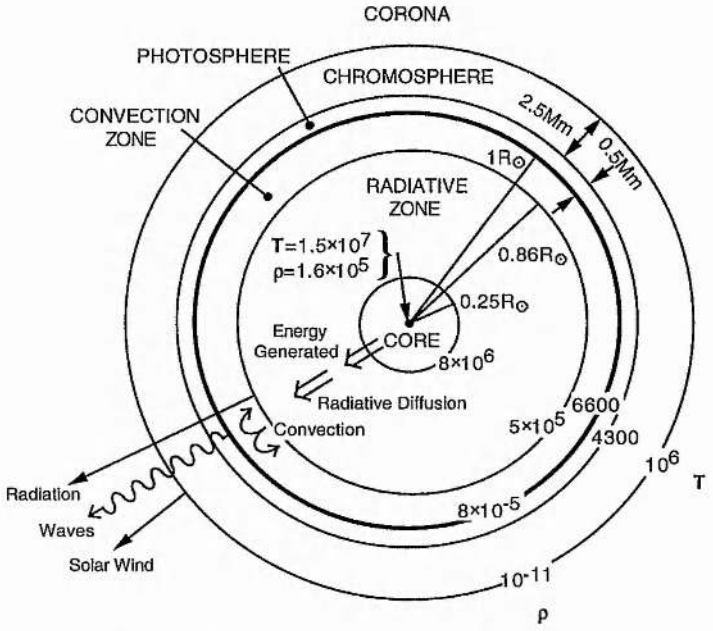

Figure 1.1: The structure of the Sun, showing temperatures in degrees Kelvin, densities in kg m^{-3} (Priest, 1982). One solar radii ($R_\odot$) is equal to 6.96×10^8 Mm.

The Sun, a massive ball of plasma compressed under its own gravitational attraction, consists of an interior (shielded from our view) and an atmosphere which can be seen using a range of instruments. The interior consists of a core with the radiative zone and then the convection zone surrounding it; the atmosphere comprises of the *photosphere*, the *chromosphere* and the *corona* which are discussed below in Section 1.2 (Figure 1.1).

The work in this thesis studies phenomena relating to the three regions in the atmosphere, in particular *x-ray bright points* which occur in the solar corona (Section 1.2.3) and *cancelling magnetic features* which occur in the photosphere (Section 1.2.1). The basic equations and assumptions used in modelling these features are discussed in Section 1.3, with Section 1.4 looking at results relating to potential magnetic fields and Section 1.5 considering reconnection. Section 1.6 describes coronal heating in general, whilst Section 1.7 gives a brief overview of the contents of the following chapters and the aims of this thesis.

1.2 Solar Observations

1.2.1 Photosphere

The Sun's lower atmosphere is called the *photosphere* after the Greek word for 'light' since it emits most of the Sun's radiation. It has a density, ρ, of $8{\times}10^{-5}$ kg m^{-3} and a number density of 10^{23} particles per cubic metre, making it 100 times rarer than the earth's atmosphere. The thickness of the photosphere is usually taken to be the distance between the surface of the Sun, the top of the convection zone at 1.0 $R_{\odot}$, which has a temperature of 6600 K, and the level of the temperature minimum of 4300 K, which is approximately 0.5 Mm above.

Below the surface of the Sun is the convection zone, a seething mass of plasma that is continuously in motion giving rise to the structures seen in the photosphere. The tops of the convection cells overshoot the upper convection zone producing a granular effect called 'granulation' that covers the whole Sun at the photospheric level. These granule cells, seen as a mosaic of irregular shapes in high resolution images, are continuously moving with about a million present at any one time. They have a mean lifetime of 8 minutes and are approximately 700 - 1500 km in diameter. The centre consists of hot rising plasma (0.4 km s^{-1}) that flows horizontally to the edges of the cells at 0.25 km s^{-1}. Also visible are two large-scale velocity patterns called 'mesogranulation' and 'supergranulation'. Less is known about mesogranules which are typically 5 - 10 Mm in size and possess speeds of 0.06 km s^{-1}. The tops of large convection cells form supergranule cells around which intricate threads of positive and negative magnetic flux that intersect the photosphere are loosely gathered. The cells, irregular in shape though often modelled as hexagons or circles, have diameters ranging from 20 - 54 Mm (average 30 Mm) and have material rising in their centres at approximately 0.1 km s^{-1}; this moves outwards to the boundaries at 0.3 - 0.4 km s^{-1} before falling at the edges with speeds of 0.1 - 0.2 km s^{-1}. The magnetic flux is known to be more intense at the cell edges than inside, with all the flux appearing in the cells dragged to the edges by convection flows. They have lifetimes of 1 - 2 days and are 10% larger nearer active regions, areas of intense mixed polarity flux (approximately 10^{-2} T (100 G) magnetic fields), than in the quiet regions where the magnetic fields are approximately 10^{-3} T (10 G).

The motions in the convection zone also cause loops of magnetic flux to be pushed up through the surface into the photosphere and appear as *emerging flux regions* containing a small bipolar pair of magnetic fragments. Each fragment of the emerged region grows in strength and size as they separate; some regions remain fairly small with typically 10^{11} Wb (10^{19} Mx) of flux, called *ephemeral regions*, whilst others grow much larger and form the sunspots of an *active region* with a total flux in the region of 10^{14} Wb (10^{22} Mx). Active regions are associated with much of the large and dynamic phenomena on the Sun such as prominences and solar flares (Section 1.2.3), but work in this thesis concentrates mainly on the surrounding regions known as *quiet regions*. Outside both active regions and quiet regions large areas of unipolar flux are found. These regions may extend over several 100 Mm and have lifetimes of a year or more. They are believed to be anchored deep in the Sun with a total flux of approximately

10^{13} Wb (10^{21} Mx) giving an average field strength of 10^{-4} T (1 G).

The quiet regions of the Sun have a mean field strength of 10^{-3} T (10 G) and are dappled with many regions of positive and negative flux. They are made up of clusters of intense flux tubes with strengths of 0.1 - 0.2 T (1 - 2 kG) (Stenflo, 1973) and tend to collect along the edges of supergranule cells or at the intersections of 3 cells. Martin *et al.* (1988) characterised these magnetic fields into 3 groups; intracell fields, network fields and ephemeral regions. Intracell fields (originally known as intranetwork fields) are relatively weak (approximately 10^{10} Wb (10^{18} Mx)) unipolar regions of magnetic flux that appear in the centre of supergranule cells and are swept radially outwards by convective motions to the boundaries where they interact with the bounding magnetic fields. With the present resolution they are observed to have diameters of a few megameters. Network fields, found on the boundaries of the supergranule cells, have fluxes of approximately 10^{11} Wb (10^{19} Mx) and are made up of residuals of intracell fields and residuals of bipoles of all scales from ephemeral regions to active regions. They are unipolar fragments of up to 10 Mm widths (present resolution). Ephemeral regions are small bipolar units of magnetic flux that grow to strengths of 10^{10} - 5×10^{11} Wb (10^{18} - 5×10^{19} Mx). As each fragment of the bipole increases in strength they diverge (at a speed of approximately 0.5 km s^{-1}) until the ephemeral region reaches a maximum diameter of between 5 and 30 Mm (mean 10 Mm). Ephemeral regions have lifetimes of 2 - 48 hrs and appear randomly orientated over the surface of the Sun predominantly between the latitudes of $\pm$ 35°. The number of ephemeral regions appearing per day was originally considered to be 100 (Harvey and Martin, 1973), but from more recent Big Bear magnetograms taken in December 1987 the figure seems more like 1200 per day (Webb *et al.*, 1993) with approximately 600 at solar minimum up to 2400 at solar maximum. Similarly K. Harvey reports (Priest *et al.*, 1994) approximately 500 - 800 born at solar minimum and 1200 - 2000 at solar maximum depending on whether the mean lifetime is taken as 8 hrs or 5 hrs. The lifetime of all the magnetic fragments is very difficult to determine since all the regions are moving and so interacting, either coalescing or cancelling, as they encounter each other. Many only live for hours whilst others, like some network fields, may last for 1 - 2 days, similar to the lifetime of the supergranule cells.

Cancelling Magnetic Features

When opposite polarity magnetic fragments move together they may produce a *cancelling magnetic feature* (Martin *et al.*, 1984). This occurs when two initially unconnected fragments converge creating an increased magnetic field gradient between them and leading to the mutual reduction of magnetic flux from each fragment. All types of magnetic fragments can form one-half of a cancelling magnetic feature with the lifetime of each cancellation and the amount of flux cancelled dependent on the type and size of the fragments (Table 1.1). Ephemeral regions have only ever been seen to diverge, never to converge, and so their bipoles cannot annihilate themselves; however one half of an ephemeral region may form a cancelling magnetic feature with any other unconnected magnetic fragment. Note that the flux measured at the present resolution for each fragment is believed to be accurate, but it probably stems from many intense flux tubes of strengths 0.1 - 0.2 T (1 - 2 kG), which scatter through the observed volume to give the size of the fragments seen. Above approximately 10% of cancelling magnetic features a tiny filament is seen to form in Hα which erupts and/or causes a chromospheric brightening (flare) (Hermans and Martin, 1986). Many of the filaments look as if they are preparing to erupt as they form and last from tens of minutes to a few hours during the cancellation process.

CMF type	flux per pole (Wb) [Mx]	size (present resolution) (Mm)	lifetime (hrs)	speed of convergence (km s^{-1})
intracell-intracell intracell-network	10^{10} $[10^{18}]$	1-5	1-5	0.3
network-network	10^{10}-10^{11} $[10^{18}$-$10^{19}]$	1-10	1-36	0.1-0.3
ephemeral region -network ephemeral region -intracell	10^{10}-5×10^{11} $[10^{18}$-$5 \times 10^{19}]$	1-10	1-36†	0.1-0.3

† Cancelling features involving ephemeral regions in general have mean lifetimes shorter than those for network-network fields. This is because their mean speed of convergence is typically faster.

Table 1.1: A comparison of different cancelling magnetic features.

1.2.2 Chromosphere

The *chromosphere* extends out for approximately 2.5 Mm above the photosphere from the temperature minimum of 4300 K. In this region the temperature rises gradually up to 3×10^4 K and then rises very dramatically through the transition region, the very thin layer of approximately 30 km width between the chromosphere and corona, up to as high as 5 - 6 $\times10^6$ K. Figure 1.2 shows how the temperature varies from the photosphere through the chromosphere into the corona.

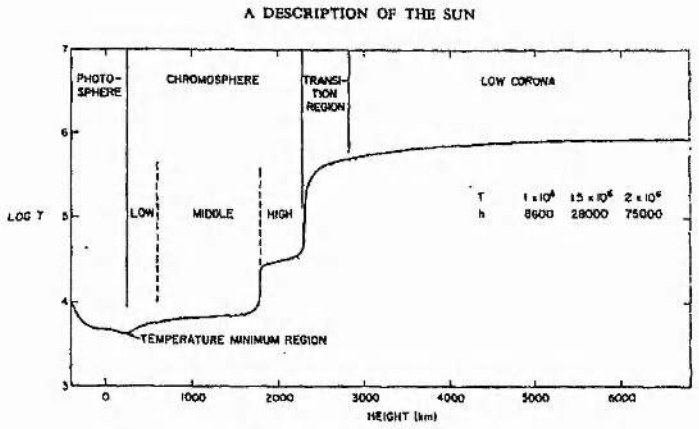

Figure 1.2: The temperature of the Sun (T) versus the height above the photosphere (Athay, 1976).

The chromosphere is observed by studying absorption lines of various wavelengths. Most of the radiation from the Sun is emitted from the photosphere, of which the majority just goes straight through the overlying atmosphere, but certain wavelengths are absorbed by overlying matter. These absorbed lines appear as dark bands in a continuous spectrum of light and provide information on the temperature (from intensity), magnetic field strength (by Zeeman splitting) and local line-of-sight plasma motions (from Doppler broadening) at the level they are absorbed. The H Balmer-alpha (Hα) absorption line

comes from the lower chromosphere so this layer is studied by using an Hα filter; the CaIIK line reveals the middle chromosphere while EUV (extreme ultra violet) emission lines are used to observe the high chromosphere including the transition region.

From these images it is known that supergranule cells, which are clearly visible, have small jets of plasma called spicules ejected from their boundaries. These jets, ejected up to 11 Mm into the corona along field lines, last for 5 - 10 minutes and have temperatures of 1 - 2 $\times 10^4$ K, so are cooler than the surrounding corona they enter. Approximately 30 spicules appear at any one time around each supergranule cell and reach speeds of up to 20 - 30 km s^{-1} and have diameters of 500 - 1200 km. In Hα images small dark features are seen, approximately 0.7 - 7 Mm long, called fibrils. They cover around 30% of the disc and are known to align themselves with the magnetic field, so giving an indication as to the direction of the magnetic field. When lots of fibrils link up they form a long thicker dark feature known as a filament, and (from comparison with photospheric data) they are observed to occur above a polarity inversion line which divides a region of predominantly positive flux from an area of mainly negative flux. Filaments are often linked with active regions and are seen at the limb as prominences, although small filaments have been observed above cancelling magnetic features. When a solar flare occurs the filament(s) may brighten and then break up, or they may just disintegrate and fade.

1.2.3 Corona

Above the photosphere and chromosphere, starting at approximately 3 Mm above the surface of the Sun the *corona* is found. It extends out into space almost limitlessly, but the inner corona, up to 100 Mm from the surface of the Sun finishing at the heliospheric boundary, is where most attention is focused when studying the solar corona. The average electron density is several times 10^{14} m^{-3}, though it falls rapidly with height. In structures like prominences, active regions and x-ray bright points, however, this is increased by factors of between 5 and 20. It has temperatures of between 2 and 6 $\times 10^6$ K and so is about 10^3 times hotter than the surface of the Sun. The sudden rise in temperature through the transition region in the upper chromosphere has mystified solar physicists for many years. It has been attributed to the magnetic field, but the exact mechanisms for this temperature rise are unknown. The corona may be observed in either white light at eclipses, or soft x-rays. It has an equivalent brightness to the full moon, approximately a millionth of the intensity of the photosphere, so it is normally obscured by the photospheric glare, but at an eclipse much of this light is cut out so that we are left with a view of the structures on the coronal limb. Since eclipses are only seen approximately once a year and last about 2 minutes Lyot created a 'coronagraph', a telescope with a disc that obscures the photospheric light and 'eclipses the Sun'. This has enabled a better study of the limb of the corona to be undertaken. The corona also emits thermally in x-rays where, at this height, the contribution from the lower atmosphere is almost totally negligible, so images may be taken by satellites or on rocket flights of the corona. They cannot be taken from the ground as the earth's atmosphere absorbs these wavelengths.

From eclipse photographs 'coronal streamers' can be seen very clearly on the limb above active regions and prominences. They consist of a closed loop structure enclosing the feature, topped with a series of open field lines that gather above the arcade to form a spike when seen end on and a spray when seen from the side. X-ray images reveal that the corona has a three-fold structure of coronal holes, coronal loops and x-ray bright points. Coronal holes are regions of open field lines, occurring above unipolar regions of flux in the photosphere, along which plasma flows outwards forming the solar wind. The solar wind initially has a velocity of 16 km s^{-1} in the inner corona increasing to super-alfénic speeds between 200 and 900 km s^{-1} at 1 AU. Coronal loops are seen in soft x-rays as bright strips of between 10 - 700 Mm in length. They interconnect active regions or merely lie within the active regions; shorter loops, either

singly or in groups creating arcades, form in the quiet regions between the active regions and coronal holes. Also there are great loop structures seen at the limb to be supporting bright dense matter; these structures, known as prominences, may be large and long lived (up to 9 months) and are generally found near the poles. Smaller and shorter lived prominences (only days) appear near active regions and can erupt forming a solar flare which ejects a mass of plasma out into the solar wind. X-ray bright points are the smallest structures making up the corona and as a key part of this thesis they are discussed in a separate section below.

X-ray Bright Points

X-ray bright points are small brightenings (seen in soft x-ray images) that appear randomly distributed over the corona in quiet regions and coronal holes. These brightenings were first discovered by Vaiana *et al.* in 1970 from a rocket image and were studied from Skylab images by Golub *et al.* (1974, 1976a and b, 1977). They are seen as a diffuse cloud that grows at 1 km s^{-1} to approximately 22 Mm diameter (Skylab), 6 Mm×9 Mm (Normal Incidence X-ray Telescope (NIXT)) with a bright inner core of approximately 4 Mm that appears and then later fades followed by the fading of the diffuse cloud. In the high resolution images with much less scatter bright points are seen to consist of complex small scale loop structures (Sheeley and Golub, 1979) with a diameter of up to 30 Mm; they are also seen to fluctuate in intensity implying intermittent heating (Habbal *et al.*, 1990). Approximately 1500 are born per day with 500 present at any one time. They are more numerous and more randomly distributed at sunspot minimum than at sunspot maximum and last between 2 and 48 hrs with a mean of 8 hrs.

They appear above pairs of opposite polarity magnetic fragments initially thought to be ephemeral regions, but the number of bright points appearing is out of phase with the solar cycle (Davis *et al.*, 1977; Golub *et al.*, 1979) whilst the number of ephemeral regions is in phase (Harvey *et al.*, 1975; Martin and Harvey, 1979). Thus the original suggestion that they are associated with bipolar regions of emerging flux seems untenable. Two key papers by K. Harvey (1984, 1985) revealed that a third of the observed dark points, proxies for the 30% largest bright points seen from the ground in helium 10830, overlie ephemeral regions and two thirds appear above cancelling magnetic features. In fact in a study by Webb *et al.* (1993) 72% of bright points were seen to lie above cancelling magnetic features and 88% above converging magnetic features, which cannot be ephemeral regions since their fragments always diverge. Also it has been found that there are approximately 3 - 4 times as many cancelling magnetic features as there are bright points appearing per day with only the strongest cancelling magnetic features ($\approx$ 20%) associated with bright points (Webb *et al.*, 1993). K. Harvey (1985) therefore suggested that most bright points are due to chance encounters of opposite polarity magnetic fragments in the network or of emerging flux with the opposite polarity network. She realised that such cancellations depend on the amount of mixed polarity areas which decrease by a factor of 6 from 95% at solar minimum (1976) to 14% solar maximum (1979 - 1980), while the number of bright points also decreases by a factor of 6 from 90 to 14. This explains the anti-correlation of bright points with the solar cycle.

About 5% - 10% of bright points flare (Golub *et al.*, 1974) with their intensity increasing by a factor of around 10. Recently results from Yohkoh show that bright points fluctuate by 30% - 200% over time scales of a few minutes to hours. Each bright point may flare more than once (its intensity increasing by a factor of 10 to 100) with long hot loops often associated with each flare. These loops brighten at speeds of 1100 km s^{-1}, extend up to hundreds of megameters from the bright point and last for approximately 10 mins or less. Results from Shibata *et al.* (1992a and b) suggest that the x-ray jets, often associated with bright point flares and active regions, have sizes of 5 - 400 Mm and velocities of 30 - 300 km s^{-1}.

Active Regions

Although in this thesis most of the work is concerned with the quiet regions of the Sun, it is worth saying a little about active regions as much of our understanding of bright points and cancelling magnetic features may, in the future, be helpful in trying to understand these much larger and more complex regions. In fact some researchers believe bright points are merely very small short-lived active regions that show some, but not all of the active region features (Sheeley and Golub, 1979). For example, some bright points form small filaments seen in the chromosphere that erupt (Hermans and Martin, 1986) and bright point flares may eject a little jet of plasma (Shibata *et al.*, 1992a and b) similar to the formation of an active region prominence and associated solar flare. Active regions are observed in the photosphere as complex magnetic field regions that have cancellation as well as coalescence taking place within them, and from this and future studies of cancelling magnetic features it is possible that a better understanding may be gained of how active regions and their associated phenomena are caused.

Active regions are visible at all three levels of the solar atmosphere. They first appear in the photosphere as an 'emerging flux region' that grows in size and strength forming a pair of sunspots that last for 2 - 3 days and then fade leaving a region of intense magnetic flux with a field strength of approximately 10^{-2} T (100 G) (at the present resolution). The sunspots are linked by a system of dark loops in the chromosphere called 'arch filaments', also visible in the corona from soft x-rays as bright loops. They last approximately 20 minutes each and are replaced by new loops from below. This continues for 10 - 15 days as the region grows until the maximum activity of the region has peaked. After this the active region decays slowly with the magnetic fields in the photosphere beginning to disperse and, in the chromosphere and corona, the arch filaments fade leaving a more prominent filament called an 'active-region filament'. This filament increases in length along the polarity inversion line in which it lies. An active region typically lasts 50 days after which the active-region filament is often left as a diffuse structure of hot loops in which a cool filament lies. This filament is known as a quiescent filament (prominence) and may stretch out up to 60 - 600 Mm in length, 50 Mm in height and 6 Mm wide as it migrates towards the poles. Amazingly these comparatively dense structures of 10^{16} - 10^{17} m^{-3} hang in the corona for as long as 300 days. At the end of their life quiescent prominences either just fade away or erupt producing coronal brightening and ejecting mass into the solar wind and sometimes even triggering a solar flare.

At some stage during the life of an active region, usually in the time leading up to the peak activity, a solar flare may occur. They are thought to be triggered in the corona by an instability in the magnetic field leading to a sudden massive conversion of magnetic energy into both thermal and kinetic energies. They appear in Hα as rapid brightenings of filaments and in soft x-rays as extremely hot loops. Flares in general last several minutes to hours and release between 10^{22} and 10^{25} J (10^{29} and 10^{32} ergs) of energy.

The Yohkoh satellite has revealed that active regions show frequent small flare-like brightenings known as active-region transient brightenings. These events have lifetimes of a few to tens of minutes and produce single or multiple bright loop structures (Shimizu *et al.*, 1992) similar to x-ray bright point flares and x-ray jets. The loop structures are typically 1 - 50 Mm, with temperatures and number densities increasing from 5×10^6 K to 7×10^6 K and from 4×10^{15} m^{-3} to 10^{16} m^{-3}, respectively, during brightening. The total energy released by an active region transient brightening is 10^{18} - 10^{22} J (10^{25} - 10^{29} ergs) which is the low end of the subflare range: this energy is released at a rate of 10^{20} W (10^{27} ergs s^{-1}). In 'active' active regions transient brightenings occur every 3 mins, whilst in 'quiet' active regions they only occur on average once every hour.

1.3 Basic Equations

In studying the Sun scientists have employed mathematics to explain the complex structure and events observed, but before any sensible mathematical model can be constructed of the solar atmosphere and its associated magnetic field, assumptions about the behaviour of the plasma must be made. By looking at events that have length scales larger than the mean free paths of the particles in the Sun's atmosphere, one may assume that the plasma is a continuous fluid and the magnetohydrodynamic (hereafter, MHD) equations may be applied. The set comprises Maxwell's equations of electromagnetism coupled with Ohm's law for an electrically neutral plasma and the equations of hydrodynamic motion.

Maxwell's Equations

Maxwell's Equations may be written as

$$\nabla \times \mathbf{B} = \mu_o \mathbf{j} + \epsilon_o \mu_o \frac{\partial \mathbf{E}}{\partial t} , \tag{1.1}$$

$$\nabla \cdot \mathbf{B} = 0 , \tag{1.2}$$

$$\nabla \times \mathbf{E} = -\frac{\partial \mathbf{B}}{\partial t} , \qquad \text{(Faraday's Law)} \tag{1.3}$$

and

$$\nabla \cdot \mathbf{E} = \frac{\rho_c}{\epsilon_o} , \tag{1.4}$$

where $\mathbf{B}$ is the magnetic induction (usually called the magnetic field), $\mathbf{E}$ is the electric field and $\mathbf{j}$ is the current density. The quantities μ_o, ϵ_o and ρ_c are, respectively, the magnetic permeability in a vacuum ($\mu_o = 4\pi \times 10^{-7}$ H m^{-1}), the permittivity of free space ($\epsilon_o = 8.85 \times 10^{-12}$ F m^{-1}) and the electric charge density.

If a dimensional analysis of Equation (1.3) is performed then it is found that $| \mathbf{E} | \sim | \mathbf{v} || \mathbf{B} |$ where $\mathbf{v}$ is a typical velocity. If $1/c^2$ is substituted in Equation (1.1) for $\epsilon_o \mu_o$, where c is the speed of light in a vacuum, then the third term in the equation is found to be of order $| \mathbf{v} |^2 / c^2$ compared with the $\nabla \times \mathbf{B}$ term. Since many phenomena in the solar atmosphere are non-relativistic and have velocities typically less than $0.1c$, this last term may be neglected and so Equation (1.1) becomes

$$\nabla \times \mathbf{B} = \mu_o \mathbf{j} , \tag{1.5}$$

which is known as Ampère's Law.

Ohm's Law

A plasma moving at a non-relativistic speed ($\mathbf{v}$) in a magnetic field ($\mathbf{B}$) is subject to an electric field ($\mathbf{v} \times \mathbf{B}$) in addition to the electric field ($\mathbf{E}$) which would act on it at rest. Ohm's law for a neutral plasma asserts that the current density is proportional to the total electric field. Hence

$$\mathbf{j} = \sigma (\mathbf{E} + \mathbf{v} \times \mathbf{B}) , \tag{1.6}$$

where σ, the electric conductivity, is measured in ohm^{-1} m^{-1}.

Hydrodynamic Equations

To complete the description of MHD, a set of equations are needed to describe the behaviour of the fluid. These include the equation of motion

$$\rho\frac{D\mathbf{v}}{Dt} = -\nabla p + \mathbf{j}\times\mathbf{B} + \rho\mathbf{g} + \rho\nu\left(\nabla^2\mathbf{v} + \frac{1}{3}\nabla\left(\nabla\cdot\mathbf{v}\right)\right), \tag{1.7}$$

where $D/Dt = \partial/\partial t + \mathbf{v}\cdot\nabla$, the equation of mass continuity

$$\frac{D\rho}{Dt} = -\rho\left(\nabla\cdot\mathbf{v}\right), \tag{1.8}$$

the ideal gas law

$$p = -\frac{R}{\mu_a}\rho T, \tag{1.9}$$

and an energy equation

$$\frac{\rho^\gamma}{\gamma-1}\frac{D}{Dt}\left(\frac{p}{\rho^\gamma}\right) = -\nabla\cdot\mathbf{q} - L_r + \frac{j^2}{\sigma}. \tag{1.10}$$

In Equations (1.7) - (1.10), $\mathbf{g} = -g\,\hat{e}_r$ is the acceleration due to gravity which acts radially outwards from the centre of the Sun, p is the plasma pressure, ρ is the plasma density, ν is the coefficient of kinematic viscosity, R the gas constant, T the absolute temperature and μ_a the mean atomic weight ($\mu_a \approx 0.6$ in the solar atmosphere except close to the photosphere where $\mu_a \approx 1.3$). In the energy equation, $\gamma(\approx 5/3)$ is the ratio of the specific heat at constant pressure (c_p) to the specific heat at constant volume (c_v), $\mathbf{q}$ is the heat flux function due to particle conduction, L_r is the radiative loss term and j^2/σ is ohmic dissipation.

Phenomena in the solar atmosphere can be modelled by the set of Equations (1.2) to (1.10). However, solving all these equations simultaneously is obviously not easy and so for progress to be made in the following chapters of this thesis a reduced form of these equations is used.

Further Approximations

The effects of viscosity are assumed negligible, so comparing the relative sizes of the terms left in the equation of motion, Equation (1.7), it is found that the left-hand side may be neglected if it is smaller than each of the three remaining terms on the right-hand side. This is true if the flow speed (v) is much smaller than the sound speed $(\gamma p_o/\rho_o)^{\frac{1}{2}}$, the Alfvén speed $B_o/\left(\mu\rho_o\right)^{\frac{1}{2}}$ and the gravitational free-fall speed $(2gl_o)^{\frac{1}{2}}$ for a vertical scale length l_o. This is often the case in the solar corona where the flow speed (v) is approximately 100 times smaller than the Alfvén speed. The result is a hydrostatic balance,

$$\mathbf{0} = -\nabla p + \mathbf{j}\times\mathbf{B} + \rho\mathbf{g}. \tag{1.11}$$

The force of gravity may be neglected by comparison with the plasma pressure gradients when the height of a structure is much smaller than the pressure scale-height, $h \ll RT/\mu_a g$. Thus if the magnetic field is assumed steady then the equations governing the magnetic field reduce to

$$\nabla \times \mathbf{B} = \mu_o \mathbf{j} \,. \tag{1.12}$$

$$\nabla \cdot \mathbf{B} = 0 \,, \tag{1.13}$$

$$\mathbf{j} \times \mathbf{B} = \nabla p \,, \tag{1.14}$$

This set of equations can also be used to describe quasi-static equilibria where the plasma is evolving, but at such a slow speed that it may be considered to be static at any one time relative to its surroundings.

The $\mathbf{j} \times \mathbf{B}$ term in Equation (1.14) is known as the Lorentz force which can be written using Equations (1.13) and (1.12) as

$$\begin{aligned} \mathbf{j} \times \mathbf{B} &= \frac{1}{\mu_o} (\nabla \times \mathbf{B}) \times \mathbf{B} \,, \\ &= \frac{1}{\mu_o} (\mathbf{B} \cdot \nabla) \mathbf{B} - \nabla \left(\frac{B^2}{2\mu_o} \right) \,. \end{aligned} \tag{1.15}$$

The first term on the right-hand side of Equation (1.15) is known as the magnetic tension term with a tension of B^2/μ_o per unit area in a tangential direction to $\mathbf{B}$ producing a net tension force whenever the field lines are curved; the second term on the right-hand side, of magnitude $B^2/2\mu_o$ per unit area, is known as the magnetic pressure term. The ratio of the plasma pressure to the magnetic pressure is

$$\beta = \frac{2\mu_o p_o}{B_o^2} \,. \tag{1.16}$$

In the solar corona $\beta \ll 1$; thus the plasma pressure may be neglected and the equation of motion becomes

$$\mathbf{j} \times \mathbf{B} = 0 \,. \tag{1.17}$$

Now, from Equation (1.12), $j_o \approx B_o / (\mu_o l_o)$. The magnetic field, $B_o \approx 10^{-2}$ T (100 G), varies over typical length scales in the solar corona of order 10^6 m, so $j_o \approx 10^{-2}$ A m^{-2}. The current density is therefore often assumed globally negligible, and $\mathbf{j}$ is often approximated to zero leaving us with just two equations

$$\nabla \times \mathbf{B} = 0 \,, \tag{1.18}$$

$$\nabla \cdot \mathbf{B} = 0 \,. \tag{1.19}$$

These two equations define a magnetic field which is said to be *current-free* or *potential*. Section 1.4 below describes various results which may be calculated for this type of field.

1.4 Potential Magnetic Field Results

Throughout this thesis magnetic field configurations in both two and three dimensions are studied. Initially, magnetic fragments in the photosphere are modelled as line or point sources depending on whether they are in two or three dimensions, respectively.

Let us first consider, in two dimensions, a line source of strength f situated at a point a on the x-axis. The magnetic field at a point (P) with position (x,y) due to this source is

$$\mathbf{B} = \frac{f}{\pi \mid \mathbf{r} \mid} \hat{\mathbf{e}}_r \, , \tag{1.20}$$

where $\mathbf{r} = (x-a)\ \hat{\mathbf{e}}_x + y\ \hat{\mathbf{e}}_y$ (i.e. the magnetic field equals the flux through a semicircle in the upper half plane from this source of strength f). So in cartesians this becomes

$$\mathbf{B} = \frac{f\,(x-a)}{\pi\left((x-a)^2+y^2\right)} \hat{\mathbf{e}}_x + \frac{fy}{\pi\left((x-a)^2+y^2\right)} \hat{\mathbf{e}}_y \, . \tag{1.21}$$

Using complex variable theory this result may be written in a much more compact form by letting $z = x + \mathrm{i}y$ and defining the magnetic field as

$$\mathcal{B}(z) = B_y(x,y) + \mathrm{i}B_x(x,y) \ : \tag{1.22}$$

thus the complex form for the magnetic field due to a line source is

$$\mathcal{B}(z) = \frac{\mathrm{i}f}{\pi\,(z-a)} \, . \tag{1.23}$$

Using this form for the magnetic field can, in many cases, be very beneficial, because not only does the result look neat, but also when structures such as current sheets are introduced they may be modelled easily as cuts in the complex plane. For example, consider the deformed magnetic field of an X-point with a vertical cut along the y-axis between $\pm L$, (Section 1.5.1: Figure 1.5c): in complex notation the magnetic field is

$$\mathcal{B}(z) = \left(z^2+L^2\right)^{\frac{1}{2}} \, , \tag{1.24}$$

whereas in vector notation a much more complicated expression describes the field, namely

$$\begin{aligned}\mathbf{B} = &\left[\frac{-1}{2}\left(\left(x^2-y^2+L^2\right) + \left(\left(x^2-y^2+L^2\right)^2+4x^2y^2\right)^{\frac{1}{2}}\right)\right]^{\frac{1}{2}} \hat{\mathbf{e}}_x \\ &+ \left[\frac{1}{2}\left(\left(x^2-y^2+L^2\right) - \left(\left(x^2-y^2+L^2\right)^2+4x^2y^2\right)^{\frac{1}{2}}\right)\right]^{\frac{1}{2}} \hat{\mathbf{e}}_y \, .\end{aligned} \tag{1.25}$$

In the following chapters when working in two dimensions a complex variable form for the magnetic field will, in general, be used; also note that potential magnetic fields may simply be added together. For example, the magnetic field for two sources one of strength f_1 the other of strength f_2 positioned at a_1 and a_2 on the x-axis, respectively, is

$$\mathcal{B}(z) = \frac{if_1}{\pi(z-a_1)} + \frac{if_2}{\pi(z-a_2)} . \tag{1.26}$$

It is therefore relatively simple to build up a more complicated field of many sources.

In two dimensions there are two ways to calculate the magnetic field lines. One is to solve

$$\frac{dy}{dx} = \frac{B_y}{B_x} . \tag{1.27}$$

This is not always simple and in many cases must be done numerically and involves the solving of an initial value problem. Alternatively the flux function (A) which satisfies

$$\begin{aligned} \mathbf{B}\cdot\nabla A &= B_x\frac{\partial A}{\partial x} + B_y\frac{\partial A}{\partial y} \\ &= 0 , \end{aligned} \tag{1.28}$$

is calculated. The gradient of the scalar field, $A(x,y)$, at any point is the vector pointing in the direction of the greatest increase in A with distance, i.e. perpendicular to the level surface at that point. This result states that the magnetic field ($\mathbf{B}$) is always perpendicular to the gradient of A: thus field lines are defined by lines of constant A.

The actual functional form of A is related to the magnetic field and is defined as the z-component of the magnetic vector potential ($\mathbf{A}$) where

$$\begin{aligned} \mathbf{B} &= \nabla\times A\hat{\mathbf{e}}_z \\ &= \frac{\partial A}{\partial y}\hat{\mathbf{e}}_x - \frac{\partial A}{\partial x}\hat{\mathbf{e}}_y : \end{aligned} \tag{1.29}$$

hence $\nabla\cdot\mathbf{B}$ is automatically satisfied as is Equation (1.28). Thus given $\mathbf{B}$ one can integrate to find A,

$$A = -\int B_y dx = \int B_x dy , \tag{1.30}$$

where the integrals are, respectively, along constant y or constant x. If the complex form for the magnetic field, $\mathcal{B}(z)$ is known, there is no need to find B_x and B_y as simply integrating directly with respect to z gives A, since

$$A = \int_o^x -B_y dx = -\mathcal{R}e\int_0^{x+iy}\mathcal{B}(z)\,dz . \tag{1.31}$$

Again this is not always possible, but can in simple cases give a convenient analytical form for the field lines. For example, taking the form for $\mathcal{B}(z)$ given above in Equation (1.26) the flux function for this situation becomes

$$\begin{aligned} A &= -\mathcal{R}e\left[\frac{if_1}{\pi}\log\left(\frac{z-a_1}{-a_1}\right) + \frac{if_2}{\pi}\log\left(\frac{z-a_2}{-a_2}\right)\right] \\ &= \frac{f_1}{\pi}\mathrm{Arg}\left(\frac{z-a_1}{-a_1}\right) + \frac{f_2}{\pi}\mathrm{Arg}\left(\frac{z-a_2}{-a_2}\right) . \end{aligned} \tag{1.32}$$

To draw field lines representing the strength of the field is fairly simple using the flux function A. Consider the magnetic field due to just a single line source at the origin of strength f. The corresponding flux function, from above, is

$$A = \frac{f}{\pi}\theta \,, \tag{1.33}$$

where θ is the angle measured from the x-axis through the origin. The field lines from a point source emanate radially outwards, so taking equal increments in θ (and therefore A) gives field lines representative of the strength of the field.

In three dimensions the magnetic field for a point source of strength f at a point $(a, b, 0)$ is

$$\mathbf{B} = \frac{f}{2\pi \mid \mathbf{r} \mid^2} \hat{\mathbf{e}}_r \,, \tag{1.34}$$

where $\mathbf{r} = (x-a)\ \hat{\mathbf{e}}_x + (y-b)\ \hat{\mathbf{e}}_y + z\,\hat{\mathbf{e}}_z$ such that the flux from the source into the upper half plane is f. As in the two-dimensional case, in cartesians, the magnetic field is

$$\begin{aligned}\mathbf{B} = & \frac{f(x-a)}{2\pi\left((x-a)^2+(y-b)^2+z^2\right)^{\frac{3}{2}}}\hat{\mathbf{e}}_x + \frac{f(y-b)}{2\pi\left((x-a)^2+(y-b)^2+z^2\right)^{\frac{3}{2}}}\hat{\mathbf{e}}_y \\ & + \frac{fz}{2\pi\left((x-a)^2+(y-b)^2+z^2\right)^{\frac{3}{2}}}\hat{\mathbf{e}}_z \,.\end{aligned} \tag{1.35}$$

Here the magnetic field may be built up again by the summing of all the fields due to the various sources, but this time they may only be drawn by solving

$$\frac{\mathrm{d}x}{B_x} = \frac{\mathrm{d}y}{B_y} = \frac{\mathrm{d}z}{B_z} \,, \tag{1.36}$$

which in most cases must be done numerically by solving the three ordinary differential equations:

$$\frac{\mathrm{d}x}{\mathrm{d}s} = \frac{B_x}{\mid \mathbf{B} \mid} \,; \tag{1.37}$$

$$\frac{\mathrm{d}y}{\mathrm{d}s} = \frac{B_y}{\mid \mathbf{B} \mid} \,; \tag{1.38}$$

$$\frac{\mathrm{d}z}{\mathrm{d}s} = \frac{B_z}{\mid \mathbf{B} \mid} \,, \tag{1.39}$$

given any initial point $(x(0), y(0), z(0))$ on a field line.

1.5 Reconnection

Although not real physical quantities, 'field lines' are very helpful concepts for understanding the properties of magnetic fields. Field lines always follow the direction of the magnetic field, with a magnetic surface defined as being tangential everywhere to the field. One can consider groups of magnetic field

lines that all appear from one particular region and all extend to another particular region as belonging to the same topological region. Reconnection is the breaking and reconnecting of field lines (Figure 1.3) and through this process magnetic fields may evolve from one configuration to another, therefore changing the topology of the field. It is an effective means of converting magnetic energy to other forms of energy, such as heat and kinetic energy: also large electric currents, electric fields and shock waves may be created through reconnection and play a role in accelerating particles to high energies. It is an important process in the heating of the corona, especially in coronal loops and x-ray bright points, in coronal mass ejections (acceleration of the solar wind), prominences, solar flares and also in dynamo generation in the interior of the Sun.

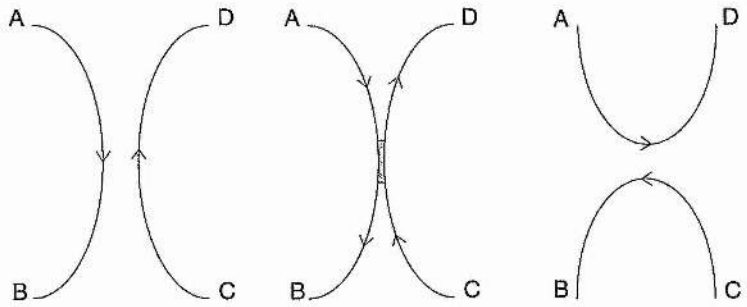

Figure 1.3: The breaking and reconnecting of field lines AB and CD to form the lines AD and CB.

To find out where reconnection can occur the *induction equation* must first be derived. From Equations (1.3), (1.5) and (1.6), **E** and **j** may be eliminated to give

$$\frac{\partial \mathbf{B}}{\partial t} = \nabla \times (\mathbf{v} \times \mathbf{B}) + \eta \nabla^2 \mathbf{B} \,, \tag{1.40}$$

where $\eta = 1/(\mu_o \sigma)$ is the magnetic diffusivity which is assumed here to be uniform. Given any velocity profile ($\mathbf{v}$), this equation will, under constraint (1.2) determine the magnetic field. A dimensional analysis of the ratio of the two terms on the right-hand side of the induction equation gives

$$\frac{\nabla \times (\mathbf{v} \times \mathbf{B})}{\eta \nabla^2 \mathbf{B}} \approx \frac{lv}{\eta} = R_m \,, \tag{1.41}$$

where l and v are typical length and velocity scales and R_m is known as the magnetic Reynolds number. A typical coronal global value of R_m is about 10^6 - 10^{12}, so for most of the solar atmosphere Equation (1.40) is taken to be

$$\frac{\partial \mathbf{B}}{\partial t} = \nabla \times (\mathbf{v} \times \mathbf{B}) \,. \tag{1.42}$$

The limit $R_m \gg 1$ is known as the perfectly conducting limit; though this does not mean that there is no current, rather that the diffusive term is negligible. An important consequence of this limit is Alfvén's Theorem:

Consider any surface S bounded by a closed contour C moving with the plasma at a local velocity $\mathbf{v}$ with a flux F crossing the surface, (see Figure 1.4). In time δt, the line element $\delta \mathbf{c}$ sweeps out an area $\mathbf{v}\delta t \times \delta \mathbf{c}$ and intuitively one sees

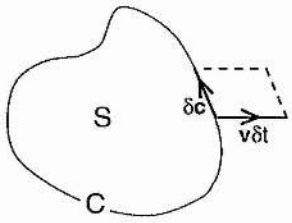

Figure 1.4: A moving plasma element of surface S with a boundary C.

$$\frac{DF}{Dt} = \int_S \frac{\partial \mathbf{B}}{\partial t} \cdot \mathrm{d}\mathbf{S} + \oint_C \mathbf{B} \cdot \mathbf{v} \times \mathrm{d}\mathbf{c} \,, \tag{1.43}$$

where the operator $D/Dt = \partial/\partial t + \mathbf{v} \cdot \nabla$. The first term on the right-hand side is due to changes in the magnetic field with time and the motion of the boundary gives rise to the second term on the right. This latter term can be rewritten as

$$-\oint_C \mathbf{v} \times \mathbf{B} \cdot \mathrm{d}\mathbf{c} \,,$$

which, after applying Stokes' Theorem, becomes

$$-\int_S \nabla \times (\mathbf{v} \times \mathbf{B}) \cdot \mathrm{d}\mathbf{S} \,.$$

Thus, if Equation (1.42) holds, Equation (1.43) becomes

$$\frac{DF}{Dt} = \int_S \left(\frac{\partial \mathbf{B}}{\partial t} - \nabla \times (\mathbf{v} \times \mathbf{B}) \right) \cdot \mathrm{d}\mathbf{S} = 0 \,. \tag{1.44}$$

Interpreting this physically it is found that the flux (F) through a surface (S) moving with the plasma is constant. Since this holds for arbitrary C, magnetic field lines must therefore move with the plasma and are considered to be 'frozen' into the plasma. This means plasma elements may move along a field line, but cannot cross from one to another. This approximation is valid for most solar MHD situations; in the solar corona, magnetic forces dominate so the plasma is pulled along by the field; in the photosphere, the inertia of the plasma dominates and the field is dragged by the plasma. The transport of magnetic field lines by fluid motion is known as magnetic advection; thus the first term on the right-hand side of the induction equation is known as the advection term and the second term, called the diffusive term, represents the ability for field lines to move (diffuse) through the plasma. This only occurs when the length scales are sufficiently small, making the diffusive term locally large, and leading to changes in the topology of the magnetic field. Field lines become disconnected from their original plasma elements and reconnected to different plasma elements in the local 'diffusive' region and give rise to a release in magnetic energy. When this occurs reconnection is said to have taken place.

Thus, for reconnection to take place, very short length scales must be present which implies steep magnetic field gradients and therefore electric currents. These short length scales may be found at magnetic neutral points (Section 1.5.1) and in current sheets (Section 1.5.2). They may also occur due to instabilities such as the tearing mode or the coalescence instabilities though these last two situations are not discussed here.

1.5.1 Neutral Points

Consider the two-dimensional potential field described by

$$\mathbf{B} = y\,\hat{\mathbf{e}}_x + x\,\hat{\mathbf{e}}_y\,.$$

The magnetic field lines for such a field form a family of rectangular hyperbola and are drawn in Figure 1.5a. The limiting field lines $y = \pm x$, drawn by dashed lines in the figure, are called *separatrices* and divide the topologically distinct field line regions. The point at which the separatrices intersect is called a *magnetic neutral point* or null point and here the magnetic field equals zero. This type of neutral point is called 'X-type', for obvious reasons, and hence the field configuration is known as the X-type field.

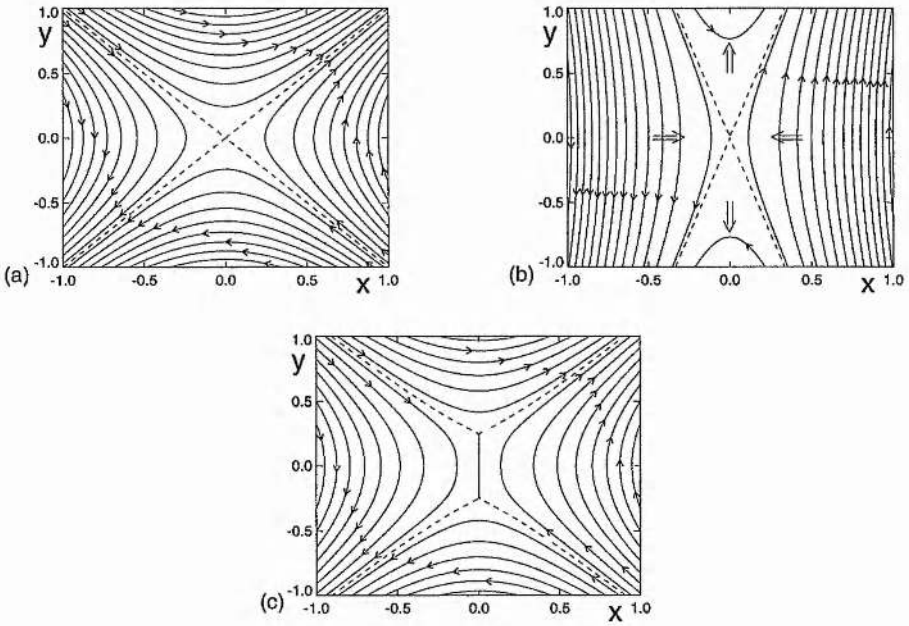

Figure 1.5: (a) The magnetic field due to an X-type neutral point. (b) A collapsed X-type neutral point with a magnetic pressure force acting inwards along the x axis and a tension force along the y-axis acting outwards. (c) the magnetic field with a small current sheet at the origin.

If the Lorentz force for the potential field is considered, Equation (1.15), it is found that the magnetic pressure and tension forces balance,

$$\mathbf{j} \times \mathbf{B} = \mathbf{0}\,. \tag{1.45}$$

However, Dungey discovered (Dungey, 1953) that if this field is perturbed slightly to give

$$\mathbf{B} = y\,\hat{\mathbf{e}}_x + (1+\alpha)\,x\,\hat{\mathbf{e}}_y\,,$$

where $\alpha > 1$, then the magnetic field is distorted as drawn in Figure 1.5b. The current density is

$$\mathbf{j} = \frac{1}{\mu_0}\nabla \times \mathbf{B} = \frac{\alpha}{\mu_0}\,\hat{\mathbf{e}}_z\,, \tag{1.46}$$

and so the Lorentz force becomes

$$\mathbf{j}\times\mathbf{B} = -\left(\frac{\alpha(1+\alpha)\,x}{\mu_0}\right)\hat{\mathbf{e}}_x + \left(\frac{\alpha y}{\mu_0}\right)\hat{\mathbf{e}}_y\,. \tag{1.47}$$

Thus there is a resulting force along the x-axis in the direction of the origin and a force along the y-axis away from the origin, so as to increase the perturbation further, implying the field is locally unstable. As the instability proceeds, the current density increases and intuitively one can envisage the collapsing X-type neutral point constricting itself into a thin sheet along the y-axis near to the origin (Figure 1.5c), making this a simple model for the formation of a current sheet.

1.5.2 Current Sheets

Green (1965) and Syrovatsky (1971) considered the slow deformation of the two-dimensional X-type field in a perfectly conducting limit. The magnetic field has components $B_x = y$ and $B_y = x$ and if a uniform electric field is imposed perpendicular to the xy-plane it drives a motion normal to the magnetic field. Ohm's law, Equation (1.6), becomes

$$\mathbf{E} + \mathbf{v}\times\mathbf{B} = \mathbf{0}\,. \tag{1.48}$$

If it is assumed that the motions with velocity $\mathbf{v}$ are much slower than the Alfvén velocity (v_A) and that the plasma pressure is small, the magnetic field will evolve through a series of equilibria with $\mathbf{j}\times\mathbf{B} = \mathbf{0}$. This implies that the current density ($\mathbf{j}$) must be zero everywhere except when $\mathbf{B} = \mathbf{0}$ where it must be non-zero to balance $\mathbf{E}$ in Ohm's law and hence there is a discontinuity in the field. This discontinuity develops into a *current sheet* as the deformation of the field continues and consists of a thin vertical sheet of current that flows in the direction of the electric field between $y = -L$ and $y = L$. The resulting magnetic field with the discontinuity is most elegantly represented as a cut in the complex plane. If $z = x + iy$, then the initial field may be written as

$$\mathcal{B}(z) = B_y + iB_x = z\,, \tag{1.49}$$

and the resulting field with the current sheet between $z = \pm iL$ becomes

$$\mathcal{B}(z) = \left(z^2 + L^2\right)^{\frac{1}{2}}\,. \tag{1.50}$$

Thus a current sheet may be formed from the collapse of an X-type neutral point. They may also be formed in other equilibrium fields, for instance:

where flux tubes have become braided or twisted through their complex foot point motions;

where loops of magnetic flux have emerged and interacted with the overlying field;

where topologically distinct arcades have moved in different directions creating a shear along separatrices;

also instabilities may give rise to current sheets: for example, a sheared field may become unstable to

a resistive instability, such as a tearing mode, forming a thin current sheet.

Depending on the rate of inflow (v_i) of the magnetic field, the current sheet will vary in size; shrinking if $v_i < \eta/l$, (where l is the width of the current sheet), growing if $v_i > \eta/l$. If $v_i = \eta/l$ the system is said to be in a steady state. Invariably there is an enhanced magnetic tension in the current sheet, which accelerates the plasma to an outflow speed of

$$v_A^* = \frac{B_e}{\sqrt{\mu\rho_c}}, \tag{1.51}$$

where v_A^* is the Alfvén velocity in m s^{-1}, B_e is the external field and ρ_c is the density in the current sheet. Using the conservation of magnetic flux (Equation 1.6) the rate at which flux enters the sheet must be equal to the rate at which it leaves such that

$$v_i B_i = v_A^* B_o, \tag{1.52}$$

where B_i and B_o are the inflow and outflow field strengths, respectively; thus if $v_i < v_A^*$ then $B_i > B_o$ and so magnetic energy must be converted to heat or kinetic energy.

The rate of reconnection is equal to the rate of change of flux in the diffusive region, $\partial\mathbf{A}/\partial t$. If the magnetic field ($\mathbf{B}$) is written as $\mathbf{B} = \nabla \times \mathbf{A}$, then from Faraday's Law (Equation (1.3))

$$\nabla \times \mathbf{E} = \frac{-\partial \mathbf{B}}{\partial t} = \frac{-\partial (\nabla \times \mathbf{A})}{\partial t}. \tag{1.53}$$

Thus,

$$| \mathbf{E} | = | \frac{\partial \mathbf{A}}{\partial t} |, \tag{1.54}$$

and $| \mathbf{E} |$ is therefore a measure of the rate of reconnection. The Alfvén Mach number (M_A) which is equal to v/v_A where v, is the velocity of the field and v_A, is the Alfvén velocity, is often used as a measure of the reconnection rate. This arises since, if the field is in a steady state the inflow speed is equal to the diffusive rate ($v_i = \eta/l$), so that,

$$\frac{\partial \mathbf{B}}{\partial t} = \mathbf{0}, \tag{1.55}$$

hence the electric field is uniform in space. Thus, from Ohm's law the rate of reconnection is

$$| \mathbf{E} | = | \mathbf{v} \times \mathbf{B} | = vB = M_A v_A B. \tag{1.56}$$

If the field (B) and Alfvén speed (v_A) are imposed at some inflow reference point, then M_A is a dimensionless measure of the reconnection rate.

In events such as solar flares and x-ray bright points the conversion of magnetic energy to heat energy takes place on the order of seconds to a few hours, thus a reasonably fast reconnection rate is required. There are many reconnection models, analytical and numerical, that have been designed to a achieve this fast rate and to explain how the magnetic energy is released. The old classic models of Sweet, Parker and Petschek (Sweet, 1958; Parker, 1957; Petschek, 1964) have now been replaced by a new generation of

reconnection models (Priest and Forbes, 1986; Priest and Lee, 1990; Strachan and Priest, 1994). These show that there are likely to be many different types of reconnection depending on the situation in which the reconnection is occurring since, the boundary conditions of a model can have a major effect on the rate of reconnection and the structure of the diffusive region and ejected plasma (Priest and Forbes, 1986). Note that the required magnetic Reynolds number, $R_m = 10^{12}$, in the solar corona cannot be reached with today's computers, thus realistic values of the resistivity in the diffusive region do not appear in numerical versions of these models (Yan *et al.* 1992; 1993). However, in the work reported in this thesis the actual reconnection mechanism is not detailed; instead it is assumed that where reconnection takes place it is fast and occurs in an extremely small current sheet near the neutral point.

A current sheet is a boundary between two plasmas which does not propagate. The magnetic field lies transverse to this boundary, so it may be considered as a tangential discontinuity across which no plasma may flow. When the current sheet is considered as part of an equilibrium structure the magnetic and plasma pressure force must balance on either side of the sheet, so

$$p_1 + \frac{B_1^2}{2\mu} = p_2 + \frac{B_2^2}{2\mu}, \tag{1.57}$$

where the subscripts 1 and 2 represent the opposite sides of the current sheet.

Inside a current sheet the resistivity and hence the diffusivity of the plasma facilitate the breaking and reconnecting of field lines. The rate at which this process proceeds is equal to η/l, where l is the width of the sheet through which the plasma is expelled.

1.6 Coronal Heating

As has already been noted (Section 1.2.3) the temperature of the solar corona is several million degrees Kelvin, some 10^2 - 10^3 times hotter than the surface of the Sun (Figure 1.2). This dramatic increase in temperature which takes place initially gradually and then much more suddenly in the transition region has not yet been properly explained. One of the first suggestions put forward was that acoustic waves, generated by turbulent motions in the convection zone, propagate upwards and steepen through the transition region to form a train of shocks before reaching the corona; this would transform their mechanical energy efficiently into thermal energy through viscous dissipation. However, short-period acoustic waves dissipate their energy at shocks in the lower chromosphere whilst the longer period waves, although forming shocks in the upper chromosphere and corona, are too scattered to have sufficient energy to heat these regions.

It is now believed that the magnetic field plays a dominant role in the heating of the corona, but the exact mechanisms which release this energy are very controversial. Evidence to support the magnetic field's involvement in the heating of the corona comes from x-ray images, which reveal that the hottest regions are those of strongest magnetic field and also from the fact that the motions of the plasma in the photosphere provide the magnetic flux with sufficient energy to heat the corona. The magnetic flux can be written mathematically in terms of the Poynting flux, since the magnetic field is much stronger than the electric field,

$$\begin{aligned} \mathbf{S} &= \frac{\mathbf{E} \times \mathbf{B}}{\mu} \\ &= \frac{-(\mathbf{v} \times \mathbf{B}) \times \mathbf{B}}{\mu} \approx \frac{vB^2}{\mu}. \end{aligned} \tag{1.58}$$

If a typical flow speed of approximately 0.1 km s^{-1} is taken with a mean field of 10^{-2} T (100 G) then **S** is of order 10^4 W m^{-2} (10^7 ergs cm^{-2} s^{-1}): similarly, if the flow speed is taken to be 0.4 km $^{-1}$ and the mean field as 5×10^{-3} T (50 G) or the flow speed as 1 km s^{-1} and the mean field as 3×10^{-3} T (30 G) then the Poynting flux is also approximately 10^4 W m^{-2} (10^7 ergs cm^{-2} s^{-1}). Thus the energy needed to balance radiation in the corona is easily greater than the estimated 3×10^2 W m^{-2} (10^5 ergs cm^{-2} s^{-1}) needed for a quiet region or the 5×10^3 W m^{-2} (5×10^6 ergs cm^{-2} s^{-1}) needed for an active region (Withbroe and Noyes, 1977).

So, having established that the magnetic field stores plenty of energy, the question still remains as to how this energy is dissipated. Firstly, this depends on the time scale of the photospheric motions (τ). Let the length of a typical coronal loop be L and the Alfvén velocity be v_A: then if τ is less than L/v_A the motions are considered rapid and MHD waves propagate upwards, whereas slow motions ($\tau > L/v_A$) result in the dissipation of energy directly from the magnetic field by current sheets and filaments. A typical loop length (L) of 10^6 m and a typical Alfvén speed of 3 km s^{-1} makes L/v_A approximately 5 minutes. In the following chapters of this thesis the typical photospheric motions are assumed to be approximately 0.5 km s^{-1}, so motions are slow ($\tau \approx$ a few hours), and the magnetic field evolves through a series of equilibria.

MHD waves, however, must not be forgotten: through mechanisms such as resonant absorption (in closed field line regions) and phase mixing of Alfvén waves (Heyvaerts and Priest, 1984) they may heat parts of the corona. In particular, in coronal holes where field lines are predominantly open there is little or no change in the magnetic field topology, so there exist few opportunities for current sheets to form and it is possible that the phase mixing of waves plays an important role in this area.

In regions of predominantly closed field lines, which show up in x-rays as closed loop structures, slow foot point motions mean that the coronal magnetic field has a tendency to evolve through a series of equilibria. The transformation from one equilibrium to another is not always steady and may result in the sudden dissipation of energy since the magnetic configurations often contain singularities such as current sheets. Active regions and related phenomena such as solar flares and prominences are therefore likely to be heated by reconnection.

X-ray bright points are also believed to be heated due to magnetic reconnection. A basic qualitative model for this process has been proposed by Priest *et al.* (1994) which satisfies many of the observed features linked with bright points and is outlined in Chapter 2. This provides a basis for much of the work in this thesis in which a possible mechanism for the heating of x-ray bright points is proposed that not only produces sufficient energy to power the bright points, but explains how this energy is released in the corona around the height at which the bright points occur.

1.7 Aims

The principle aim of the work in this thesis is to provide an explanation as to how x-ray bright points, an important part of the corona, are heated: thus it is hoped one third of the coronal heating dilemma may be solved. In addressing this problem work is also carried out to establish how a bright point's complex structure is formed and what part the associated cancelling magnetic feature plays in the creation of the bright point.

Chapter 2 establishes the original converging flux model, outlining all the related observations and produces both a qualitative and quantitative model for the interaction of two equal, but opposite polarity magnetic fragments in an overlying horizontal field in which a bright point and cancelling magnetic feature are created; the lifetime of the bright point plus the energy released are calculated. This model is then

extended to incorporate two unequal opposite polarity magnetic fragments and reveals new interesting features in Chapter 3. Chapter 4 studies the interaction of 3 poles to see if the extra magnetic fragments affect the amount of energy released during the bright point. In Chapter 5 the ideas from the converging flux model are used to explain the complex structure of two observed bright points from all available existing data. A model is then created incorporating the more complex field of a supergranule cell to study the formation of a bright point and cancelling magnetic feature through the various possible interactions of an ephemeral region bipole (Chapter 6). Finally, the thesis is concluded in Chapter 7 where the previous chapters are summarised and a discussion is presented on possible extensions to, and uses of, this work.

Chapter 2

The Basic Converging Flux Model

2.1 Introduction

A qualitative model for an x-ray bright point and associated cancelling magnetic feature proposed by Priest *et al.* in 1994, called the *converging flux model*, forms the basis for the next three chapters. This model is outlined in Section 2.2, first explaining the observations relating to both bright points and cancelling magnetic features and then describing the qualitative model they put forward. In Section 2.3 suggestions are made as to how more complex configurations may interact. A simple mathematical model is set up following the ideas of the first section in Section 2.4. The total energy released during the bright point is calculated (Section 2.5), as are the timings predicted for the bright point (Section 2.6). The forms through which the neutral points evolve are looked at in Section 2.7, with Section 2.8 concluding the work in this chapter.

2.2 Qualitative X-ray Bright Point Model

It is only in the past two to three years that researchers have really begun to accept that bright points are associated with cancelling magnetic features and until this year no model had been proposed explaining their formation and association. Bright points were only discovered in 1970 and cancelling magnetic features in 1984, so there has been little work done on either of the features and even less on observing both simultaneously. Nevertheless Priest *et al.* (1994), in summarising all the existing observations, noticed that the observations relating to bright points appear to fall into three categories from which a qualitative model was established explaining the different topologies through which the magnetic field evolves during the three phases.

Observations

First there is the *pre-interaction phase* where magnetic fragments of opposite polarity slowly approach one another in the photosphere. The fragments have typical diameters of 5 Mm and converge at speeds of approximately 0.3 km s^{-1}. In the overlying chromosphere very few fibrils are seen linking the opposite polarity fragments (Martin *et al.*, 1985; Martin, 1988): in fact as the fragments approach one another fibrils have been observed to turn away from the fragments so as not to link them (Martin, 1986).

Secondly, an *interaction phase* occurs in which energy is released in the corona as an x-ray bright point or, in He 10830, as a dark point. The bright point is seen to begin before the fragments in the

photosphere come into contact and cancel (Harvey, 1985; Webb *et al.*, 1993) and lasts for between 2 and 48 hrs (Golub *et al.*, 1974), with a mean lifetime of 8 hrs. More recent results from Yohkoh's soft x-ray telescope (SXT) estimate lifetimes of 2 mins - 5 days for the bright points with a mean of 12 hrs (Harvey et al., 1992). Also from these Yohkoh images, long hot loops and x-ray jets have been observed in association with flaring bright points (Shibata *et al.*, 1992a,b; Uchida, 1993; Tsuneta, 1993; Strong *et al.*, 1992); the jets vary from 5 - 400 Mm long and have velocities of 30 - 300 km s^{-1}.

Finally the *cancellation phase* is observed. Here, between the photospheric fragments, a steepening magnetic field gradient develops (Martin, 1986) and slowly the fragments mutually reduce in flux and form a cancelling magnetic feature (20% of cancelling magnetic features are associated with bright points and 72% of bright points with cancelling magnetic features (Webb *et al.*, 1993)). Cancelling magnetic features last over a range of lifetimes depending on how much flux is being cancelled and at what speeds the fragments are approaching, which in turn is dependent on what type of fragments are interacting (Section 1.2.1). In general, however, cancelling magnetic features last for 1 - 36 hrs; the fragments have diameters of between 1 and 10 Mm and converge at 0.1 - 0.3 km s^{-1}. The fragments typically have fluxes of between 10^{10} and 5×10^{11} Wb (10^{18} and 5×10^{19} Mx) with approximately 1 - 2 $\times 10^{10}$ Wb (1 - 2 $\times 10^{18}$ Mx) of flux lost per hour during the cancellation (Wang *et al.*, 1988). Hermans and Martin (1986) noticed that sometimes, well after the cancellation has begun, a tiny filament is formed and erupts, and/or a small chromospheric brightening (flare) is seen. Most of the little filaments last for only tens of minutes to a few hours. It is estimated, with the present resolution, that approximately 10% of cancelling magnetic features have associated tiny erupting filaments, but as yet there have been no studies linking bright points to them. Also many ejecta associated with bright point and dark point flares are like surges or jets. From Webb *et al.* (1993) it was found that the cancellation phase overlaps the interaction phase.

Qualitative Model

From all these observations Priest *et al.* (1994) suggested the key physical processes central to most bright points which are depicted in the qualitative diagram of Figure 2.1. The model has several phases (relating to the observations): a *pre-interaction phase*, an *interaction phase* and a *cancellation phase*. In the *pre-interaction phase* the two opposite polarity magnetic fragments are situated in an overlying field far apart so as not to be connected and are approaching one another slowly, in agreement with the observations (speed of approach approximately 0.3 km s^{-1}, Alfvén speed about 100 km s^{-1} such that the magnetic field evolves quasi-statically) (Figure 2.1a). If the overlying field has a component out of the plane, then this will agree with the observed lack of connecting fibrils. As the fragments close in on each other they eventually form an X-type neutral point between them in the photosphere (Figure 2.1b), which during the *interaction phase* rises as the fragments now interact and reconnect (Figure 2.1c). The energy liberated from this coronal reconnection appears as an x-ray bright point that starts well before the fragments come into contact and lasts during their continued convergence; the brighter inner core is likely to appear near the X-type neutral point. During the reconnection process that powers the bright point, evaporation injects hot plasma along the newly reconnected field lines. Some of these field lines are connected to the far-off fragments that produce the overlying field: when these are injected with hot plasma they may create x-ray jets and very long hot loops, as observed to be linked with bright points (Figure 2.1d). Evidence for this type of behaviour comes from Shibata *et al.* who, in 1992, suggested that these jets are produced by evaporation driven by reconnection between emerging flux and a pre-existing coronal field. In Priest *et al.*'s model the long field lines extend out equally from each side of the bright point, but this, of course, will not always be the case in less symmetric situations where a single loop would brighten, as is often observed. Finally the fragments come into contact and the *cancellation*

phase begins with reconnection in the photosphere (Figure 2.1e). The bright point lasts until at least the first part of the cancellation starts. The fluxes decrease until either the fragments cease to approach one another or until one or both fragments have been completely cancelled. In the situation shown in the figure below, the initial fragments are of equal, but opposite magnetic flux, so the final state has a horizontal flux tube above the photosphere and another flux tube that remains below the photosphere (Figure 2.1f).

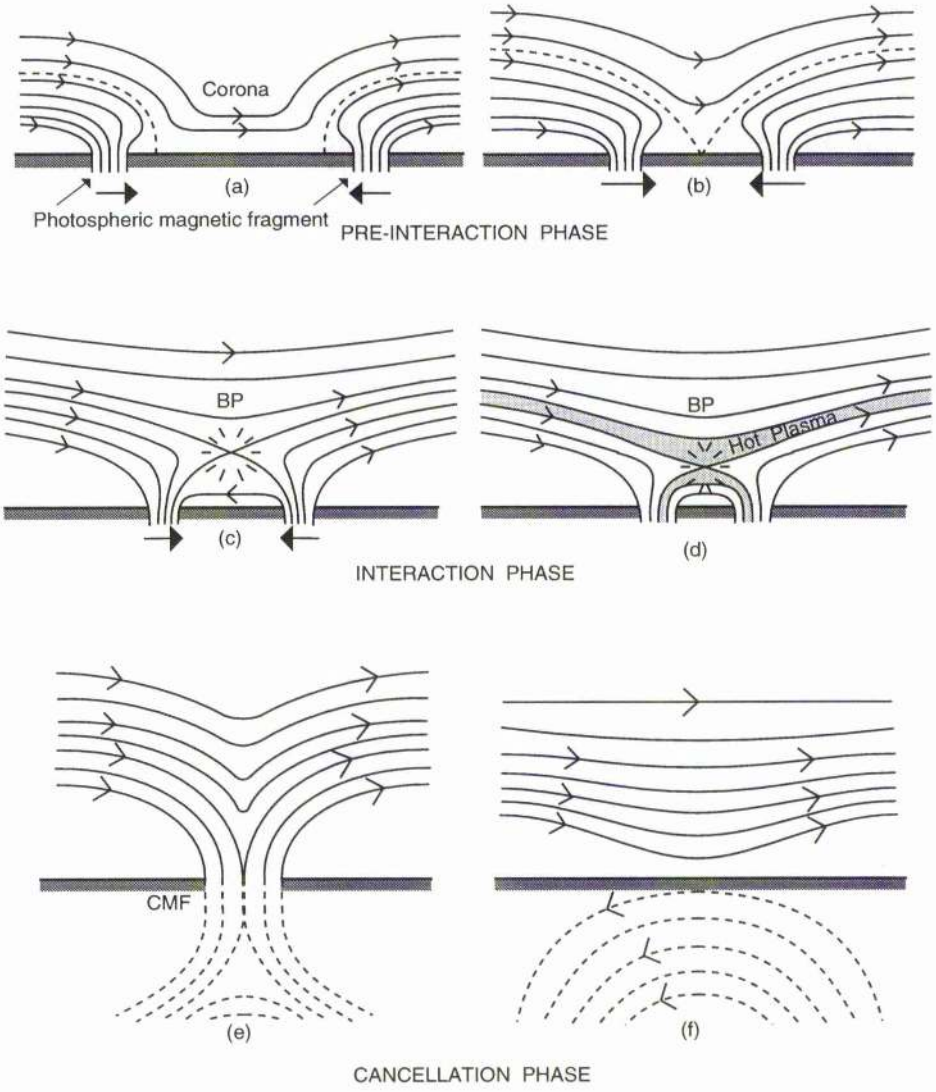

Figure 2.1: A qualitative picture of the converging flux model. (a) and (b) show the *pre-interaction phase* where the fragments, initially unconnected, move together until their first field lines meet to form a neutral point. The *interaction phase* is depicted by (c) and (d) and creates the bright point as the fragments move together. Reconnection in the photosphere shown by (e) is the *cancellation phase*, which when completed leaves us with the final state shown in (f) (Priest *et al.*, 1994).

2.3 Other Configurations

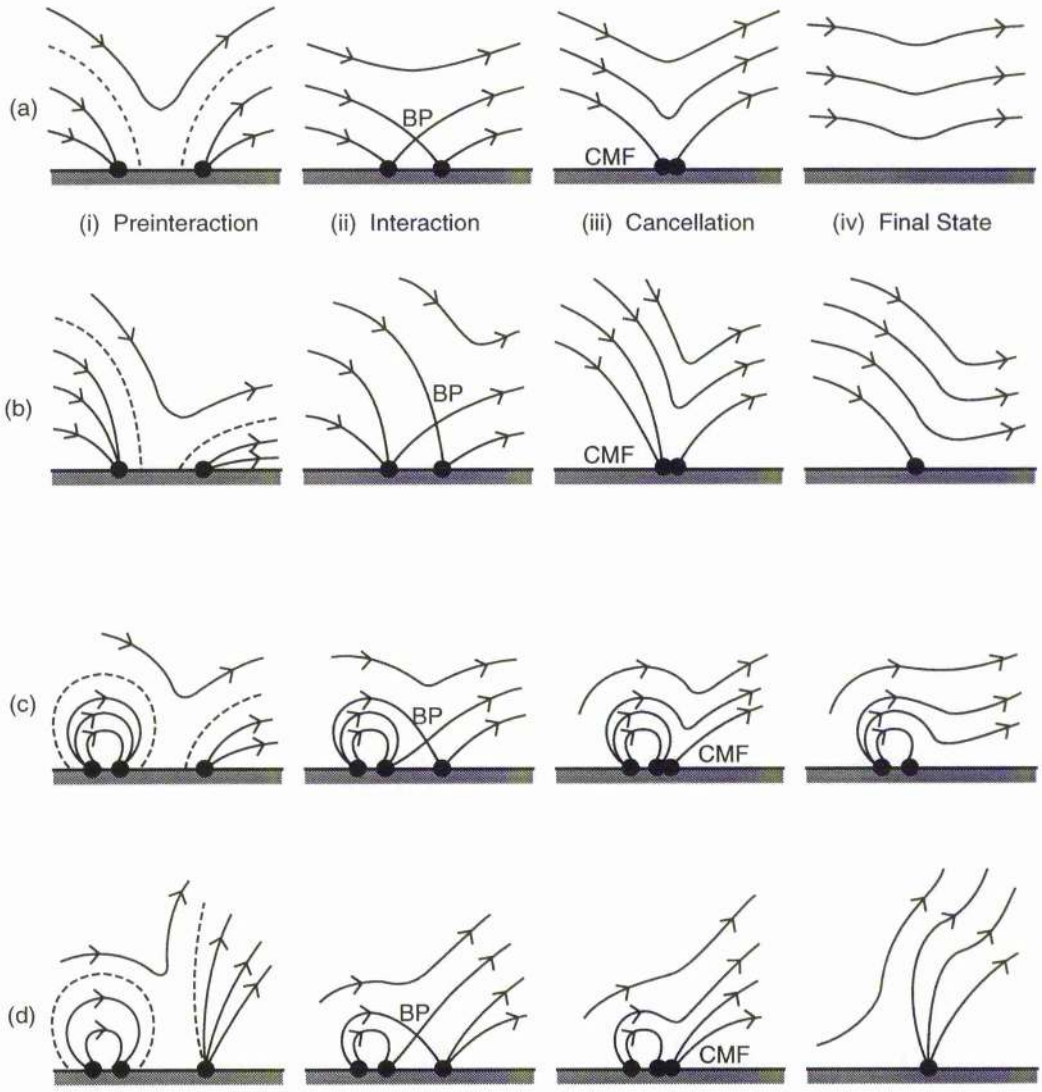

Figure 2.2: The magnetic configurations for (a) two equal sources, (b) two unequal sources, (c) a strong bipolar pair of fragments interacting with a weak field region and (d) a weak bipolar pair interacting with a stronger fragment, as they evolve through the (i) pre-interaction, (ii) interaction, (iii) cancellation and (iv) final phases.

Priest *et al.* (1994) also suggest in their paper how more complex configurations might interact since it is unlikely that both magnetic fragments will be exactly equal in strength (Figure 2.2). They sketch the structure of the magnetic field in the pre-interaction, interaction, cancellation and final states for four different cancelling magnetic features. In each case one or both elements may be moving, but this does not effect the resulting magnetic configurations, since it is the relative motion that counts. In Figure 2.2a the two magnetic fragments are assumed to be of equal strength, as described earlier, and seen most commonly in interactions between network-network and intracell-intracell cancellations. Here the final state involves just that of the background field. Figure 2.2b also depicts two magnetic fragments, but this

time one is much stronger (larger) than the other. Again the interaction evolves through the same phases, though here in the final state the residue of the larger fragment is left after cancellation in the overlying field. This type of cancellation is most likely to occur between strong network fields and weak intracell fields. The interaction of a strong ephemeral region with a weak intracell field is shown in Figure 2.2c where one fragment of the ephemeral region reconnects with the intracell source creating the bright point and cancelling magnetic feature and leaving the two, now unequal, ephemeral region fragments in the overlying field. Finally, in Figure 2.2d, a weaker ephemeral region cancels with a strong network field. This time, after the bright point and cancellation have taken place through the usual stages, the weaker ephemeral region fragment completely cancels with the stronger network field leaving two sources of the same strength, namely the remaining ephemeral region fragment and the reduced network field region, which then coalesce to produce a source of equal strength to the original network field region.

2.4 Basic Model

The key to Priest *et al.*'s model (1994) is the overlying field. They realised that the important point is to have the opposite polarity magnetic fragments initially unconnected to satisfy the observations and to enable energy to be released as they link up and create the bright point. So a model involving just two fragments, one positive and the other negative is not sufficient to model a bright point, for obviously the fragments are always connected and there is never any change in the topology of the magnetic field or energy release. Also the magnetic fragments below the bright point are observed to converge at about 0.3 km s^{-1}, much slower than the Alfvén speed in the photosphere of 10 - 100 km s^{-1}, so it is reasonable to assume that as the magnetic fragments move closer the magnetic field evolves through a series of quasi-static states.

Thus in this two-dimensional basic model (following the principles of the Priest *et al.* converging flux situation (1994)) the two magnetic sources are modelled as line sources, one of strength f, the other of strength $-f$, positioned on the x-axis at a and $-a$, respectively, where the x-axis is in the plane of the photosphere and the y-axis is directed vertically upwards. There is also a background horizontal field of strength B_o overlying these fragments, such that the magnetic field for this situation, written in complex notation, is

$$\begin{aligned} \mathcal{B}_p(\mathrm{z}) &= B_{py}(x,y) + \mathrm{i}B_{px}(x,y) \\ &= \mathrm{i}B_o + \frac{\mathrm{i}f}{\pi(\mathrm{z}-a)} - \frac{\mathrm{i}f}{\pi(\mathrm{z}+a)}, \end{aligned}$$

where $\mathrm{z} = x + \mathrm{i}y$, and B_{px} and B_{py} are, respectively, the components of the potential magnetic field in the horizontal and vertical directions. Rearranging one finds

$$\mathcal{B}_p(\mathrm{z}) = \frac{\mathrm{i}B_o\left(\mathrm{z}^2 - x_n^2\right)}{\left(\mathrm{z}^2 - a^2\right)}, \tag{2.1}$$

where $x_n^2 = a^2 - 2af/\pi B_o$. The associated flux function (A_p) which equals

$$A_p(x,y) = -\mathcal{R}e\int_0^{x+\mathrm{i}y} \mathcal{B}_p(\mathrm{z})\,\mathrm{dz}, \tag{2.2}$$

may be calculated simply following the method shown in Appendix A giving

$$A_p = B_o \left[y + \frac{(a^2 - x_n^2)}{2a} \mathrm{Arg}\left(\frac{a-z}{a+z}\right) \right] , \tag{2.3}$$

where $-\pi \leq \mathrm{Arg}\,(z) \leq \pi$.

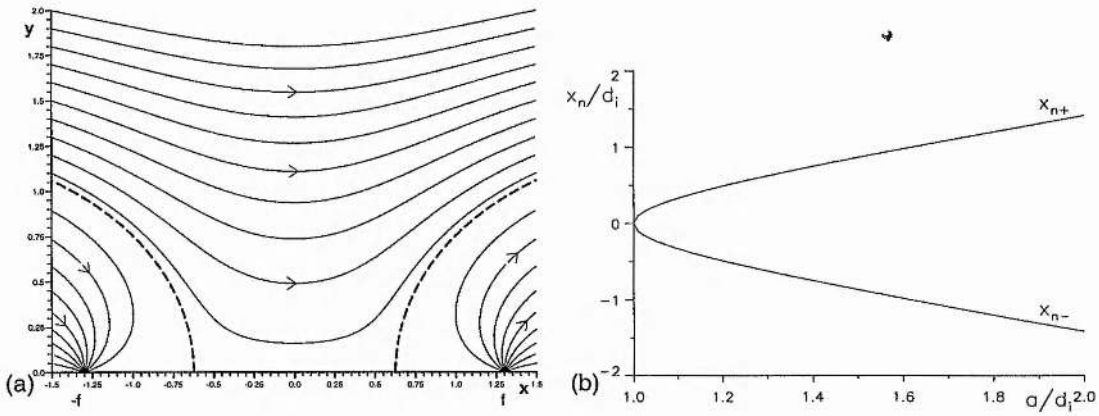

Figure 2.3: (a) The magnetic field in the pre-interaction phase with poles of strength $f = \pi B_o/2$ situated at a half separation $a = 1.3$ in an overlying field of strength $B_o = 10^{-3}$ T (10 G). (b) The half channel width (x_n) normalised with respect to the interaction distance d_i versus the normalised half separation (a/d_i).

The qualitative model described requires the fragments to be initially unconnected to satisfy the observations and to create the first stage of the bright point. Thus the *pre-interaction phase* is established if $x_n^2 > 0$, that is if $a > 2f/\pi B_o$ and its magnetic field configuration is drawn in Figure 2.3a. There are two neutral points on the photosphere at

$$z_n = \pm x_n = \pm\sqrt{a^2 - \frac{2af}{\pi B_o}} , \tag{2.4}$$

which mark the edges of the channel between the fragments containing the overlying field. Figure 2.3b shows how the half channel width (x_n) varies with respect to the half separation (a) of the poles as the field evolves equipotentially.

As the half separation (a) of the fragments decreases, so does the width of the channel between them, until it completely disappears to leave only one neutral point at $z_n = 0$, the origin. At this point the magnetic fragments come into contact for the first time: the fragments are then said to be situated at a half separation (d_i) which is referred to as the *interaction distance*, where

$$d_i = \frac{2f}{\pi B_o} . \tag{2.5}$$

The corresponding complex magnetic field ($\mathcal{B}_p\,(z)$) for this configuration is

$$\mathcal{B}_p\,(z) = \frac{\mathrm{i}B_o z^2}{(z^2 - a^2)} , \tag{2.6}$$

and the flux function (A_p), which equals (Appendix A)

$$A_p = B_o \left[y + \frac{a}{2} \mathrm{Arg}\left(\frac{a-z}{a+z} \right) \right] , \tag{2.7}$$

is drawn in Figure 2.4.

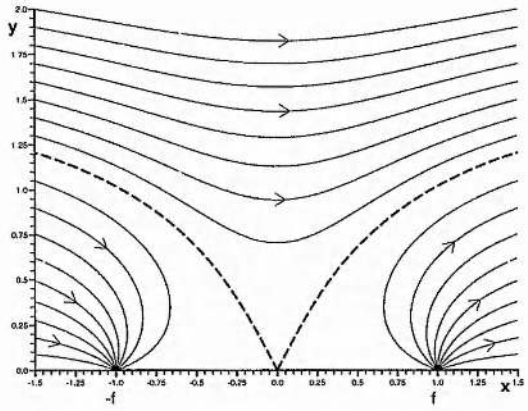

Figure 2.4: The magnetic field when the fragments of strength $f = \pi B_o/2$ are positioned at the interaction distance $d_i = 1.0$ in an overlying field $B_o = 10^{-3}$ T (10 G).

As the magnetic fragments come closer, a decreases further such that $a < 2f/\pi B_o$ and the magnetic field and flux function become

$$\mathcal{B}_p(z) = \frac{\mathrm{i}B_o\left(z^2 + y_n^2\right)}{\left(z^2 - a^2\right)} , \tag{2.8}$$

$$A_p = B_o \left[y + \frac{a^2 + y_n^2}{2a} \mathrm{Arg}\left(\frac{a-z}{a+z} \right) \right] , \tag{2.9}$$

where $y_n^2 = 2af/\pi B_o - a^2 = a\left(d_i - a\right)$ and the neutral points now appear at

$$z_n = \pm \mathrm{i} y_n = \pm \mathrm{i} \sqrt{\frac{2af}{\pi B_o} - a^2} . \tag{2.10}$$

Thus it is found that there is one neutral point at a height (y_n) above the photosphere as shown in Figure 2.5a: this is called the *interaction phase*. As the fragments move closer together to $a < d_i$, it is assumed that reconnection takes place continuously in a very small current sheet at the neutral point; the topology of the magnetic field changes and the two magnetic fragments become increasingly connected. The energy released from this process will power the bright point: thus the neutral point corresponds to the position of the bright point. The actual mechanism for this reconnection is not described, but from observations the temperature and the density of a bright point fluctuate (Habbal *et al.*, 1990), therefore reconnection may occur through an impulsive bursty regime (Priest, 1986).

The height of the neutral point (y_n) may be plotted against a, the half separation of the poles, Figure 2.5b. As a decreases the neutral point initially rises to a maximum height of $d_i/2$ above the photosphere at a half separation of $a = d_i/2$, then decreases to the photosphere which it reaches when $a = 0$. When the two fragments are completely connected to each other ($a = 0$) they cancel to leave the background overlying horizontal field.

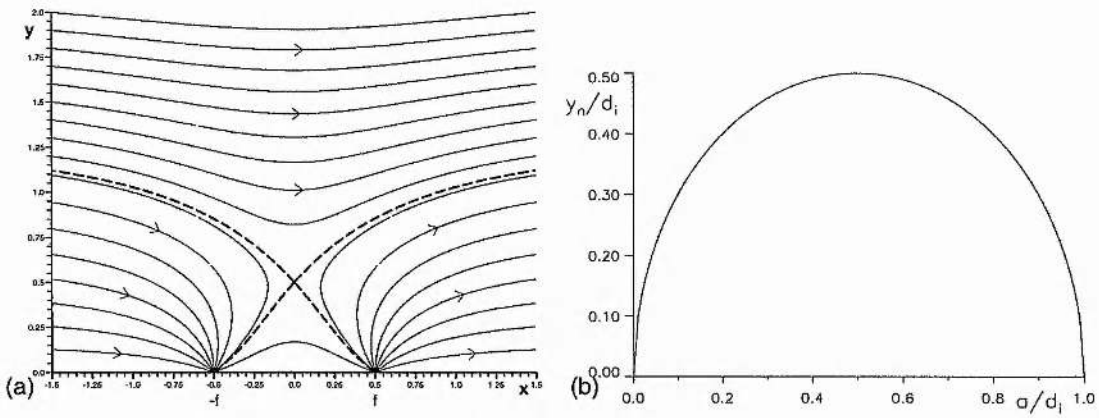

Figure 2.5: (a) The interaction phase magnetic field due to poles of strength $f = \pi B_o/2$ situated at a half separation $a/d_i = 0.5$ in an overlying field of strength $B_o = 10^{-3}$ T (10 G). (b) The normalised neutral point height y_n/d_i above the photosphere for the normalised half separations a/d_i between 0.0 and 1.0.

2.5 Free Energy

2.5.1 Formation of a Current Sheet

In the preceeding scenario the magnetic field was always taken to be potential and thus does not contain any free energy. If, however, it is assumed that there is no reconnection as the fragments move together, the topology of the field is preserved, so that when $a \leq d_i$ a current sheet forms. The energy (W) of this new field with the current sheet will then be greater than that of the potential field (W_p) by the amount released through reconnection, which is equivalent to the amount expended during the total bright point. One may, therefore, conduct a thought experiment in which a current sheet is grown purely to find out if there is sufficient energy available from the reconnection process to power the bright point and not because it is believed that a current sheet extending from the photosphere to the corona really exists.

Let us, therefore, assume that no reconnection occurs as the fragments converge. The current sheet will start growing when the fragments first come into contact ($a = d_i$). At this point there is a neutral point on the photosphere at the origin, since the system is basically symmetric about the y-axis: this must be one end point of the current sheet if the topology of the field is to be preserved, and the current sheet must grow vertically upwards along the y-axis to a height h, say. Also, if a configuration with the same normal field along the x-axis as in the potential case is to be maintained, then one can calculate the configuration by including an image current sheet along the y-axis from 0 to $-h$. Thus from Titov's (1992) paper, which presents a method of calculating two-dimensional potential magnetic configurations with current sheets, the resulting magnetic field has the form

$$\mathcal{B}(z) \;=\; \mathcal{P}(z)\,\mathcal{Q}(z)\;,$$

where

$$\mathcal{Q}(z) \;=\; z\left(z^2+h^2\right)^{\frac{1}{2}}\;, \tag{2.11}$$

and

$$\mathcal{P}(z) = \frac{1}{\mathrm{i}\pi}\int_{-\infty}^{\infty}\frac{B_y(\xi,0)}{(\xi-z)\,\mathcal{Q}(\xi)}\mathrm{d}\xi\,. \tag{2.12}$$

In this situation the normal component of the magnetic field along the x-axis, $B_y(\xi,0)$ is equal to

$$B_y(\xi,0) = f\left[-\delta(\xi+a)+\delta(\xi-a)\right]\,, \tag{2.13}$$

so that

$$\mathcal{P}(z) = \frac{\mathrm{i}2f}{\pi\left(a^2+h^2\right)^{\frac{1}{2}}\left(z^2-a^2\right)}\,, \tag{2.14}$$

and

$$\mathcal{B}(z) = \frac{\mathrm{i}2fz\left(z^2+h^2\right)^{\frac{1}{2}}}{\pi\left(a^2+h^2\right)^{\frac{1}{2}}\left(z^2-a^2\right)}\,. \tag{2.15}$$

Now this magnetic field with the current sheet must be such that at large distances it approximates to a uniform field of strength B_o, as in the potential situation. Thus as $z \longrightarrow \infty$

$$\mathcal{B}(z) \longrightarrow \frac{\mathrm{i}2f}{\pi\left(a^2+h^2\right)^{\frac{1}{2}}} \longrightarrow \mathrm{i}B_o\,, \tag{2.16}$$

which implies that

$$B_o = \frac{2f}{\pi\left(a^2+h^2\right)^{\frac{1}{2}}}\,, \tag{2.17}$$

or substituting in for the interaction distance d_i,

$$a^2 + h^2 = d_i^2\,. \tag{2.18}$$

Rearranging, a relation for the height of the current sheet in terms of a and d_i may be found, namely,

$$h = \sqrt{d_i^2 - a^2}\,, \tag{2.19}$$

and so, at $a = d_i$, the height of the current sheet is zero and as $a \to 0$, h tends to a maximum height of d_i (Figure 2.6b). The magnetic field for the current sheet configuration, therefore, becomes

$$\mathcal{B}(z) = \frac{\mathrm{i}B_o z\left(z^2+h^2\right)^{\frac{1}{2}}}{\left(z^2-a^2\right)}\,, \tag{2.20}$$

and is drawn in Figure 2.6a when the poles are at $a = \pm 0.5$, d_i is assumed to be 1.0 and $B_o = 10^{-3}$ T (10 G).

As before, the flux function (A) is calculated and using the substitution $w^2 = z^2 + h^2$ it is found that

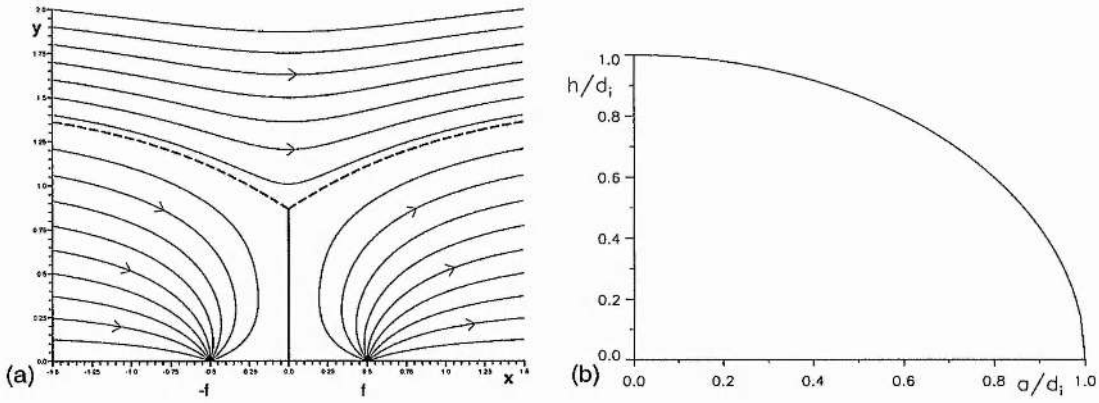

Figure 2.6: (a) The magnetic field configuration due to a current sheet of height $h = \sqrt{0.75}$ where the poles, strength $f = \pi B_o/2$, are situated at a half separation $a/d_i = 0.5$ in an overlying field of strength $B_o = 10^{-3}$ T (10 G). (b) The normalised current sheet height (h/d_i) is plotted against the normalised half separation (a/d_i).

$$A = -\mathcal{R}e \int_h^{\left(z^2+h^2\right)^{\frac{1}{2}}} \frac{\mathrm{i}B_o w^2}{w^2 - d_i^2} \mathrm{d}w \,, \tag{2.21}$$

which may be evaluated to give

$$A = B_o \left[Y + \frac{d_i}{2} \mathrm{Arg}\left(\frac{d_i - (X + \mathrm{i}Y)}{d_i + (X + \mathrm{i}Y)} \right) \right] , \tag{2.22}$$

where $X = \left(\left(\alpha^2 + \beta^2\right)^{\frac{1}{2}} /2 + \alpha/2 \right)^{\frac{1}{2}}$, $Y = \left(\left(\alpha^2 + \beta^2\right)^{\frac{1}{2}} /2 - \alpha/2 \right)^{\frac{1}{2}}$ and $\alpha = x^2 - y^2 + h^2$, $\beta = 2xy$. It can therefore be shown that when $y = 0$,

$$A(x,y) = \begin{cases} -f & x \leq -a \\ 0 & -a < x < a \\ -f & x \geq a \end{cases} , \tag{2.23}$$

and when $x = 0$

$$A(0,y) = \begin{cases} 0 & 0 < y < h \\ B_o \left(y^2 - h^2\right)^{\frac{1}{2}} + \frac{B_o d_i}{2} \mathrm{Arg}\left(\frac{d_i - \mathrm{i}\left(y^2-h^2\right)^{\frac{1}{2}}}{d_i + \mathrm{i}\left(y^2-h^2\right)^{\frac{1}{2}}} \right) & y \geq h \end{cases} . \tag{2.24}$$

If the character of this magnetic field is now investigated one expects to find that near $z = \pm a$ the magnetic field will be the same as that due to the pole there and so as $z \to a$

$$B(z) \longrightarrow \frac{\mathrm{i}B_o \left(a^2 + h^2\right)^{\frac{1}{2}}}{2(z-a)} \longrightarrow \frac{\mathrm{i}f}{\pi(z-a)} , \tag{2.25}$$

as expected, by substitution of Equations (2.18) and (2.5). Similarly as $z \to -a$,

$$\mathcal{B}(z) \longrightarrow \frac{-iB_o\left(a^2+h^2\right)^{\frac{1}{2}}}{2(z+a)} = \frac{-if}{\pi(z+a)}, \tag{2.26}$$

but, note here, that care must be taken as to which side of the current sheet is being considered so that the correct sign of $\left(z^2+h^2\right)^{\frac{1}{2}}$ is chosen.

Also a check can be made to ensure that the flux crossing the upper half of the y-axis between 0 and ∞ in the initial magnetic field configuration, before the current sheet appears, is equal to that crossing the upper half of the y-axis with the current sheet as is expected if the frozen-in flux condition is satisfied:

$$\begin{aligned} F_p &= \int_0^\infty B_{px}\,|_{x=0}\,dy \\ &= \int_0^\infty \mathcal{I}m\left[\mathcal{B}_p(iy)\right]dy \\ &= \int_0^\infty \frac{B_o y^2}{y^2+d_i^2}dy \qquad (2.27) \\ &= \int_0^\infty B_o dy - \frac{B_o d_i \pi}{2} \\ &= \int_0^\infty B_o dy - f\,. \qquad (2.28) \end{aligned}$$

Thus the flux (F_p) is equal to that from the overlying magnetic field of strength B_o minus the flux f that goes into the sink at $z=-a$, as expected.

The flux across the y-axis in the magnetic field configuration with the current sheet is

$$\begin{aligned} F &= \int_0^\infty B_x\,|_{x=0}\,dy \\ &= \int_0^\infty \mathcal{I}m\left[\mathcal{B}(iy)\right]dy \\ &= \int_h^\infty \frac{B_o y\left(y^2-h^2\right)^{\frac{1}{2}}}{y^2+a^2}dy\,, \qquad (2.29) \end{aligned}$$

since, if $0<y<h$ then $y^2-h^2<0$ and there is only a B_y component along the y-axis, whereas if $y>h$ then $y^2-h^2>0$ and there is only a B_x component. Using the substitution $Y^2=y^2-h^2$ the above equation becomes

$$F = \int_0^\infty \frac{B_o Y^2}{Y^2+d_i^2}dY\,, \tag{2.30}$$

which is identical to Equation (2.27). Thus the flux equals

$$F = \int_0^\infty B_o dy - f = F_p\,, \tag{2.31}$$

and so is indeed preserved, indicating that the frozen-in flux condition is satisfied.

2.5.2 Free Magnetic Energy

To find the energy stored in the current sheet a similar method to that by Low and Hu (1983) is adopted. The total magnetic energy in a volume (V) with boundary (S) is

$$W = \frac{1}{2\mu}\int_V B^2 \mathrm{d}V \,. \tag{2.32}$$

Since our field configuration is potential, save at the current sheet, the magnetic field ($\mathbf{B}$) may be written as

$$\mathbf{B} = \nabla \times \mathbf{A} \,, \tag{2.33}$$

where $\mathbf{A} = A\hat{\mathbf{e}}_z$ and A is the flux function. Thus Equation (2.32) becomes

$$\begin{aligned} W &= \frac{1}{2\mu}\int_V \mathbf{B}\cdot(\nabla\times\mathbf{A})\,\mathrm{d}V \\ &= \frac{1}{2\mu}\int_V \mathbf{A}\cdot(\nabla\times\mathbf{B})\,\mathrm{d}V \;+\; \frac{1}{2\mu}\int_V \nabla\cdot(\mathbf{A}\times\mathbf{B})\,\mathrm{d}V \,. \end{aligned} \tag{2.34}$$

By application of Gauss' Divergence Theorem and Ampère's Law (Equation (1.5)),

$$\nabla \times \mathbf{B} = \mu\mathbf{j} \,, \tag{2.35}$$

where $\mathbf{j} = j\hat{\mathbf{e}}_z$ and j is the current density, the energy may now be written as

$$W = \frac{1}{2}\int_V \mathbf{A}\cdot\mathbf{j}\,\mathrm{d}V \;-\; \frac{1}{2\mu}\int_S (\mathbf{A}\times\mathbf{B})\cdot\mathrm{d}\mathbf{S} \,. \tag{2.36}$$

In this two-dimensional model it is the energy stored above the photosphere that is of interest. Therefore V is taken to be the upper half of the xy plane with depth d_i, say, in the z direction and $\mathrm{d}\mathbf{S}$ is the outward normal surface element to the boundary. So, letting I_c be the total current flowing in the current sheet and A_c be the constant value of the flux function along the current sheet, the total magnetic energy for the volume becomes

$$\begin{aligned} \frac{W}{d_i} &= \frac{1}{2}I_cA_c \;+\; \frac{1}{2\mu}\int_{-\infty}^{\infty}[\mathbf{A}\times\mathbf{B}]_{y=0}\cdot-\hat{\mathbf{e}}_y\mathrm{d}x + \frac{1}{2\mu}\int_0^{\infty}[\mathbf{A}\times\mathbf{B}]_{x\to\infty}\cdot\hat{\mathbf{e}}_x\mathrm{d}y \\ &\quad + \frac{1}{2\mu}\int_{\infty}^{-\infty}[\mathbf{A}\times\mathbf{B}]_{y\to\infty}\cdot\hat{\mathbf{e}}_y\mathrm{d}x + \frac{1}{2\mu}\int_{\infty}^{0}[\mathbf{A}\times\mathbf{B}]_{x\to-\infty}\cdot-\hat{\mathbf{e}}_x\mathrm{d}y \,. \end{aligned} \tag{2.37}$$

Now $\mathbf{A}\times\mathbf{B} = -AB_y\,\hat{\mathbf{e}}_x + AB_x\,\hat{\mathbf{e}}_y$, and so

$$\begin{aligned} \frac{W}{d_i} &= \frac{1}{2}I_cA_c \;-\; \frac{1}{2\mu}\int_{-\infty}^{\infty}[AB_x]_{y=0}\,\mathrm{d}x - \frac{1}{2\mu}\int_0^{\infty}[AB_y]_{x\to\infty}\,\mathrm{d}y \\ &\quad - \frac{1}{2\mu}\int_{-\infty}^{\infty}[AB_x]_{y\to\infty}\,\mathrm{d}x - \frac{1}{2\mu}\int_0^{\infty}[AB_y]_{x\to-\infty}\,\mathrm{d}y \,. \end{aligned} \tag{2.38}$$

This may be further reduced, since at infinity the magnetic field with the current sheet approximates that of a horizontal field, $\mathbf{B} = B_o\,\hat{\mathbf{e}}_x$. Thus, as $x \to \pm\infty$, the magnetic field has no B_y component. Also, as $y \to \infty$, the magnetic field is horizontal, so the flux function A_∞ that is found will be constant with respect to x. Thus taking $A_c = 0$ without loss of generality (Equation (2.24))

$$\frac{W}{d_i} = -\frac{1}{2\mu}\int_{-\infty}^{\infty}[AB_x]_{y=0}\,\mathrm{d}x - \frac{1}{2\mu}\int_{-\infty}^{\infty}A_\infty B_o \mathrm{d}x\,. \tag{2.39}$$

The potential magnetic field, $\mathbf{B}_p = \nabla \times A_p\,\hat{\mathbf{e}}_z$, for the same situation has the same normal field on $y = 0$ as the magnetic field $\mathbf{B}$ above, such that $A_p = A$ on $y = 0$ and $\mathbf{B}_p$ has a corresponding horizontal field at infinity of strength B_o, so $A_{p\infty} = A_\infty$. Therefore the potential magnetic energy (W_p) is

$$\frac{W_p}{d_i} = -\frac{1}{2\mu}\int_{-\infty}^{\infty}[AB_{px}]_{y=0}\,\mathrm{d}x - \frac{1}{2\mu}\int_{-\infty}^{\infty}A_\infty B_o \mathrm{d}x\,, \tag{2.40}$$

and the free magnetic field stored (W_F), the difference between the total and potential energies, is

$$W_F = -\frac{d_i}{2\mu}\int_{-\infty}^{\infty}[A\,(B_x - B_{px})]_{y=0}\,\mathrm{d}x\,. \tag{2.41}$$

Now the total magnetic field is made up of three components

$$\mathbf{B} = \mathbf{B}_p + \mathbf{B}_c + \mathbf{B}_{ci}\,, \tag{2.42}$$

where $\mathbf{B}_p$ is, of course, the potential field due to the sources, $\mathbf{B}_c$ is the field due to the current sheet and $\mathbf{B}_{ci}$ is the field due to the image current sheet. On $y = 0$, $\mathbf{B}_{cx} = \mathbf{B}_{cix}$ and the free energy may be written elegantly as

$$W_F = -\frac{d_i}{2\mu}\int_{-\infty}^{\infty}2\,[AB_{cx}]_{y=0}\,\mathrm{d}x\,, \tag{2.43}$$

which, since AB_{cx} is an even function of x, becomes

$$W_F = -\frac{2d_i}{\mu}\int_{0}^{\infty}[AB_{cx}]_{y=0}\,\mathrm{d}x\,. \tag{2.44}$$

On the x-axis, $y = 0$,

$$A\,(x,0) = \begin{cases} 0 & 0 \le x < a \\ -f & a \le x < \infty \end{cases}\,, \tag{2.45}$$

and B_{cx} may be calculated by use of the Biot-Savart Law for a two-dimensional geometry, that is

$$\mathbf{B}_c = \frac{\mu}{2\pi}\int_c \frac{\mathbf{j}\times\mathbf{r}}{|\,\mathbf{r}\,|^2}\mathrm{dc}\,, \tag{2.46}$$

where $\mathbf{j} = j\,\hat{\mathbf{e}}_z$ and j is the current density per unit length: j may be calculated by use of Ampère's Law,

$$\begin{aligned} \nabla \times \mathbf{B} &= \left(\frac{\partial B_y}{\partial x} - \frac{\partial B_x}{\partial y} \right) \hat{\mathbf{e}}_z \\ &= \mu j \, \hat{\mathbf{e}}_z \, , \end{aligned} \tag{2.47}$$

and, since $B_x = 0$ along the current sheet, this reduces to

$$\frac{\partial B_y}{\partial x} = \mu j \, . \tag{2.48}$$

To find the current density per unit length, it is first assumed that the current sheet has a finite width 2ϵ, say, such that one can integrate across the sheet before taking the limit $\epsilon \to 0$ to give an infinitesimally thin sheet. Thus

$$\begin{aligned} \int_{-\epsilon}^{\epsilon} j\,(x,y)\,\mathrm{d}x &= \frac{1}{\mu} \int_{-\epsilon}^{\epsilon} \frac{\partial B_y}{\partial x} \mathrm{d}x \\ &= \frac{2}{\mu} \left[B_y \right]_0^{\epsilon} \\ &= \frac{2}{\mu} B_y \mid_{x=0} \\ &= \frac{2}{\mu} \mathcal{R}e \left[\mathcal{B}\,(\mathrm{i}y) \right] \, , \end{aligned}$$

and therefore

$$j\,(y) = \frac{2 B_o y \left(h^2 - y^2\right)^{\frac{1}{2}}}{\mu \left(y^2 + a^2\right)} \, , \tag{2.49}$$

where $0 < y < h$.

Now applying the Biot-Savart Law in two dimensions, with $\mathbf{r} = x \, \hat{\mathbf{e}}_x - y \, \hat{\mathbf{e}}_y$ and $\mathrm{d}\mathbf{c} = \mathrm{d}y \, \hat{\mathbf{e}}_x$ since only the x component of the field is of interest,

$$\begin{aligned} B_{cx} &= \frac{\mu}{2\pi} \int_0^h \frac{y j\,(y)}{x^2 + y^2} \mathrm{d}y \\ &= \frac{B_o}{\pi} \int_0^h \frac{y^2 \left(h^2 - y^2\right)^{\frac{1}{2}}}{\left(x^2 + y^2\right)\left(y^2 + a^2\right)} \mathrm{d}y \, . \end{aligned} \tag{2.50}$$

The free energy now becomes

$$W_F = \frac{-2 d_i}{\mu} \int_a^{\infty} \frac{-f B_o}{\pi} \int_0^h \frac{y^2 \left(h^2 - y^2\right)^{\frac{1}{2}}}{\left(y^2 + a^2\right)\left(x^2 + y^2\right)} \mathrm{d}y \, \mathrm{d}x \, , \tag{2.51}$$

which may be first integrated with respect to x to give

$$W_F = \frac{B_o^2 d_i^2}{\mu} \int_0^h \frac{(h^2 - y^2)^{\frac{1}{2}}}{(y^2 + a^2)} \left[\frac{\pi y}{2} - y \tan^{-1} \frac{a}{y} \right] \mathrm{d}y \,, \tag{2.52}$$

and then partly integrated with respect to y giving the stored energy as

$$W_F = \frac{B_o^2 d_i^3}{2\mu} \left[\pi \left(\frac{1}{2} \ln \left(\frac{1 + h/d_i}{1 - h/d_i} \right) - h/d_i \right) - 2 \int_0^{h/d_i} \frac{Y \left(h^2/d_i^2 - Y^2 \right)^{\frac{1}{2}}}{(Y^2 + a^2/d_i^2)} \tan^{-1} \frac{a/d_i}{Y} \mathrm{d}Y \right] . \tag{2.53}$$

Thus the free energy stored in the current sheet may be written in terms of a factor dependent on a and d_i alone and the term $B_o^2 d_i^3 / 2\mu$, which corresponds to the energy in a cube of side d_i.

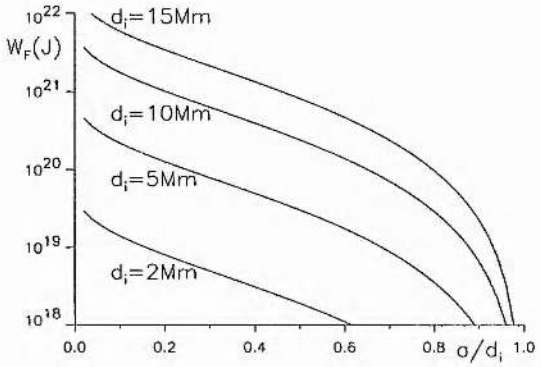

Figure 2.7: Typical values of the free energy (W_F) as the fragments move together for a given background field of strength $B_0 = 10^{-3}$ T (10 G) and interaction distances of $d_i = 2, 5, 10, 15$ Mm.

The free energy may now be calculated numerically from the above equation for a range of values of B_o and d_i. In Figure 2.7 the energy stored is plotted versus the normalised half separation (a/d_i) for $B_o = 10^{-3}$ T (10 G) and d_i =2, 5, 10, 15 Mm. The normal x-ray bright point emission is 10^{16} - 10^{17} W (10^{23} - 10^{24} ergs s^{-1}) (Golub *et al.*, 1974) thus over a period of 8 hrs (the typical bright point lifetime) the total amount of energy released is between 3×10^{20} and 3×10^{21} J (3×10^{27} and 3×10^{28} ergs) which corresponds to the values predicted from our model when $d_i = 5$ - 10 Mm and $B_o = 10^{-3}$ T (10 G).

2.6 Timing

An estimate of the lifetime of the bright point may be made by assuming the bright point will be visible in the corona whilst the neutral point is above the photosphere, (i.e. throughout the interaction phase). The interaction phase starts when the poles are at a half separation $a = d_i$, and ends when $a = 0$. Therefore, if it is assumed that the poles are converging at a velocity v, the lifetime of the bright point (t_{bpt}) equals

$$t_{bpt} = \frac{d_i}{v} \,. \tag{2.54}$$

Now the typical velocity (v) of approach of fragments in a cancelling magnetic feature is 0.3 km s^{-1} (Section 1.2.1, Table 1.1), whilst the range of the interaction distance (d_i) may be calculated as follows.

Equation (2.5) arose from our two-dimensional model and states that d_i, the interaction distance, is the distance at which the magnetic field from a pole of half flux f is equal to half the ambient field strength (B_o). However, to find a realistic value for d_i the corresponding interaction distance (d_i^*) in a three-dimensional situation must be considered. The magnetic field at a distance d_i^* from a point source of half flux f is $f/2\pi d_i^{*2}$. Thus equating this to half the ambient field strength (B_o),

$$d_i^* = \left(\frac{f}{\pi B_o}\right)^{\frac{1}{2}} . \tag{2.55}$$

The flux f for a cancelling magnetic feature is normally between 10^{10} and 5×10^{11} Wb (10^{18} and 5×10^{19} Mx) and the average field strength in a quiet region is 10^{-3} T (10 G). Therefore d_i^* would typically range from 1.8 - 12.6 Mm. This is consistent with the observations of Webb *et al.* (1993). The lifetime (t_{bpt}) for a bright point from this simple model is therefore predicted to be between 2 and 12 hrs, which is consistent with the observations. In fact an interaction distance (d_i) of 8.5 Mm and convergence (v) of 0.3 km s^{-1} gives rise to a bright point for approximately 8 hrs, the observed mean lifetime for bright points.

2.7 Neutral Points

It is interesting to consider what types of neutral points appear as the magnetic field evolves through the first two stages of the model. These are investigated by taking a closer look at the magnetic field near the neutral point by performing a Taylor series expansion of the field about the neutral point and considering only the lowest order term. In the pre-interaction phase there are neutral points at $z = \pm x_n$, and near these points the field can be written as

$$\mathcal{B}(z) = \frac{\pm \mathrm{i} 2 B_o x_n (z \mp x_n)}{x_n^2 - a^2} . \tag{2.56}$$

The magnetic field is of first order in terms of $z \mp x_n$ near these points and the flux function (A) is of the form

$$A = \frac{\pm 2 B_o x_n}{x_n^2 - a^2} (x \mp x_n) y . \tag{2.57}$$

Thus the field lines are given by

$$y = \frac{C}{x \mp x_n} , \tag{2.58}$$

where C is an arbitrary constant and the magnetic field near the neutral point at $z = x_n$ is drawn in Figure 2.8a.

The neutral point in the intervening stage, between the pre-interaction and interaction phases, when the poles have a half separation of d_i is at $z = 0$. This is a special situation where there is only one neutral point in the field, which in its vicinity has a magnetic field of the form

$$\mathcal{B}(z) = \frac{\mathrm{i} B_o z^2}{d_i^2} , \tag{2.59}$$

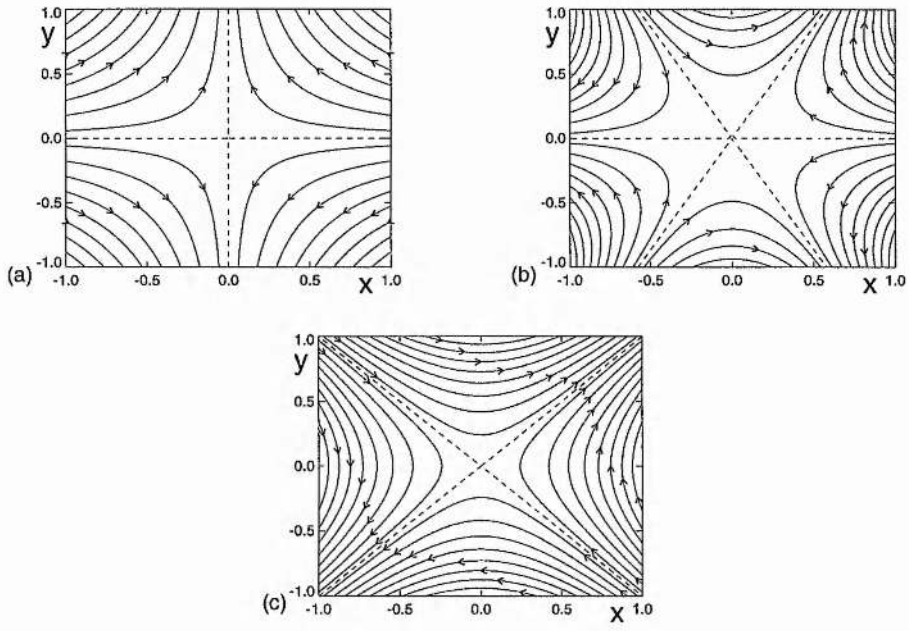

Figure 2.8: The magnetic field due to (a) a first order +-point, (b) a second order neutral point and (c) a first order X-point.

with a corresponding flux function (A) of

$$A = \frac{B_o}{3d_i^2}\left(3x^2y - y^3\right) . \tag{2.60}$$

The field lines for this neutral point which is second order, drawn in Figure 2.8b, are given by

$$x^2 = \frac{C + y^3}{3y} . \tag{2.61}$$

Later, in the interaction phase, there are again two neutral points, one above and the other below the photosphere at $z = \pm iy_n$. The magnetic field near $z = iy_n$ is of the form

$$\mathcal{B}(z) \;=\; \frac{2B_o y_n (z - iy_n)}{y_n^2 + a^2} . \tag{2.62}$$

Again the flux function (A) may be calculated

$$A = \frac{B_o y_n}{y_n^2 + a^2}\left(y^2 - 2y_n y - x^2\right) , \tag{2.63}$$

and the field lines are given by

$$x^2 = (y - y_n)^2 - C^2 , \tag{2.64}$$

where C is an arbitrary constant. This first order X-point is drawn in Figure 2.8c.

So initially the magnetic field has two first order +-points which come together as the poles converge to momentarily form a second order neutral point before transforming into two first order X-points one above and the other below the photosphere.

2.8 Conclusion

The model proposed here gives a reasonable explanation for the creation of an x-ray bright point and associated cancelling magnetic feature. Two line sources of equal strength, but opposite polarity are situated on the x-axis representing the two fragments of a cancelling magnetic feature that move together through a series of quasi-static states in an overlying horizontal field in which they reconnect releasing energy in the form of a bright point. Although very simple it agrees well with many of the key observations outlined by Priest *et al.* (1994). Initially the line sources are situated sufficiently far apart such that they are unconnected; this is known as the pre-interaction phase in which observers see no connecting fibrils in the chromosphere between the cancelling magnetic fragments. As the two fragments converge a bright point appears above in the corona. This is explained in the model by the existence of an X-type neutral point above the photosphere at which reconnection occurs and therefore energy is released (interaction phase). This lasts whilst the fragments come together, vanishing in the cancellation phase when the cancelling magnetic feature starts, as observed, due to reconnection in the photosphere. The magnetic field gradient is seen to steepen (Martin, 1986) between the two opposite polarity magnetic fragments before they cancel, so it likely that here the reconnection takes place through a flux pile-up mechanism (Priest and Forbes, 1986).

The lifetime of the bright point is estimated given typical values for the velocity of convergence of $v = 0.3$ km s^{-1}, strength of the background field of 10^{-3} T (10 G) and interaction distance (d_i) of 8.5 Mm (equivalent to a flux of 2.3×10^{11} Wb (2.3×10^{19} Mx) being cancelled from each fragment), and it agrees well with the average observed lifetime of 8 hrs. A calculation of the total energy released during reconnection is made by allowing a current sheet to form and evaluating the energy it stores. The typical value found is of the order 10^{20} - 10^{21} J (10^{27} - 10^{28} ergs) which again is equivalent to the observed value. This energy is sufficient to produce either a classic or flaring bright point; for example, two fragments of strength 2.3×10^{11} Wb (2.3×10^{19} Mx) in an overlying field of strength 10^{-3} T (10 G), therefore with an interaction distance of 8.5 Mm can produce, during cancellation, either 3.5×10^{16} W (3.5×10^{23} ergs s^{-1}) for 8 hrs (as observed for a normal bright point) or 2.5×10^{16} W (2.5×10^{23} ergs s^{-1}) for 7 hrs 55 mins and then emit a further 10^{18} W (10^{25} ergs s^{-1}) for 5 mins before fading (comparable to the observed powers for a bright point flare). This model, therefore, seems quite promising despite its simplicity.

Chapter 3

The Unequal Cancelling Flux Model

3.1 Introduction

In the basic converging flux model described in the previous chapter the opposite polarity magnetic fragments that cause the cancelling magnetic feature were assumed to be of the same strength. However this is only a special case and in general the fragments will be of different sizes and strengths. In this chapter the converging flux model is generalised to accommodate fragments of differing flux. Section 3.2 outlines the model and studies the magnetic configurations through which the fragments evolve. A discussion on the timing, height and position of the bright point appears in Section 3.3 whilst, in Section 3.4, first the magnetic field with a current sheet and then the free energy stored in the current sheet are evaluated. Section 3.5 contains the conclusions.

3.2 Interaction of Two Unequal Sources in a Uniform Field.

Consider two poles, one of strength $-g$ situated at $z = -a$ on the real axis of the complex plane and the other of strength f positioned at $z = a$; they represent two magnetic regions of opposite sign and differing strengths lying in the plane of the photosphere. The y-axis corresponds to a vertical axis extending from the photosphere into the chromosphere and corona. It is assumed that there is a horizontal uniform magnetic field overlying these poles produced by distant sources. The original converging flux model pointed out that an overlying field is important, but why use a horizontal field? As a first approximation, such a horizontal field is reasonable on both observational and theoretical grounds since Hα pictures of the chromosphere invariably show fibril structures crossing supergranule cells. In addition most of the photospheric magnetic flux is concentrated into strong magnetic field regions such as sunspots or intense flux tubes at supergranule boundaries, so that as this extends upwards it fans out to produce a predominantly horizontal structure, at least in the lower corona. The potential magnetic field for this situation is assumed to evolve quasi-statically as in the previous model and can be written using complex variable theory in terms of the complex function $\mathcal{B}_p(z)$, where $z = x + iy$,

$$\begin{aligned} \mathcal{B}_p(z) &= B_{py}(x,y) + iB_{px}(x,y) \\ &= iB_o + \frac{if}{\pi(z-a)} - \frac{ig}{\pi(z+a)} \end{aligned}$$

$$= \frac{iB_o\left(z^2 + (f' - g')\,z + a\,(f' + g' - a)\right)}{z^2 - a^2}, \tag{3.1}$$

where $B_{px}(x, y)$ and $B_{py}(x, y)$ are the components of the potential magnetic field $B_p(x, y)$ parallel and perpendicular to the plane of the photosphere, respectively, B_o is the strength of the ambient magnetic field, a is the half-separation of the poles, $f' = f/(\pi B_o)$ and $g' = g/(\pi B_o)$.

The position z_n, of the neutral points, can be found by determining where $\mathcal{B}_p = 0$, namely

$$z_n^2 + (f' - g')\,z_n + a\,(f' + g' - a) = 0, \tag{3.2}$$

which has solution,

$$z_n = \frac{-(f' - g') \pm \sqrt{(f' - g')^2 - 4a\,(f' + g' - a)}}{2}. \tag{3.3}$$

When z_n is purely real and single-valued there will be a single neutral point which lies on the photosphere; this happens when

$$(f' - g')^2 - 4a\,(f' + g' - a) = 0,$$

which implies

$$a = \frac{f' + g'}{2} \pm \sqrt{f'g'}.$$

Let

$$d_i = (f' + g')/2 + \sqrt{f'g'}, \tag{3.4}$$

be called the *interaction distance* and

$$d_c = (f' + g')/2 - \sqrt{f'g'}, \tag{3.5}$$

be called the *capture distance*. When $f = g$ (the particular case studied in the converging flux model) $d_c = 0$ and d_i reduces to the value $(2f')$ as seen in Chapter 2. Initially, when the poles have a half-separation of $a > d_i$ (the pre-interaction phase), they are unconnected and there are two neutral points given by Equation (3.3) on the photosphere (Figure 3.1a). Figure 3.2a shows how the two neutral points converge as the half-separation (a) tends to d_i. As the poles move together they first come into contact when $a = d_i$, the interaction distance. This indicates the start of the interaction phase and a neutral point forms on the x-axis at $z_n = -(f' - g')/2$, as shown in Figure 3.1b. During the interaction phase the poles continue moving together, their half-separation (a) lies in the range $d_c < a < d_i$. Here z_n is given by

$$z_n = (x_n, y_n) = \left(\frac{-(f' - g')}{2}, \frac{\sqrt{4a\,(f' + g' - a) - (f' - g')^2}}{2}\right). \tag{3.6}$$

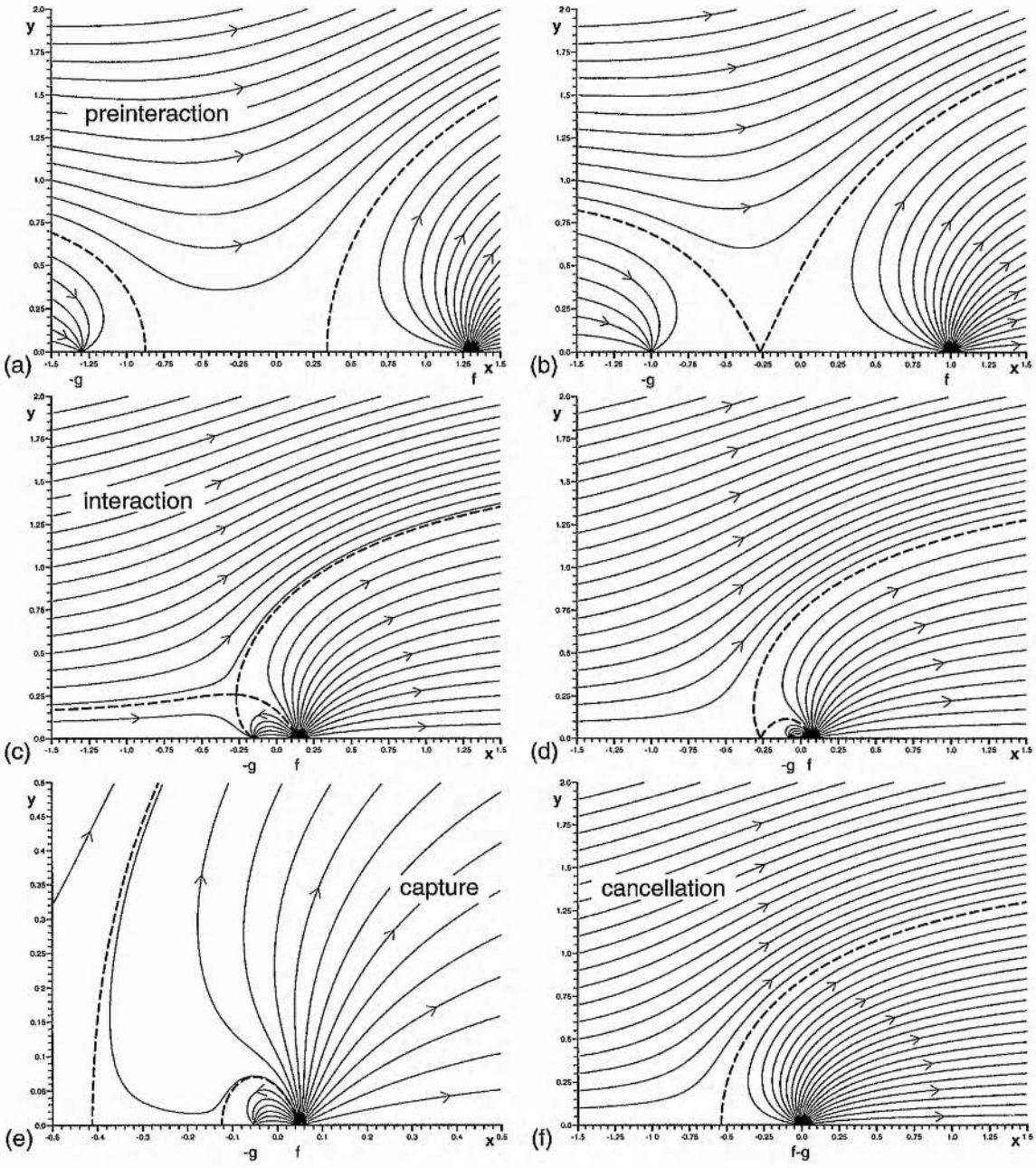

Figure 3.1: The magnetic field due to two poles of strengths $f\,(=3g)$ and $-g$, positioned, respectively, at $z = a$ and $z = -a$ with a uniform background field of strength $B_o = 10^{-3}$ T (10 G), where d_i, the interaction distance, is normalised to 1.0, and so $g = \pi B_o / \left(2+\sqrt{3}\right)$. (a) The half-separation, $a = 1.3$, of the poles is greater than the interaction distance, d_i (the pre-interaction phase). (b) $a = d_i$ and an X-type neutral point is formed. (c) When $a = 0.15$ the X-type neutral point is positioned above the photosphere (during the interaction phase). (d) At $a = d_c = \left(2-\sqrt{3}\right) / \left(2+\sqrt{3}\right)$ the capture phase starts. The region showing the magnetic field is then enlarged in (e) where $a = 0.05$ and pole $-g$ is completely "captured" by pole f. Zero separation of the poles in (f) shows the cancellation phase.

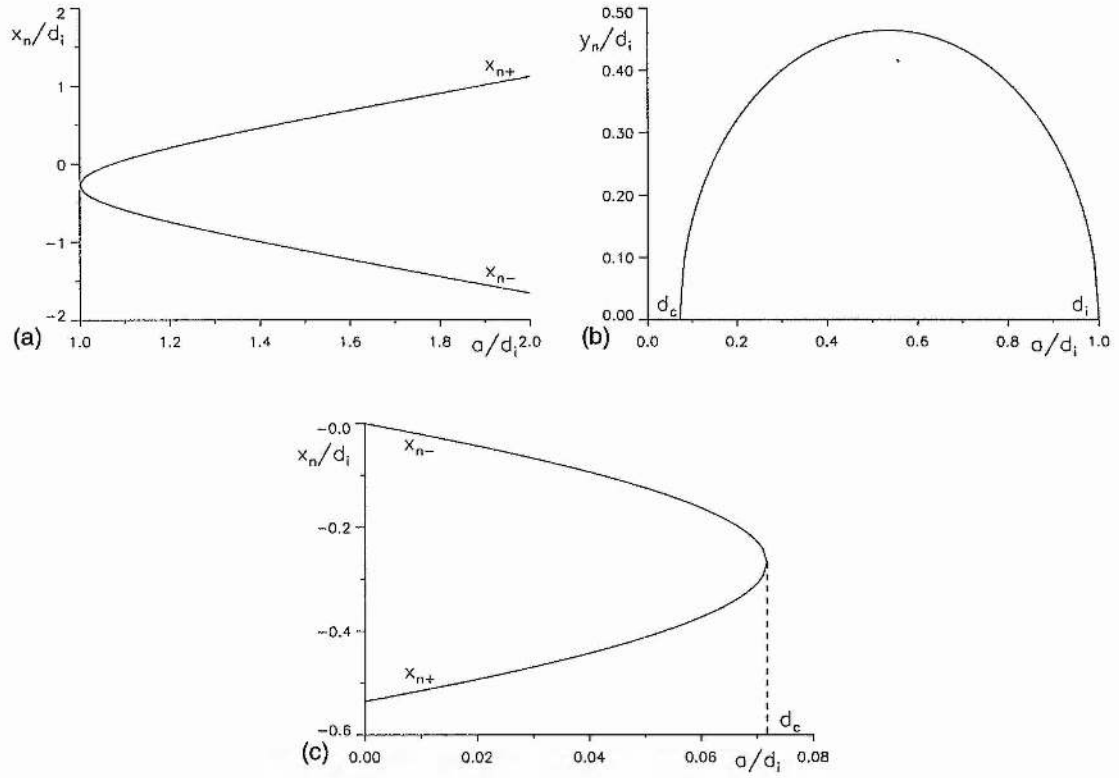

Figure 3.2: (a) For poles $f\,(=3g)$ and $-g = -\pi B_o/\left(2+\sqrt{3}\right)$, a graph of the positions of the neutral points x_{n+} and x_{n-} on the photosphere against the normalised half-separation (a/d_i) when a is greater than the interaction distance (d_i). (b) The normalised height of the neutral point (y_n/d_i) above the photosphere is plotted versus the normalised half-separation (a/d_i) when $d_c < a < d_i$. (c) A graph of the positions of the neutral points x_{n+} and x_{n-} on the photosphere plotted against a/d_i which varies between 0.0 and d_c (the capture distance) for the above poles.

It has both real and imaginary parts, so the X-type neutral point lies above the photosphere, as seen in Figure 3.1c. It is interesting to note that the neutral point does not move horizontally relative to the midpoint, 0, between the two sources as the poles move from d_i to d_c, but it only moves vertically (Figure 3.2b). Instead, in the frame of the point 0, the weaker of the two poles is seen to move under the neutral point, so the x-ray bright point will not lie directly above the cancelling magnetic feature when it starts, but it will be located to one side as seen in Figure 3.1c. A maximum height is gained by the X-type neutral point when $\mathrm{d}y_n/\mathrm{d}a = 0$, which occurs when $a = (f' + g')/2$, and $y_n = y_{nmax} = \sqrt{f'g'}$, as shown in Figure 3.2b.

The neutral point descends back down to the photosphere once more, where at $a = d_c$, the capture distance, the weaker pole becomes fully connected to the stronger pole (Figure 3.1d). As the two poles continue to move together reconnection ceases and the *capture phase* starts. With the weaker pole now fully connected to the stronger pole, two neutral points appear on the photosphere lying to the left of the poles (Figure 3.1e). The neutral points diverge until the poles have zero separation (Figure 3.2c), when at $a = 0$ in this model the cancellation phase starts (Figure 3.1f).

3.3 Bright Point Characteristics

The interaction distance (d_i) depends on the ratio of the strengths of the poles. If it is assumed that $f = kg$, where k is a constant ($k > 0$), d_i and d_c can be written as

$$d_i = \left(\frac{k+1}{2} + \sqrt{k}\right) g' , \tag{3.7}$$

and

$$d_c = \left(\frac{k+1}{2} - \sqrt{k}\right) g' . \tag{3.8}$$

If f is bigger than g (i.e. $k > 1$), then as k increases the interaction and capture distances increase. If g is bigger than f (i.e. $k < 1$), then as k decreases (i.e. g becomes proportionally bigger) the interaction distance decreases, but the capture distance increases (Figure 3.3a).

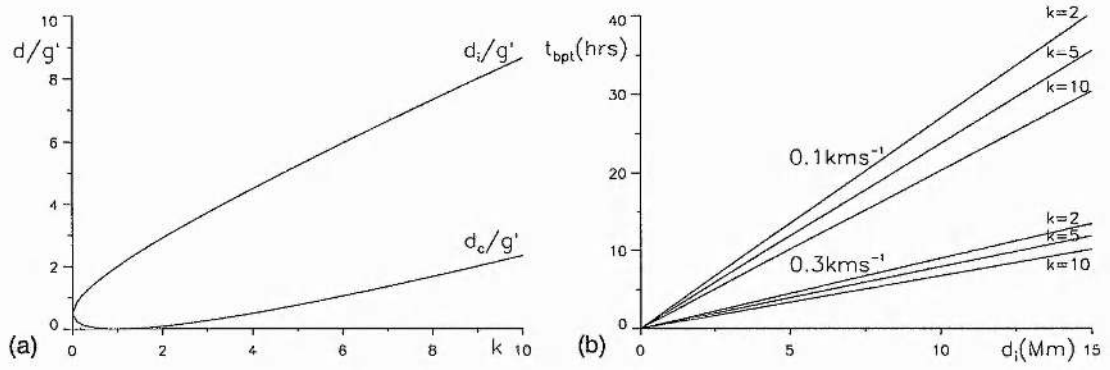

Figure 3.3: (a) A graph of the values of the interactive distance (d_i) and capture distance (d_c) versus k ($= f/g$), the pole strength ratio. (b) The predicted lifetimes (t_{bpt}) for x-ray bright points versus the interaction distance (d_i) when the velocities of interaction of the poles are 0.3 km s^{-1} and 0.1 km s^{-1} and the pole strength ratios (k) are 2, 5 and 10.

If the typical velocity of two interacting fragments is taken to be v, then the typical life time (t_{bpt}) for an x-ray bright point will be

$$t_{bpt} = \frac{d_i - d_c}{v} = \frac{2\sqrt{k} d_i}{\left((k+1)/2 + \sqrt{k}\right) v} . \tag{3.9}$$

For intracell-network cancellations, v is approximately 0.3 km s^{-1} and k is approximately 10, and so interaction distances of 2 Mm, 5 Mm and 10 Mm, respectively, give the lifetimes (t_{bpt}) for the bright points of 1.4, 3.4 and 6.8 hrs. By comparison, the observed cancellation times are 1 - 5 hrs. Ephemeral region-network or ephemeral region-intracell cancellations have velocities (v) of approximately 0.1 - 0.3 km s^{-1} and k approximately 5, and so interaction distances of 2 Mm, 5 Mm, 10 Mm and 15 Mm give lifetimes for the bright points of 5 - 2, 12 - 4, 24 - 8, 36 - 12 hrs, respectively. Observed cancellation times are 1 - 36 hrs. Network-network cancellations have v of approximately 0.1 - 0.3 km s^{-1} and k approximately 2 and

so interaction distances of 5 Mm, 10 Mm and 15 Mm produce lifetimes for the bright points of 14 - 5, 27 - 9, 40 - 14 hrs, respectively (Figure 3.3b). Again 1 - 36 hrs are the observed cancellation times. x-ray bright points are known to have lifetimes between 2 and 48 hrs (Golub *et al.*, 1974), so from the lifetimes predicted by this model it is easy to see why such a great range could arise. If k is of order 1 and d_i large then the bright point will have a long lifetime, as in the network-network cancellations with d_i = 10 - 15 Mm. If k is large and d_i small a short bright point lifetime ensues, as seen with intracell-network cancellations with d_i = 2 - 5 Mm.

On the Sun the magnetic fragments that cancel to produce cancelling magnetic features have a non-zero width, so one may consider briefly a model with sources having a non-zero width $2w$, say. Suppose the half-separation (a) is measured to the centre of the sources and that cancellation begins when $a = w$ (rather than $a = 0$) when the sources come into contact. The capture phase will only exist if $d_c > w$: thus one may estimate these values. For instance, the typical width of intracell and network fields is 1 - 5 Mm, with respect to the present resolution, so cancellation will start at half-separations (w) of around 2.5 Mm. In intracell-network cancellations, k is approximately 10 and interaction distances of 2 Mm, 5 Mm and 10 Mm give capture distances (d_c) of 0.5 Mm, 1.3 Mm and 2.7 Mm, respectively, using Equations (3.7) and (3.8). This implies that only those intracell fields with the largest interaction distances will exhibit a capture phase after the bright point and before the cancelling magnetic feature. When a capture phase does occur, the height of the reconnected field lines will usually be relatively low, below the chromosphere, and so no fibrils will appear. For ephemeral regions, the typical widths of fragments are 1 - 5 Mm as before. Ephemeral region-network or ephemeral region-intracell cancellations have pole strength ratios (k) of approximately 5 and so interaction distances of 2 Mm, 5 Mm, 10 Mm and 15 Mm, respectively, give capture distances of 0.3 Mm, 0.7 Mm, 1.5 Mm and 2.2 Mm; therefore in these types of cancelling magnetic features a capture phase is unlikely to be seen other than in the situations where the sources start interacting at distances of more than 15 Mm. This implies that photospheric cancellation will probably start before the end of the x-ray bright point, as seen in most situations on the Sun. Network fields have sizes of 1 - 10 Mm, and therefore cancellation will start at half-separations of about 5 Mm. In network-network cancellations with k approximately 2 and interaction distances of 5 Mm, 10 Mm and 15 Mm, the capture distances are found to be 0.15 Mm, 0.3 Mm and 0.44 Mm, respectively, implying that a capture phase is very unlikely to occur, and the cancelling magnetic feature will probably start relatively soon into the life of the bright point.

Of course, magnetic fragments are unlikely to be of equal size in reality and so cancellation will not necessarily start right at the midpoint between the fragment centres. Also, the magnetic fragments may well start to cancel before they actually come into contact as reconnection in the photosphere may cause some submergence, but the above considerations give explanations as to why cancelling magnetic features and x-ray bright points overlap in timing and give an idea as to which type of cancellation is most likely to give rise to a bright point before the cancellation itself starts.

The position of the X-type neutral point in the interaction phase can be written in terms of k and d_i, as

$$x_n = \frac{-\left(\sqrt{k}-1\right) d_i}{\left(\sqrt{k}+1\right)}, \tag{3.10}$$

as can the maximum height of the X-type neutral point

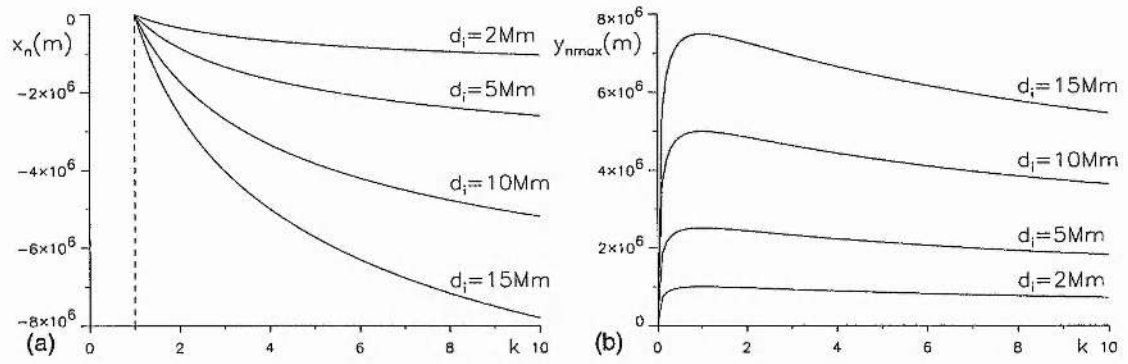

Figure 3.4: (a) A graph of the position of the X-type neutral point during the interaction phase versus the pole strength ratio k for interaction distances (d_i) of 2 Mm, 5 Mm, 10 Mm and 15 Mm. (b) A graph of the maximum height (y_{nmax}) of the X-type neutral point above the photosphere against k, for interaction distances (d_i) of 2 Mm, 5 Mm, 10 Mm and 15 Mm.

$$y_{nmax} = \frac{2\sqrt{k}d_i}{\left(\sqrt{k}+1\right)^2}. \tag{3.11}$$

They are plotted in Figure 3.4, where it is found that, as the pole strength ratio (k) increases, the position of the X-type neutral point in the interaction phase, and hence the bright point, moves further away from the midpoint of the sources (Figure 3.4a). As the interaction distance increases, the neutral point also moves further from the midpoint of the sources. In the intracell-network cancellations, k is approximately 10 and cancellations will start at a half-separation of about 2.5 Mm, so interaction distances greater than 5 Mm will give an x-ray bright point offset from the cancelling magnetic feature. In network-network cancellations, however, k is approximately 2 and the cancellation will start at about 5 Mm, so the x-ray bright point is likely to be directly above the cancelling magnetic feature. From Figure 3.4b the height of the X-type neutral point decreases with k and d_i, and therefore network-network cancellations will produce bright points higher in the corona than intracell-network cancellations.

3.4 Energy Release.

3.4.1 Formation of a Current Sheet.

An estimation for the energy release may be obtained by first supposing that reconnection is not allowed to take place, so that when the poles reach the half-separation distance (d_i) a current sheet will start to form and grow as the poles continue moving together. It will extend up from the photosphere from a point $(x_1, 0)$ to a point (x_2, y_2), say. The form for the magnetic field, given as a complex function, is

$$\begin{aligned} \mathcal{B}(z) &= B_y(x,y) + \mathrm{i}B_x(x,y) \\ &= \frac{\mathrm{i}E(z-x_1)\left((z-x_2)^2+y_2^2\right)^{\frac{1}{2}}}{z^2-a^2}, \end{aligned} \tag{3.12}$$

where E is a constant and a is the half-separation, as before. The following boundary conditions are found by considering the asymptotic behaviour of the magnetic field:

(i) At large distances the magnetic field must tend to that of the overlying uniform field in the same way as the potential field, $\mathcal{B}_p(z)$, so that,
as $z \longrightarrow \infty$, $\quad \mathcal{B}(z) \longrightarrow \mathcal{B}_p(z) \longrightarrow iB_o$;

(ii) Near $z = a$ the magnetic field behaves like a source of strength f, and so
as $z \longrightarrow a$, $\quad \mathcal{B}(z) \longrightarrow if/(\pi(z-a))$;

(iii) Similarly near $z = -a$ the magnetic field behaves like a sink of strength $-g$, so
as $z \longrightarrow -a$, $\quad \mathcal{B}(z) \longrightarrow -ig/(\pi(z+a))$.

After expanding the expressions for $\mathcal{B}(z)$ and $\mathcal{B}_p(z)$ the first boundary condition gives,

$$iE\left(1 - \frac{x_1}{z} - \frac{x_2}{z}\right) = iB_o + \frac{if/\pi}{z} - \frac{ig/\pi}{z} + O\left(\frac{1}{z^2}\right) . \tag{3.13}$$

Thus equating terms of order unity and z^{-1}

$$E = B_o , \tag{3.14}$$

and

$$x_1 + x_2 = -(f' - g') . \tag{3.15}$$

The next two conditions give, respectively,

$$f' = \frac{1}{2a}(a - x_1)\left((a - x_2)^2 + y_2^2\right)^{\frac{1}{2}} , \tag{3.16}$$

$$g' = \frac{1}{2a}(a + x_1)\left((a + x_2)^2 + y_2^2\right)^{\frac{1}{2}} . \tag{3.17}$$

These two equations can be solved to give x_2 and y_2 in terms of x_1,

$$x_2 = -a\left(\frac{f'^2}{(a - x_1)^2} - \frac{g'^2}{(a + x_1)^2}\right) , \tag{3.18}$$

$$y_2 = \sqrt{2a^2\left(\frac{f'^2}{(a - x_1)^2} + \frac{g'^2}{(a + x_1)^2}\right) - a^2 - x_2^2} . \tag{3.19}$$

Eliminating x_2 from Equations (3.15) and (3.18) an expression in terms of x_1, a, $g'$and f' may be found

$$\left(f' - \frac{af'^2}{(a - x_1)^2}\right) - \left(g' - \frac{ag'^2}{(a + x_1)^2}\right) + x_1 = 0 , \tag{3.20}$$

or, after completing the two squares (Parnell, Priest and Titov, 1994),

$$\left(\frac{g'}{(a + x_1)} - \frac{(a + x_1)}{2a}\right)^2 - \left(\frac{f'}{(a - x_1)} - \frac{(a - x_1)}{2a}\right)^2 = 0 . \tag{3.21}$$

This equation factorises into a quadratic and a cubic for x_1, namely

$$x_1^2 + (f' - g')\, x_1 + a\,(f' + g' - a) \;=\; 0\,, \tag{3.22}$$

$$F(x_1) \;\equiv\; x_1^3 - a\,(a + g' + f')\, x_1 + a^2\,(g' - f') \;=\; 0\,. \tag{3.23}$$

Solving the quadratic, which is identical to Equation (3.2) and hence related to the potential state, does not give any real roots in the interval $d_c < a < d_i$ and no real roots between $-a$ and a in the interval $0 < a < d_c$. The cubic $F(x_1)$ must therefore contain the value of x_1 required. First it is ascertained whether the roots of $F(x_1)$ are real or imaginary. This is done by differentiating Equation (3.23) with respect to x_1 to discover the values of x_1 for which $F(x_1)$ has a minimum or maximum:

$$x_{1\min} \;=\; +\sqrt{\frac{a^2 + a\,(g' + f')}{3}}\,; \tag{3.24}$$

$$x_{1\max} \;=\; -\sqrt{\frac{a^2 + a\,(g' + f')}{3}}\,. \tag{3.25}$$

If $F(x_{1\min})$ is less than zero and $F(x_{1\max})$ is greater than zero there exist three real distinct roots of $F(x_1) = 0$, this condition may be written as

$$|\, g' - f' \,| \;<\; \frac{2\,(a + g' + f')^{\frac{3}{2}}}{3\sqrt{3a}}\,. \tag{3.26}$$

The right-hand side of Equation (3.26) is differentiated with respect to a to find the turning point which occurs when $a = (g' + f')/2$. This gives a minimum, which when substituted back into the right-hand side of (3.26) gives

$$|\, g' - f' \,| \;<\; (g' + f')\,. \tag{3.27}$$

Thus, for all positive values of g' and f' and $0 < a < d_i$, $F(x_1) = 0$ has three real and distinct roots. It now remains to prove that only one of these roots lies in the interval $(-a,a)$.

From Equation (3.23), expanding about $-a$ with $x_1 = -a + \delta$, gives

$$\delta^3 - 3a\delta^2 + \left(2a^2 - a\,(g' + f')\right)\delta + 2a^2 g' \;=\; 0\,. \tag{3.28}$$

Assuming that the roots to this cubic are α, β, γ then

$$-\alpha\beta\gamma \;=\; 2a^2 g' \;>\; 0\,, \tag{3.29}$$

which implies that at least one of the roots is negative; moreover either one or all the roots are negative. Equating the coefficients of δ^2 implies

$$\alpha + \beta + \gamma \;=\; 3a\,, \tag{3.30}$$

so that not all the roots are negative. Therefore at most one root is negative, which implies that one and only one root of Equation (3.23) is less than $-a$.

Similarly expanding about a by putting $x_1 = a + \delta$ gives

$$\delta^3 + 3a\delta^2 + \left(2a^2 - a\left(g' + f'\right)\right)\delta - 2a^2 f' \;=\; 0\,. \tag{3.31}$$

Again assuming that the roots to this cubic are α, β, γ one finds

$$\alpha\beta\gamma \;=\; 2a^2 f' \;>\; 0\,. \tag{3.32}$$

So either one or all the roots are positive. Considering the coefficients of δ^2 gives

$$\alpha + \beta + \gamma \;=\; -3a\,. \tag{3.33}$$

Thus not all the roots are positive, so at most one root is positive and hence one and only one root of Equation (3.23) is greater than a. The remaining root therefore must lie in the range $-a < x_1 < a$ which satisfies the frozen-in flux condition. So there exists a unique solution satisfying the boundary conditions for the end point of the current sheet which equals

$$x_1 \;=\; \frac{-(S+T)}{2} + \mathrm{i}\frac{\sqrt{3}}{2}(S-T)\,, \tag{3.34}$$

where $S \;=\; \left(U + \left(U^2 + V^3\right)^{\frac{1}{2}}\right)^{\frac{1}{3}}$, $T^3 \;=\; \left(U - \left(U^2 + V^3\right)^{\frac{1}{2}}\right)^{\frac{1}{3}}$, $U \;=\; -a^2\left(g' - f'\right)/2$ and $V \;=\; -a\left(a + g' + f'\right)/3$.

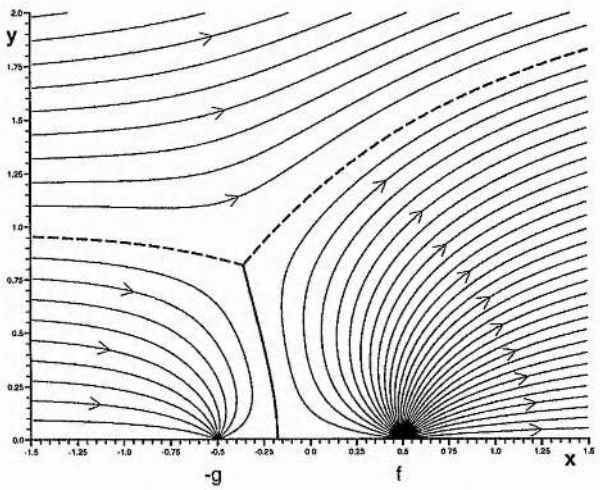

Figure 3.5: A plot of the magnetic field with a current sheet according to Equation (3.12) for a positive pole of strength $f\,(=3g)$ situated at z = 0.5, a negative pole of strength $-g = -\pi B_o/\left(2+\sqrt{3}\right)$ situated at z = −0.5 and the background field B_o of strength 10^{-3} T (10 G). Lengths have all been normalised with respect to d_i.

The end-points of the current sheet may now be calculated from Equations (3.34), (3.18) and (3.19) . It is interesting to note that, by using conservation of flux the above boundary conditions can be found instead by solving the appropriate integrals for the flux across $x = x_1$ for $0 \leq y < \infty$, across $y = 0$ for $-\infty < x \leq x_1$ and across $y = 0$ for $x_1 \leq x < \infty$, respectively.

The magnetic field due to the current sheet may be drawn (Figure 3.5) using Equation (3.12) with $E = B_o$, x_1 given by (3.34) and solving for x_2 and y_2 from Equations (3.34), (3.18) and (3.19). Figure 3.6 shows the end-points of the current sheet plotted in the xy-plane for the half-separation (a) between 0.0 and d_i, where the poles have a strength ratio of $k = 3$ and lengths are normalised with respect to d_i. The shape of the current sheet for $a = 0.02$ is represented by a dashed curve.

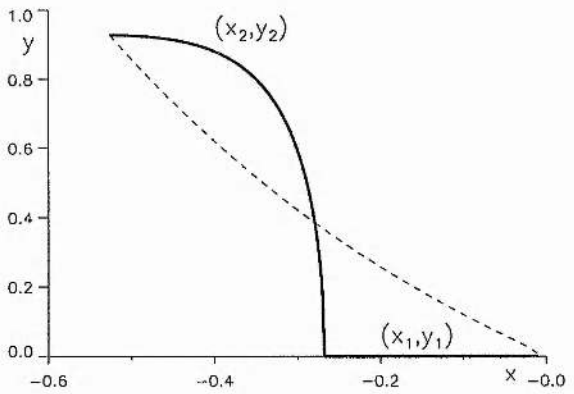

Figure 3.6: The positions of the end-points of the current sheet for two poles f and $-g$, where $f = 3g$, are plotted in the xy-plane lying between 0.02 and the interaction distance (d_i). The location of the current sheet when $a = 0.02$ is indicated by a dashed curve.

3.4.2 Free Magnetic Energy.

The free energy stored in the current sheet can be calculated analytically by again following the method of Low and Hu (1983). However, it is not easy to calculate the magnetic field due to the current sheet, so instead the energy is calculated from Equation (2.41) which is

$$\frac{W_F}{d_i} = \frac{-1}{2\mu} \int_{-\infty}^{\infty} \left[A\left(B_x - B_{px}\right)\right]_{y=0} \mathrm{d}x \,, \tag{3.35}$$

where B_x, B_{px} and A along $y = 0$ are found to be

$$B_x = \mathcal{I}\mathrm{m}\left[\mathcal{B}\left(x\right)\right] = \frac{B_o\left(x - x_1\right)\left(\left(x - x_2\right)^2 + y_2^2\right)^{\frac{1}{2}}}{x^2 - a^2} \,, \tag{3.36}$$

$$B_{px} = \mathcal{I}\mathrm{m}\left[\mathcal{B}_p\left(x\right)\right] = B_o + \frac{f}{\pi\left(x - a\right)} - \frac{g}{\pi\left(x + a\right)} \,, \tag{3.37}$$

$$A = \begin{cases} -\pi B_o g' \left(= -g\right) & x \leq -a \\ 0 & -a < x < a \\ -\pi B_o f' \left(= -f\right) & x \geq a \end{cases} \,. \tag{3.38}$$

So the free energy stored in the current sheet can be written as

$$\frac{W_F}{d_i} = \frac{-1}{2\mu}\int_{-\infty}^{-a} -\pi B_o g' \left[B_x - B_{px}\right]_{y=0} \mathrm{d}x + \frac{-1}{2\mu}\int_{a}^{\infty} -\pi B_o f' \left[B_x - B_{px}\right]_{y=0} \mathrm{d}x \,. \tag{3.39}$$

This can be solved analytically, by first evaluating the indefinite integrals,

$$\begin{aligned}\int B_{px}\,|_{y=0}\,\mathrm{d}x &= \int B_o + \frac{f}{\pi\,(x-a)} - \frac{g}{\pi\,(x+a)}\mathrm{d}x \\ &= B_o\left\{x + f'\log\left[x-a\right] - g'\log\left[x+a\right]\right\}\,,\end{aligned} \tag{3.40}$$

$$\int B_x\,|_{y=0}\,\mathrm{d}x = \int \frac{B_o\,(x-x_1)\left((x-x_2)^2+y_2^2\right)^{\frac{1}{2}}}{x^2-a^2}\mathrm{d}x\,, \tag{3.41}$$

which, using partial fractions, can be written as

$$\int B_x\,|_{y=0}\,\mathrm{d}x = \frac{B_o\,(a-x_1)}{2a}\int \frac{Q\,(x)}{x-a}\mathrm{d}x + \frac{B_o\,(a+x_1)}{2a}\int \frac{Q\,(x)}{x+a}\mathrm{d}x\,, \tag{3.42}$$

where $Q\,(x) = \left((x-x_2)^2+y_2^2\right)^{\frac{1}{2}}$.
$Q\,(x)$ may be rearranged (Parnell, Priest and Titov, 1994) to give

$$Q^2\,(x) = (x-a)^2 + 2\,(a-x_2)\,(x-a) + Q^2\,(a)\,, \tag{3.43}$$

$$Q^2\,(x) = (x+a)^2 - 2\,(a+x_2)\,(x+a) + Q^2\,(-a)\,, \tag{3.44}$$

thus the two integrals in Equation (3.42) may be rewritten as

$$\int \frac{Q\,(x)}{x-a}\mathrm{d}x = Q\,(x) + (a-x_2)\int \frac{dx}{Q\,(x)} + Q^2\,(a)\int \frac{dx}{(x-a)\,Q\,(x)}\,, \tag{3.45}$$

$$\int \frac{Q\,(x)}{x+a}\mathrm{d}x = Q\,(x) - (a+x_2)\int \frac{dx}{Q\,(x)} + Q^2\,(-a)\int \frac{dx}{(x+a)\,Q\,(x)}\,. \tag{3.46}$$

So Equation (3.42) becomes

$$\begin{aligned}\int B_x\,|_{y=0}\,dx = B_o\Bigg\{&Q\,(x) - (x_1+x_2)\int \frac{dx}{Q\,(x)} + \frac{(a-x_1)\,Q^2\,(a)}{2a}\int \frac{dx}{(x-a)\,Q\,(x)} \\ &+ \frac{(a+x_1)\,Q^2\,(-a)}{2a}\int \frac{dx}{(x+a)\,Q\,(x)}\Bigg\}\,.\end{aligned} \tag{3.47}$$

The remaining three integrals can easily be solved (Appendix B) to give

$$\int \frac{\mathrm{d}x}{Q\,(x)} = \log\left[Q\,(x) + x - x_2\right]\,, \tag{3.48}$$

$$\int \frac{\mathrm{d}x}{(x-a)\,Q(x)} = \frac{-1}{\mid Q(a) \mid} \log\left[\frac{Q^2(a)+(a-x_2)(x-a)+\mid Q(a) \mid Q(x)}{x-a}\right], \tag{3.49}$$

$$\int \frac{\mathrm{d}x}{(x+a)\,Q(x)} = \frac{-1}{\mid Q(-a) \mid} \log\left[\frac{Q^2(-a)-(a+x_2)(x+a)+\mid Q(-a) \mid Q(x)}{x+a}\right]. \tag{3.50}$$

Using Equations (3.15), (3.16) and (3.17) the final expression for Equation (3.41) is

$$\begin{aligned}\int B_x \mid_{y=0} \mathrm{d}x = B_o \Big\{ & Q(x) + (f'-g') \log\left[Q(x)+x-x_2\right] \\ & - f' \log\left[\frac{Q^2(a)+(a-x_2)(x-a)+\mid Q(a) \mid Q(x)}{x-a}\right] \\ & - g' \log\left[\frac{Q^2(-a)-(a+x_2)(x+a)+\mid Q(-a) \mid Q(x)}{x+a}\right]\Big\} :\end{aligned} \tag{3.51}$$

thus, if Equation (3.40) is subtracted from this equation then

$$\begin{aligned}\int \left[B_x - B_{px}\right] \mid_{y=0} \mathrm{d}x = B_o \Big\{ & Q(x) - x + (f'-g') \log\left[Q(x)+x-x_2\right] \\ & - f' \log\left[Q^2(a)+(a-x_2)(x-a)+\mid Q(a) \mid Q(x)\right] \\ & - g' \log\left[\frac{Q^2(-a)-(a+x_2)(x+a)+\mid Q(-a) \mid Q(x)}{(x+a)^2}\right]\Big\}.\end{aligned} \tag{3.52}$$

Now applying the limits of the first integral in Equation (3.39) from $-\infty$ to $-a$ to the above equation (Appendix C) and noting that $Q(x) = -\mid Q(x) \mid$, gives

$$\begin{aligned}\int_{-\infty}^{-a} \left[B_x - B_{px}\right]_{y=0} \mathrm{d}x = B_o \Big\{ & a - x_2 - \mid Q(-a) \mid - g' \log\left[\frac{\left(\mid Q(-a) \mid + a + x_2\right)^2}{4Q^2(-a)}\right] \\ & - f' \log\left[\frac{2\left(\mid Q(a) \mid\mid Q(-a) \mid + 2a(a-x_2) - Q^2(a)\right)}{\left(\mid Q(-a) \mid + a + x_2\right)\left(\mid Q(a) \mid + a - x_2\right)}\right]\Big\}.\end{aligned} \tag{3.53}$$

Similarly, applying the limits to the integral in Equation (3.52) from a to ∞ (Appendix C), where this time $Q(x) = \mid Q(x) \mid$, gives

$$\begin{aligned}\int_{a}^{\infty} \left[B_x - B_{px}\right]_{y=0} \mathrm{d}x = B_o \Big\{ & a - x_2 - \mid Q(a) \mid - f' \log\left[\frac{\left(\mid Q(a) \mid + a - x_2\right)^2}{4Q^2(a)}\right] \\ & - g' \log\left[\frac{8a^2\left(\mid Q(-a) \mid - a - x_2\right)}{\left(Q^2(-a) - 2a(a+x_2) + \mid Q(a) \mid\mid Q(-a) \mid\right)\left(\mid Q(a) \mid + a - x_2\right)}\right]\Big\}.\end{aligned} \tag{3.54}$$

Thus the free energy stored in the current sheet is finally

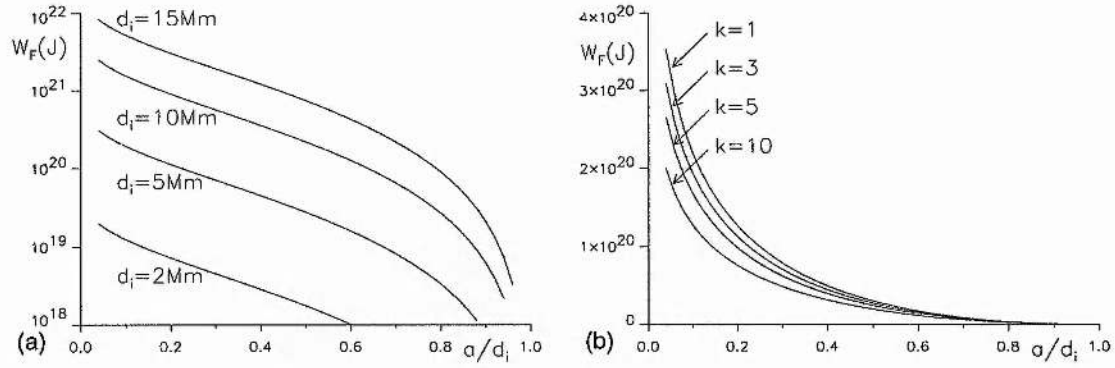

Figure 3.7: The free energy (W_F) in Joules as a function of a/d_i when the background field B_o is 10^{-3} T (10 G) for (a) different values of the interaction distance (d_i) when the pole strength ratio $k = 3$, and for (b) different values of k, the ratio of the pole strengths, with $d_i = 5$ Mm.

$$W_F = \frac{d_i \pi B_o}{2\mu} \int_{-\infty}^{-a} g' \left[B_x - B_{px}\right]_{y=0} \mathrm{d}x + \frac{d_i \pi B_o}{2\mu} \int_{a}^{\infty} f' \left[B_x - B_{px}\right]_{y=0} \mathrm{d}x$$

$$= \frac{d_i \pi B_o^2}{2\mu} \left\{ -g' \left(\mid Q\left(-a\right) \mid -a - x_2\right) - f' \left(\mid Q\left(a\right) \mid -a + x_2\right) - g'^2 \log \left[\frac{\left(\mid Q\left(-a\right) \mid +a + x_2\right)^2}{4Q^2\left(-a\right)} \right] \right.$$

$$\left. - f'^2 \log \left[\frac{\left(\mid Q\left(a\right) \mid +a - x_2\right)^2}{4Q^2\left(a\right)} \right] - f'g' \log \left[\frac{4\left(\mid Q\left(a\right) \mid\mid Q\left(-a\right) \mid +2a\left(a - x_2\right) - Q^2\left(a\right)\right)^2}{\left(\mid Q\left(-a\right) \mid +a + x_2\right)^2 \left(\mid Q\left(a\right) \mid +a - x_2\right)^2} \right] \right\} . \quad (3.55)$$

The free magnetic energy (W_F) stored in the current sheet is plotted in Figure 3.7a on a logarithmic scale as a function of a/d_i for interaction distances d_i = 2 Mm, 5 Mm, 10 Mm and 15 Mm, with a background field strength $B_o = 10^{-3}$ T (10 G), where the pole strengths are $f' = 3g'$, $g' = d_i/\left(2+\sqrt{3}\right)$. Figure 3.7b shows the free magnetic energy versus a/d_i for different pole strength ratios, k = 1, 3, 5 and 10, where the interaction distance is 5 Mm and the ambient field B_o is 10^{-3} T (10 G). An average x-ray bright point with a lifetime of 8 hours emits a total energy of 3×10^{20} - 3×10^{21} J (3×10^{27} - 3×10^{28} ergs), which correspond to the energies attained in Figure 3.7a for interaction distances from 5 - 10 Mm and for pole strength ratios of 1 - 3 in Figure 3.7b.

3.5 Conclusion

The development in this chapter of the converging flux model of Priest *et al.* (1994) for the interaction of two magnetic sources of opposite sign and differing strengths agrees with many key x-ray bright point and cancelling magnetic feature observations. As in Chapter 2, the pre-interaction phase shows unconnected sources suggesting that there are no chromospheric fibrils linking the magnetic fragments. Also an x-ray bright point is created in the interaction phase due to reconnection in the corona; this bright point is shown to lie near the cancelling magnetic feature, but not necessarily directly above it. Again cancellation of the magnetic fragments occurs by reconnection in the photosphere: however in this model a new phase is found to start at the end of the interaction phase, called the capture phase, where the weaker pole is

fully connected to the stronger pole as the poles continue to converge. This helps explain why the onset of the cancelling magnetic feature may occur during or after the bright point phase and explains why some bright points are seen to occur above converging features and not cancelling features (Webb *et al.*, 1993).

With the added variation in the ratio of the pole strengths, the complete range of bright point lifetimes may be explained and it would be informative if future observational studies compared the bright point properties with the ratio of the cancelling magnetic feature source strengths. For example, the model suggests that two poles of similar strengths ($k \approx 1$) and a large interaction distance would give a long bright point lifetime, as in network-network cancellations, whereas in intracell-network cancellations where $k = 10$, say, and $d_i = 2$ - 5 Mm the bright point would only last a few hours. The model suggests that not all types of cancelling magnetic feature will have a capture phase, but such a phase is more likely to occur in intracell-network cancellations. This means that in this type of cancelling magnetic feature the x-ray bright point would be expected to start well before the cancellation and it may even have finished before the fragments start cancelling. In a network-network cancellation the cancelling magnetic feature is likely to begin several hours before the bright point ends.

An estimate is given of the amount of energy that can be released at any one time during the bright point; it would also be interesting to compare the predicted energies with future coordinated x-ray bright point and cancelling magnetic feature observations, since the variation in the ratio of pole strengths gives a range of total energies released during the bright point. Two poles with a pole ratio of 10 and interaction distance of 5 Mm (intracell-network cancellation) in an overlying field of 10^{-3} T (10 G) would create an x-ray bright point with a total energy emission of 2×10^{20} J (2×10^{27} ergs), whereas a network-network cancellation with a pole ratio of 3 and interaction distance of 15 Mm in the same overlying field of strength 10^{-3} T (10 G) would produce a total of 10^{22} J (10^{29} ergs) of energy. The model also suggests that bright points are more likely to lie directly above their cancellation sites for network-network cancellations between strong magnetic fragments of similar strengths, whereas bright points may be offset to one side of the cancelling magnetic fragment when cancellations between magnetic fragments of dissimilar strengths occur, as in intracell-network cancellations.

Chapter 4

X-ray Bright Point Model for Three Poles

4.1 Introduction

Following the analytical methods developed in the previous converging flux models for two poles, it is now fairly simple to extend this analysis to a study of three poles in an overlying field. The situation chosen is the interaction of a bipolar pair of magnetic fragments with a single magnetic source of different strength. They are situated initially far apart within an overlying uniform background magnetic field, such that they are unconnected. The line source then moves towards the bipole releasing energy through reconnection in the corona in the form of a bright point and creating a cancelling magnetic feature due to reconnection in the photosphere. In this study the two scenarios, labelled (c) and (d) in Figure 2.2, which were first described in Priest *et al.* (1994), are investigated. They represent the interaction of an ephemeral region with an intracell region or an ephemeral region with a network field.

In the first section (Section 4.2) the model is outlined and set up. The magnetic configurations through which the field evolves are depicted for the interaction of an ephemeral region with both an intracell and a network region. The height, position and path of the bright point are discussed. The free energy associated with each bright point is calculated in Section 4.3, which also includes a calculation of the field with the current sheet. In Section 4.4 the dependence of the lifetime of the bright point on various parameters is evaluated; Section 4.5 concludes the chapter.

4.2 Outline of Model

The bipole, consisting of two line sources of strength g and $-g$, situated at positions $-a$ and 0 on the x-axis and the line source of strength f, positioned at $x = b$, are lying in an overlying horizontal field of strength B_o. The x-axis represents the photosphere, whilst the y-axis extends vertically upwards into the chromosphere and corona. As in the previous situations, the poles representing the magnetic fragments are assumed to move much slower than the Alfvén speed, therefore allowing the field to evolve through a series of quasi-static states. The magnetic field, written in complex notation where $z = x + \mathrm{i}y$, is

$$B_p(z) = B_{py}(x,y) + \mathrm{i}B_{px}(x,y)$$

$$= \mathrm{i}B_o + \frac{\mathrm{i}g}{\pi(z+a)} - \frac{\mathrm{i}g}{\pi z} + \frac{\mathrm{i}f}{\pi(z-b)}$$

$$= \frac{\mathrm{i}B_o\left(z^3 + (a-b+f')z^2 + a(f'-g'-b)z + abg'\right)}{(z+a)z(z-b)}$$

$$= \frac{\mathrm{i}B_o F(z)}{(z+a)z(z-b)}\,, \tag{4.1}$$

where B_o is the strength of the ambient magnetic field, $f' = f/(\pi B_o)$ and $g' = g/(\pi B_o)$. The expression for the magnetic field contains a cubic (F) with respect to z, so it has a maximum of three roots and, therefore, normally the configuration contains three neutral points. As in the two previous converging flux models, the special cases where the field has fewer than the standard number of neutral points are sought. Thus it is assumed that there are only two real roots (α and β) corresponding to neutral points on the x-axis. They form a cubic which can be written as

$$(z-\alpha)(z-\beta)^2 = z^3 - (\alpha+2\beta)z^2 + (2\alpha\beta+\beta^2)z - \alpha\beta^2\,. \tag{4.2}$$

Equating the coefficients of this cubic with those in $F(z)$ gives two unknowns in three equations,

$$-(\alpha+2\beta) = a-b+f'\,, \tag{4.3}$$

$$2\alpha\beta+\beta^2 = a(f'-g'-b)\,, \tag{4.4}$$

$$-\alpha\beta^2 = abg'\,. \tag{4.5}$$

Eliminating α from Equations (4.3) and (4.4) gives

$$\beta^2 + \frac{2}{3}(a-b+f')\beta + \frac{a}{3}(f'-g'-b) = 0\,: \tag{4.6}$$

therefore

$$\beta = \frac{-1}{3}(a-b+f') \pm \frac{1}{3}\sqrt{(a-b+f')^2 - 3a(f'-g'-b)}\,, \tag{4.7}$$

and from Equation (4.3) α is found to be

$$\alpha = \frac{-1}{3}(a-b+f') \mp \frac{2}{3}\sqrt{(a-b+f')^2 - 3a(f'-g'-b)}\,. \tag{4.8}$$

For the magnetic field to be physical the single root (α) must be less than $-a$ and the double root (β) must lie in the interval 0 to b. Thus the positive root of β and, therefore, the negative root of α are the only physical solutions. This agrees with the third boundary condition, since the right-hand side of Equation (4.5) is always greater than zero: therefore α must be negative for the equality to hold.

Is it possible to have three equal roots? That would mean, $\alpha = \beta$, which implies

$$(a - b + f')^2 - 3a(f' - g' - b) = 0 . \tag{4.9}$$

Grouping this equation in terms of $f' - b$ gives

$$G(f' - b) = (f' - b)^2 - a(f' - b) + a^2 + 3ag' = 0 ; \tag{4.10}$$

therefore $f' - b$ becomes

$$f' - b = \frac{a}{2} \pm \frac{\mathrm{i}}{2}\sqrt{3a^2 + 12ag'} . \tag{4.11}$$

The values a, f' and g' are always real and positive, implying b is imaginary when $\alpha = \beta$. However, b is always real and so the assumption that there are three real equal roots is false: therefore the magnetic field can never contain only one neutral point.

For there to be two real roots, $G(x)$ must always be greater than zero for all real x. This is in fact always true, since $G(x)$ is a continuous function with respect to x,

$$G(0) = a^2 + 3ag' > 0 , \tag{4.12}$$

and, from above, $G(x)$ never equals zero: therefore, it must always be greater that zero.

There are two physical situations when the magnetic field has two neutral points. These situations occur at the transition stages between the pre-interaction and interaction stages and between the interaction and cancellation phases. The position of the positive pole of strength f at these points is called $b = d_i$ (the interaction distance) and $b = d_c$ (the cancellation distance), respectively, in line with the previous two chapters. In the final stage, when $b = 0$, there will also be two neutral points, but this is a degenerate case, containing just two positive poles.

The actual values of d_i and d_c are not simple to find. If all three roots of $F(x)$ are sought then they reduce to a set of just two real distinct solutions when the discriminate is zero. The discriminate (D) equals

$$D = U^2 + V^3 , \tag{4.13}$$

where $U = \left(9a_1a_2 - 27a_3 - 2a_1^3\right)/54$, $V = \left(3a_2 - a_1^2\right)/9$, and $a_1 = a - b + f'$, $a_2 = a(f' - g' - b)$ and $a_3 = abg'$. Substituting in the dimensionless parameters: $a' = a/g'$, $b' = b/g'$, $k = f'/g'$ and $x = k - b'$, then a_1 , a_2 and a_3 can be written as

$$a_1 = (x + a')\, g' , \tag{4.14}$$

$$a_2 = a'(x - 1)\, g'^2 , \tag{4.15}$$

$$a_3 = a'(k - x)\, g'^3 . \tag{4.16}$$

The discriminate (D) may then be expanded in terms of x, a' and k only, giving

$$(a'+4)\,x^4 - 2\left(a'^2+4a'+2k\right)x^3 + a'\left(a'^2+2a'-8+6k\right)x^2 + 2a'\left(a'^2+(4+3k)\,a'+18k\right)x$$

$$+a'\left((1-4k)\,a'^2+(4-18k)\,a'-27k^2\right) \;=\; 0\,. \qquad (4.17)$$

This does not immediately present an analytical solution: however it may be solved numerically. The interaction distance and the capture distance are therefore equal to

$$d_i = (k - x_i\,(a', k))\,g'\,, \qquad (4.18)$$

$$d_c = (k - x_c\,(a', k))\,g'\,, \qquad (4.19)$$

respectively, where x_i and x_c are roots of Equation (4.17) and $x_i < x_c < k$.

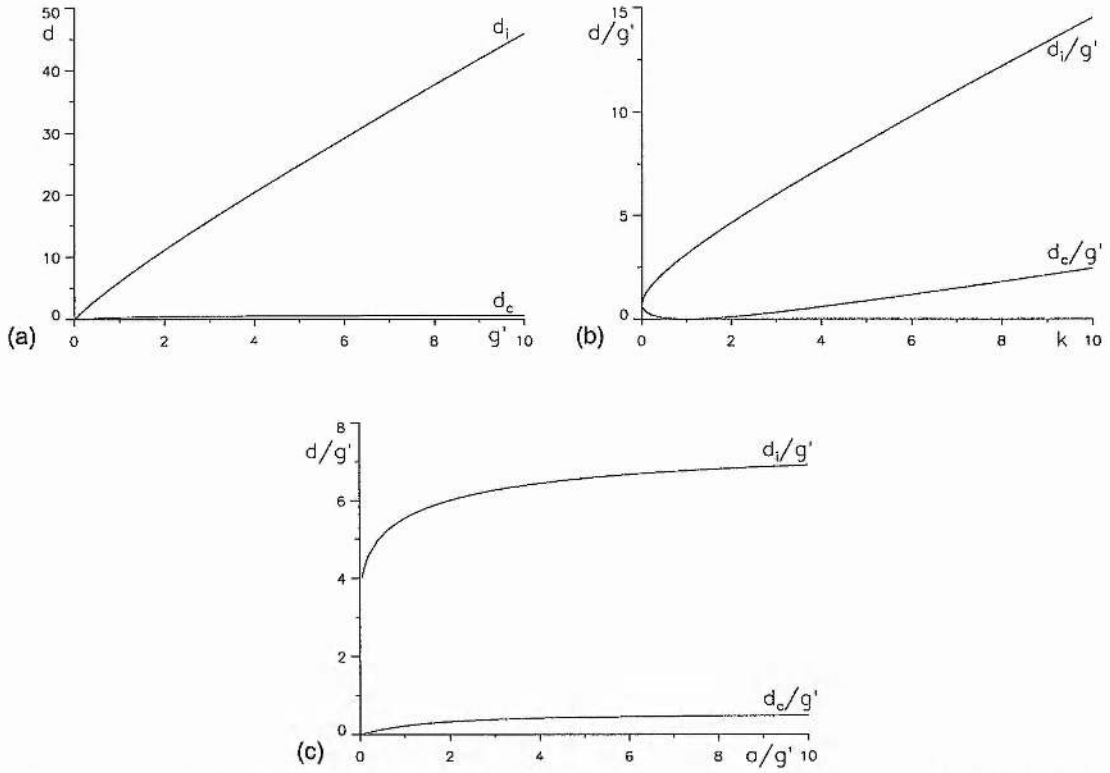

Figure 4.1: (a) shows the interaction distance (d_i) and the capture distance (d_c) versus the bipole strength (g') for $k = 3$ and $a = 2$ Mm. Normalised interaction and capture distances (d_i/g' and d_c/g') are plotted against (b) the pole strength ratio (k) for $a = 2$ Mm and (c) the normalised bipole width (a/g') for $k = 3$.

Figure 4.1a shows plots of d_i and d_c versus g' showing how the flux (g) varies with respect to d_i and d_c. Figures 4.1b and 4.1c show plots of d_i/g' and d_c/g' against k and a, respectively, showing that if $k > 1$ both d_i and d_c increase, whereas if $k < 1$ then d_c increases whilst d_i decreases as k tends to zero. This is similar to the dependence seen in the unequal poles case (Figure 3.3a). If a is large then d_c and d_i become almost independent of a: however, for small a they rapidly decrease.

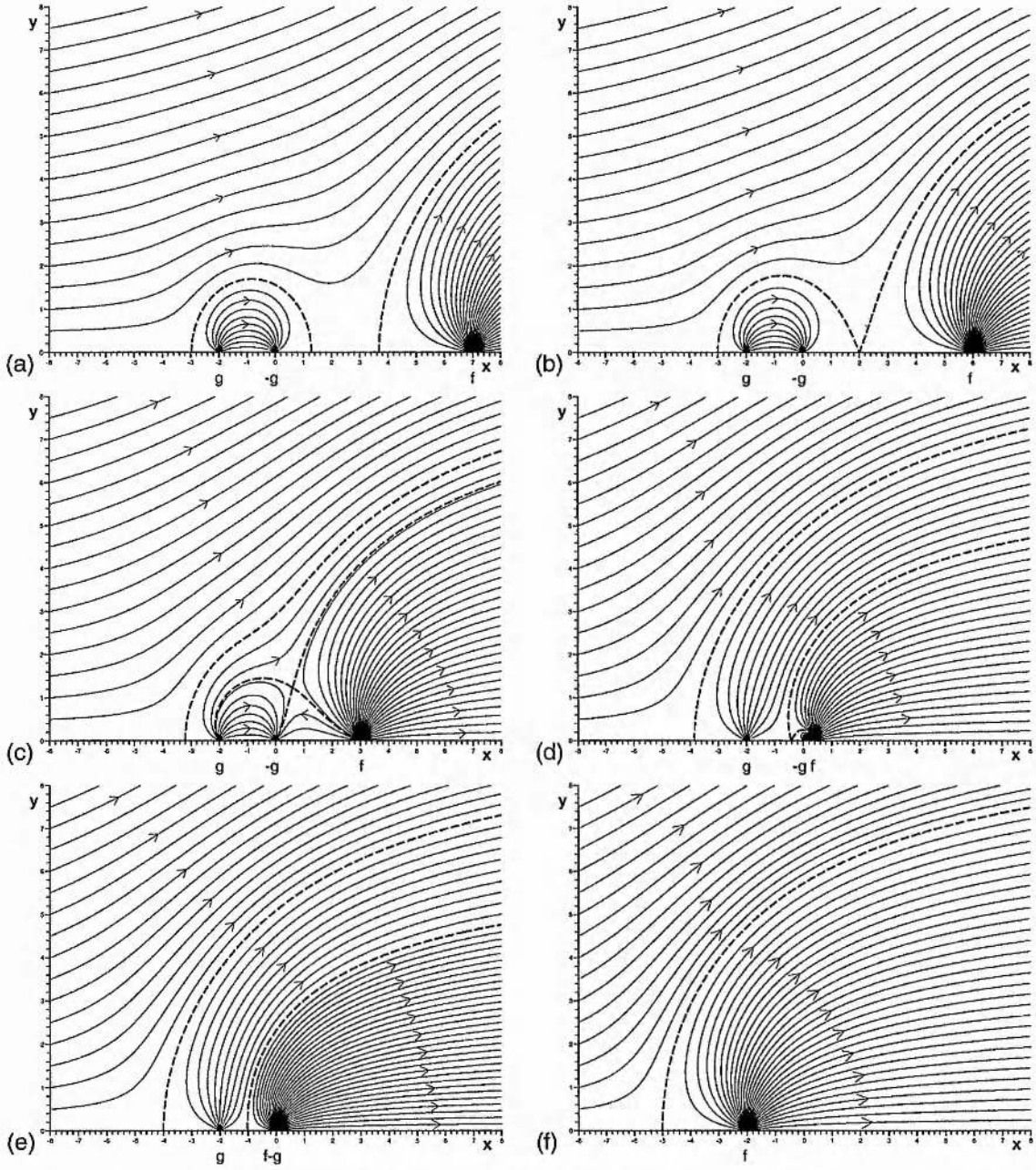

Figure 4.2: Magnetic field configurations for an ephemeral region-network interaction, where the overlying field is of strength, $B_o = 10^{-3}$ T (10 G), $k = 3$ and the bipole width (a) is 2 Mm. The bipole is situated with the positive pole at $x = -2$ Mm and the negative pole at $x = 0$, with their strengths equal to $g = \pi \times 10^3$ Wb m^{-1} ($\pi \times 10^9$ Mx cm^{-1}). The network field is positioned at $x = b$. (a) Initially, $b = 7$ Mm, such that the bipole and network region are unconnected. (b) The network field and the negative fragment come into contact for the first time at the interaction distance ($b = d_i = 6$ Mm) with an X-type neutral point at $x = 2$ Mm. (c) The interaction phase with $b = 3$ Mm and the X-point above the photosphere. (d) The negative fragment is fully captured by the stronger network field at $b = d_c = 0.33$ Mm. (e) At the end of the cancellation phase the positive bipolar fragment is isolated at $x = -2$ Mm and the negative bipolar fragment has been cancelled with the network field to leave a fragment of strength $f - g = 2\pi \times 10^3$ Wb m^{-1} ($2\pi \times 10^9$ Mx cm^{-1}). (f) The two positive sources coalesce to leave one source of strength $f = 3\pi \times 10^3$ Wb m^{-1} ($3\pi \times 10^9$ Mx cm^{-1}), at $x = -2$ Mm.

The magnetic configurations through which the magnetic field evolves are drawn for the two scenarios in Figures 4.2 and 4.4. In Figure 4.2 the bipole is of strength $g = \pi \times 10^3$ Wb m^{-1} ($\pi \times 10^9$ Mx cm^{-1}), orientated such that the positive pole is situated at $x = -a = -2$ Mm and the negative pole at $x = 0$. The line source, of strength $f = 3\pi \times 10^3$ Wb m^{-1} ($3\pi \times 10^9$ Mx cm^{-1}), is positioned at $x = b$, where b decreases as the fragments converge. Thus the bipole is weaker than the line source and the ratio of the pole strengths (k) is 3, so this represents the interaction of a weak ephemeral region with a network field region. The overlying field is of strength $B_o = 10^{-3}$ T (10 G). In Figure 4.2a, $b = 7$ Mm and the field is said to be in the pre-interaction phase, since the bipole is unconnected to the positive source of strength f. As b decreases, the channel between the bipole and the network fragment narrows until, at $b = d_i = 6$ Mm (the interaction distance), they come into contact for the first time, Figure 4.2b. This signifies the start of the interaction phase. Now, as the network fragment closes in on the negative fragment of the bipole, an X-type neutral point rises above the x-axis (into the corona) indicating the position of the bright point (Figure 4.2c). This phase continues until the negative fragment of the bipole is fully captured by the larger positive line source, now situated at $b = d_c = 0.33$ Mm (the capture distance) with the X-point once more on the x-axis (photosphere) and the bright point having ended (Figure 4.2d). The two poles carry on converging through the capture phase, Figure 4.2e, until they actually touch, at which point the cancellation phase commences, $b = 0$. The field remaining after cancellation contains two positive sources of strength, $\pi \times 10^3$ Wb m^{-1} ($\pi \times 10^9$ Mx cm^{-1}) and $2\pi \times 10^3$ Wb m^{-1} ($2\pi \times 10^9$ Mx cm^{-1}) which converge to leave a final configuration in which there is one source of strength $3\pi \times 10^3$ Wb m^{-1} ($3\pi \times 10^9$ Mx cm^{-1}) in the overlying uniform field, Figure 4.2f.

The positions of the neutral points (x_n, x_{n+} and x_{n-}) throughout the interaction of the three poles are

$$x_n = S + T - \frac{1}{3}(a - b + f') \ , \tag{4.20}$$

$$x_{n+} = \frac{-1}{2}(S + T) - \frac{1}{3}(a - b + f') + \mathrm{i}\frac{\sqrt{3}}{2}(S - T) \ , \tag{4.21}$$

$$x_{n-} = \frac{-1}{2}(S + T) - \frac{1}{3}(a - b + f') - \mathrm{i}\frac{\sqrt{3}}{2}(S - T) \ , \tag{4.22}$$

where $S = \left(U + \left(U^2 + V^3\right)^{\frac{1}{2}}\right)^{\frac{1}{3}}$, $T = \left(U - \left(U^2 + V^3\right)^{\frac{1}{2}}\right)^{\frac{1}{3}}$, $U = \left(9a_1a_2 - 27a_3 - 2a_1^3\right)/54$, $V = \left(3a_2 - a_1^2\right)/9$ and $a_1 = a - b + f'$, $a_2 = a(f' - g' - b)$ and $a_3 = abg'$.

They are drawn as b varies for the above situation of $k = 3$, $a = 2$ Mm and $g = \pi \times 10^3$ Wb m^{-1} ($\pi \times 10^9$ Mx cm^{-1}) in Figure 4.3. The first frame shows the first neutral point (x_n) which remains on the x-axis, to the left of the bipole, throughout the convergence of the poles (Figure 4.3a). In the following three frames the other two neutral points are plotted. First, in the pre-interaction phase where they are seen to converge at $b = d_i$ and form one neutral point on the photosphere (Figure 4.3b). Then in Figure 4.3c one neutral point rises above the x-axis tracing out the trajectory of the bright point in the corona whilst b decreases from d_i to d_c in the interaction phase. Finally, the last frame shows the neutral points separating again, as they diverge along the x-axis during the capture phase (Figure 4.3d).

The interaction of an ephemeral region with an intracell field is depicted in Figure 4.4, when the pole ratio $k = 1/3$. The bipole has strength $g = \pi \times 10^3$ Wb m^{-1} ($\pi \times 10^9$ Mx cm^{-1}) and is situated with the positive pole at $x = -a = -2$ Mm and the negative pole at $x = 0$, with the line source of strength $f = (1/3)\pi \times 10^3$ Wb m^{-1} ($(1/3)\pi \times 10^9$ Mx cm^{-1}) situated at $x = b$ where b varies. A horizontal

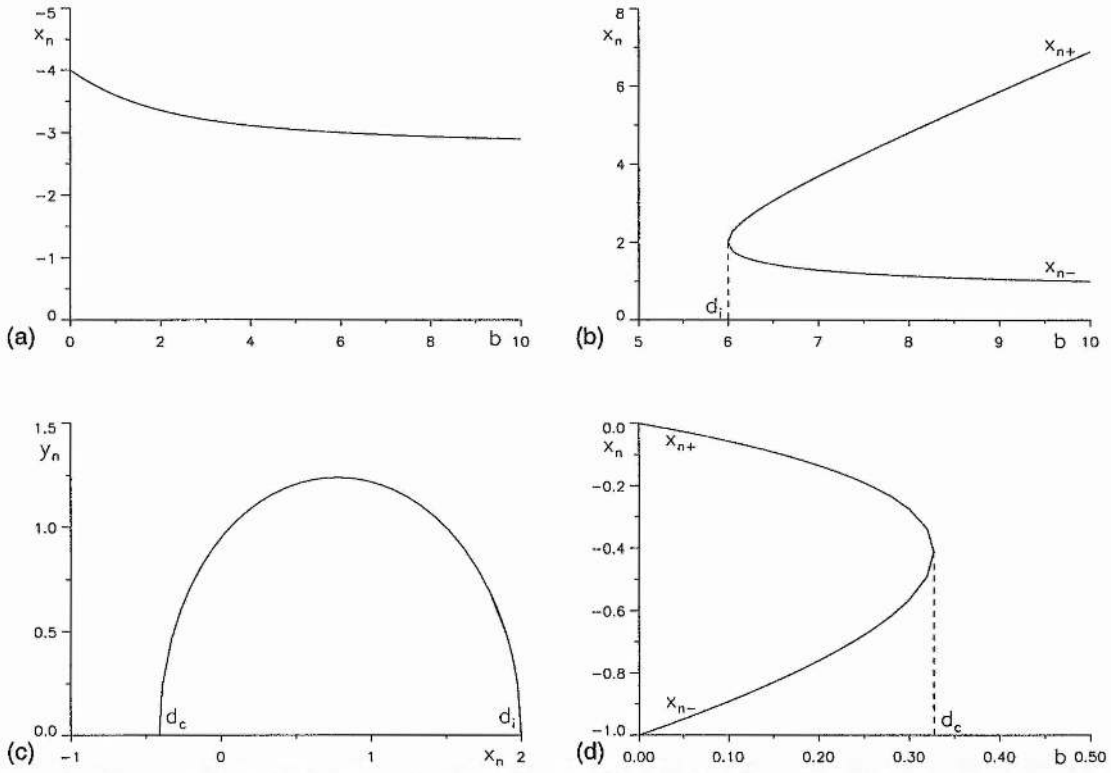

Figure 4.3: The positions of the neutral points in an ephemeral region-network interaction, where the pole strength ratio $k = 3$, the bipole width $a = 2$ Mm, the bipole strength $g = \pi \times 10^3$ Wb m^{-1} ($\pi \times 10^9$ Mx cm^{-1}). (a) The neutral point that is always real is plotted against the position (b) of the line source. (b) The position of the other two neutral points, situated between the bipole and line source, during the pre-interaction phase as b decreases. (c) The trajectory of the bright point in the xy plane, for $d_c < b < d_i$, in the interaction phase. (d) The two neutral points diverging during the capture phase plotted against b.

field of strength $B_o = 10^{-3}$ T (10 G) over-lies the magnetic fragments. Initially the positive intracell source is situated such that it is unconnected to the bipole, Figure 4.4a. The intracell fragment converges towards the negative bipolar fragment until, at $b = d_i = 1.89$ Mm an X-type neutral point appears on the x-axis (photosphere) signifying the start of the interaction phase, Figure 4.4b. Now, as the positive line source moves nearer the bipole, an X-type neutral point rises above the x-axis: here reconnection takes place releasing sufficient energy to produce a bright point (Figure 4.4c). The bright point rises up into the corona, but does not reach anywhere near the height of the neutral point in the previous case. The interaction phase ends when the line source becomes fully captured by the negative bipolar fragment and $b = d_c = 0.12$ Mm (Figure 4.4d). The capture phase is depicted in Figure 4.4e, with Figure 4.4f showing the final state in which the positive line source has cancelled with the negative bipolar fragment to leave an unequal pair of bipolar fragments in the overlying field.

Again the positions of the neutral points are plotted as b decreases (Figure 4.5). Figure 4.5a shows that the first neutral point barely moves at all throughout the convergence of the poles. In Figure 4.5b the two neutral points converge as b decreases to d_i in the pre-interaction phase. Figure 4.5c shows that the bright point does not reach as high in the corona as in the first scenario; this is because the interaction distance (d_i) is smaller and hence the amount of flux reconnected is less. In the capture phase,

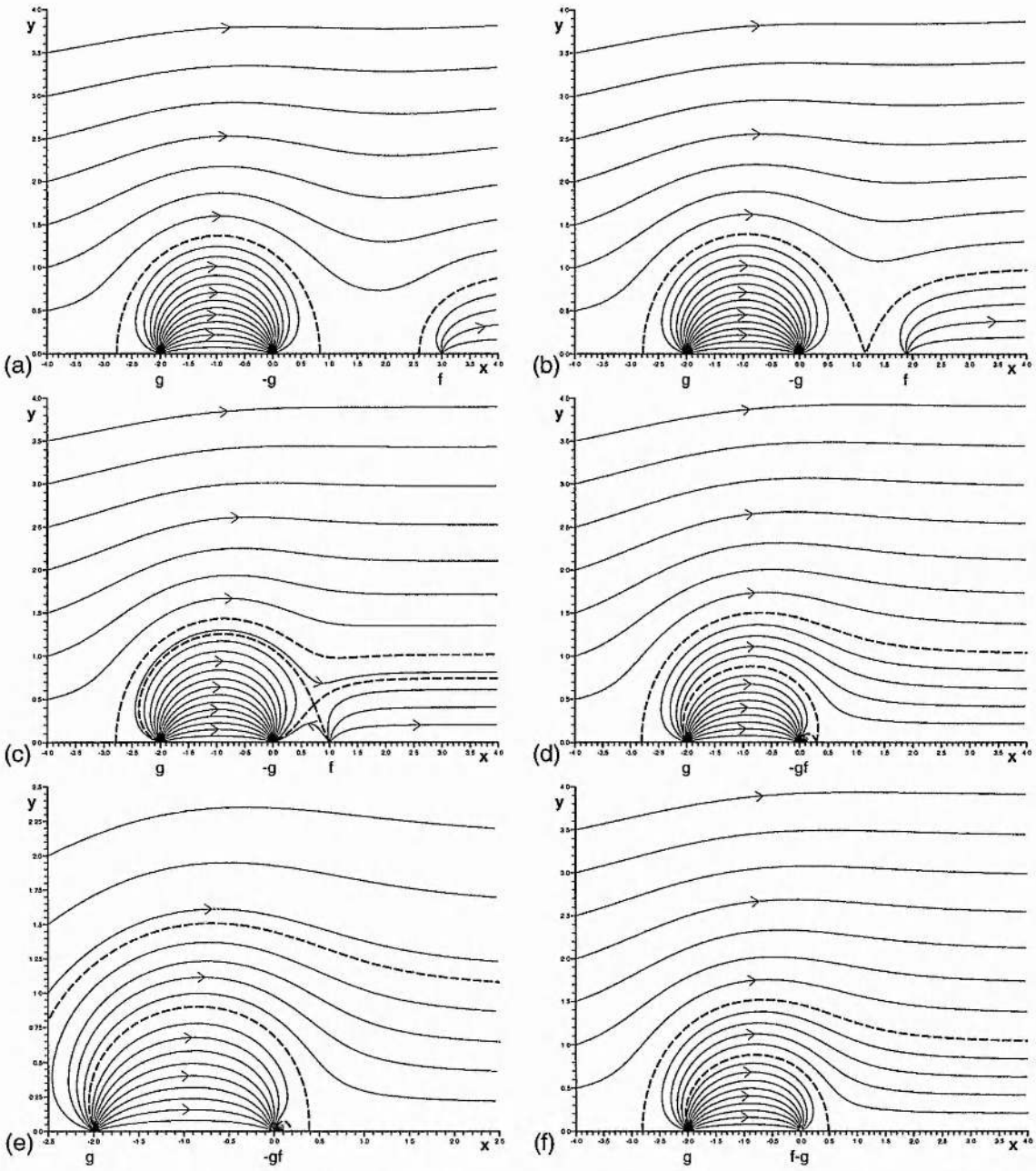

Figure 4.4: The configurations through which the magnetic field evolves during the interaction of an ephemeral region of width $a = 2$ Mm, strength $g = \pi \times 10^3$ Wb m^{-1} ($\pi \times 10^9$ Mx cm^{-1}) and an intracell field of strength $f = (1/3)\,\pi \times 10^3$ Wb m^{-1} ($(1/3)\,\pi \times 10^9$ Mx cm^{-1}), situated at $x = b$. The overlying field has strength $B_o = 10^{-3}$ T (10 G) and the pole strength ratio $k = 1/3$. (a) The pre-interaction phase with the line source at $b = 3$ Mm. (b) At $b = d_i = 1.89$ Mm the intracell and ephemeral region come into contact for the first time. (c) The intracell is at $b = 1$ Mm and the bright point is above the corona in the interaction phase. (d) The end of the interaction phase occurs when $b = d_c = 0.12$ Mm and the intracell is fully connected to the negative bipole fragment for the first time. (e) A close-up of the magnetic field in the capture phase when $b = 0.05$ Mm (f) The cancellation phase and final state with the bipole now reduced to a positive source of strength $g = \pi \times 10^3$ Wb m^{-1} ($\pi \times 10^9$ Mx cm^{-1}) and a negative pole of strength $f - g = -\,(2/3)\,\pi \times 10^3$ Wb m^{-1} ($(2/3)\,\pi \times 10^9$ Mx cm^{-1}).

Figure 4.5d, the neutral points diverge again. The distance over which the bright point occurs is also shorter in the second case, so the bright point is not likely to last as long. The position of the bright points in these scenarios moves relative to the magnetic sources, unlike the two pole cases discussed in Chapters 2 and 3, though it does remain over the area of the cancelling magnetic feature.

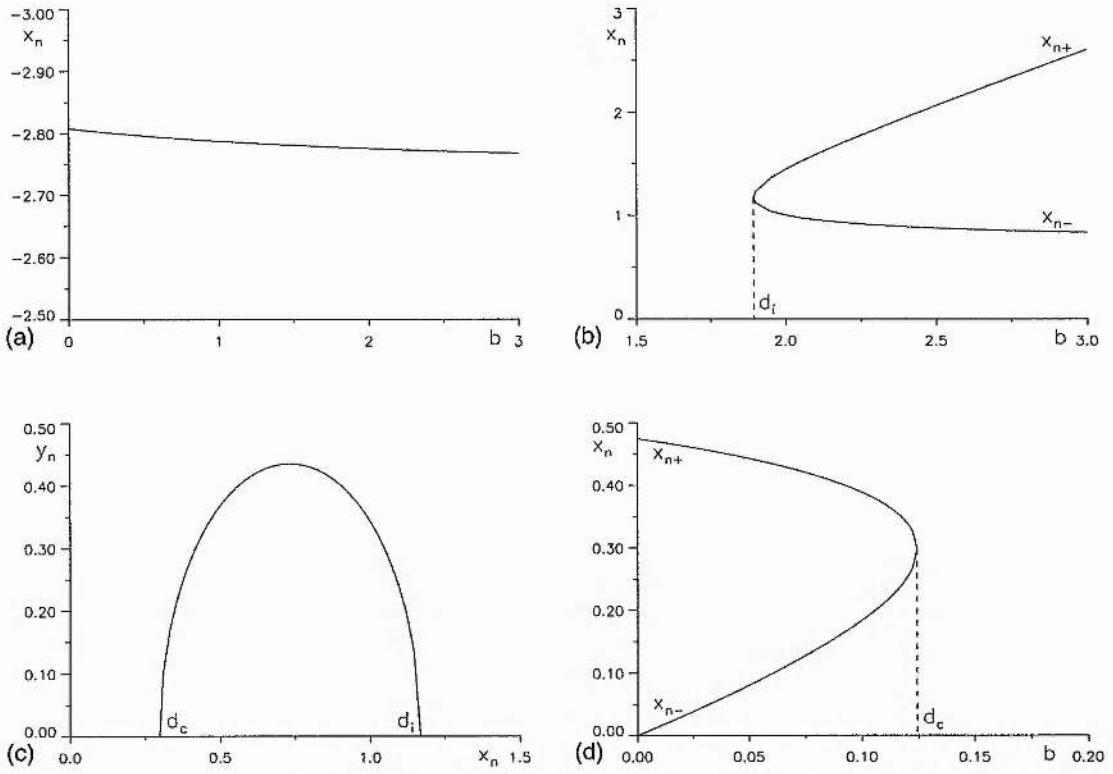

Figure 4.5: The neutral point positions in an ephemeral region-intracell interaction where the pole strength ratio (k) is 1/3, the bipole width $a = 2$ Mm and the bipole strength $g = \pi \times 10^3$ Wb m^{-3} ($\pi \times 10^9$ Mx cm^{-1}). (a) is a plot of the consistently real neutral point against the intracell position, b. The two neutral points between the intracell and ephemeral region are plotted in (b) the pre-interaction phase, versus b, (c) the interaction phase in the xy plane of the fragments and (d) the cancellation phase, against b.

4.3 Free Energy

4.3.1 Calculation of the Current Sheet

As in the previous situations, the total energy released during the bright point is of interest. It is estimated by calculating the energy stored in a current sheet which is allowed to form by assuming that, as the poles converge, no reconnection takes place. The magnetic field for this configuration with a current sheet, which has end points $(x_1, 0)$ and (x_2, y_2), is

$$\mathcal{B}(z) = \frac{\mathrm{i}E(z-x_3)(z-x_1)\left((z-x_2)^2+y_2^2\right)^{\frac{1}{2}}}{(z+a)z(z-b)}, \tag{4.23}$$

where x_3 is the position of a neutral point in the field and E is a constant. There are five unknowns in this equation: thus five boundary conditions are required, which may all be derived from the asymptotic behaviour of the field. Two are found from the fact that the field with the current sheet in tends to infinity in the same manner as that of the potential field which reduces to the background field at infinity, such that

$$\begin{aligned} \mathrm{i}E\left(1-\frac{x_1}{z}-\frac{x_2}{z}-\frac{x_3}{z}-\frac{a}{z}+\frac{b}{z}\right) &= \mathrm{i}B_o+\frac{\mathrm{i}g/\pi}{z}-\frac{\mathrm{i}g/\pi}{z}+\frac{\mathrm{i}f/\pi}{z}+\mathrm{O}\left(\frac{1}{z^2}\right) \\ &= \mathrm{i}B_o\left(1+\frac{f'}{z}\right)+\mathrm{O}\left(\frac{1}{z^2}\right) . \end{aligned} \tag{4.24}$$

Equating terms of unity and $1/z$ gives

$$E = B_o , \tag{4.25}$$

and

$$x_1+x_2+x_3 = -(f'+a-b) . \tag{4.26}$$

The final three boundary conditions are found from the fact that near the poles the field must behave like the sources there, so,

$$g' = \frac{-(a+x_3)(a+x_1)\left((a+x_2)^2+y_2^2\right)^{\frac{1}{2}}}{a(a+b)} , \tag{4.27}$$

$$g' = \frac{-x_3x_1\left(x_2^2+y_2^2\right)^{\frac{1}{2}}}{ab} , \tag{4.28}$$

$$f' = \frac{(b-x_3)(b-x_1)\left((b-x_2)^2+y_2^2\right)^{\frac{1}{2}}}{b(a+b)} . \tag{4.29}$$

Rearranging Equations (4.27), (4.28), and (4.29) gives, respectively,

$$y_2^2 = \left(\frac{g'a(a+b)}{(a+x_3)(a+x_1)}\right)^2-(a+x_2)^2 , \tag{4.30}$$

$$y_2^2 = \left(\frac{g'ab}{x_3x_1}\right)^2-x_2^2 , \tag{4.31}$$

$$y_2^2 = \left(\frac{f'b(a+b)}{(b-x_3)(b-x_1)}\right)^2-(b-x_2)^2 . \tag{4.32}$$

By taking Equation (4.31) from Equations (4.30) and (4.32), x_2 may be written as two different functions dependent on x_1 and x_3 only, namely

$$x_2 = \frac{1}{2a}\left(\left(\frac{g'a\,(a+b)}{(a+x_3)\,(a+x_1)}\right)^2 - \left(\frac{g'ab}{x_3x_1}\right)^2 - a^2\right), \tag{4.33}$$

$$x_2 = \frac{-1}{2b}\left(\left(\frac{f'b\,(a+b)}{(b-x_3)\,(b-x_1)}\right)^2 - \left(\frac{g'ab}{x_3x_1}\right)^2 - b^2\right). \tag{4.34}$$

These, when substituted into Equation (4.26) give two simultaneous equations in x_3 and x_1,

$$-2\,(x_3+x_1) - 2f' - a + 2b = \left(\frac{g'\,(a+b)}{(a+x_3)\,(a+x_1)}\right)^2 a - \left(\frac{g'b}{x_3x_1}\right)^2 a, \tag{4.35}$$

$$2\,(x_3+x_1) + 2f' + 2a - b = \left(\frac{f'\,(a+b)}{(b-x_3)\,(b-x_1)}\right)^2 b - \left(\frac{g'a}{x_3x_1}\right)^2 b, \tag{4.36}$$

which may be solved numerically to give solutions for $x_3 < -a$ and $0 < x_1 < b$, which satisfy the frozen-in flux condition. These solutions may then be used to calculate x_2 and y_2 from either Equation (4.33) or (4.34) and any one of Equations (4.30), (4.31) or (4.32).

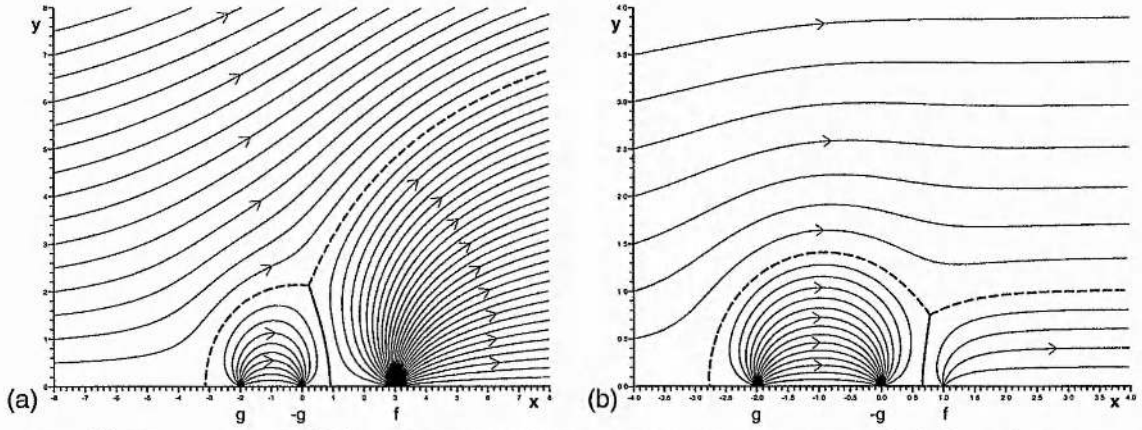

Figure 4.6: (a) The magnetic field configuration for an ephemeral region-network field with a current sheet, where $k = 3$, the bipole has width 2 Mm and strength $g = \pi \times 10^3$ Wb m^{-1} ($\pi \times 10^9$ Mx cm^{-1}) and the line source at $b = 3$ Mm has strength, $f = 3\pi \times 10^3$ Wb m^{-1} ($3\pi \times 10^9$ Mx cm^{-1}). (b) The magnetic field for an ephemeral region-intracell configuration, when the pole strength ratio $k = 1/3$, the bipole has width 2 Mm and strength $g = \pi \times 10^3$ Wb m^{-1} ($\pi \times 10^9$ Mx cm^{-1}) and the intracell fragment has strength $f = (1/3)\,\pi \times 10^3$ Wb m^{-1} ($(1/3)\,\pi \times 10^9$ Mx cm^{-1}), positioned at $b = 1$ Mm.

The magnetic field configuration may then be drawn, including the current sheet, for a weak bipole and a strong line source (ephemeral region-network interaction) (Figure 4.6a) and in Figure 4.6b, for a strong bipole and weak line source (ephemeral region-intracell interaction). The end points of the current sheet are plotted for both scenarios as b decreases from the interaction distance (d_i) to zero in Figures 4.7a and 4.7b. The current sheet for the network interaction is much larger than in the intracell case: this is because the total amount of flux reconnected is greater in the network scenario. In Figures 4.7c and 4.7d the movement of the neutral point (x_3) along the x-axis as b decreases is plotted for each scenario. In the ephemeral region-network case the neutral point moves quite far, but in the ephemeral region-intracell case it hardly moves at all.

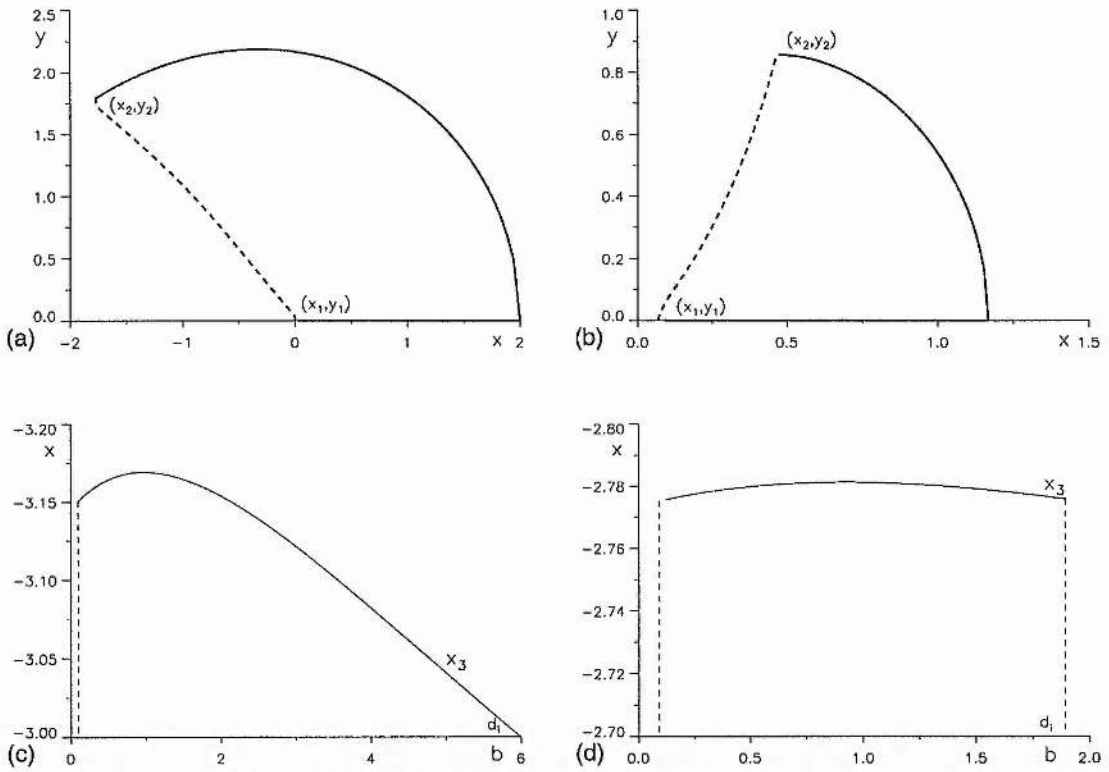

Figure 4.7: The positions of the end points of the current sheet (solid) as b decreases from d_i and the current sheet (dashed) when b is almost 0, for (a) an ephemeral region-network interaction where $k = 3$, and (b) an ephemeral region-intracell scenario where $k = 1/3$. In (c) and (d) the position of the neutral point (x_3) in the field is plotted as b decreases from d_i for, respectively, an ephemeral region-network $k = 3$ cancellation and a $k = 1/3$ ephemeral region-intracell case.

4.3.2 Energy Calculation

The actual free energy in the system is calculated following the steps laid out in the previous chapter. As before the free energy is evaluated from Equation (2.41),

$$\frac{W_F}{d_i} = \frac{-1}{2\mu}\int_{-\infty}^{\infty}\left[A\left(B_x - B_{px}\right)\right]_{y=0}\mathrm{d}x\,, \tag{4.37}$$

where A along $y = 0$ is found to be

$$A(x,0) = \begin{cases} 0 & x < -a \\ -g & -a < x < 0 \\ 0 & 0 < x < b \\ -f & x > b \end{cases}. \tag{4.38}$$

Since A is independent of x the energy may be written in terms of two integrals

$$\frac{W_F}{d_i} = \frac{-A(x,0)}{2\mu}\left\{\int_{-\infty}^{\infty} B_x\,|_{y=0}\,\mathrm{d}x - \int_{-\infty}^{\infty} B_{px}\,|_{y=0}\,\mathrm{d}x\right\}. \tag{4.39}$$

The x components of the potential magnetic field (B_{px}) and the magnetic field containing the current sheet (B_x) are

$$B_{px} = \mathcal{I}m\left[\mathcal{B}_p(x)\right] = B_o + \frac{g}{\pi(x+a)} - \frac{g}{\pi x} + \frac{f}{\pi(x-b)}, \tag{4.40}$$

and

$$B_x = \mathcal{I}m\left[\mathcal{B}(x)\right] = \frac{B_o(x-x_3)(x-x_1)\left((x-x_2)^2+y_2^2\right)^{\frac{1}{2}}}{(x+a)x(x-b)}. \tag{4.41}$$

The integrals in Equation (4.39) can be solved indefinitely:

$$\int B_{px}\,|_{y=0}\,dx = B_o\left\{x + g'\log[x+a] - g'\log[x] + f'\log[x-b]\right\}; \tag{4.42}$$

$$\begin{aligned}\int B_x\,|_{y=0}\,dx = {} & \frac{B_o(a+x_3)(a+x_1)}{a(a+b)}\int\frac{Q(x)}{x+a}dx - \frac{B_o x_3 x_1}{ab}\int\frac{Q(x)}{x}dx \\ & + \frac{B_o(b-x_3)(b-x_1)}{b(a+b)}\int\frac{Q(x)}{x-b}dx,\end{aligned} \tag{4.43}$$

where $Q(x) = \left((x-x_2)^2+y_2^2\right)^{\frac{1}{2}}$ and the integral

$$\int\frac{Q(x)}{x+a},$$

has already been solved in Chapter 3 (Equations (3.46), (3.48) and (3.50)). It equals

$$\begin{aligned}\int\frac{Q(x)}{x+a}dx = {} & Q(x) - (a+x_2)\log[Q(x)+x-x_2] \\ & - |\,Q(-a)\,|\log\left[\frac{Q^2(-a) - (a+x_2)(x+a) + |\,Q(-a)\,|\,Q(x)}{x+a}\right];\end{aligned} \tag{4.44}$$

thus the remaining two integrals may be solved simply by substituting in $a=0$ and $a=-b$, respectively into the above equation,

$$\begin{aligned}\int\frac{Q(x)}{x}dx = {} & Q(x) - x_2\log[Q(x)+x-x_2] \\ & - |\,Q(0)\,|\log\left[\frac{Q^2(0) - x_2 x + |\,Q(0)\,|\,Q(x)}{x}\right],\end{aligned} \tag{4.45}$$

$$\begin{aligned}\int\frac{Q(x)}{x-b}dx = {} & Q(x) + (b-x_2)\log[Q(x)+x-x_2] \\ & - |\,Q(b)\,|\log\left[\frac{Q^2(b) + (b-x_2)(x-b) + |\,Q(b)\,|\,Q(x)}{x-b}\right].\end{aligned} \tag{4.46}$$

These may be combined to give

$$\int B_x \mid_{y=0} \mathrm{d}x = B_o \left\{ \left(\frac{-g'}{\mid Q(-a) \mid} + \frac{g'}{\mid Q(0) \mid} + \frac{f'}{\mid Q(b) \mid} \right) Q(x) \right.$$
$$- \left(\frac{-g'(a+x_2)}{\mid Q(-a) \mid} + \frac{g'x_2}{\mid Q(0) \mid} + \frac{f'(x_2-b)}{\mid Q(b) \mid} \right) \log [Q(x) + x - x_2]$$
$$+ g' \log \left[\frac{Q^2(-a) - (a+x_2)(x+a) + \mid Q(-a) \mid Q(x)}{x+a} \right] - g' \log \left[\frac{Q^2(0) - x_2 x + \mid Q(0) \mid Q(x)}{x} \right]$$
$$\left. - f' \log \left[\frac{Q^2(b) + (b-x_2)(x-b) + \mid Q(b) \mid Q(x)}{x-b} \right] \right\}, \tag{4.47}$$

which may be simplified by noticing

$$\frac{-g'}{\mid Q(-a) \mid} + \frac{g'}{\mid Q(0) \mid} + \frac{f'}{\mid Q(b) \mid} = 1, \tag{4.48}$$

and

$$\frac{-g'(a+x_2)}{\mid Q(-a) \mid} + \frac{g'x_2}{\mid Q(0) \mid} + \frac{f'(x_2-b)}{\mid Q(b) \mid} = -f'. \tag{4.49}$$

Thus, subtracting Equation (4.42) from (4.47),

$$\int [B_x - B_{px}]_{y=0} \mathrm{d}x = B_o \left\{ Q(x) - x + f' \log \left[\frac{Q(x) + x - x_2}{Q^2(b) + (b-x_2)(x-b) + \mid Q(b) \mid Q(x)} \right] \right.$$
$$\left. + g' \log \left[\frac{(Q^2(-a) - (a+x_2)(x+a) + \mid Q(-a) \mid Q(x)) x^2}{(Q^2(0) - x_2 x + \mid Q(0) \mid Q(x))(x+a)^2} \right] \right\}. \tag{4.50}$$

Putting in the limits of integration from $-a$ to 0 and remembering that $Q(x) = - \mid Q(x) \mid$ (Appendix D), gives

$$\int_{-a}^{0} [B_x - B_{px}]_{y=0} \mathrm{d}x = B_o \left\{ \mid Q(-a) \mid - \mid Q(0) \mid - a \right.$$
$$+ g' \log \left[\frac{4Q^2(-a) Q^2(0)}{(Q^2(0) + ax_2 + \mid Q(0) \mid\mid Q(-a) \mid)(Q^2(-a) - a(a+x_2) + \mid Q(-a) \mid\mid Q(0) \mid)} \right]$$
$$\left. + f' \log \left[\frac{(\mid Q(0) \mid + x_2)(Q^2(b) - (a+b)(b-x_2) - \mid Q(b) \mid\mid Q(-a) \mid)}{(\mid Q(-a) \mid + a + x_2)(Q^2(b) - b(b-x_2) - \mid Q(b) \mid\mid Q(0) \mid)} \right] \right\}. \tag{4.51}$$

The limits of integration from b to ∞, with $(Q(x) = \mid Q(x) \mid)$ (Appendix D), give

$$\int_{b}^{\infty} [B_x - B_{px}]_{y=0} \mathrm{d}x = B_o \left\{ b - x_2 - \mid Q(b) \mid + f' \log \left[\frac{4Q^2(b)}{(\mid Q(b) \mid + b - x_2)^2} \right] \right.$$
$$\left. + g' \log \left[\frac{(a+b)^2 (\mid Q(-a) \mid - (a+x_2))(Q^2(0) - bx_2 + \mid Q(0) \mid\mid Q(b) \mid)}{b^2 (\mid Q(0) \mid - x_2)(Q^2(-a) - (a+b)(a+x_2) + \mid Q(b) \mid\mid Q(-a) \mid)} \right] \right\}. \tag{4.52}$$

Therefore the free energy released from the field is

$$
\begin{aligned}
W_F &= \frac{\pi B_o^2 d_i}{2\mu}\left\{g'\int_{-a}^{0}\left[B_x - B_{px}\right]_{y=0}\mathrm{d}x + f'\int_{b}^{\infty}\left[B_x - B_{px}\right]_{y=0}\mathrm{d}x\right\} \\
&= \frac{\pi B_o^2 d_i}{2\mu}\left\{g'\left(\mid Q\left(-a\right)\mid - \mid Q\left(0\right)\mid -a\right) - f'\left(\mid Q\left(b\right)\mid -b+x_2\right) + f'^2\log\left[\frac{4Q^2\left(b\right)}{\left(\mid Q\left(b\right)\mid +b-x_2\right)^2}\right]\right. \\
&+ g'^2\log\left[\frac{4Q^2\left(-a\right)Q^2\left(0\right)}{\left(Q^2\left(0\right)+ax_2+\mid Q\left(0\right)\parallel Q\left(-a\right)\mid\right)\left(Q^2\left(-a\right)-a\left(a+x_2\right)+\mid Q\left(-a\right)\parallel Q\left(0\right)\mid\right)}\right] \\
&+ \left.g'f'\log\left[\frac{\left(\mid Q\left(-a\right)\mid -\left(a+x_2\right)\right)^2\left(Q^2\left(b\right)-\left(a+b\right)\left(b-x_2\right)-\mid Q\left(-a\right)\parallel Q\left(b\right)\mid\right)^2}{\left(\mid Q\left(0\right)\mid -x_2\right)^2\left(Q^2\left(b\right)-b\left(b-x_2\right)-\mid Q\left(b\right)\parallel Q\left(0\right)\mid\right)^2}\right]\right\}. \qquad (4.53)
\end{aligned}
$$

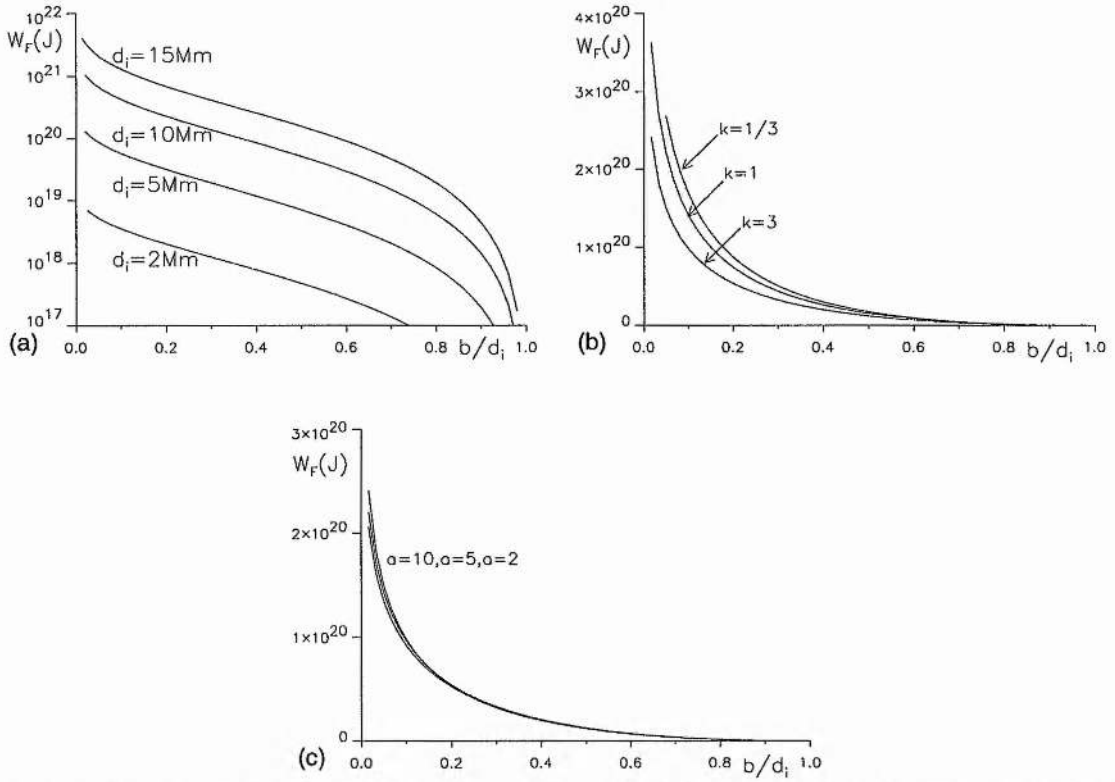

Figure 4.8: The free energy (W_F) measured in Joules released during the bright point versus the normalised position (b/d_i) of the positive line source for: (a) interaction distances of d_i =2, 5, 10, 15 Mm where $B_o = 10^{-3}$ T (10 G), $a = 2$ Mm and $k = 3$; (b) pole strength ratios (k) of 1/3, 1, 3 when $B_o = 10^{-3}$ T (10 G), $a = 2$ Mm and $d_i = 6$ Mm; (c) different bipole widths, a =2, 5, 10 Mm when $B_o = 10^{-3}$ T (10 G), $k = 3$ and $d_i = 6$ Mm.

Figure 4.8 plots the free energy (W_F) released during the bright point versus the position of the line source (b/d_i). In all cases the energy released is sufficient to produce a bright point and is a similar size to that released in the two pole scenarios of the earlier chapters. In Figure 4.8a the interaction distance (d_i) is varied, for constant k, a and B_o and shows that the energy released increases rapidly with increasing d_i. Figure 4.8b shows that, as the ratio of the pole strengths is increased, relatively little

change is seen in the energy. Finally in Figure 4.8c the size of the bipole a is increased: here an even smaller effect on the energy is seen with most energy released in the $a = 2$ case and the least expended in the $a = 10$ case. Thus the energy is mainly dependent on the interaction distance, which is a measure of the total flux reconnected and hence cancelled in the system. Note in Figure 4.8b that the $k = 1/3$ scenario has a higher energy released than in the $k = 3$ case: this is because to create an interaction distance of d_i=6 Mm in both cases, the total flux in the system must be greater in the $k = 1/3$ case than in the $k = 3$ case.

4.4 Bright Point Lifetime

The lifetime of the bright point (t_{bpt}) may also be evaluated given the speed of convergence (v) of the intracell or network fragment and equals

$$t_{bpt} = \frac{d_i - d_c}{v} . \tag{4.54}$$

This is a function of a, k, d_i and v and must be calculated numerically, since analytical solutions of d_i and d_c are not known. The time of the bright point is plotted in Figure 4.9 versus the interaction distance d_i. Figure 4.9a shows that if the fragments have the same strengths ($k = 1$) then the bright point will last longer than if they are of differing strengths. Figure 4.9b indicates that the larger the width of the bipole the longer the bright point will last. Obviously the bright point lasts longer if the fragments are converging at slower speeds: for example a convergence of $v = 0.1$ km s^{-1} produces bright points of 30 - 40 hrs, whilst bright points with lifetimes of less than 10 hrs converge at $v = 0.3$ km s^{-1}. The actual lifetimes of the bright points are comparable with the observed times of 2 - 48 hrs and appear similar to those predicted in the unequal cancelling flux case.

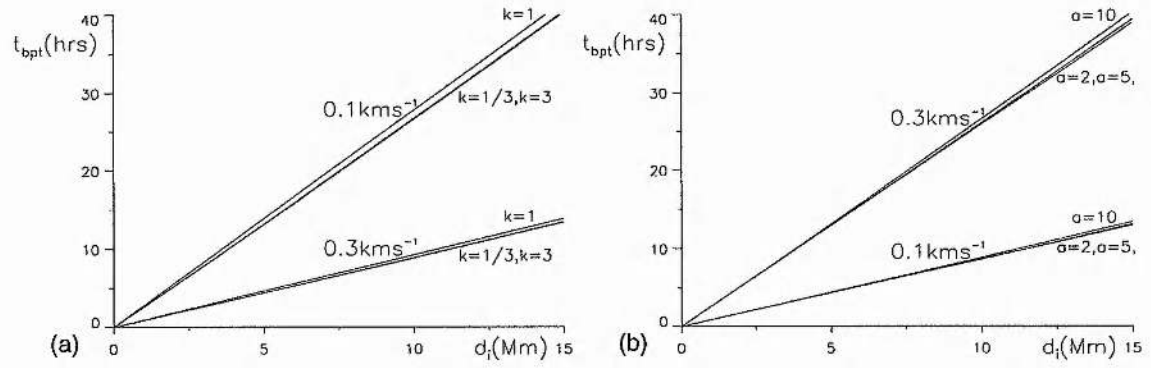

Figure 4.9: The lifetime of the bright point versus the interaction distance (d_i) for velocities of convergence 0.1 km s^{-1} and 0.3 km s^{-1} for (a) pole ratios k =1/3, 1, 3 and (b) bipole widths of a =2, 5, 10 Mm.

4.5 Conclusion

A converging flux model has been developed in this chapter to model the interaction of a bipolar region with a single magnetic fragment such as ephemeral region-network or ephemeral region-intracell cancellations. The model consists of a single line source moving towards a bipole of different strength in a

background horizontal magnetic field. The magnetic field evolves through a series of quasi-static states, where initially the magnetic bipole and line source are unconnected in the pre-interaction phase; then as the line source moves nearer they begin to reconnect during the interaction phase forming a bright point above the photosphere which rises and then lowers when the reconnection is complete. The capture phase follows in which the weaker of the line source and bipole fragment is fully connected to the stronger of the two. The fragments remain connected until they come into contact and cancel. As in the previous converging flux models these stages agree with the observations for bright points and cancelling magnetic features laid out by Priest *et al.* (1994).

In studying the lifetime of the bright point, both intracell and network cancellations lasted for the observed time scale of between 2 and 48 hrs. If the interaction distance is the same and the pole strength ratio is k or $1/k$, then the lifetimes of the bright points are very similar. This is probably because the interaction distance is a measure of the total flux that is cancelled, so if the rate of flux cancellation, that is the rate of convergence of the poles, is the same then one would expect similar lifetimes. However, it is more likely that in an ephemeral region-intracell cancellation less flux would be cancelled and therefore a shorter lived bipole would appear. For example, in the two magnetic field evolution scenarios (Figures 4.2 and 4.4), the ephemeral region-network cancellation has a pole strength ratio $k = 3$, bipole strength, $g = \pi \times 10^3$ Wb m^{-1} ($\pi \times 10^9$ Mx cm^{-1}) and interaction distance $d_i = 6$ Mm: therefore it has a lifetime of approximately 14 hrs, whereas the ephemeral region-intracell cancellation has $k = 1/3$, $g = \pi \times 10^3$ Wb m^{-1} ($\pi \times 10^9$ Mx cm^{-1}) and $d_i = 1.89$ Mm and therefore a lifetime of 4 - 5 hrs. The larger the width of the bipole (a) the longer the bright point lasts, however, the actual increase in the length of the lifetime is marginal.

The energy released from the bright point is also affected similarly with the ratio of the pole strengths (k) and the bipole width (a) having a limited effect if the interaction distance is kept constant. However, varying the interaction distance and hence the total amount of flux reconnected during the bright point has a large effect on the energy released. One would, therefore, expect a cancelling magnetic feature between an ephemeral region and an intracell (where less flux is reconnected and hence the interaction distance is smaller) to be less bright than in an ephemeral region-network cancellation where the interaction distance would be large.

Also in this model it is found that the height and position of the bright point are no longer completely stationary as in the two previous converging flux models, but they do remain almost directly above the cancelling magnetic feature. The height of the bright point is, of course, dependent on the amount of flux reconnected, and therefore dependent on both k and d_i, so one would expect an ephemeral region-intracell interaction to have a bright point lower in the corona than a ephemeral region-network cancellation.

Overall, the extra magnetic fragment of the bipole which does not take part in the cancellation does not seem really to have any effect on the lifetime or free energy of the bright point. In fact, the values attained in this model seem to be very similar to the previous two models which produce energies and bright point lifetimes of the order of the observed readings. This is encouraging and reinforces our faith in the usefulness of the converging flux model.

Chapter 5

Models of Three-Dimensional X-ray Bright Points

5.1 Introduction

The soft x-ray NIXT images of the lower solar corona have fine detail that clearly shows the structure contained in bright points. This structure almost certainly traces out the magnetic field, whose line of sight component may be observed from magnetograms of the photosphere. An attempt is made here to model observed bright points using available observational data from both rocket and ground-based observatories. The aim is to try and explain how the complex structure of bright points arises following the principles of the converging flux model. Two bright points that appeared on 11^{th} July 1991 (eclipse day) are chosen for this study. Section 5.2 describes the observational data used, whilst Section 5.3 outlines the stages involved in the study of each bright point. Initially there is a consideration of the structure of the transverse magnetic field components in the photosphere. Then a purely two-dimensional look at all the poles lined up in the photosphere (along the x-axis) gives a simple view of the magnetic field line structure. Work in three dimensions tries to model the magnetic structures emanating from the surface of the Sun, with emphasis on the form of the separatrix surfaces and the separator. Finally a comparison of the observed brightenings of the bright point in the lower solar corona and possible reconnected (illuminated) field lines is made in an attempt to explain the structure of the bright point. The separatrices and separator are calculated in both two dimensions and three dimensions (Section 5.4). In Section 5.5 bright point I is studied and in Section 5.6 bright point II. The conclusions are contained in Section 5.7.

5.2 Observations

The bright points studied are from a full disc soft x-ray image (Figure 5.1) taken by the Normal Incidence X-ray Telescope (NIXT) on a rocket flight on the 11^{th} July 1991 at the same time as the eclipse totality seen from Hawaii. The NIXT instrument was launched on a NASA sounding rocket from White Sands Missile Range at 17:25 UT. NIXT observes the full disc of the Sun with a resolution better than 1"; it is described in detail by Spiller *et al.* (1991). The multilayer mirror has a pass band of 1.4 Å at 63.5 Å and includes the wavelengths of the emission lines of Mg X and Fe XVI that are formed at temperatures T$\approx 10^6$ K and 3×10^6 K, respectively.

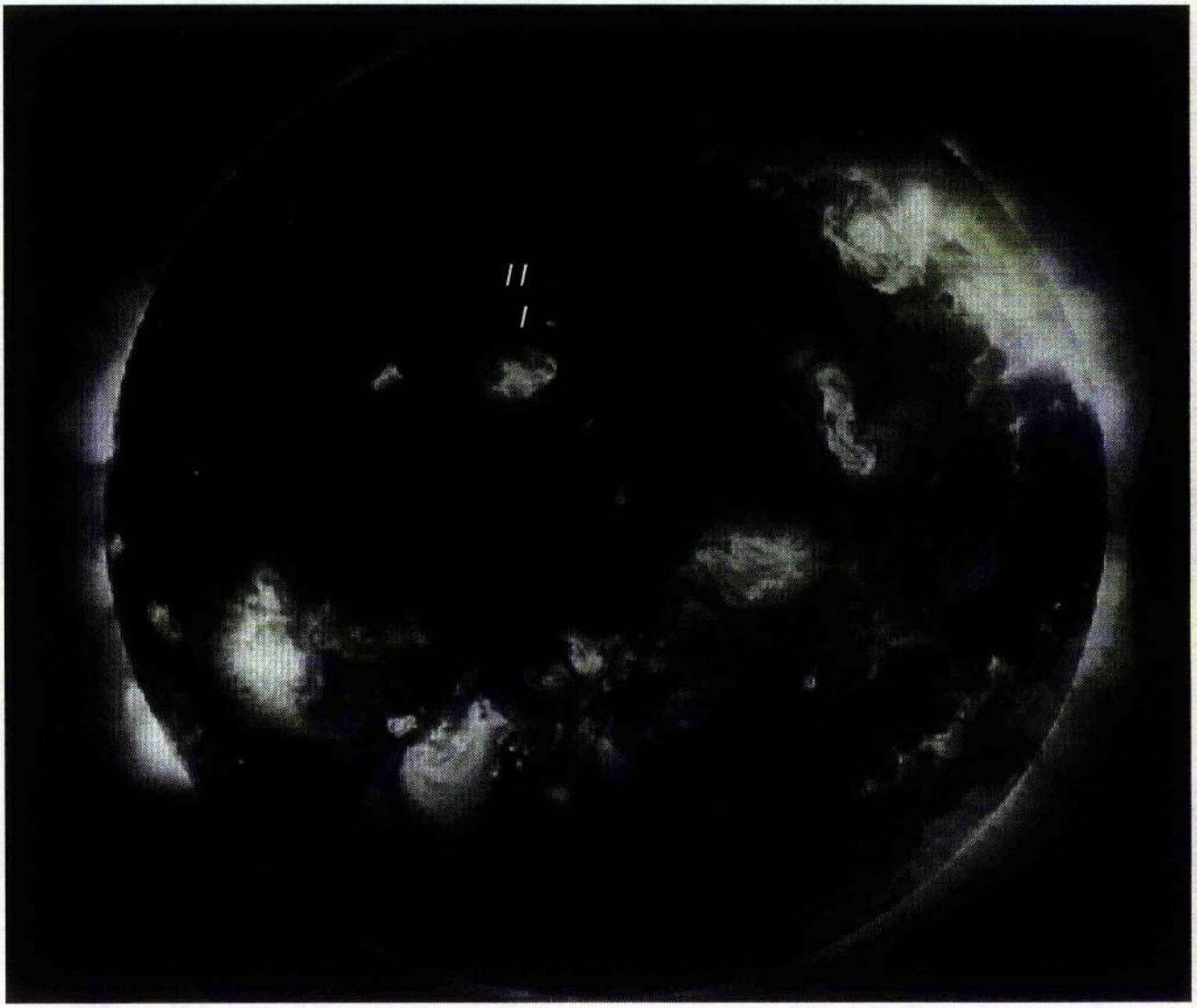

Figure 5.1: A full-disc soft x-ray image of the sun taken by the NIXT telescope on the 11^{th} July 1991. The x-ray bright points studied are labelled I and II (courtesy of L. Golub). Note, for interest, that on the right of the picture the moon is just coming into view before the eclipse.

The full disc x-ray image reveals five distinctive bright points, two of which are labelled I and II in Figure 5.1. This paper concentrates on bright point's I and II which on enlarged x-ray images (Figure 5.2) are shown to have a bright inner core, with a more diffuse cloud of complex structure extending outwards.

The corresponding Kitt Peak magnetograms taken on 11^{th} July for the region directly below the bright points show the normal component of the magnetic field. Contour plots made from the magnetograms, given at two resolutions (low resolution: Figures 5.3a and 5.3b; high resolution: Figures 5.7 and 5.15), show the intensity and structure of the normal components of the magnetic field in the photosphere. The higher resolution contour plots have equivalent resolution to that of the NIXT full disc images. Regions of positive magnetic field are depicted by solid black contours and negative magnetic field regions by black dashed contours. The contour spacing varies from plot to plot (see Figure captions), outlining positive

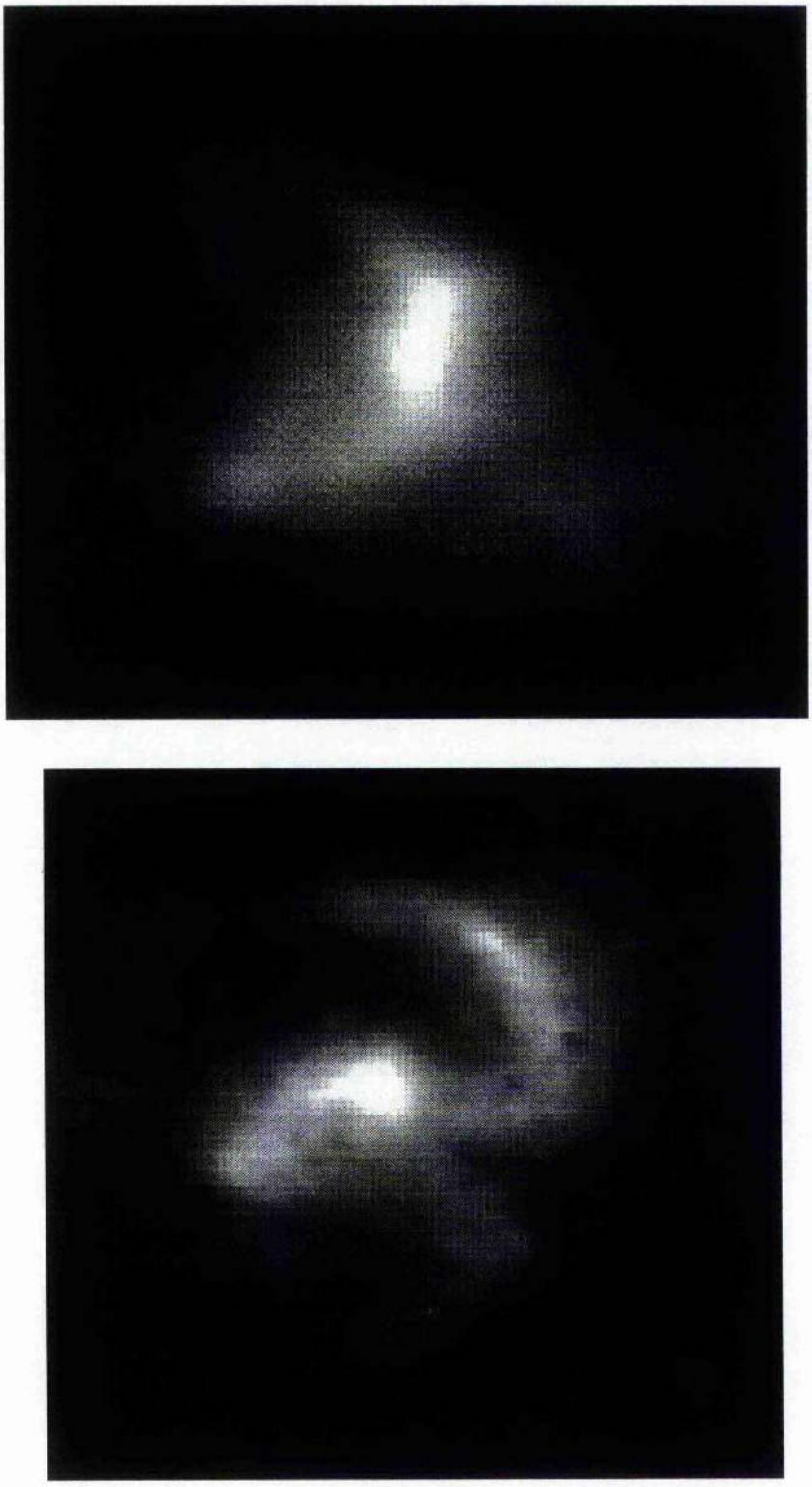

Figure 5.2: The soft x-ray images of bright points I and II taken by the NIXT telescope on the 11^{th} July 1991.

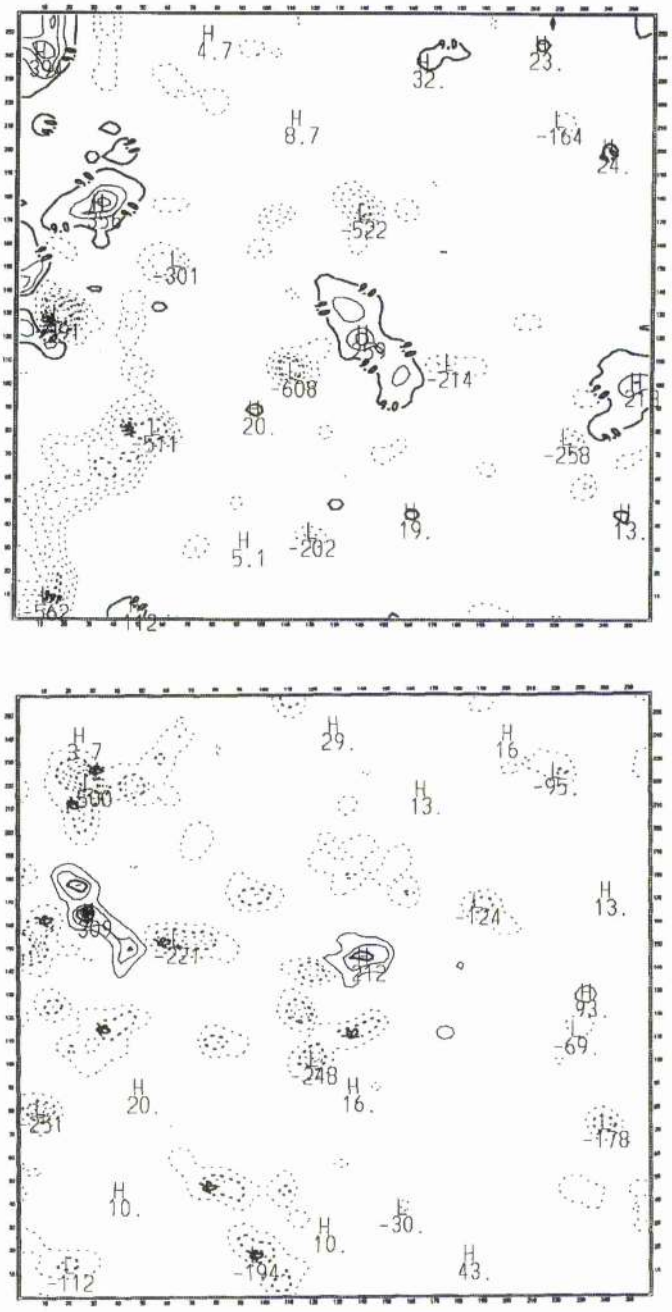

Figure 5.3: The low-resolution contour plots taken from the Kitt Peak magnetogram (courtesy of K.Harvey) corresponding to the area of the photosphere below bright points: (a) bright point I is contoured from -991 to 309 and has interval spacings of 100 whilst (b) bright point II is contoured from -322 to 278 and has interval spacings equal to 60. Solid curves depict positive regions and dashed ones negative regions.

and negative magnetic regions of various intensities and sizes. The following model tries to ascertain the most important features which give rise to the observed bright point.

5.3 The Stages Involved in Each Bright Point Study

Initially the contour plots of the normal component of the magnetic field in conjunction with the soft x-ray image of the bright point are considered and various questions asked. Which regions, positive or negative, are connected with the observed brightening? How are these regions likely to be moving, interacting and evolving in order to cause the brightening?

Following the philosophy of the converging flux model, a model for each specific bright point can be set up consisting of poles of various strengths representing the magnetic regions believed to play vital roles in the life of the bright point. According to this model, as the poles move, field lines will reconnect and brighten due to the injection of heat or plasma along them by the reconnection process itself. Examples of this behaviour have been seen with Yohkoh (Tsuneta, 1993; Shibata *et al.*, 1992a,b; Strong *et al.*, 1992).

To model the magnetic fields it is assumed that there are no regions of emerging flux and that only the movement and interaction (cancellation) of existing magnetic regions give rise to the brightenings in the corona. Of course, due to the limited number of magnetograms available, the motion of these regions and the validity of this assumption are difficult to determine, but here it is taken as a working hypothesis. Possible motions of the important poles are considered and the final dynamic situation proposed for each bright point, because it is suggested by the converging flux model and accounts for the observed brightenings in a natural way.

It is supposed that the photosphere below each bright point consists of a series of discrete magnetic sources and sinks. Let Φ be the magnetic potential due to m poles, namely,

$$\Phi = \sum_{i=1}^{m} \frac{f_i}{\left((x-a_i)^2+(y-b_i)^2+z^2\right)^{\frac{1}{2}}}, \tag{5.1}$$

where f_i is strength of the pole i situated at position $(a_i, b_i, 0)$ on the photosphere ($z = 0$). Then the corresponding magnetic field ($\mathbf{B} = -\nabla\Phi$) with components (B_x, B_y, B_z) is

$$\mathbf{B} = \left(\sum_{i=1}^{m} \frac{f_i\,(x-a_i)}{\left((x-a_i)^2+(y-b_i)^2+z^2\right)^{\frac{3}{2}}}, \sum_{i=1}^{m} \frac{f_i\,(y-b_i)}{\left((x-a_i)^2+(y-b_i)^2+z^2\right)^{\frac{3}{2}}}, \sum_{i=1}^{m} \frac{f_i z}{\left((x-a_i)^2+(y-b_i)^2+z^2\right)^{\frac{3}{2}}} \right). \tag{5.2}$$

To estimate the magnitude of flux from each magnetic fragment it is assumed that each source is circular and that the contours form a dome, defined by

$$X = d_i \cos\frac{\pi}{2B_i} Z, \tag{5.3}$$

where $0 \leq X \leq d_i$ and d_i is the radius of the source whose centre is defined as the point at which the normal component of the magnetic field is a maximum, and $0 \leq Z \leq B_i$, with B_i taken to be the

maximum normal component of the magnetic field. Thus, by considering the volume of revolution about the Z-axis the total magnetic flux (f_i) of the fragment is found to be

$$f_i = \frac{\pi d_i^2 B_i}{2} . \tag{5.4}$$

The distances between the magnetic fragments (a_i and b_i) are measured from their centres. The actual length scales were calculated by relating the full disc image to the Kitt Peak magnetograms from which the contour plots were made.

In both cases two plots of the magnetic field lines transverse to the photosphere are drawn. These show the *separatrices*, the field lines which divide topologically distinct regions and extend to or from the X-type neutral points, the reconnection points in the photosphere. In the first plot the magnetic poles are in the positions dictated by the observed magnetic contour plots for the given bright point and in the second plot one magnetic pole is moved. A comparison of these two plots enables a decision to be made as to which field lines are likely to have been reconnected and which field lines would therefore brighten.

The positions of the neutral points in the field are found by numerically solving the two simultaneous equations

$$\begin{aligned} B_x &= \sum_{i=1}^{m} \frac{f_i (x_n - a_i)}{\left((x_n - a_i)^2 + (y_n - b_i)^2\right)^{\frac{3}{2}}} = 0 , \\ B_y &= \sum_{i=1}^{m} \frac{f_i (y_n - b_i)}{\left((x_n - a_i)^2 + (y_n - b_i)^2\right)^{\frac{3}{2}}} = 0 . \end{aligned} \tag{5.5}$$

where (x_n, y_n) are the coordinates of the neutral points in the $z = 0$ plane. The way in which the separatrices are found is discussed in Section (5.4.1).

A schematic two-dimensional depiction of the reconnection in each bright point may be set up by placing poles in a straight line and considering the resulting magnetic field above the photosphere. Using complex variable theory, let $z = x + iy$, where the x-axis is the line in the photosphere along which the poles lie and the y-axis is directed vertically upwards from the photosphere. The complex magnetic potential $\mathcal{B}$, is defined as $\mathcal{B}(z) = B_y + iB_x$, where $\mathbf{B}(x, y) = B_x \hat{\mathbf{e}}_x + B_y \hat{\mathbf{e}}_y$, so that

$$\mathcal{B}(z) = \sum_{i=1}^{m} \frac{f_i}{(z - a_i)} , \tag{5.6}$$

where m is the number of poles, f_i is the strength of pole i situated at position $(a_i, 0)$ on the photosphere. This has a corresponding flux function (A) satisfying $\mathbf{B} = \nabla \times \mathbf{A}$, where $\mathbf{A} = A\hat{\mathbf{e}}_z$. Therefore, $B_x = \partial A/\partial y$, $B_y = -\partial A/\partial x$ and

$$A(x, y) = \sum_{i=1}^{m} f_i \mathrm{Arg}\left(\frac{a_i - z}{a_i}\right) . \tag{5.7}$$

Equally spaced field lines are drawn by plotting $A = i\pi/n + A_{io}$ where n is an integer, and A_{io} is the value of the flux function $A(a_i + \delta, 0)$, where δ is small and positive and the integer i corresponds to only the positive poles (or only the negative poles).

In three dimensions, using the form for the magnetic field given in Equation (5.2), the separatrix surfaces and the separator, if applicable, may be drawn (see Section 5.4.2). *Separatrix surfaces* are the three-dimensional extension of two-dimensional separatrices and divide topologically distinct regions. The *separator* is the intersection of the separatrix surfaces: it is a field line that extends from one neutral point to another. When a pole is moved, field lines near the separator reconnect to form new field lines which brighten due to the injection of heat and plasma along them. How long the field lines remain bright depends on their cooling times; typical conductive and radiative time scales may be calculated assuming constant pressure, with the net cooling time given by

$$\tau = \frac{\tau_c \tau_r}{\tau_c + \tau_r} , \tag{5.8}$$

at a given density. Considering first the heat loss purely due to conduction, it is found that the energy equation has the form,

$$\rho c_p \frac{\mathrm{D}T}{\mathrm{D}t} = -\nabla \cdot \mathbf{q} , \tag{5.9}$$

where c_p is the specific heat at a constant pressure and $\mathbf{q}$ is the heat flux function which can be written as

$$\mathbf{q} = -\kappa \nabla T , \tag{5.10}$$

where κ is the thermal conduction tensor and is taken to be $\kappa_{\|}$ since conduction parallel to the field lines is much greater than perpendicular conduction. By performing a dimensional analysis Equation (5.9) determines the conduction time,

$$\tau_c = \frac{\rho c_p l^2}{\kappa_{\|}} . \tag{5.11}$$

The typical coronal value of $\kappa_{\|}$ is approximately $9 \times 10^{-12}\, T^{\frac{5}{2}}$ W m^{-1} K^{-1} ($9 \times 10^{-7}\, T^{\frac{5}{2}}$ ergs s^{-1} cm^{-1} K^{-1}), and l is the characteristic length of a loop at a given height: therefore

$$\tau_c = 4 \times 10^{-12} n_e l^2 T^{-\frac{5}{2}} . \tag{5.12}$$

where n_e is the electron number density in m^{-3}.

If heat loss is through radiation effects alone, the energy equation may be written as

$$\rho c_p \frac{\mathrm{D}T}{\mathrm{D}t} = n_e^2 Q(T) , \tag{5.13}$$

since in the chromosphere and corona the plasma is completely ionised and the atmosphere may be considered as 'optically thin'. An analytical approximation to $Q(T)$ is

$$Q(T) = \chi T^{\alpha} \text{ W m}^3 , \tag{5.14}$$

where the constants $\chi(T)$ and $\alpha(T)$ are given in Table 5.1 from a paper by Rosner *et al.* (1978).

Range of T(K)	χ	α
$10^{4.3}$ - $10^{4.6}$	$10^{-34.85}$	0
$10^{4.6}$ - $10^{4.9}$	10^{-44}	2
$10^{4.9}$ - $10^{5.4}$	$10^{-34.2}$	0
$10^{5.4}$ - $10^{5.75}$	$10^{-23.4}$	-2
$10^{5.75}$ - $10^{6.3}$	$10^{-34.94}$	0
$10^{6.3}$ - 10^{7}	$10^{-30.73}$	$-2/3$

Table 5.1: Values for α and χ for temperatures T in Kelvin (Rosner *et al.*, 1978).

Thus the radiative cooling time (τ_r) is found to be

$$\tau_r = 3 \times 10^{-23} \frac{T}{n_e Q(T)} . \tag{5.15}$$

From Withbroe and Noyes (1977) the constant pressure (p/k_B) in the transition region and corona is taken to be $n_e T = 2 \times 10^{21}$ m^{-3} K (2×10^{15} cm^{-3} K) ($k_B \approx 1.381 \times 10^{-23}$ kg m s^{-1} K^{-1}); thus the Table 5.2 (adapted from Habbal *et al.* (1990)) shows the typical cooling times for loops of various temperatures in the corona and transition region. Newly reconnected field lines will therefore remain hot (bright) for tens of minutes in the corona, but for only seconds in the transition region. If the average velocity of a field line in the corona is between 1 - 10 km s^{-1}, then field lines up to 5 Mm from their reconnection site may appear bright.

	Transition Region		Corona	
T(K)	2×10^5	5×10^5	10^6	3×10^6
$Q(T)$ (W m^3)	9×10^{-35}	10^{-35}	10^{-35}	5×10^{-36}
[ergs cm^3 s^{-1}]	[9×10^{-22}]	[10^{-22}]	[10^{-22}]	[5×10^{-23}]
n_e (m^{-3})	10^{16}	4×10^{15}	2×10^{15}	6.7×10^{14}
l (m)	10^6	10^6	10^7	10^7
τ_c (s)	9×10^3	362	800	17
τ_r (s)	7	375	1.5×10^3	1.5×10^4
τ (s)	7	184	521	17

Table 5.2: Typical cooling times for bright points with constant pressure $p/k_B = n_e T = 2 \times 10^{21}$ m^{-3} K (2×10^{15} cm^{-3} K).

5.4 Calculation of the Separatrices and Separator

The field lines that make up the separatrix surfaces (separatrices) cannot always be calculated analytically, so there needs to be a means of identifying them. They are all field lines, so if one point on a separatrix can be found then the whole separatrix may be calculated by integrating along it numerically, as for any

other field line. To calculate the start points of the separatrices their fundamental property is considered; that is, separatrices are defined as the field lines that extend from (to) a point source to (from) a neutral point.

5.4.1 In Two Dimensions

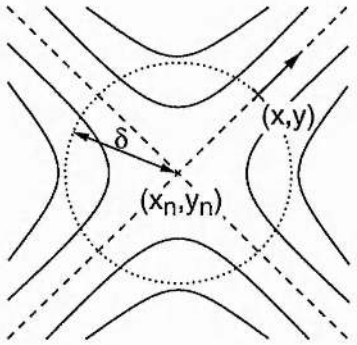

Figure 5.4: The gradient of the separatrix (dashed) through the point (x, y) which lies a distance δ from the neutral point (x_n, y_n) equals the gradient of the line through (x, y) and (x_n, y_n).

In two dimensions the magnetic field at points on a small circle of radius δ around a neutral point (x_n, y_n) are considered. All the separatrices to or from the neutral point must cross the circle, so if δ is sufficiently small the gradient of the separatrix field line at its intersection with the circle will equal the gradient of the radius of the circle at that point (Figure 5.4). Thus if the field line through a point (x, y) is a separatrix then

$$\frac{y - y_n}{x - x_n} = \frac{\mathrm{d}y}{\mathrm{d}x} = \frac{B_y(x, y)}{B_x(x, y)} . \tag{5.16}$$

Now $x = x_n + \delta\cos\theta$ and $y = y_n + \delta\sin\theta$, and so

$$\tan\theta = \frac{B_y(x_n + \delta\cos\theta, y_n + \delta\sin\theta)}{B_x(x_n + \delta\cos\theta, y_n + \delta\sin\theta)} , \tag{5.17}$$

which may be rearranged to give

$$F(\theta) = B_y(x_n + \delta\cos\theta, y_n + \delta\sin\theta)\cos\theta - B_x(x_n + \delta\cos\theta, y_n + \delta\sin\theta)\sin\theta = 0 . \tag{5.18}$$

Thus to find the start points of the separatrices the roots of $F(\theta)$ must be found, given a small value for δ. In two dimensions there are 4 solutions at an X-point.

5.4.2 In Three Dimensions

Field lines in the separatrix surfaces extend out into three dimensions above the plane of the poles forming a surface. Initially a similar method to the one used above to find the two-dimensional separatrices was attempted. This proved ineffective: thus a more robust, but time consuming, method is employed. By

noting that the surfaces divide topologically distinct regions, so that lines just below the surface extend from (to) A to (from) B and lines just above will extend from (to) A to (from) C, then the surface may be found by identifying the points at which field lines switch from AB to AC lines.

For Figure 5.11 this was done by defining a grid in the xy-plane which extends over a region larger than the area enclosed by the separatrices, already found by the two-dimensional method, lying in the $z = 0$ plane. At each point (x_i, y_j) on this grid, field lines through successive, equally spaced positions in the z-direction are labelled as either AB or AC lines depending on whether they end at pole B or pole C. Thus the points (x_i, y_j, z_k) and (x_i, y_j, z_{k+1}) at which the change-over from AB to AC lines occurs indicates approximately the region in which the separatrix surface lies above the point (x_i, y_j). To find the separatrix surface accurately the distance between (x_i, y_j, z_k) and (x_i, y_j, z_{k+1}) is subdivided again into equally spaced points, with the field lines through these points labelled as before, until the change-over in which the surface lies is found. This method is then applied iteratively until the distance between the points $(z_k - z_{k+1})$ is less than a given tolerance. This then gives us one point on the separatrix surface, so continuing in the same manner for all positions on the grid, points may be found lying over the whole separatrix surface. Thus the surface may be drawn: however, it is fairly time consuming and does not indicate what the field lines in the surfaces look like.

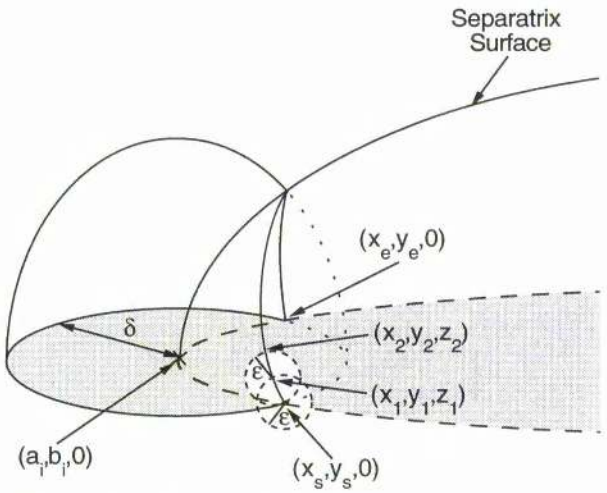

Figure 5.5: A hemisphere of radius δ is located around the pole $(a_i, b_i, 0)$. It intersects the separatrices (dashed) in the $z = 0$ plane at points $(x_s, y_s, 0)$ and $(x_e, y_e, 0)$ and the separatrix surface at points (x_1, y_1, z_1) and (x_2, y_2, z_2) which are situated a distance ϵ apart.

To draw separatrix surfaces made up of field lines one may simply use one set of the points, say (x, y_j, z) where j varies from 0 to n, as start points of the field lines, or a new set may be found. In the diagrams drawn in Figure 5.12, a new set of start points for the field lines is found, since the first set although equally spaced in x and y, is not equally spaced over the surface and thus the field lines produced tend to be centralised at the top of the surface. The new start points are found by the same iterative method except this time the points are searched for over a hemisphere of radius δ centred at the point source $(a_i, b_i, 0)$ on the surface. The point at which one of the separatrices in the $z = 0$ plane intersects this hemisphere of radius δ is labelled $(x_s, y_s, 0)$ and the other $(x_e, y_e, 0)$. A search is conducted around the point $(x_s, y_s, 0)$ at a distance ϵ for a point lying on the surface of the hemisphere and the separatrix surface. This point, when found, is labelled (x_1, y_1, z_1) and is then used as the centre of the next circle, radius ϵ, on which the next point on the separatrix surface lies (x_2, y_2, z_2). The method is

repeated until the final point $(x_e, y_e, 0)$ is reached (Figure 5.5). This enables field lines to be drawn that indicate the intensity of the field in the separatrix surface.

The separator, the intersection of the two separatrix surfaces, is a field line: thus to draw the separator just one point on it needs to be found. To find this point a method similar to that for finding the surfaces is applied. This time, however, a line d lying in the xy plane cutting the projection of the separator on to the x-axis is chosen, Figure 5.6a. At equally spaced intervals along this line, points lying in the dz plane on the two separatrix surfaces can be found. If all the points on the separatrix surface through the two positive poles are labelled (d_i, z_{pi}) and all those on the surface which intersects the negative poles are called (d_i, z_{ni}), then a point on the separator is one in which $z_{pi} = z_{ni}$. So at each point d_i the difference between z_{pi} and z_{ni} is evaluated as i increases, until the sign of $z_{pi} - z_{ni}$ changes (Figure 5.6b). This indicates that the separator lies between d_{i-1} and d_i; thus the same steps are repeated for equally spaced intervals between d_{i-1} and d_i, until the difference between z_{pi} and z_{ni} is less than a given tolerance. The point (d_i, z_{pi}) (or in three dimensions (x_{di}, y_{di}, z_{pi})) is then said to be lying on the separator.

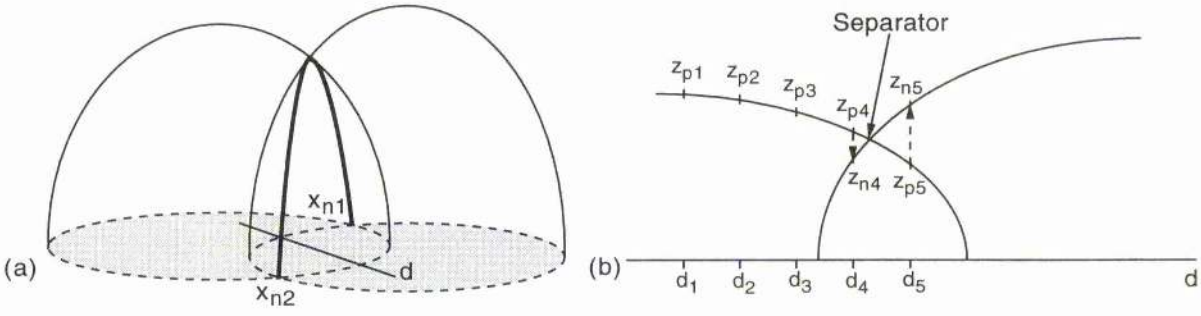

Figure 5.6: (a) The line d lies in the plane of the photosphere below the separator (thick), the interaction of the two separatrix surfaces. (b) At equal intervals along d the positions of the separatrix surfaces, z_{pi} and z_{ni}, are found: thus by considering the distance between the points on the surfaces the separator may be located.

5.5 Bright Point *I*

In the specific case of bright point I it is supposed that the photosphere below the bright point consists of four main magnetic regions A, B, C and D labelled in Figure 5.7. Poles A, B, C and D are estimated to have maximum normal magnetic field strengths (B_i) of 3.91, 2.32, -2.58 and -8.18×10^{-2} T ($\times 10^4$ G), respectively, and radii (d_i) of 2.16, 2.16, 1.8 and 3.6 Mm; thus their fluxes (f_i) are calculated to be 2.9, 1.7, -1.3 and -16.6×10^{11} Wb (or $\times 10^{19}$ Mx), respectively. The poles are assumed to be situated in positions (1.0,0.0,0.0), (0.87,0.69,0.0), (0.0,0.0,0.0) and $(-0.76, -0.33, 0.0)$, respectively, where the origin is taken as the centre of magnetic region C, the small negative region, and the direction of a line from pole C to pole A is taken to be along the x-axis. A distance of one unit corresponds to approximately 10 Mm (14 arcsec) on the Sun.

By using Equation (5.2) a plot of the magnetic field lines transverse to the photosphere can be drawn, Figure 5.9a. Since only one magnetogram was taken at the time of the bright point the actual motions of the magnetic fragments are unknown, but it is assumed that pole C moves towards pole B and away from

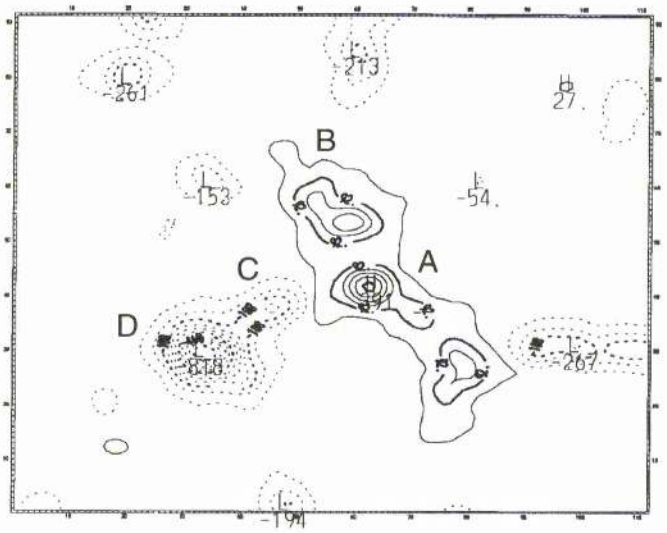

Figure 5.7: Bright point I's high-resolution contour plot taken from the Kitt Peak magnetogram (courtesy of K.Harvey). Solid curves depict positive regions and dashed ones negative regions with the plot contoured from -818 to 372 with intervals of 70. The main magnetic regions A, B, C and D believed to be involved in the formation of the bright point are labelled.

poles A and D to position (0.5,0.4,0.0), as shown in Figure 5.9b . This would imply that new field lines from B to C and from A to D would form; these field lines are shaded in Figure 5.9b since it is assumed that heat or plasma is injected along these lines and causes them to brighten. The angles at which the separatrices leave the magnetic sources in the two figures are compared in order to estimate the region of newly reconnected field lines. The shaded area approximates the shape of the bright point fairly well, though of coarse these lines lie only in the photosphere, but they do give a reasonable indication of what the structure in the corona would be like. Here, neither the flow pattern of the field nor the cooling rates of the plasma are taken into account in deciding which field lines would be bright; thus in practise it is possible that some of the field lines shaded would have faded by the time the fragment C reaches its new position. This would also depend upon exactly which mechanism the field lines reconnect by, whether it was at a steady rate or impulsive. However as a first approximation this result seems encouraging.

The brighter inner core is thought to be situated in the lower solar corona over the neutral points, the centres of reconnection in the photosphere, as sketched in Figure 5.8.

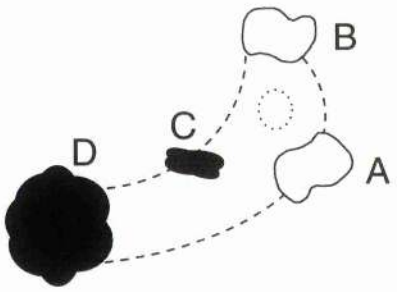

Figure 5.8: A sketch of the relative position of bright point I, outlined by the dashed line, with the brighter inner core, outlined by the dotted line, above the positive magnetic poles A and B (shaded in white) and the negative magnetic poles C and D (shaded in black) in the photosphere.

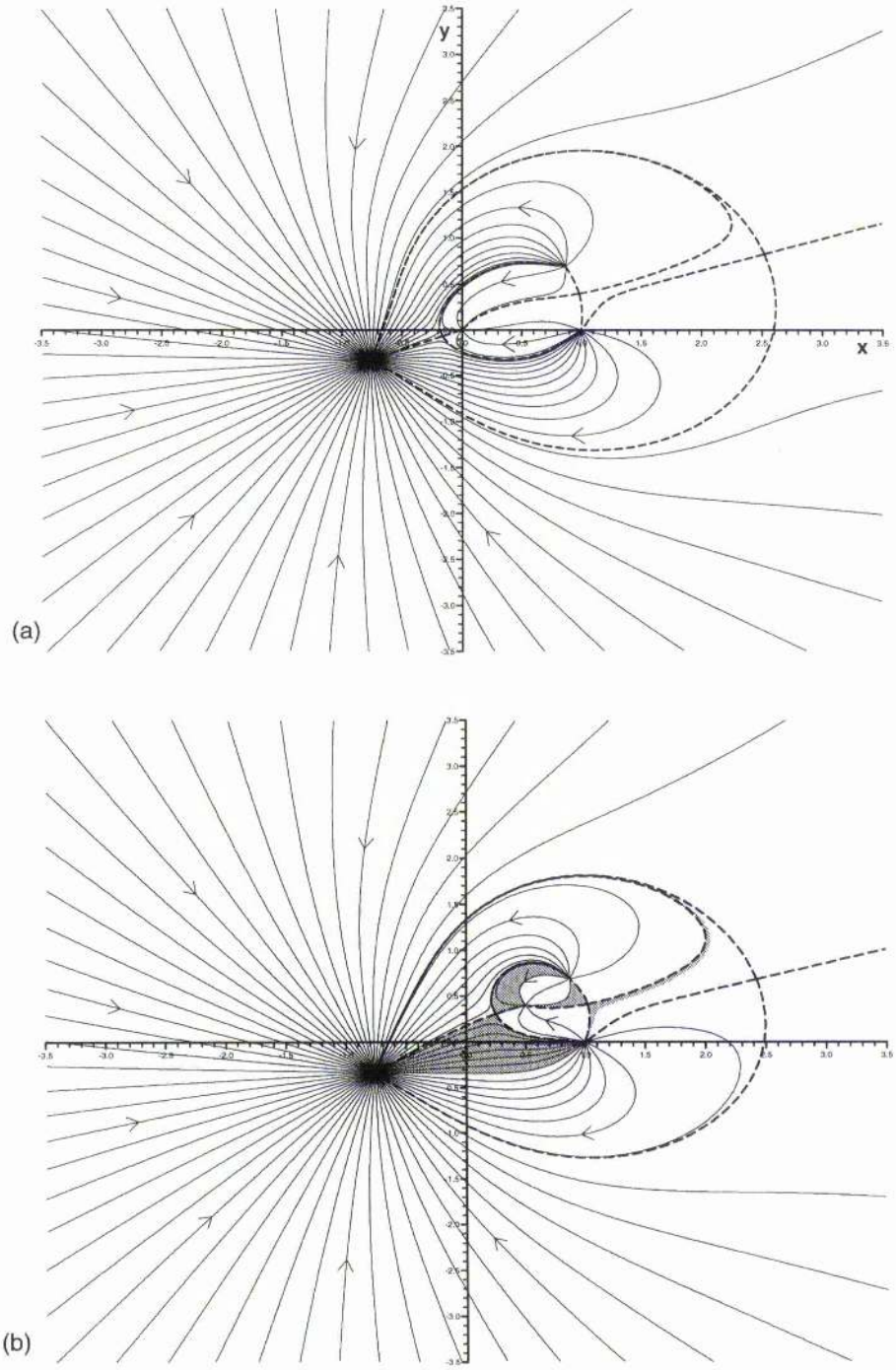

Figure 5.9: (a) A contour plot for bright point I of the potential magnetic field lines lying in the photosphere, due to poles of strengths 2.9, 1.7, -1.3 and -16.6, respectively, positioned at A (1.0,0.0), B (0.87,0.69), C (0.0,0.0) and D $(-0.76, -0.33)$ in the $z = 0$ plane. (b) Corresponding potential field lines when the pole C of strength -1.3 has moved to (0.5,0.4) in the $z = 0$ plane. The shaded regions represent newly reconnected field lines.

A schematic two-dimensional depiction of the reconnection is set up by situating poles A, B, C and D of strengths 2.9, 1.7, -1.3 and -16.6 at 0.6, 0.0, 0.3 and -0.7, respectively, on the x-axis (Figure 5.10a). Pole C of strength -1.3 moves to 0.1 on the x-axis as shown in Figure 5.10b, with new field lines from B to C and from A to D being formed and illuminated.

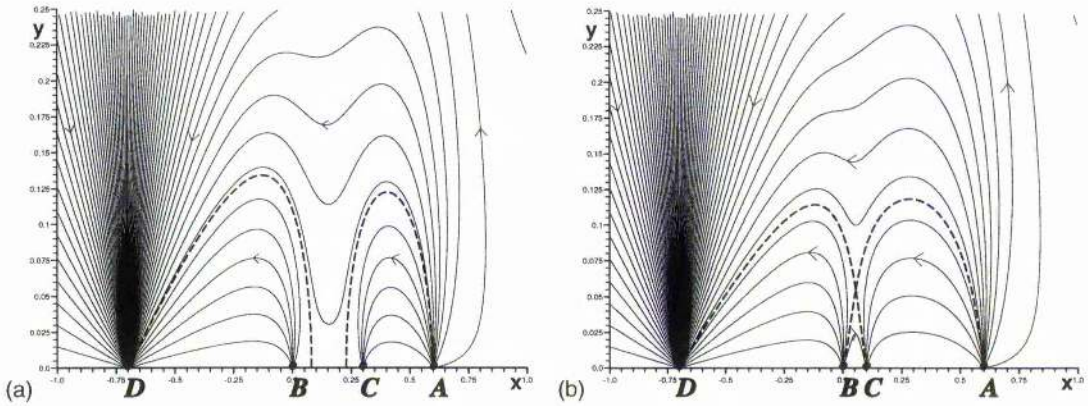

Figure 5.10: (a) Magnetic field lines due to poles of strengths 2.9, 1.7, -1.3, -16.6 and at positions 0.6, 0.0, 0.3 and -0.7, respectively, along the x-axis. (b) Corresponding field lines when the pole of strength -1.3 has moved from 0.3 to 0.1 on the x-axis.

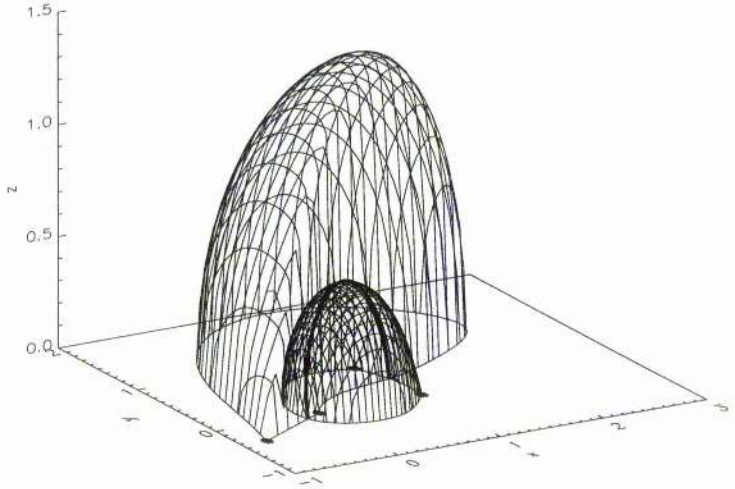

Figure 5.11: The shape of the separatrix surfaces and the separator (thick) is shown due to poles (labelled by dots) of strengths 2.9, 1.7, -1.3, -16.6 at positions A (1.0,0.0), B (0.87,0.69), C (0.0,0.0) and D $(-0.76, -0.33)$, respectively, in the $z = 0$ plane.

Using the strengths and initial positions relating to the two-dimensional transverse magnetic field line plots for this bright point, the separatrix surfaces and the separator are drawn (Figure 5.11). The larger separatrix surface enclosing poles A, B and C is not drawn since it plays no part in the reconnection process and therefore does not effect the bright point. Figures 5.12a and 5.12b show the separator and the structure of the magnetic field lines lying in each of these surfaces. It is interesting to note that the large separatrix surface is made up of field lines starting from the far neutral point and ending at either of the two negative poles and that the smaller separatrix surface is made up of field lines starting from

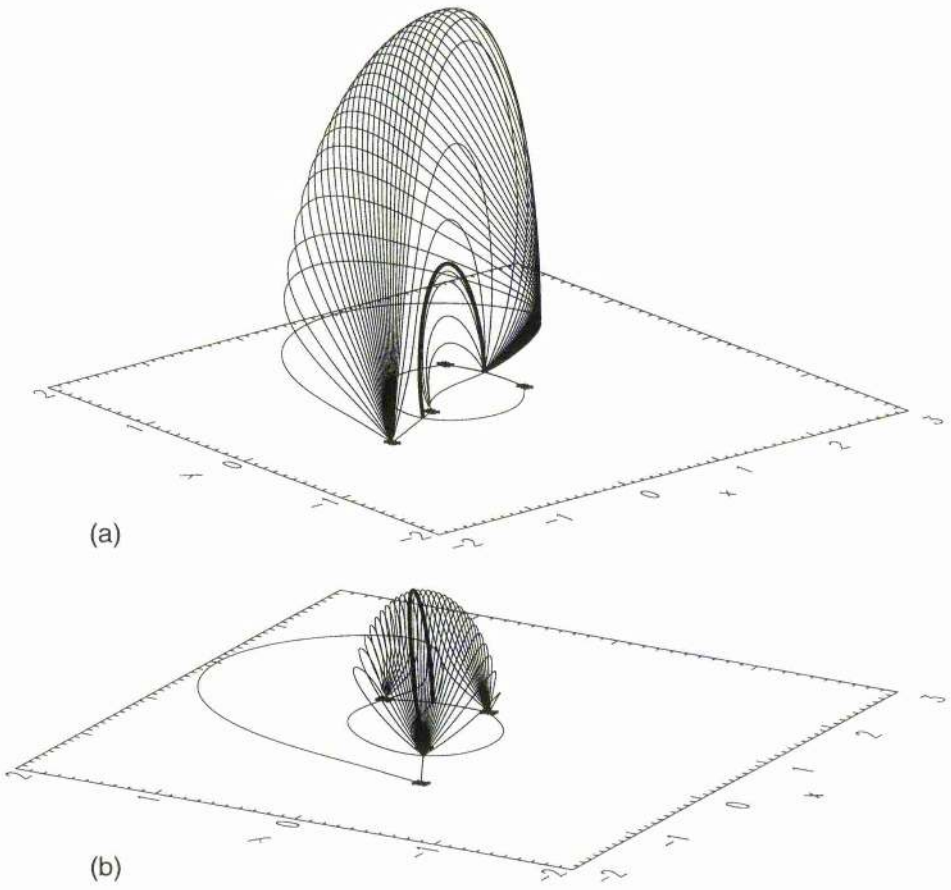

Figure 5.12: The structure of the magnetic field lines lying in the separatrix surfaces and passing through (a) the negative poles and (b) the positive poles of bright point I.

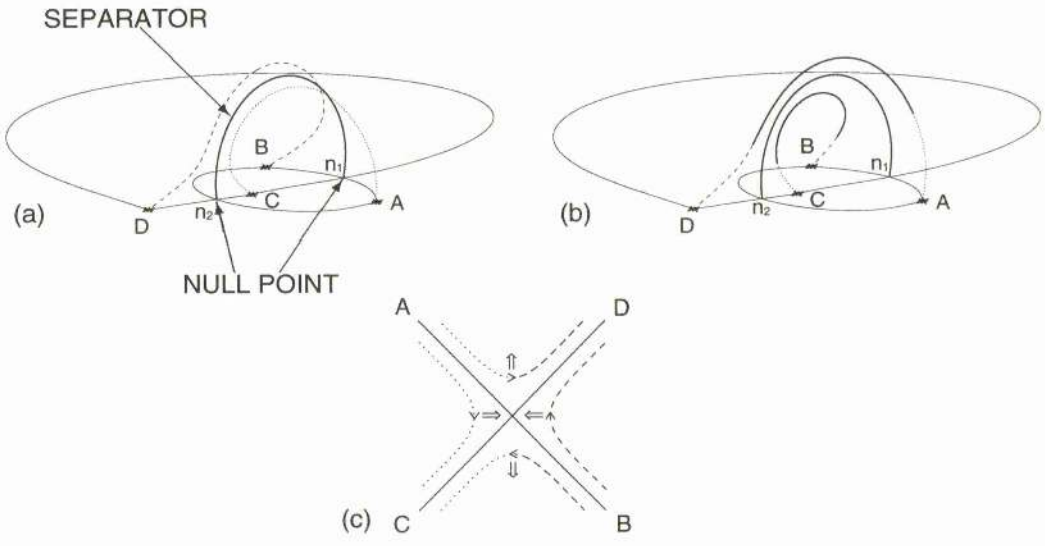

Figure 5.13: Three-dimensional reconnection along a separator (thick). (a) Field lines AC (dotted) and BD (dashed) before reconnection. (b) New field lines AD and BC after reconnection. (c) Reconnection in two dimensions of lines AC (dotted) and BD (dashed) to form the lines AD and BC.

either of the two positive poles and ending at the near neutral point. The separator is the only field line that connects the two neutral points by starting at the far one and ending at the near one; it is assumed that reconnection takes place near the separator.

As pole C moves towards B, field lines such as the two shown in Figure 5.13a, from A to C (dotted) and from B to D (dashed) move such that they form field lines from A through the neutral point n_1 along the separator to neutral point n_2 then into pole C, and from B through n_1 along the separator to n_2 and into D. These lines break simultaneously at the neutral points n_1 and n_2 and reconnect to form field lines from A through n_1 and n_2 along the separator to D and from B through n_1 and n_2 to C: thus new field lines from A to D and from B to C are created (Figure 5.13b). This mechanism of reconnection is similar to that described by Priest and Forbes (1992) in their magnetic flipping model.

The new field lines will brighten due to the injection of heat and plasma along them. The reconnection and movement of the 'bright' field lines may be fast relative to the time it takes for the hot plasma along the field lines to cool. This would mean the field lines such as the ones shown in Figure 5.14 would be bright. Looking down from above, these field lines outline a similar shape to that seen in the soft x-ray image of bright point I.

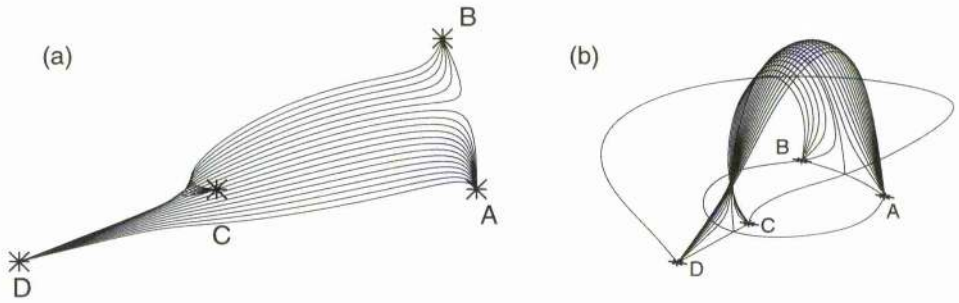

Figure 5.14: Bright point I. Several magnetic field lines, from poles A to D and B to C which have been reconnected due to the movement of pole C towards pole B and away from pole A, viewed from above and from the side.

5.6 Bright Point *II*

The photosphere below bright point II is assumed to consist of four main magnetic regions A, B, C and D labelled in Figure 5.15. The maximum normal magnetic field strengths (B_i) are estimated to be 2.18, -0.82, -1.83 and -3.10×10^{-2} T (or $\times 10^4$ G), and their radii (d_i) are assumed to be 4.4, 2.65, 1.95 and 1.71 Mm, respectively; therefore their strengths are calculated to be 6.6, -0.9, -1.1 and -1.4×10^{11} Wb (or $\times 10^{19}$ Mx). The positions (0.0,0.0,0.0), (-0.33,1.46,0.0), (0.0,-1.39,0.0) and (-0.93,-0.33,0.0) correspond, respectively, to the poles A, B, C and D, with pole A (the only positive pole) taken to lie at the origin and with the negative y-axis in the direction of a line from pole A to pole C. As before, a distance of one unit corresponds to approximately 10 Mm (14 arcsec) on the Sun.

The transverse magnetic fields are plotted in Figure 5.16a. In Figure 5.16b it is assumed that pole A has moved towards pole D, away from poles B and C to position ($-0.4, -0.2$,0.0) causing field lines originally unconnected to either B, C or D, and lying in between poles B and C to reconnect; either they can reconnect with field lines from A to B to form new lines from A to B and from A extending

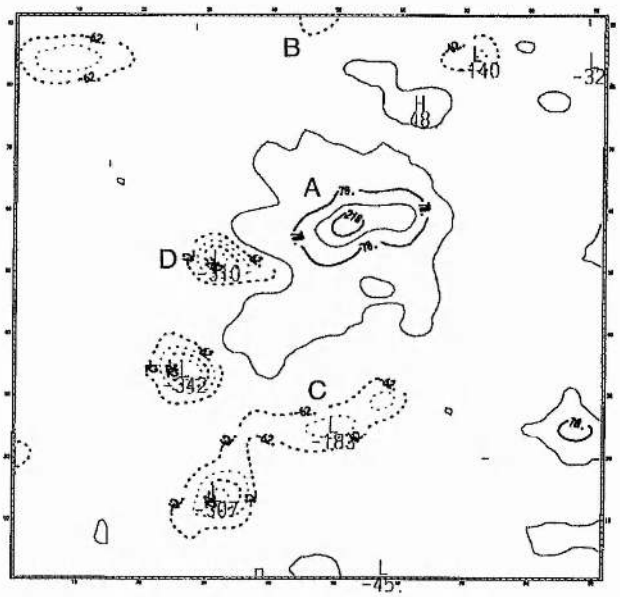

Figure 5.15: A high-resolution contour plot taken from the Kitt Peak magnetogram (courtesy of K.Harvey) of the photosphere below bright point *II*. It is contoured from −342 to 218 and has an interval spacing of 70 with the solid curves depicting positive regions and dashed ones the negative regions. The main magnetic regions A, B, C and D believed to be involved in the formation of the bright point are labelled.

outwards and unconnected to B, C or D and lying between B and D; or they can reconnect with field lines from A to C to form new field lines from A extending outwards lying between C and D that are unconnected to B, C or D and new field lines from A to C. The movement also causes field lines originally unconnected to either B, C or D and lying between poles D and B to reconnect with lines from A to D to form new field lines from A to D and field lines extending outwards from A lying between D and C, but unconnected to either pole. Since A is moving towards D, Figure 5.16 reveals that there seem to be fewer field lines connecting to the far-off negative pole in the xy plane between poles B and C and more between poles B and D, and C and D: therefore it seems reasonable to suggest that the newly reconnected field lines from A to B and from A to C appear on the left-hand side of the lobes enclosing B and enclosing C and not the right-hand side. Also since A, as it moves towards D, moves downwards from B to D this suggests that field lines on the pole B side of the lobe enclosing D are reconnected. As before, to estimate the area of field lines reconnected, a comparison of the angle at which the separatrices leave the magnetic sources is made. The newly reconnected field lines, injected with plasma or heat are likely to brighten; thus the new field lines from A to B, A to C and A to D brighten and are shaded in Figure 5.16b. However this time not all the field lines are shaded; those from A extending out to a far-off negative fragment are not shaded as it is assumed they do not brighten. This assumption is not unreasonable since the heat along these very long field lines spreads out, or the plasma injected is spread along the length of the field lines, so that it is not visible in soft x-rays.

The bright cores of bright point *II* overlie the centres of reconnection at the X-type neutral points and the positive pole A (See Figure 5.17). Since the upper arm of the bright point is more distinctive than the lower it is likely that more field lines from A to B are reconnected than from A to C as would

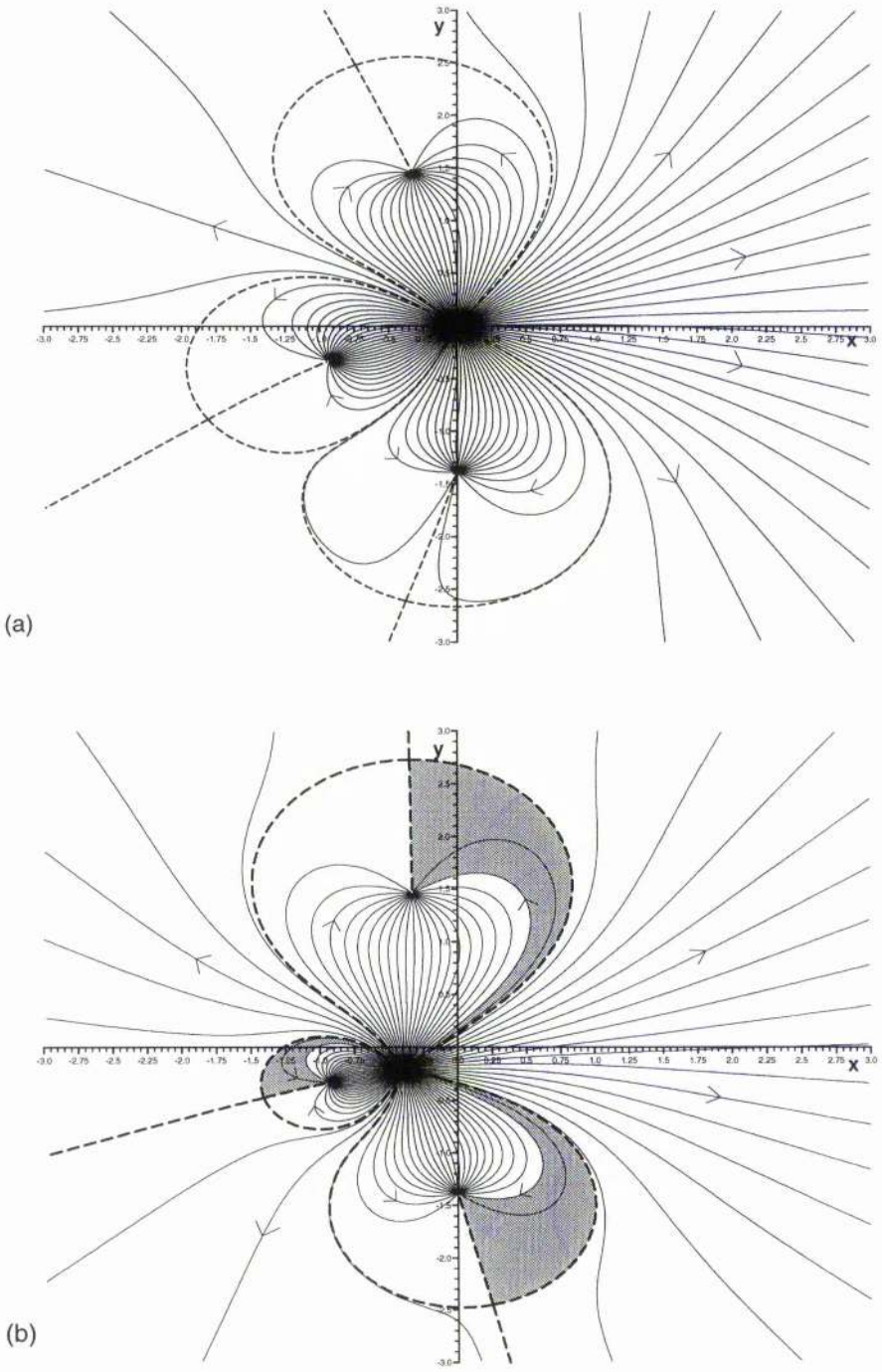

Figure 5.16: (a) A contour plot of the photospheric potential magnetic field lines related to bright point II, with poles of strengths 6.6, -0.9, -1.1 and -1.4, respectively, positioned at A (0.0,0.0), B $(-0.33, 1.46)$, C $(0.0, -1.39)$ and D $(-0.93, -0.33)$ in the $z = 0$ plane. (b) Corresponding potential field lines when the pole A of strength 6.6 has moved to $(-0.4, -0.2)$ in the $z = 0$ plane. The newly reconnected field lines are shaded.

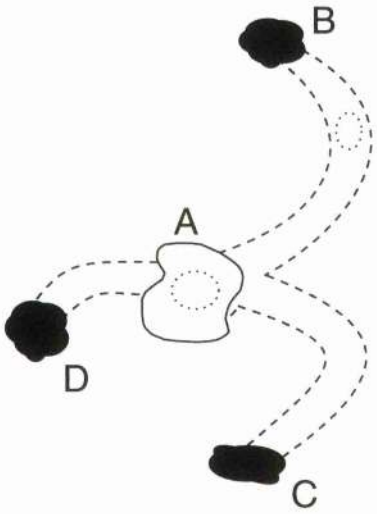

Figure 5.17: A sketch of the relative positions of bright point II, outlined by the dashed curves and its brighter inner cores, outlined by the dotted curves, above the positive magnetic pole A (shaded in white), and the negative magnetic poles B, C and D (shaded in black) in the photosphere.

be produced by a movement down and across of the positive pole A.

In this case the two-dimensional side-on view used to give a simplified look at the reconnection is set up by poles A, B(or C) and D of strengths 6.6, -0.9 and -1.4 being placed at 0.0, 0.6 and -0.5, respectively, on the x-axis, (Figure 5.18a). Figure 5.18b has pole A of strength 6.6 situated at -0.25 on the x-axis, as shown. These figures do not indicate that any reconnection has taken place as pole A has moved, so the reconnection can only be seen in this case by looking at the field lines in the $z = 0$ plane or in three dimensions.

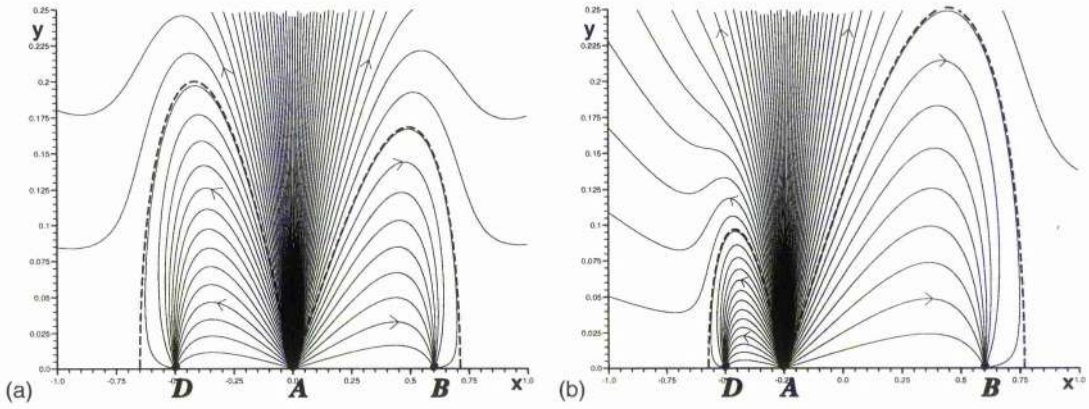

Figure 5.18: (a) Magnetic field lines due to poles of strengths 6.6, -0.9 and -1.4 and at positions A 0.0, B 0.6 and D -0.5, respectively, along the x-axis. (b) Corresponding field lines when the pole of strength 6.6 is moved from 0.0 to -0.25 along the x-axis in the photosphere below bright point II.

In three dimensions, as for bright point I, the strengths and initial positions relating to the poles in the two-dimensional transverse magnetic field plots for this bright point are used, and again using Equation (5.2) the separatrix surfaces are drawn. There are three separatrix surfaces (Figure 5.19), each

forming a dome which encloses field lines from the positive pole to just one of the poles B, C or D.

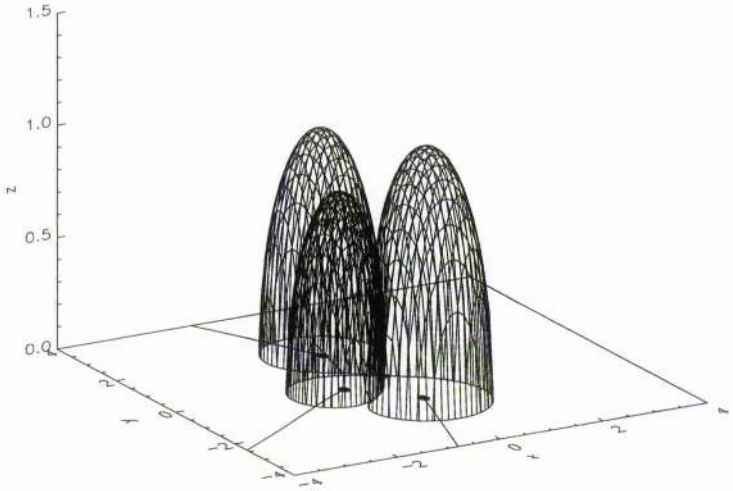

Figure 5.19: The shape of the separatrix surfaces of bright point II, due to to poles (labelled by dots) of strengths 6.6, -0.9, -1.1, -1.4 at positions A (0.0,0.0), B (-0.33,1.46), C (0.0,-1.39) and D ($-0.93, -0.33$), respectively, in the $z = 0$ plane.

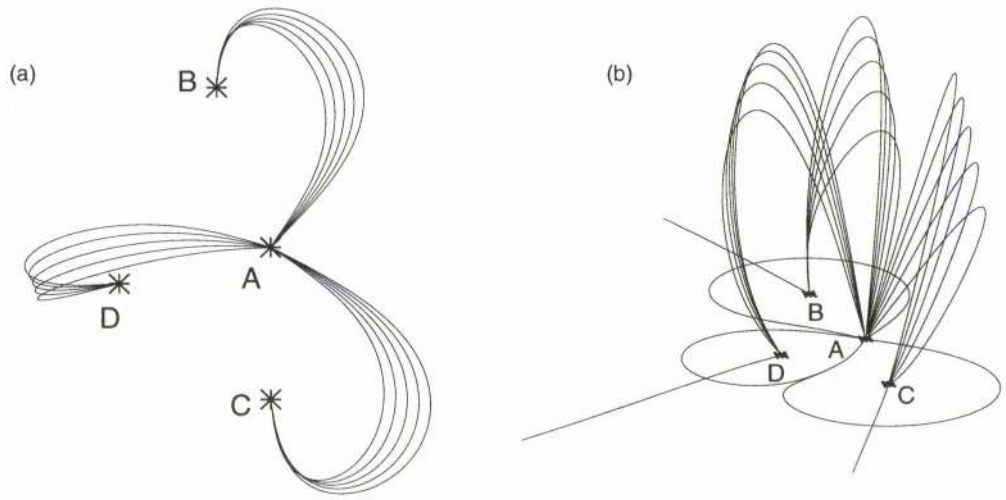

Figure 5.20: Several reconnected field lines from pole A to B, A to C and A to D which are believed to brighten and cause the observed soft x-ray image for bright point II.

The domes are formed from field lines in the surface from positive pole A to a neutral point lying in the photosphere. There are also six more separatrix lines lying in the photosphere, which do not form part of a separatrix surface. These are the field lines that extend from the three neutral points to the enclosed negative point sinks, B, C or D, or to the far-off negative pole (Figure 5.19). A proposed name for the two separatrices through each neutral point is a *spine* (Priest and Titov, 1995) since it forms the central

line along which the reconnection is focussed; thus the reconnection in this bright point is very different from that about a separator, as in bright point I. It is assumed that the reconnection at each of these neutral points takes place in the normal two-dimensional manner apart from the fact that the field lines that actually reconnected do not necessarily lie in the same plane, hence field lines extending out into the corona may reconnect.

Figure 5.20 shows the newly reconnected field lines believed to remain bright when the positive pole A moves nearer pole D. As in the discussion for the transverse field plot, it is assumed that the long unconnected field lines will not brighten and that the reconnection and motion of the bright field lines is faster than the cooling time of the hot plasma along the field lines.

5.7 Conclusion

By the use of Priest *et al.*'s (1994) converging flux model for x-ray bright points, a plausible explanation for the observed brightenings has been developed from the high-resolution soft x-ray image of bright points I and II. It is assumed that only the movement and interaction of magnetic regions causes the bright points. As the magnetic regions move together, reconnection takes place at the three-dimensional neutral points and along the separator to form newly reconnected field lines which are injected with heat or plasma and brighten in the shape of the observed form.

Contour plots from Kitt Peak magnetograms of the photosphere below the bright point are studied and the magnetic regions believed to play key roles are modelled as point sources and point sinks. It is suspected in both cases that four magnetic regions, (two positive and two negative for bright point I, and one positive and three negative for bright point II) are central to the formation and life of the bright points. Field lines from these magnetic poles are sketched in two and three dimensions just before and after reconnection. By assuming the movement of a particular pole it was found that the field lines injected with heat or plasma (and therefore bright) are approximately the shape and size of the observed soft x-ray brightenings for the bright point and the brighter inner cores overlie the centres of reconnection on the separator, so being heated directly from the reconnection itself.

In this study the behaviour predicted is of a natural and simple nature, relying on the motion of the magnetic regions and cancellation of flux to release energy to create the bright point. This is likely not always to be the case, since emergence of flux can also cause bright points, but in general many more bright points are created by cancellation than emergence. The importance of these two effects is likely to vary from one bright point to another (Webb *et al.*, 1993, Harvey, 1985). The limited number of high-resolution observations of bright points means there is no firm evidence as to what direction the different poles are moving or whether there is any important flux emergence, but models have been set up here which do lead to a reasonable explanation for the bright points.

Chapter 6

A Model for the Formation of an X-ray Bright Point due to the Interaction of an Ephemeral Region in a Supergranule Cell

6.1 Introduction

X-ray bright points are seen mostly at the edges of supergranule cells above cancelling magnetic features involving network fields (Habbal *et al.*, 1990). This is not surprising, since most cancelling magnetic features occur between network-network fields, ephemeral region-network fields and intracell-network fields (Wang *et al.*, 1988) and therefore at the edges of supergranule cells. So, to extend the converging flux models of Chapters 2 - 4, the field due to a supergranule cell is used here as the ambient field, thus improving the earlier models which had a purely horizontal field. Also, the magnetic fragments are more realistically modelled by finite sources so that the cancellation phase of the interaction may be studied in more detail. First, the structure of the supergranule cell is discussed in Section 6.2 and leads to the calculation of a potential model for the magnetic field above such a cell (Section 6.3). In Section 6.4 a model is developed for the magnetic field of an ephemeral region where its bipolar fragments are treated as finite sources. From a consideration of the observations, five scenarios for the interaction of an ephemeral region in a supergranule cell are suggested (Section 6.5). These scenarios are investigated with the results presented in the next three sections: Section 6.6 shows the *diverging ephemeral region* case; in Section 6.7 the *asymmetric diverging ephemeral region* case is looked at, which in turn may be split into two: the first has the fragments orientated positive then negative, whilst the second has them orientated negative then positive; finally, in Section 6.8 the *co-moving ephemeral region* case is studied which is divided as above into two scenarios. The results for these scenarios suggest that bright point flares and active-region transient brightenings may be related; this is discussed in Section 6.9 with this chapter completed in Section 6.10 by a conclusion.

6.2 Supergranule Cell Structure

Supergranule cells were first studied by Leighton *et al.* (1962) and are the tops of large convection cells in which material rises in the centre and is swept radially outwards to the boundaries of the cell at 0.3 - 0.4 km s^{-1} before it descends at the cell edges back down into the convection zone. It was found by Stenflo (1973) that the magnetic field in the photosphere is much stronger at the boundaries of a supergranule cell than in its centre. The boundary magnetic fields are not evenly distributed along the cell edge, but are concentrated mainly at the junctions between three cells and are believed to be made up of clumps of intense flux tubes which form network fields. Further out from the photosphere this flux expands due to decreasing plasma pressure until, in the corona, it has become relatively uniform. The cells have a mean diameter of 30 Mm and lifetimes of 1 - 2 days, and so the resulting magnetic fields may be assumed quasi-static since these time scales are much larger than the typical Alfvén times. As a model for the supergranule cell field a potential magnetic field approximation is sought to Gabriel's model of the magnetic field in a supergranule (Gabriel, 1976). A two-dimensional model is set up with the field in the photosphere rooted at two network fragments on the edges of each cell. Above the cell, the field in the chromosphere spreads out to create a more horizontal set of field lines towards the centre of the cell, which are drawn out into the corona above to form a uniform vertical field.

6.3 Model for the Supergranule Field

The two-dimensional magnetic field $\mathbf{B} = B_x\hat{\mathbf{e}}_x + B_y\hat{\mathbf{e}}_y$ is assumed here to be potential and therefore satisfies

$$\nabla \cdot \mathbf{B} = 0\,, \tag{6.1}$$

$$\nabla \times \mathbf{B} = \mathbf{0}\,. \tag{6.2}$$

Writing $\mathbf{B} = \nabla \times \mathbf{A}$, where $\mathbf{A}$ is the flux function and $\mathbf{A} = A_{sg}\,\hat{\mathbf{e}}_z$, automatically satisfies Equation (6.1) and Equation (6.2) becomes

$$\nabla^2 A_{sg} = 0\,. \tag{6.3}$$

An approximation to Gabriel's model may now be found by solving Laplace's Equation (Equation (6.3)) with the following boundary conditions

$$B_x = 0 \qquad \text{on} \quad x = \pm 1\,, \tag{6.4}$$

$$B_x \longrightarrow 0 \qquad \text{as} \quad y \longrightarrow \infty\,, \tag{6.5}$$

$$B_y \longrightarrow B_o \qquad \text{as} \quad y \longrightarrow \infty\,, \tag{6.6}$$

where B_o is the mean strength of the coronal field and the width of the cell is taken to be 2 in dimensionless units. If the x-axis is assumed to be at a constant height of a few 100 km above the surface of the Sun, approximately at the temperature minimum, where the vertical magnetic field is concentrated in the supergranule network, from magnetograms which are also taken at approximately this height, the final boundary condition along $y = 0$ may be taken as

$$B_y = \begin{cases} B_{sg} & -1 \leq x \leq -1+d \\ 0 & -1+d < x < 1-d \\ B_{sg} & 1-d \leq x \leq 1 \end{cases} , \tag{6.7}$$

where d is the dimensionless half width of the network magnetic fragments at the boundary of the cells and B_{sg} is the magnetic field in the network boundary fragments. Magnetograms such as those taken at the Kitt Peak and Big Bear Observatories give uniform fields for the fragments of between 2 and 8×10^{-3} T (20 and 80 G), whereas in reality these fragments are actually made up of a bundle of intense flux tubes with diameters up to 300 km and strengths of about 0.1 to 0.2 T (1 - 2 kG). The flux contained in a network fragment is observed to be approximately 10^{11} Wb (10^{19} Mx): this is equivalent to having either one fragment of radius 3 Mm and field strength 5×10^{-3} T (50 G) or having 45 intense tubes of strengths 0.1 T (10^3 G) and radii of 100 km.

Using separation of variables, the solution to Equation (6.3) may be written in the form

$$A_{sg} = X(x)\,Y(y) . \tag{6.8}$$

Now, if periodicity is assumed in the x-direction, it is found that B_y is an even function of x and B_x an odd function, so using the first boundary condition (Equation (6.4)) the function $X(x)$ is found to be

$$X = a_n \sin(n\pi x) .$$

The second boundary condition (Equation (6.5)) gives the form for the function $Y(y)$ as

$$Y = e^{-n\pi y} .$$

Thus the function XY becomes

$$XY = \sum_{n=1}^{\infty} a_n \sin(n\pi x)\, e^{-n\pi y} . \tag{6.9}$$

However, the x-derivative of this function ($-B_y$) tends to 0 as $y \longrightarrow \infty$ and therefore does not satisfy Equation (6.6), the third boundary condition, so an extra term must be added of the form $-B_o x$. The flux function A_{sg} now becomes

$$A_{sg} = \sum_{n=1}^{\infty} a_n \sin(n\pi x)\, e^{-n\pi y} - B_o x , \tag{6.10}$$

where the coefficients a_n are found by satisfying the remaining boundary condition, Equation (6.7), to be

$$a_n = \frac{-(-1)^n\, 2B_{sg}}{(n\pi)^2} \sin(n\pi d) . \tag{6.11}$$

Since the system is closed, the total magnetic flux leaving and entering the cell must be zero. No flux crosses the vertical boundaries of the supergranule cell (Equation (6.4)) and so the flux crossing the $y = 0$ line must equal the flux leaving at infinity, which implies

$$B_{sg} = \frac{B_o}{d} , \tag{6.12}$$

so that Equation (6.11) becomes, finally,

$$a_n = \frac{-(-1)^n 2B_o}{(n\pi)^2 d} \sin(n\pi d) . \tag{6.13}$$

The magnetic field due to the supergranule cell with a given overlying field (B_o) and given boundary fragment width (d) may now be found from the flux function (6.10) and Equation (6.13).

The parameters so far have been given in dimensionless units, but if it is assumed that the supergranule cell has diameter 30 Mm, 1 unit length corresponds to 15 Mm, and Equation (6.12) becomes

$$15B_o = dB_{sg} . \tag{6.14}$$

If the overlying field (B_o) is of strength 10^{-3} T (10 G), as in a quiet-region, and the magnetic field (B_{sg}) is equal to 5×10^{-3} T (50 G) (the observed value for quiet-region network fragments), then the width of the cell boundary fragments (d) is 3 Mm. Whereas, if the magnetic field strength in the area overlying an active-region is taken to be 10^{-2} T (100 G) with B_{sg} of 3×10^{-2} T (300 G) (equal to the observed active-region field values), then the width of the cell boundary fragment (d) would be 5 Mm. Figure 6.1a shows a quiet-region supergranule cell with $B_o = 10^{-3}$ T (10 G) and $d = 3$ Mm, with the separatrix from the neutral point at the origin shown by a dashed line.

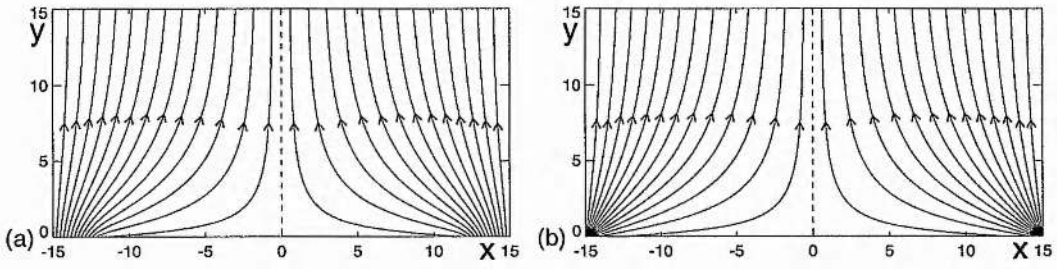

Figure 6.1: (a) The background magnetic field in a quiet-region supergranule cell with overlying field strength of 10^{-3} T (10 G) and network boundary field widths of 3 Mm and (b) with overlying field strength 10^{-3} T (10 G) and boundary fragment widths of 150 km.

It is interesting to note that if, instead, the network fragments are assumed to be intense flux tubes of strength 0.1 T (1000 G), then in a quiet region supergranule of strength, $B_o = 10^{-3}$ T (10 G) their widths would be 150 km, and the magnetic field looks very similar to that produced by line poles (Figure 6.1b). This indicates that in the converging flux models the use of line sources to model magnetic regions is simple, but not unreasonable.

6.4 Ephemeral Region Field

Since the overlying field is anchored in the photosphere at finite regions of network field, the magnetic fragments that form the ephemeral region are also modelled as finite. An ephemeral region is basically a pair of opposite polarity magnetic fragments with equal strength flux which may be modelled as two unipolar regions with an overlying potential field. First, it is noted that the magnetic field in two dimensions at a point P with coordinates (x, y) due to a line source of strength B_1 situated at the origin is

$$\mathbf{B} = \frac{B_1}{\pi \mid \mathbf{r} \mid} \hat{\mathbf{e}}_r \,, \tag{6.15}$$

where $\mathbf{r} = x\,\hat{\mathbf{e}}_x + y\,\hat{\mathbf{e}}_y$. The flux function $(A\hat{\mathbf{e}}_z)$ which satisfies $\mathbf{B} = \nabla \times A\,\hat{\mathbf{e}}_z$ is then

$$A = \frac{B_1}{\pi}\theta + constant \,, \tag{6.16}$$

where $\theta = \tan^{-1}(y/x)$. The x-axis is assumed to be at approximately the height of the temperature minimum, and close to the height at which magnetograms observe the Sun's photospheric flux. Then for a finite source with uniform field strength B_1 situated between points $a - w/2$ and $a + w/2$ on the x-axis, the flux function $A_f\hat{\mathbf{e}}_z$ becomes, with $\Theta = \tan^{-1}(y/(x - x'))$,

$$A_f(x,y) = \int_{a-\frac{w}{2}}^{a+\frac{w}{2}} \frac{B_1}{\pi}\left(\Theta - \frac{\pi}{2}\right) dx' \tag{6.17}$$

$$= \int_{a-\frac{w}{2}}^{a+\frac{w}{2}} \frac{B_1}{\pi} \tan^{-1}\left(\frac{x'-x}{y}\right) dx'$$

$$= \frac{B_1}{\pi}\left(\frac{-y}{2}\ln\left[\frac{\left(\left(a+\frac{w}{2}-x\right)^2+y^2\right)}{\left(\left(a-\frac{w}{2}-x\right)^2+y^2\right)}\right]\right.$$

$$\left. + \left(a-\frac{w}{2}-x\right)\tan^{-1}\left(\frac{a-\frac{w}{2}-x}{-y}\right) - \left(a+\frac{w}{2}-x\right)\tan^{-1}\left(\frac{a+\frac{w}{2}-x}{-y}\right)\right) . \tag{6.18}$$

The magnetic flux function (A_{eph}) due to a positive source situated at a_1 of width w and a negative source also of width w situated at a_2 (both of uniform field strength B_1) is therefore,

$$A_{eph}(x,y) = \frac{B_1}{\pi}\left(\frac{-y}{2}\ln\left[\frac{\left(\left(x-\left(a_2+\frac{w}{2}\right)\right)^2+y^2\right)\left(\left(x-\left(a_1-\frac{w}{2}\right)\right)^2+y^2\right)}{\left(\left(x-\left(a_1+\frac{w}{2}\right)\right)^2+y^2\right)\left(\left(x-\left(a_2-\frac{w}{2}\right)\right)^2+y^2\right)}\right]\right.$$

$$+ \left(a_2-\frac{w}{2}-x\right)\tan^{-1}\left(\frac{a_2-\frac{w}{2}-x}{-y}\right) - \left(a_2+\frac{w}{2}-x\right)\tan^{-1}\left(\frac{a_2+\frac{w}{2}-x}{-y}\right)$$

$$\left. - \left(a_1-\frac{w}{2}-x\right)\tan^{-1}\left(\frac{a_1-\frac{w}{2}-x}{-y}\right) + \left(a_1+\frac{w}{2}-x\right)\tan^{-1}\left(\frac{a_1+\frac{w}{2}-x}{-y}\right)\right) . \tag{6.19}$$

The field lines may be drawn for this ephemeral region by plotting contours of A_{eph}. In particular Figure 6.2 shows the field for a fragment width $w = 3$ Mm and uniform field strength $B_1 = 10^{-3}$ T (10 G) and sources set on the x-axis at positions $-a$ and a, where $a = 4.5$ Mm.

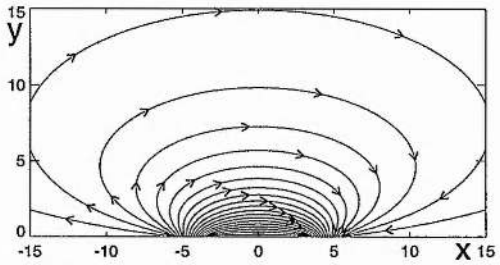

Figure 6.2: The magnetic field due to an ephemeral region with finite sources of width 3 Mm positioned at ± 4.5 Mm, with uniform source strengths of 5×10^{-3} T (50 G).

6.5 Interactions of an Ephemeral Region in a Supergranule Cell

The magnetic flux function (A) for the magnetic field due to an ephemeral region in a background supergranule cell field is equal to

$$A = A_{sg} + A_{eph} ,$$

where A_{sg} is given by Equations (6.10) and (6.13) and A_{eph} by Equation (6.19). In the following situations the background supergranule cell field is held fixed with only the size (strength) and position of the ephemeral magnetic fragments changing.

Bipolar or ephemeral regions are known to appear near the centres of supergranule cells. They emerge due to convective motions below the surface of the Sun, diverging as they appear at a speed of approximately 0.5 km s^{-1} until the ephemeral region reaches a maximum size of about 10 Mm (Harvey and Martin, 1973; Martin and Harvey, 1979). As they diverge, each fragment grows in strength up to a maximum of between 10^{10} - 5×10^{11} Wb (10^{18} - 5×10^{19} Mx). The convection flows below the surface of the Sun also carry the ephemeral region fragments at about 0.3 km s^{-1} towards the edges of the supergranule cell. Here the fragments come into contact with the unipolar network fields that form the boundaries of the cell. If the ephemeral region fragment and network field are of the same polarity they will coalesce, but if they are of opposite polarity they will cancel with one another and so form a cancelling magnetic feature. Again the following models are assumed quasi-static with the velocities of the magnetic fragments having no affect on the magnetic field and vice versa. Thus, in calculating the speeds of the ephemeral region fragments, just the underlying convection motions in the cell and the separate diverging motion of the ephemeral region during its growth phase are taken into account.

Depending on whether the ephemeral region emerges in the centre of the cell or to one side of the cell, there are five possible resulting scenarios. If the ephemeral region appears in the middle of the cell its individual fragments will emerge either side of the cell centre and therefore will be carried by the convection motions in opposite directions to the edges of the cell. This case will be known as the *diverging ephemeral region* situation and is discussed in Section 6.6. However, when an ephemeral region emerges just to one side of the cell centre, the divergence of the fragments may be such that one polarity of the ephemeral region crosses the cell centre and the ephemeral fragments will end up interacting with opposite sides of the supergranule cell, as before, but at different times. Section 6.7 discusses this case

which is referred to as an *asymmetric diverging ephemeral region.* This case may in turn be split into two situations, one where the positive fragment is to the left of the negative fragment and the other where the negative ephemeral region fragment is to the left of the positive ephemeral region fragment. The final scenarios (Section 6.8) involve the ephemeral region again emerging to one side of the cell centre near the network fields such that the fragments diverge, but this time do not cross over into the other side of the cell: thus both cancel and coalesce with the same network fragment. Again this situation may be split into two cases, one in which the positive ephemeral region fragment is to the left of the network fragment and in the other where the ephemeral region orientation is reversed.

In all the following models the supergranule cells are either considered to be in a quiet region or an active region. If the cell is a quiet region supergranule then $B_o = 10^{-3}$ T (10 G), $B_{sg} = 5 \times 10^{-3}$ T (50 G) and $d = 3 \times 10^3$ km; these correspond to the observed values which show that unipolar network fields in the photosphere have strengths of 2 - 8 $\times 10^{-3}$ T (20 - 80 G) and widths between 1 and 10 Mm. Active region supergranules have overlying field strengths of approximately 10^{-2} T (100 G) with fragment widths larger than those in quiet-region supergranules: therefore for our active region cells $B_o = 10^{-2}$ T (100 G), $B_{sg} = 3 \times 10^{-2}$ T (300 G) and $d = 5 \times 10^3$ km. It is also worth remembering that this is purely the boundary magnetic field of one particular cell. There will be, of course, in our model a fragment of width $3{\times}10^3$ km and strength 5×10^{-3} T (50 G) (quiet-region) or $5{\times}10^3$ km and strength 3×10^{-2} T (300 G) (active-region) at the boundary of the adjoining cell, since it is assumed that the magnetic field due to the supergranule cells is periodic in the x-direction.

An ephemeral region emerging in the centre of a supergranule cell may have magnetic fragments of varying sizes and strengths. In the following models it is assumed that the strength of the uniform field in the fragments (B_1) remains the same at all times and that it is equal to the strength of the uniform magnetic field in the supergranule cell network fields, namely, $B_1 = B_{sg} = 15 \times 10^3 B_o/d$. This means that the strength of the ephemeral region in the model is proportional to the width of the fragments, with, in this study, the ephemeral region fragments attaining maximum widths (w) of between $0.1d$ and d. The ratio of the ephemeral region fragment width to the supergranule boundary width (w/d) will be denoted by k and is an important parameter in our models.

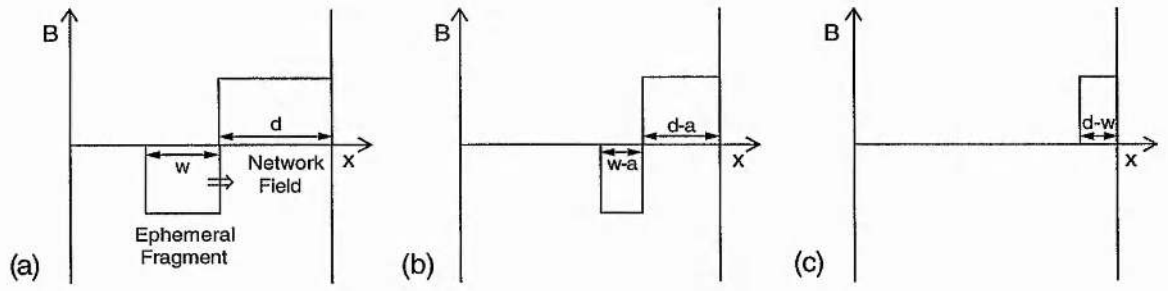

Figure 6.3: (a) The cancellation phase starts when the fragments come into contact for the first time. (b) Part way through cancellation and the fragment widths have decreased by equal amounts. (c) The network region has a width of $d - w$ when the cancellation has ended.

It is assumed that the cancellation phase does not start until the two opposite polarity fragments are touching (Figure 6.3a). Since each fragment has the same normal magnetic field component on the photosphere (i.e. $B_1 = B_{sg}$) the widths of the fragments decrease by the same amount as the ephemeral fragment continues to move towards the network and so they mutually lose equal amounts flux

(Figure 6.3b). At the end of the cancellation phase, the ephemeral region fragment has been completely cancelled and the network region has been reduced to a width of $d - w$ (Figure 6.3c).

To model this, the ephemeral region fragment that cancels is split into two magnetic regions with widths w_2' and w_3' and positions a_2' and a_3' that vary during cancellation (which is assumed to start at $t = 0$) in the following manner:

$$\begin{aligned} a_2' &= 15 \times 10^3 - d - kd/2 + vt/2 \\ a_3' &= 15 \times 10^3 - d + vt/2 \\ w_2' &= kd - vt \\ w_3' &= vt \end{aligned} \qquad 0 \leq t \leq kd/v \,, \tag{6.20}$$

(where v is the velocity of the ephemeral region fragment) such that the cancelling fragments constantly remain in contact. In the following sections this is not mentioned in the equations calculating the positions of the ephemeral region fragments, since in drawing the magnetic field structures positions are chosen only at the very beginning and end of the cancellation phase (other than in the active region case when the poles have half-cancelled and then it is assumed that the width of the cancelled fragment is $w/2$ and the field strength $2B_1$). It is only when the demise of the bright point coincides with the cancellation phase that one needs to utilise these equations and, even then, the difference in lifetimes is only minutes or less.

6.6 Diverging Ephemeral Region

In the diverging ephemeral region case, the emerging bipolar fragments appear straddling the centre of the cell, its fragments being carried off to opposite sides of the supergranule cell. An example of such an interaction is described by Wang *et al.* (1988) in their Figure 1 where an ephemeral region is seen emerging at 18.35 as a small bipolar region. As it develops and separates, the negative fragment begins to collide and cancel with a positive network before 21.23; whilst this cancellation is occurring the positive ephemeral fragment is merging with a different positive network fragment on the opposite side of the supergranule cell.

It is therefore supposed in this situation that the ephemeral region fragments in the centre of the cell move at a constant velocity; one at v km s^{-1} and the other at $-v$ km s^{-1}. It is assumed that the fragments maintain this velocity until they have either been completely cancelled or coalesced. The actual magnitude of the speed has no effect on the type of configurations through which the magnetic field evolves in this particular situation as long as it is less than the Alfvén speed. Thus if the left-hand ephemeral region fragment is situated at position $a_1 = -a$ on the x-axis and the right-hand one is at $a_2 = a$ and if they have constant speeds, then

$$\begin{aligned} a_1 &= -vt \\ a_2 &= vt \end{aligned} \,, \tag{6.21}$$

where a_1 and a_2 are measured in km and the widths of the fragments (in km) equals

$$w = \begin{cases} 2vt & 0 \leq t \leq kd/(2v) \\ kd & t > kd/(2v) \end{cases} \,. \tag{6.22}$$

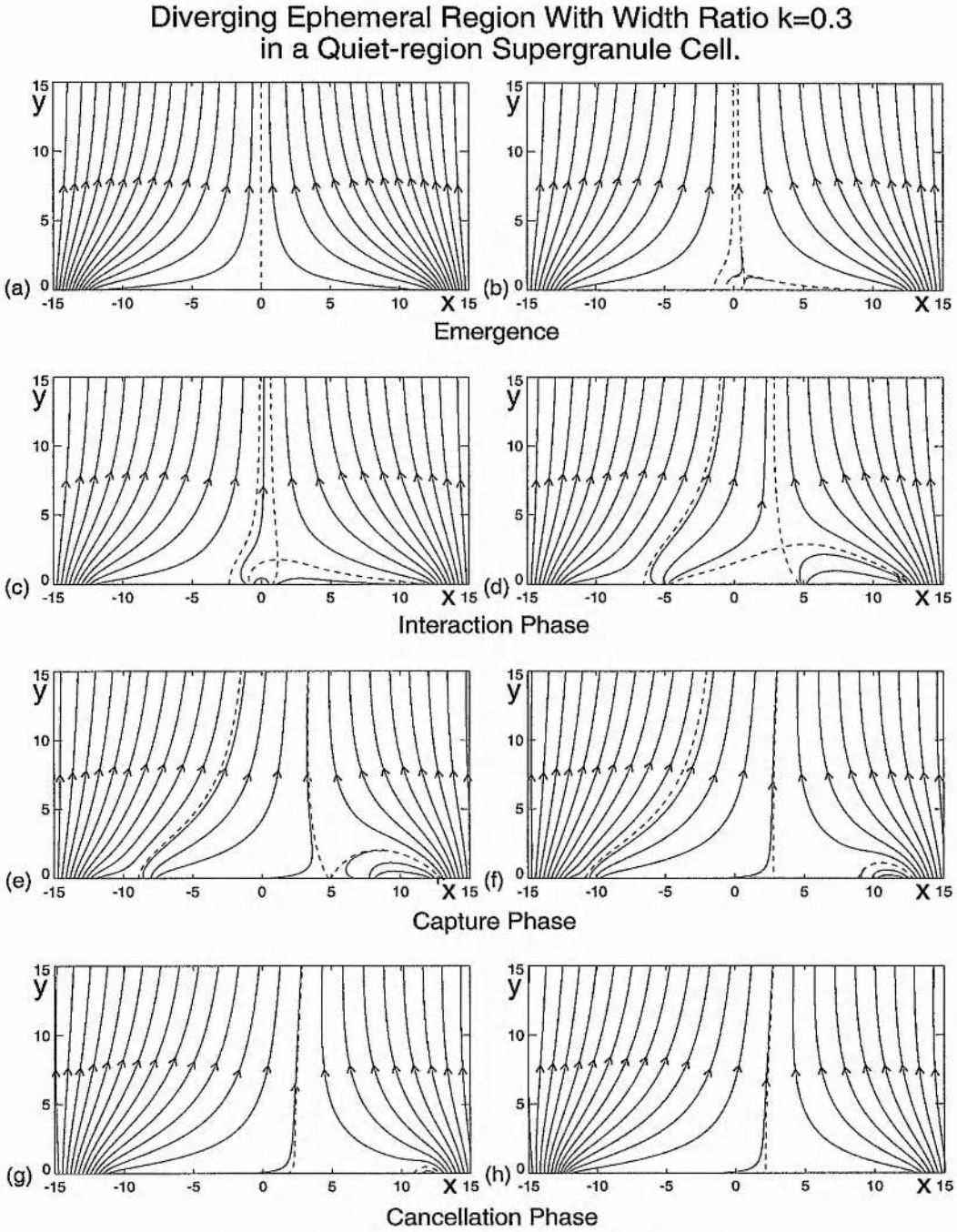

Figure 6.4: The magnetic field configurations for the stages during the life of a diverging ephemeral region of width ratio $k = 0.3$ in a supergranule cell. The ephemeral region has a uniform field strength of 5×10^{-3} T (50 G) with fragment width (w) of 900 km, and is orientated such that its positive pole is at $-a$ and its negative pole is at a. (a) The quiet-region supergranule cell field. (b) The ephemeral region emerges and a neutral point is formed above ($a = 225$ km). (c) The neutral point has risen above the photosphere ($a = 450$ km). (d) The neutral point is high in the corona ($a = 5.0 \times 10^3$ km). (e) The bright point ends ($a = d_c = 7.9 \times 10^3$ km). (f) During the capture phase ($a = 10^4$ km). (g) Onset of the cancellation phase ($a = 11.6 \times 10^3$ km). (h) The ephemeral region has now been completely cancelled/coalesced and the distorted supergranule field remains.

An ephemeral region is considered with fragments of width $w = 900$ km, emerging into a quiet-region supergranule cell, with parameter values $B_o = 10^{-3}$ T (10 G) and $d = 3 \times 10^3$ km, thus having a fragment width ratio (k) of 0.3. The magnetic configurations in Figure 6.4 show the stages in the emergence, interaction and cancellation of the ephemeral region. Figure 6.4a depicts the initial background supergranule field, and as the bipolar fragments emerge an X-type neutral point is seen overlying the emerging pair (Figure 6.4b). This implies that there is no (or only a very short) pre-interaction phase and that the emergence of the ephemeral fragments almost immediately gives rise to an interaction phase. If the energy released at the neutral point is large enough a bright point will be seen in the corona. The X-type neutral point (and hence the bright point) continue to rise and move away from the cell centre as the bipolar fragments diverge throughout the interaction phase, Figure 6.4c. If the network is made up of positive magnetic fragments the bright point will move in the same direction as the negative ephemeral fragment (as seen here) and in the direction of the positive ephemeral fragment for negative network fields. Here the negative ephemeral fragment effectively moves underneath the neutral point as the divergence continues (Figure 6.4d). The bright point fades when the neutral point descends back down to the photosphere, which happens when the fragments are at a distance from the cell centre of $a = d_c$ (the capture distance, which in this case equals 7.9×10^3 km). It is at this point that the capture phase begins (Figure 6.4e). The ephemeral fragments continue to diverge under the influence of the convection motions, (Figure 6.4f), with the capture phase lasting until the fragments touch the boundary supergranule network fields (Figure 6.4g). They are now situated at a half separation of $a = 15 \times 10^3 - d - w/2$ Mm (in this case $a = 11.6 \times 10^3$ km) which indicates the onset of the cancellation/coalescence phase. Now, as the fragments continue to move apart the negative fragment cancels with the positive boundary region, whilst on the opposite side of the cell the positive ephemeral fragment merges with the other positive network field. The cancelling magnetic feature and coalescing feature continue until all of the ephemeral regions flux has been either cancelled or merged, respectively (Figure 6.4h). The net overlying supergranule field will then have one unipolar region with an increased flux strength of $B_{sg}d + B_1 w$ (equal to 2.0×10^4 Wb m^{-1} (or 2.0×10^{10} Mx cm^{-1}) in this case) and the other reduced to a flux strength of $B_{sg}d - B_1 w$, (equal to 1.1×10^4 Wb m^{-1} (or 1.1×10^{10} Mx cm^{-1}) in this case). Thus in this particular situation it is found that the cancelled unipolar region now has almost half the flux of the coalesced unipolar region.

A comparison may be made of this relatively weak ($k = 0.3$) case with that of a scenario where a stronger ephemeral region with fragments of width ratio $k = 0.7$ (actual fragment width $w = 2.1 \times 10^3$ km) interacts in a quiet region. The stages of this interaction are seen in the frames of Figure 6.5. Figure 6.5a shows the quiet-region supergranule cell background field. The X-type neutral point is seen to appear rising up almost immediately the bipolar fragments emerge, (Figure 6.5b): thus again the interaction phase is immediately entered. The bright point (neutral point) continues to rise, gaining a greater height than in the $k = 0.3$ case (Figures 6.5c, 6.5d) and also moving further across the cell, so remaining longer above the photosphere than in the previous case. In fact, the bright point is still high above the photosphere at the onset of cancellation/coalescence at $a = 11.0 \times 10^3$ km (Figure 6.5e), only descending back down to the photosphere at $a = d_c = 12.1 \times 10^3$ km (Figure 6.5f). So in this case there is no gap between the demise of the bright point and onset of the cancelling magnetic feature and the fragments, now already cancelling or merging, continue to do so as the ephemeral region diverges further until cancellation/coalescence is complete (Figure 6.5h). It is found that the remaining supergranule background network flux regions have one fragment of strength 2.6×10^4 Wb m^{-1} (2.6×10^{10} Mx cm^{-1}) (coalesced) and the other of strength 0.5×10^4 Wb m^{-1} (0.5×10^{10} Mx cm^{-1}) (cancelled); the reduced supergranule boundary fragment is now effectively a sixth of the size of the increased boundary fragment.

Figure 6.6 shows the trajectory of the X-type neutral point above the temperature minimum (x-axis)

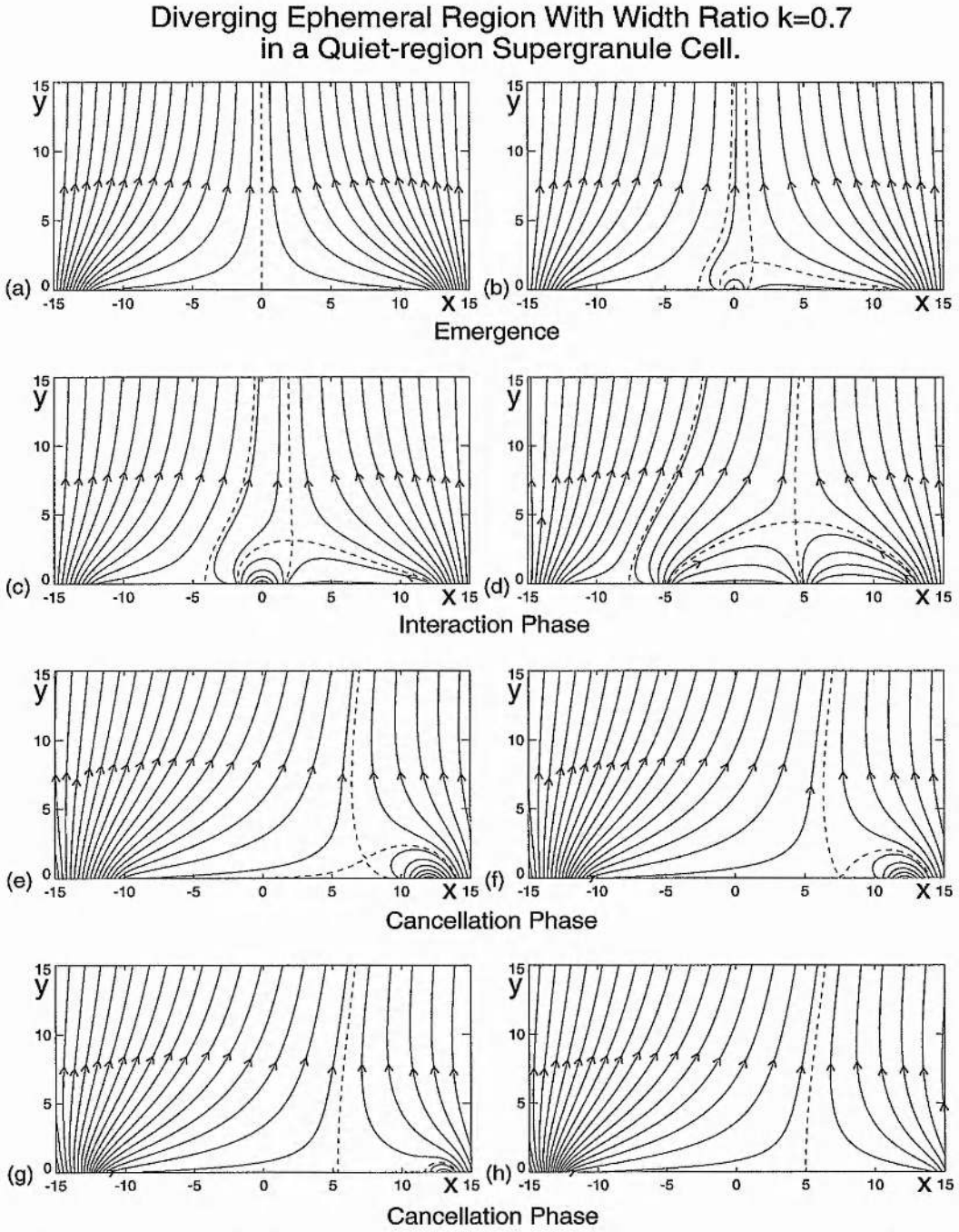

Figure 6.5: The stages through which a diverging ephemeral region with width ratio $k = 0.7$ evolves in a quiet-region supergranule cell. (a) The background supergranule field. (b) Already a neutral point is seen in the corona ($a = 525$ km, $w = 1.1 \times 10^3$ km). (c) The ephemeral region is now fully emerged ($w = 2.1 \times 10^3$ km, $a = 1.1 \times 10^3$ km). (d) The ephemeral region fragments have diverged ($a = 5.0 \times 10^3$ km). (e) At the onset of cancellation the bright point is still in the corona ($a = 11.0 \times 10^3$ km). (f) The bright point ceases ($a = 12.0 \times 10^3$ km). (g) Half-way through cancellation ($a = 12.5 \times 10^3$ km). (h) The completion of cancellation and coalescence leaves the supergranule cell very distorted.

in the right-hand half of the supergranule cell as the ephemeral fragments diverge for five fragment width ratios (k) from 0.1 to 0.9. The various symbols on the x-axis denote the positions of the negative ephemeral fragment, whilst those on the trajectories denote the corresponding positions of the bright point (neutral point) for the various k values. It can clearly be seen that the larger (stronger) the ephemeral fragment, the higher the neutral point (bright point) reaches in the corona and also the further the bright point moves. In the $k = 0.1$ case the bright point reaches only a height of less than 2×10^3 km and is completely finished by the time the negative fragment reaches 6×10^3 km. However, in the $k = 0.9$ case the bright point climbs to over 5×10^3 km and is still seen in the corona even after the negative fragment has passed 12×10^3 km.

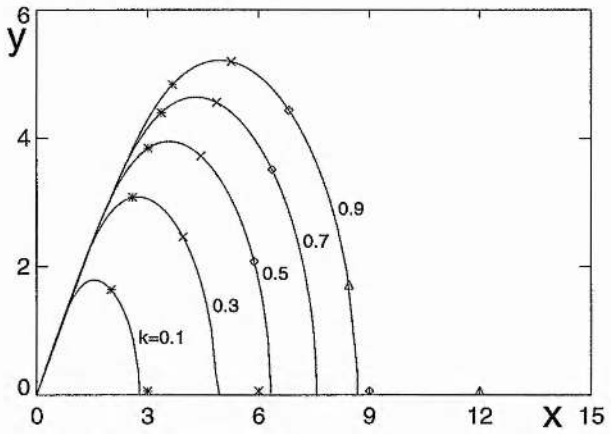

Figure 6.6: The trajectory of the neutral point (bright point) in the corona for a cancelling magnetic feature formed by the interaction of a diverging ephemeral region in a quiet-region supergranule cell of width ratios $k = 0.1, 0.3, 0.5, 0.7$ and 0.9. The symbols ($*$, $\times$, $\diamond$ and $\triangle$) on the graphs mark, respectively, the positions of the bright point for each value of k when the negative ephemeral region fragment is at 3, 6, 9 and 12 ($\times10^3$) km, respectively, from the centre of the cell.

In Figure 6.7 the emergence and interaction of an ephemeral region in an active-region supergranule cell is considered ($B_o = 10^{-2}$ T (100 G) and $d = 5 \times 10^3$ km). The ratio of the ephemeral to boundary fragment widths (k) is again taken to be 0.3: thus the width (w) of the ephemeral fragments is 1.5×10^3 km, where the normal field component B_1 ($= B_{sg}$) $= 3 \times 10^{-2}$ T (300 G). Figure 6.7a shows the magnetic configuration of an active-region cell and as in the previous cases the bright point appears more or less as soon as the bipolar fragments emerge (Figure 6.7b). The bright point (neutral point) rises (Figure 6.7c) and remains in the corona until the fragments have reached a capture distance (d_c) of 7.7×10^3 km, similar to that for the quiet-region $k = 0.3$ case (Figure 6.7d) whereupon the bright point fades. Figure 6.7e shows the fragments at positions $a = 9.0 \times 10^3$ km during the capture phase which lasts until $a = 9.3 \times 10^3$ km, at which point the cancellation phase starts for the negative fragment and the coalescence phase starts for the positive magnetic fragment (Figure 6.7f). In Figure 6.7g half of the negative ephemeral magnetic fragment has been cancelled and in Figure 6.7h the negative ephemeral fragment has been completely cancelled; the remaining network fragments now have fluxes of 2.0×10^5 Wb m^{-1} (2.0×10^{11} Mx cm^{-1}) and 1.1×10^5 Wb m^{-1} (1.1×10^{11} Mx cm^{-1}), similar to the quiet-region case with a ratio of approximately two.

In Figure 6.8 the trajectory of the bright point in an active-region supergranule cell is drawn for fragment width ratios (k) of 0.1, 0.3, 0.5, 0.7, 0.9. Again the height of the bright point is given for particular positions of the negative ephemeral region fragment, marked by the various symbols. The

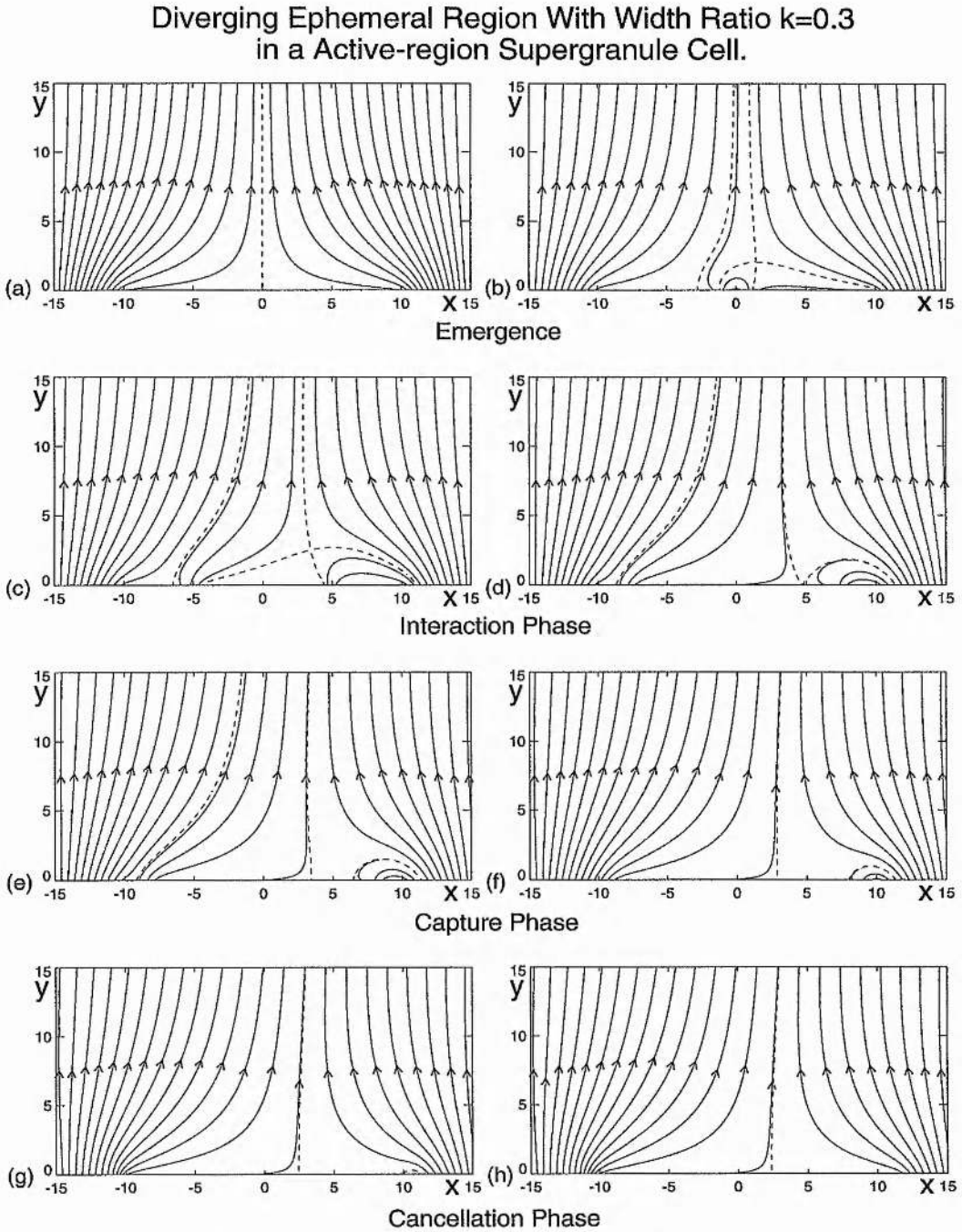

Figure 6.7: A diverging ephemeral region with width ratio (k) of 0.3 evolving in an active-region supergranule cell. (a) The active-region supergranule cell field. (b) A neutral point is visible (a = 750 km). (c) The neutral point is high in the corona ($a = 5.0{\times}10^3$ km). (d) The interaction phase has ended ($a = d_c = 7.7{\times}10^3$ km). (e) During the capture phase ($a = 9.0 \times 10^3$ km). (f) The cancellation phase begins ($a = 9.3{\times}10^3$ km). (g) Half-way through cancellation ($a = 10.4{\times}10^3$ km, w = 750 km). (h) The supergranule cell is left distorted with the left-hand coalesced network region having almost twice as much flux as the right-hand cancelled region.

trajectories follow basically a similar pattern to Figure 6.6, but the heights of the bright points in the active-region cell are less than those in the quiet cell by just under 500 km in the $k = 0.9$ case and a few hundred kilometres in the $k = 0.1$ case. Also the bright points in the active-region cell do not move as far as they do in the quiet-region cell. From the symbols it can be seen that there is no bright point for any k value in the active cell when the negative fragments are at $12{\times}10^3$ km on the photosphere. This is because for most k values the fragments do not reach $12{\times}10^3$ km since cancellation is complete before then and in the $k = 0.9$ case cancellation is more or less complete by that stage.

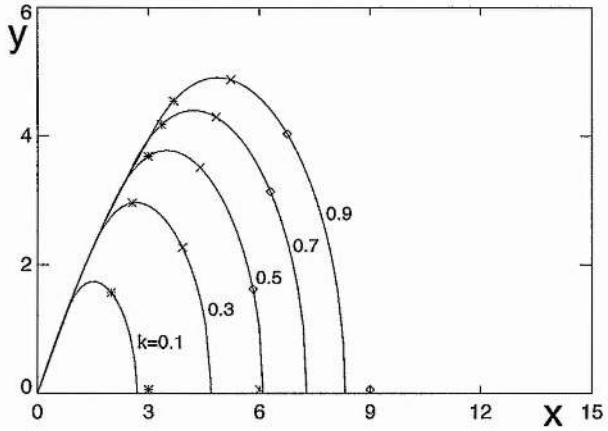

Figure 6.8: The right-hand half of an active-region supergranule cell is seen here with the path that the neutral point (bright point) traces drawn as a diverging ephemeral region of width ratio $k = 0.1$, 0.3, 0.5, 0.7 and 0.9 emerges and diverges in the cell. The symbols ($*$,$\times$ and $\diamond$) on the x-axis denote the positions of the negative ephemeral region fragment whilst on the graphs they denote the corresponding positions of the bright points at those distances (all lengths are given in 10^3 km).

If the actual velocities of the ephemeral region fragments are now considered, the lifetimes of the bright points and cancelling magnetic features may be evaluated. Since the fragments have been assumed to be moving at a constant speed, the lifetime of a bright point (t_{bpt}) is equal to the time it takes for the negative fragment to move to the capture distance (d_c) at a velocity v,

$$t_{bpt} = \frac{d_c}{v}.$$

The fragments are observed in the photosphere to move at speeds of between 0.1 - 1.0 km s^{-1}. If initially v is taken as 0.1 km s^{-1}, lifetimes of up to 30 hrs for the bright point are obtained. If, however, the velocity is taken to be 0.3 km s^{-1} lifetimes reach a maximum of 10hrs (Figure 6.9a), whereas maximum lifetimes of only 4hrs are reached for a velocity of 0.8 km s^{-1} (Figure 6.9b). The time at which the cancelling magnetic feature starts relative to the bright point time, $t_{cmf} = \left(15 \times 10^3 - d - w/2\right)/v$, and the time of demise of the cancelling magnetic feature, $t_{end} = \left(15 \times 10^3 - d + w/2\right)/v$, may also be plotted. These times are shown, respectively, as a dotted curve and a dashed curve in Figures 6.9a and 6.9b, with the bright point lifetimes indicated by the solid line. The dotted and dashed curves also indicate the beginning and end of coalescence of the positive ephemeral region fragment which is taking place simultaneously at the opposite side of the supergranule cell. It can be seen that for all the quiet-region cell interactions there is a distinctive capture phase for k values of 0.6 or less, but for width ratios (k) greater than 0.7 there is still a bright point even after the onset of cancellation and so no capture phase. In all cases the bright point ends before the end of cancellation in the photosphere.

In the active-region cell case, the bright point lifetimes are several hours shorter for a comparable velocity of 0.3 km s^{-1} of the ephemeral region and so too is the length of the capture.phase (Figure 6.9c). In fact, in most cases now (for all $k > 0.45$) there is no capture phase as the cancellation phase lasts for up to 5/3 (d_{active}/d_{quiet}) times as long as in the quiet-region case for equivalent velocity (v). This is not surprising since the width of the network and ephemeral region fragments are much bigger.

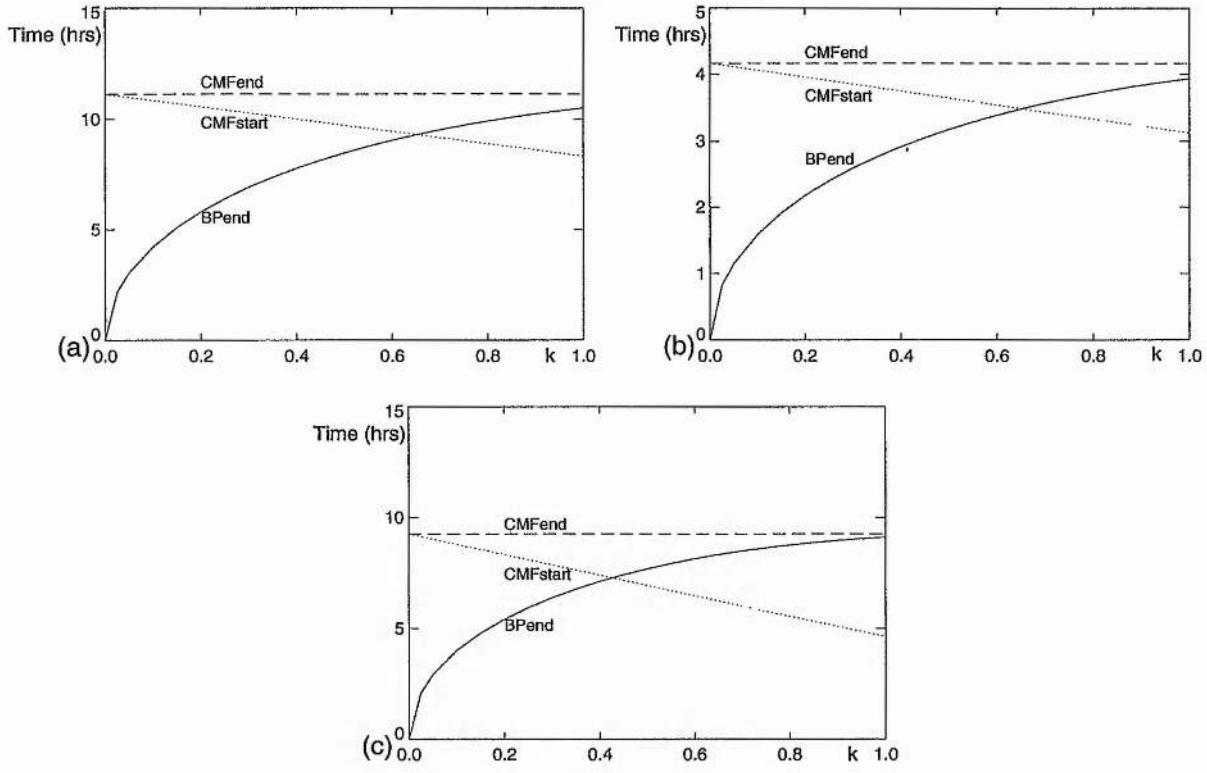

Figure 6.9: Graphs showing time in hours versus the width ratio (k) for a diverging ephemeral region, where the lifetime of the bright point is given by a solid line, the onset of cancellation (coalescence) by a dotted line and the cessation of the cancelling magnetic feature (coalescence) by a dashed line in a quiet-region supergranule cell where the velocity divergence of the two fragments is (a) 0.3 km s^{-1} and (b) 0.8 km s^{-1} and (c) in an active-region supergranule where $v = 0.3$ km s^{-1}.

6.7 Asymmetric Diverging Ephemeral Region

If an ephemeral region emerges offset from the centre of the supergranule cell and if it diverges fast enough during its growth stage, then one fragment will be seen moving in the direction of the supergranule flow whilst the other may be able to move in the opposite direction, opposing the supergranule motion. In some cases this type of divergence may carry the fragment opposing the motion across the cell centre into the other half of the supergranule. Here it may still be driven initially by the divergent growth of the ephemeral region: then, as the ephemeral region stops growing, the plasma motions in the supergranule will continue to pull the two opposite polarity fragments apart. This motion continues until the first fragment comes into contact with the network field at the boundary of the cell, where the fragment will

either cancel or become merged with the network. The other ephemeral region fragment, which may not yet have reached the opposite supergranule boundary, will continue drifting towards the boundary where it will either merge or cancel with the network field. Examples of this sort of cancellation are described by: Martin (1984) in her Figure 6, where an ephemeral region emerges and the positive fragment is cancelled with a negative network fragment whilst the negative ephemeral region fragment remains unaffected by cancellation or coalescence; and by Livi *et al.* (1985) in their Figure 4, where the negative ephemeral region fragment cancels with a positive network region whereas the positive fragment continues to move towards another positive network region.

In the asymmetric diverging scenario the ephemeral region bipole is orientated such that the negative fragment is on the right-hand side in the positive-negative case and on the left-hand side in the negative-positive case. The ephemeral region is initially born 10^3 km to the right of the supergranule cell centre and is assumed to be diverging at 0.5 km s^{-1} with the supergranule cell (drift) motion of 0.3 km s^{-1} dragging the ephemeral region towards the right-hand boundary. Thus the left-hand fragment has an effective velocity of -0.2 km s^{-1} and the right-hand one an effective velocity of 0.8 km s^{-1}. The ephemeral region grows at these speeds until the left-hand fragment crosses over into the left-hand half of the supergranule cell where it is now no longer opposing the motion of the supergranule cell and so has a new effective velocity of -0.8 km s^{-1}. Thus if a_1 is the position of the left-hand ephemeral region fragment and a_2 the position of the right-hand one then

$$\begin{aligned} a_1 &= 10^3 - 0.2t \\ a_2 &= 10^3 + 0.8t \end{aligned} \qquad 0 \leq t \leq 5000\,. \tag{6.23}$$

During the initial emergence of the ephemeral region, the fragments remain in contact as they grow (at a rate of 1 km s^{-1}) to their maximum strengths; from then onwards they remain at a constant width,

$$w = \begin{cases} t & 0 \leq t \leq kd \\ kd & kd < t \leq 5000 \end{cases}\,. \tag{6.24}$$

The ephemeral region fragments now diverge at this rate until the growth period is finished, which in this model is taken to be when the ephemeral region reaches a size of 10^4 km and the left- and right-hand fragments are situated, respectively, at distances of -2.5×10^3 km and 7.5×10^3 km from the centre of the supergranule cell.

$$\begin{aligned} a_1 &= -0.8\,(t - 5000) \\ a_2 &= 5 \times 10^3 + 0.8\,(t - 5000) \\ w &= kd \end{aligned} \qquad 5000 < t \leq 8125\,. \tag{6.25}$$

The fragments are now no longer being driven apart and are thus free to drift to the edges of the cell by convection at a speed of 0.3 km s^{-1}. In the first case the negative fragment reaches the network boundary first and continues to drift at 0.3 km s^{-1} as it cancels. Meanwhile the positive fragment drifts and finally merges with the other boundary network field at a velocity of -0.3 km s^{-1}. In the second scenario, coalescence takes place first as the positive fragment, moving at 0.3 km s^{-1}, reaches the right-hand edge of the supergranule cell with the negative fragment moving towards the opposite boundary at -0.3 km s^{-1} where it later forms a cancelling magnetic feature. This movement is defined mathematically by the equations:

$$\begin{aligned} a_1 &= -2.5 \times 10^3 - 0.3\,(t - 8125) \\ a_2 &= 7.5 \times 10^3 + 0.3\,(t - 8125) \qquad 8125 < t \leq t_1\ ; \\ w &= kd \end{aligned} \tag{6.26}$$

$$\begin{aligned} a_1 &= -7 \times 10^3 - kd/2 - 0.3\,(t - t_1)) \\ a_2 &= 12 \times 10^3 + kd/2 \qquad t_1 < t \leq t_2\ , \\ w &= kd \end{aligned} \tag{6.27}$$

where $t_1 = 23125 + 5kd/3$ and $t_2 = 23125 + (50000 + 5kd)/3$. In all these equations the lengths are measured in km and velocities in km s^{-1}.

6.7.1 Positive-Negative Case

In the positive-negative case the ephemeral region is orientated with the positive source on the left-hand side and the negative one on the right-hand side of the bipole. Figure 6.10 depicts the stages in this type of growth and cancellation of an ephemeral region in a quiet supergranule cell with width ratio (k) of 0.3 (i.e. fragment widths of 900 km and field strength of 5×10^{-3} T (50 G)). Figure 6.10a shows the background supergranule cell field into which the ephemeral region emerges at a point 10^3 km just to the right of the centre of the supergranule cell (Figure 6.10b). A bright point is seen more or less immediately after the ephemeral region emerges, so again there is no pre-interaction phase. The bright point continues to rise, moving to the right throughout the interaction phase, as the fragments diverge (Figure 6.10c) until the negative fragment reaches a distance $a_2 = d_c = 8.3 \times 10^3$ km, at which point the bright point fades and the neutral point is once more on the x-axis, (Figure 6.10d). As the ephemeral region fragments continue to diverge, a capture phase is seen, shown in Figure 6.10e, which lasts until the negative fragment is at position $a_2 = 11.6 \times 10^3$ km, and the positive fragment is at position $a_1 = -6.6 \times 10^3$ km, whereupon the negative fragment starts to cancel with the network field (Figure 6.10f). Cancellation of the negative fragment is complete by the time the positive fragment is at position $a_1 = -7.5 \times 10^3$ km (Figure 6.10g); this remaining half of the ephemeral region continues to drift outwards to the boundary of the supergranule cell where it coalesces with the network field there to give the final magnetic field configuration seen in Figure 6.10h. The resulting flux strengths of the network fragments are 2.0×10^4 Wb m^{-1} (2.0×10^{10} Mx cm^{-1}) and 1.1×10^4 Wb m^{-1} (1.1×10^{10} Mx cm^{-1}), as in the $k = 0.3$ quiet-region diverging ephemeral region case, so their ratio is approximately 2:1.

The bright point trajectories for this type of ephemeral region interaction have been drawn in Figure 6.11a. Again the symbols indicate the positions of the bright point at various different positions of the negative fragment of the ephemeral regions with different k values. In this scenario all the bright points are over by the time the negative fragment reaches 12×10^3 km, indicating that these bright points are shorter-lived than in the previous situation. It can be seen that, in comparison with the diverging ephemeral region case (Figure 6.6), the bright point does not reach so high in the corona, a maximum of just under 5×10^3 km for a width ratio of 0.9. Nor does it move so far across the supergranule cell from its start point. Also the rise and fall of the bright point is marginally faster in this situation, with the bright point climbing to its maximum height initially rapidly then slowing before rising rapidly again as it peaks. This is due to the change in motion of the fragments in the photosphere.

The lifetime of the bright point (d_c/v) is calculated in the same manner as before, since there is no pre-interaction phase, remembering this time that in some cases the velocity (v) changes during the

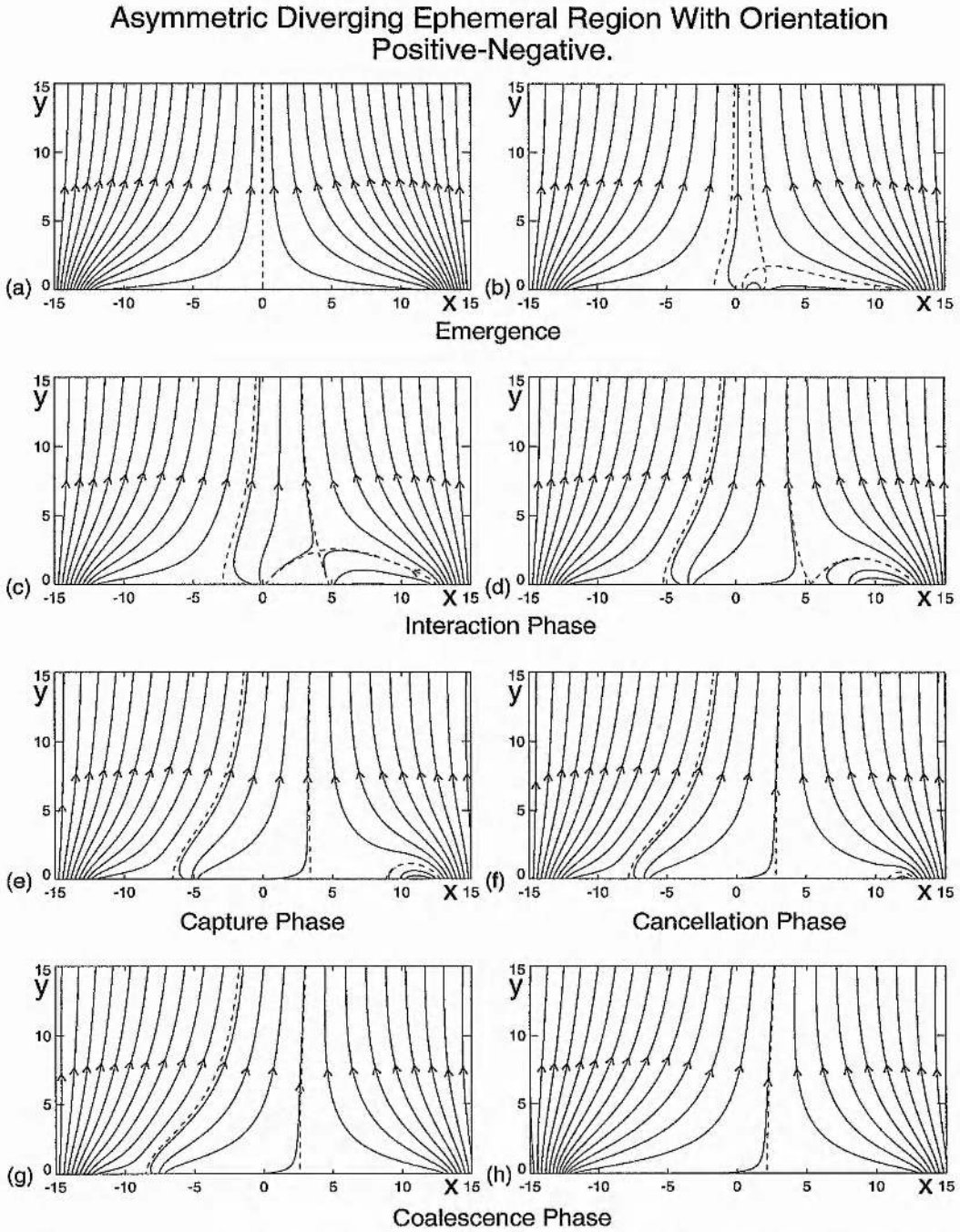

Figure 6.10: The stages through which an asymmetric diverging positive-negative ephemeral region with width ratio 0.3 evolves in a quiet-region supergranule cell. (a) The quiet-region supergranule field. (b) The emerged ephemeral region is now fully developed (a_1 = 820 km, $a_2 = 1.7 \times 10^3$ km). (c) As the ephemeral region diverges the neutral point rises ($a_1 = 0$ km, $a_2 = 5{\times}10^3$ km). (d) The negative fragment is fully captured ($a_1 = -3.3{\times}10^3$ km and $a_2 = 8.3{\times}10^3$ km). (e) The capture phase ($a_1 = -5.0{\times}10^3$ km and $a_2 = 10^4$ km). (f) The cancellation phase starts ($a_1 = -6.6{\times}10^3$ km, $a_2 = 11.6{\times}10^3$ km). (g) The negative fragment is fully cancelled, but the positive fragment continues to diverge ($a_1 = -7.5{\times}10^3$ km). (h) The positive fragment merges with the network supergranule field producing a distorted background field.

interaction phase and is drawn in Figure 6.11b. It lasts for up to a maximum of 8 hrs for a width ratio (k) of approximately 1, with a capture phase seen in all cases of k less than 0.6, and the cancellation is well under way for all k values greater than 0.65 before the bright point finishes. Again the bright point is seen to finish before the cancelling magnetic feature finishes and both the bright point and cancelling magnetic feature are completed by the time the positive ephemeral region fragment starts to coalesce with the network at the supergranule cell boundary.

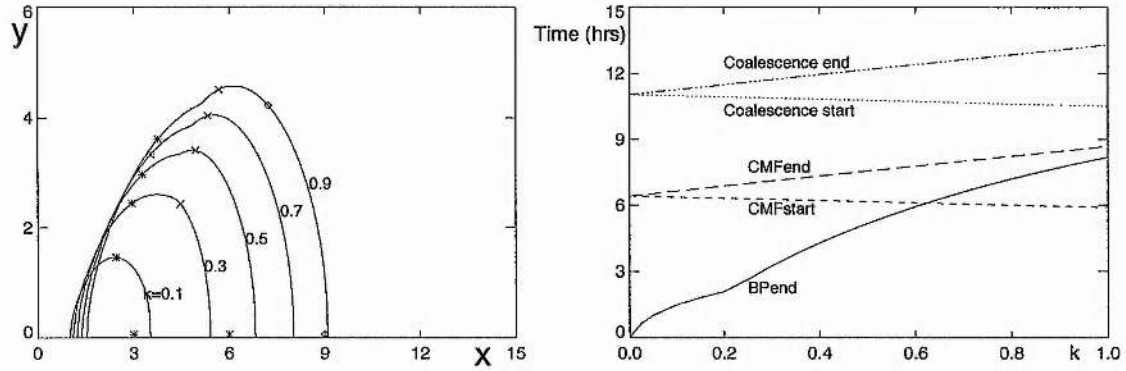

Figure 6.11: (a) The neutral point (bright point) trajectories for an asymmetric diverging positive-negative ephemeral region with width ratio (k) of 0.1, 0.3, 0.5, 0.7 and 0.9 in a quiet-region supergranule cell. The symbols ($*$,$\times$ and $\diamond$) mark the height of the neutral point for each k value when the negative ephemeral region fragment is situated at 3, 6 and 9 ($\times 10^3$) km, respectively. (b) The interaction of this ephemeral region produces, for differing width ratios (k), the bright point lifetimes indicated by the solid line and a cancelling magnetic feature and coalescing feature that starts and finishes with respect to the bright point indicated by the dashed and dotted curves, respectively.

6.7.2 Negative-Positive Case

In the negative-positive case the ephemeral region is orientated such that the negative source is to the left of the positive bipolar fragment. Figure 6.12 shows the emergence and interaction of an ephemeral region in a quiet-region supergranule cell where $w = 900$ km, so the width ratio (k) is 0.3. Initially the cell background field is the same as in all the earlier quiet-region supergranule cases (Figure 6.12a), with the ephemeral region first seen emerging in the right-hand side of the supergranule cell 10^3 km from the cell centre (Figure 6.12b). Almost immediately the interaction phase is entered and a bright point is again seen to appear as soon as the ephemeral region emerges. The ephemeral region separates and grows as it is dragged towards the right-hand edge of the cell, with the bright point rising as it moves in the direction of the negative fragment towards the left-hand boundary (Figure 6.12c). Now, as the ephemeral region diverges, the negative fragment crosses over into the left-hand half of the supergranule with the bright point continuing to rise and move leftwards and at the same time the positive fragment is drifting towards the right-hand network field where it coalesces (Figure 6.12d). By Figure 6.12e the positive fragment is completely coalesced and the neutral point between the network and the negative fragment, positioned at $a_2 = d_c = -8.2 \times 10^3$ km, is once again on the photosphere indicating the end of the bright point and onset of the capture phase. As the negative fragment is dragged outwards, the capture phase continues (Figure 6.12f) until the onset of cancellation when $a_2 = -11.6 \times 10^3$ km (Figure 6.12g). The

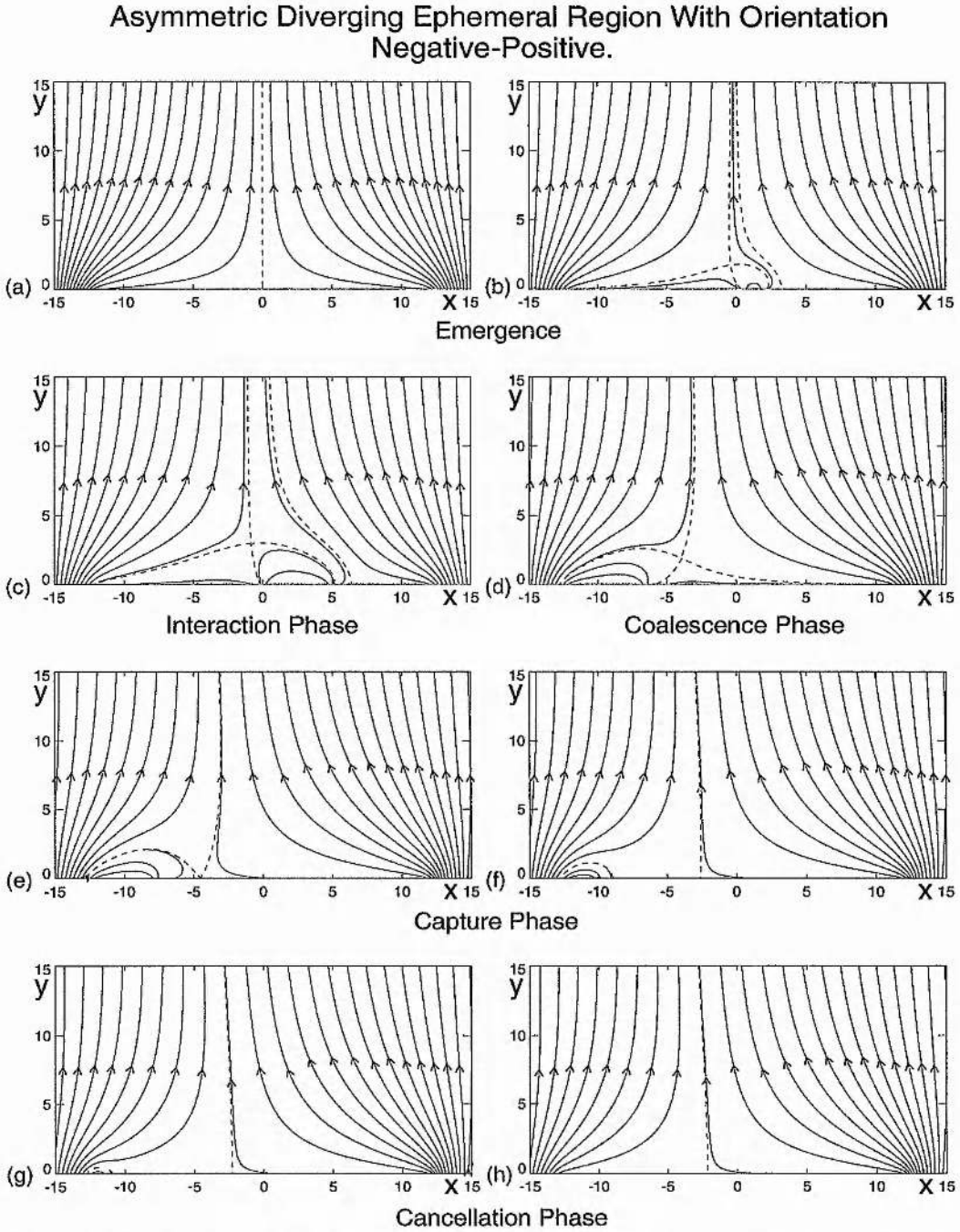

Figure 6.12: An asymmetric diverging negative-positive ephemeral region interacts in a quiet-region supergranule cell where the width ratio (k) is 0.3. (a) The background supergranule cell field. (b) The ephemeral region fragments are situated at $a_2 = 820$ km and $a_1 = 1.7\times10^3$ km. A neutral point lies to the left of the ephemeral region. (c) The neutral point moves higher in the corona ($a_1 = 0.0$ km, $a_2 = 5.0$ km). (d) Onset of coalescence ($a_1 = -6.6\times10^3$ km, $a_2 = -11.6\times10^3$ km). (e) Coalescence is complete and the bright point fades ($a_1 = -7.7\times10^3$ km). (f) The capture phase continues as the negative fragment drifts outwards ($a_1 = -10^4$ km). (g) The onset of cancellation ($a_1 = -11.6\times10^3$ km). (h) When the negative fragment has completely cancelled the network flux on the left is approximately half the size of the network region on the right.

final supergranule cell field configuration is seen in Figure 6.12h, where cancellation is complete and the network fragments have a flux ratio of approximately 1:2, with actual flux strengths of 1.1×10^4 Wb m^{-1} (1.1×10^{10} Mx cm^{-1}) and 2.0×10^4 Wb m^{-1} (2.0×10^{10} Mx cm^{-1}) for the cancelled and coalesced regions, respectively.

As in the previous cases, the trajectories of the bright points for five different k values are plotted (Figure 6.13a). The bright points produced from this scenario move to the left, the side on which the cancelling magnetic feature will occur. They rise to a greater height in the corona than in either of the previous cases, with the $k = 0.9$ bright point almost reaching a distance of 6×10^3 km into the corona. The rate of climb of the bright point above the photosphere is very rapid compared to the other scenarios, but the rate of fall is similar. In each case the bright point moves a similar distance to the diverging ephemeral region bright points. Again the symbols indicate the positions of the bright points for particular positions of the negative ephemeral region fragment in the left-hand side of the supergranule cell. The bright point is high in the corona when the negative fragment is in the middle of the cell for all k values and it is still above the photosphere in the $k = 0.9$ case when the negative fragment has moved to -12×10^3 km, implying that the bright point is long-lived.

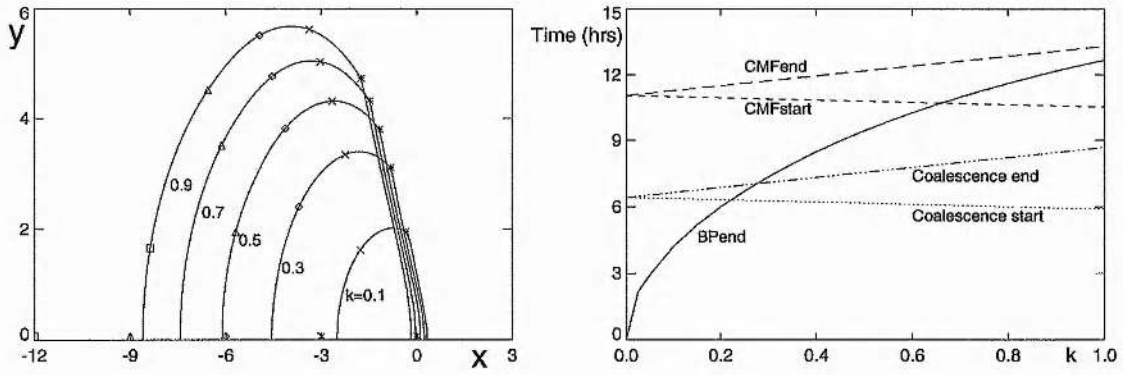

Figure 6.13: (a) Part of a quiet-region supergranule cell with paths of the neutral point (bright point) for width ratios (k) of 0.1, 0.3, 0.5, 0.7 and 0.9 plotted as an asymmetric diverging negative-positive ephemeral region interacts in the cell. The symbols ($*$,$\times$, $\diamond$ and $\triangle$ and $\square$) indicate the positions of the negative ephemeral region fragment (0, -3, -6, -9 and -12 $\times 10^3$ km, respectively) on the x-axis and the corresponding heights of the bright point for each k value. (b) The lifetime of a bright point (solid), relative to the start and finish (dashed) of a cancelling magnetic feature and coalescence stage (dotted), given in hours for various width ratios (k) of an asymmetric diverging negative-positive ephemeral region in a quiet-region supergranule cell.

The timings of the bright point, cancelling magnetic feature and coalescence stage may be calculated and are shown in Figure 6.13b by solid, dashed and dotted curves, respectively. It shows that the bright point may last up to a maximum of 13 hrs and, as in all the previous situations, the bright point finishes before the cancelling magnetic feature ends. There is no capture phase for width ratios of greater than 0.7 where there is still a bright point after cancellation has begun, but for k less than 0.6 there is a capture phase which in many cases may last a long time in comparison to the bright point and cancellation times. The coalescence stage takes place in all cases after the start of the bright point and seems to have no effect on the lifetime of the bright point at all.

6.8 Co-moving Ephemeral Region

As in the asymmetric diverging ephemeral region situation the ephemeral region emerges offset from the centre of the supergranule cell, but this time the fragments appear further from the centre of the cell such that they always remain on one side of the cell. If the fragments are diverging quickly enough one fragment will move towards the centre of the cell, though never crossing to the other side of the cell, whilst the other fragment moves outwards to the supergranule boundary. This time, therefore, when the growth stage of the ephemeral region ends, the fragments are carried by the outward flow in the cell to the same side of the supergranule. The first fragment will either cancel or coalesce with the network field at the perimeter of the cell, depending on its polarity, and the remaining fragment later coalesces or cancels with the same network field, thus restoring the cell to its original structure. As yet there have been no reports of this type of behaviour in supergranule cells, but there seems no fundamental reason why this should not be possible.

In these situations the ephemeral region emerges 4×10^3 km from the centre of the cell with the fragments diverging at 0.5 km s^{-1} in the surrounding plasma that is moving at 0.3 km s^{-1}, such that the left-hand fragment moves at -0.2 km s^{-1} whilst the right-hand one moves at 0.8 km s^{-1} (as in the asymmetric diverging case) and so

$$\begin{aligned} a_1 &= 4\times10^3 - 0.2t \\ a_2 &= 4\times10^3 + 0.8t \end{aligned} \qquad 0 \le t \le t_1 \,, \tag{6.28}$$

where $t_1 = 10^4$. As in the two previous cases the ephemeral region fragment widths increase at a rate of 1 km s^{-1} whilst they remain in contact, until they reach their maximum size of kd and so

$$w = \begin{cases} t & 0 \le t \le kd \\ kd & kd < t \le t_1 \end{cases} \,. \tag{6.29}$$

These velocities are maintained until the ephemeral region is 10^4 km across, then the ephemeral region stops its growth phase and the fragments begin to 'co-move' towards the boundary of the cell dragged by the convection motions at a rate of 0.3 km s^{-1}: i.e.

$$\begin{aligned} a_1 &= 2\times10^3 + 0.3\,(t - t_1) \\ a_2 &= 12\times10^3 + 0.3\,(t - t_1) \\ w &= kd \end{aligned} \qquad t_1 \le t \le t_2 \,, \tag{6.30}$$

where $t_2 = 10^4 + 5kd/3$. At this point the right-hand fragment will have been either cancelled or coalesced with just the left-hand fragment remaining. This fragment will continue to drift with the convection motions of the cell at a speed of 0.3 km s^{-1} until it reaches the edge of the supergranule cell where it merges (cancels) with the network field, so that

$$\begin{aligned} a_1 &= 2\times10^3 + 0.3\,(t - t_1) \\ a_2 &= 12\times10^3 + kd/2 \\ w &= kd \end{aligned} \qquad t_2 \le t \le t_3 \,, \tag{6.31}$$

where $t_3 = 10^5/3 + 5kd/3$. Obviously, the orientation of the ephemeral region will make a big difference to the timing and position of the bright point; in the first scenario the ephemeral region is situated positive-negative with the negative fragment nearer the edge of the cell, and vice versa in the second case with the positive fragment nearer the boundary.

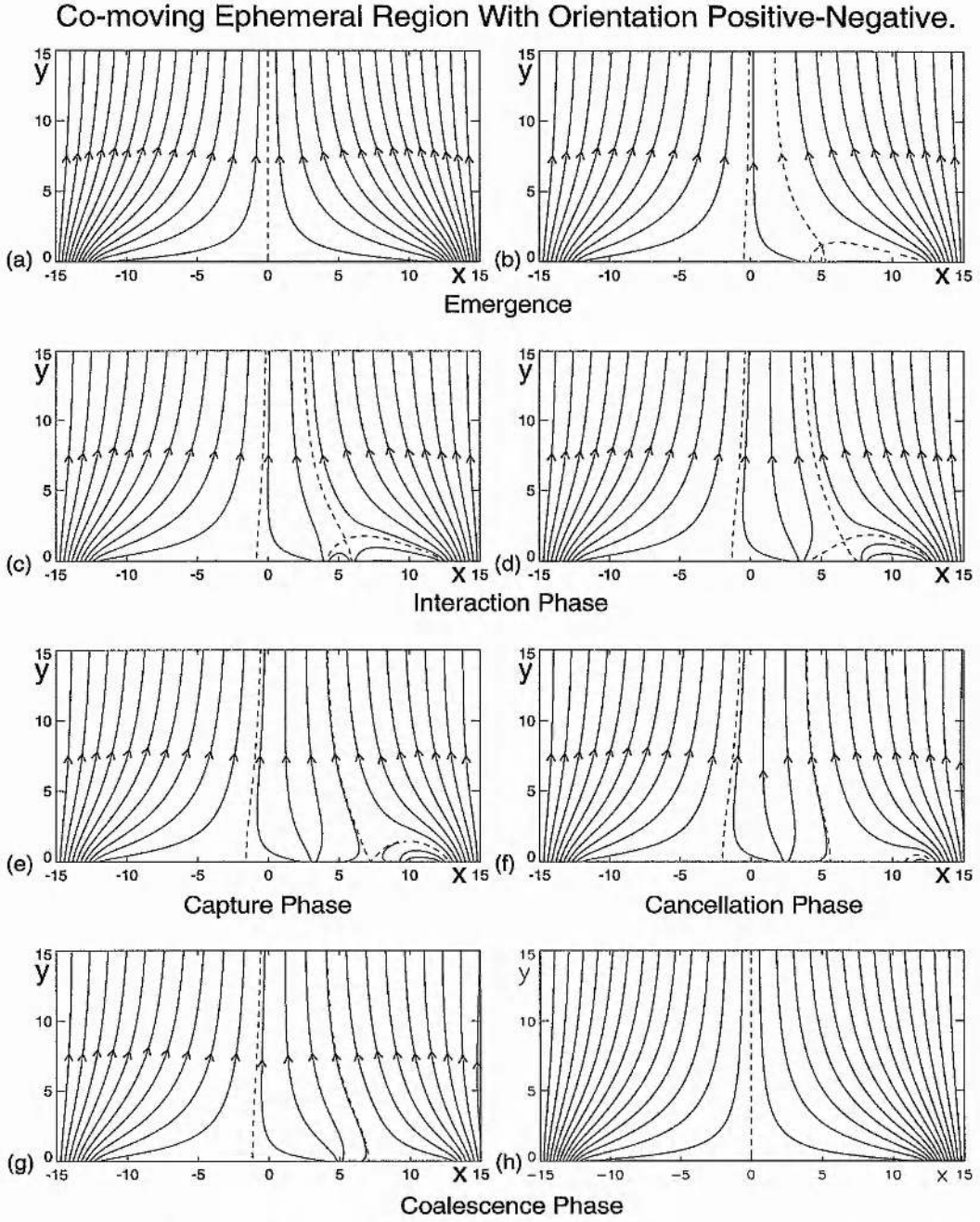

Figure 6.14: The interaction of a positive-negative co-moving ephemeral region with $k = 0.3$. (a) The initial background field is that of a quiet-region supergranule cell. (b) The bright-point appears immediately the ephemeral region emerges ($a_1 = 3.8 \times 10^3$ km, $a_2 = 4.7 \times 10^3$ km). (c) The bright point is higher in the corona ($a_1 = 3.5 \times 10^3$ km, $a_2 = 6.0 \times 10^3$ km). (d) The ephemeral region fragments have diverged ($a_1 = 3.0 \times 10^3$ km, $a_2 = 8.0 \times 10^3$ km). (e) The bright point fades ($a_1 = 5.0 \times 10^3$ km, $a_2 = 9.0 \times 10^3$ km). (f) Cancellation starts ($a_1 = 1.6 \times 10^3$ km, $a_2 = 11.6 \times 10^3$ km). (g) The remainder of the ephemeral region is dragged by convection motions in the cell ($a_1 = 5.0 \times 10^3$ km, $a_2 = 12.5 \times 10^3$ km). (h) When the negative fragment reaches the network boundary it coalesces with the flux to restore the original field.

6.8.1 Positive-Negative Case

The ephemeral region emerges in the right-hand half of the supergranule cell orientated such that the positive fragment of the bipole is the left-hand fragment. The resulting interaction as the ephemeral region of width ratio (k) of 0.3 grows and cancels in a quiet-region supergranule cell of background field strength 10^{-3} T (10 G) and network field widths $3{\times}10^3$ km is shown in Figure 6.14. In the first frame (Figure 6.14a) the background supergranule cell is drawn into which the ephemeral region emerges $4{\times}10^3$ km from the centre of the cell. An X-type neutral point appears immediately above the x-axis creating a bright point in the corona as the ephemeral region diverges (Figure 6.14b). The bright point rises further into the corona, though still remaining relatively low during the growth of the ephemeral region as its fragments separate (Figures 6.14c and 6.14d). When the ephemeral region fragments are situated at $a_1 = 2.8 \times 10^3$ km and $a_2 = d_c = 9.0 \times 10^3$ km, the negative fragment is fully captured by the right-hand network fragment and the bright point fades (Figure 6.14e). The ephemeral region continues its divergence as the cancelling magnetic feature starts when $a_1 = 1.6 \times 10^3$ km and $a_2 = 11.6 \times 10^3$ km (Figure 6.14f). By the time the cancelling magnetic feature has ended, the remaining ephemeral region fragment is being dragged by the convection in the cell ($a_1 = 2.5 \times 10^3$ km, $a_2 = 12.5 \times 10^3$ km) (Figure 6.14g). Now the remaining pole of the ephemeral region is left to drift with the convective motions of the supergranule cell to the right-hand edge of the supergranule where, upon contact with the network fragment, it starts to coalesce, eventually recreating the initial supergranule field (Figure 6.14h).

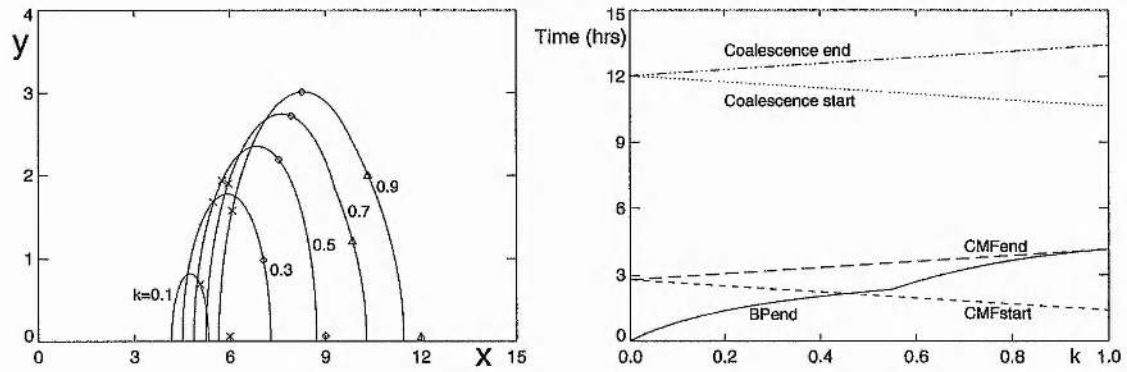

Figure 6.15: (a) The trajectory of the bright point in the xy-plane for k values of 0.1, 0.3, 0.5, 0.7 and 0.9 for a positive-negative co-moving ephemeral region in a quiet-region supergranule. The symbols ($\times$, $\diamond$ and $\triangle$) denote, along the x-axis, the positions of the negative fragment and on the bright point paths, the respective positions of the bright points for the given position of the negative fragment. (b) The lifetimes of the bright point (solid), cancelling magnetic feature (dashed) and coalescence phase (dotted) are plotted for this ephemeral region against the width ratio (k).

The height and position of the bright point in the corona are once again plotted with the symbols indicating the bright point positions relative to various positions of the negative ephemeral region fragment (Figure 6.15a). The basic trajectory of the bright point is similar to all the previous cases, but it only reaches a maximum height of $3{\times}10^3$ km for the $k = 0.9$ case, which in comparison to the earlier scenarios is very low. This is because the negative ephemeral region fragment is nearer the network field than in the previous cases and so the interaction phase is much shorter, which implies that the bright point lifetimes will be shorter. This is confirmed in Figure 6.15b which shows the lifetime of the bright point against k,

attains a maximum lifetime of 6 hrs. Here for $k > 0.45$ there is no capture phase and the bright point overlaps the cancellation phase and the coalescence of the positive fragment does not occur until several (maximum of 6 hrs) later.

6.8.2 Negative-Positive Case

The ephemeral region is situated such that the negative fragment is to the left of the positive source when it emerges in the right-hand side of the supergranule cell. Again the supergranule cell is considered to be in a quiet region with an ephemeral region of width ratio $k = 0.3$. Figure 6.17a shows the background supergranule cell field. The ephemeral region appears 4×10^3 km from the centre of the cell, as above, but this time a bright point does not appear immediately and for the first time there is a pre-interaction phase (Figure 6.17b). Instead, the bright point only starts when $a_1 = d_i = 3.8 \times 10^3$ km and $a_2 = 5.0 \times 10^3$ km, at which point a neutral point develops on the photosphere (Figure 6.17c) and rises into the corona as the fragments continue to diverge (Figure 6.17d). During this divergence the positive fragment begins to coalesce with the right-hand network field at the boundary of the supergranule cell. By the time the coalescence has ended, the driven divergence of the negative fragment has ceased and the remaining ephemeral region source is moving towards the cell boundary due to convection motions in the cell (Figure 6.17e). The bright point continues until this negative fragment becomes fully captured by the right-hand network field at which point it fades as the X-point drops back down to the photosphere ($a_1 = d_c = 5.5\times10^3$ km, $a_2 = 12.5\times10^3$ km) (Figure 6.17f). Now the negative fragment continues moving to the edge of the cell where at $a_1 = 11.6 \times 10^3$ km a cancelling magnetic feature starts (Figure 6.17g). This ends when the fragment is fully cancelled and restores the supergranule cell field back to its original structure (Figure 6.17h).

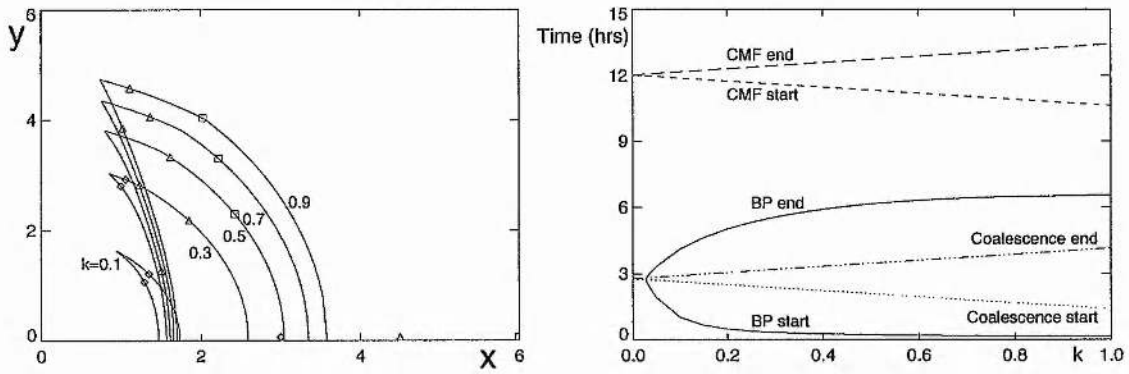

Figure 6.16: (a) The paths of the bright points are plotted in the xy-plane for the interaction of a co-moving negative-positive ephemeral region in a quiet-region supergranule cell for k values 0.1, 0.3, 0.5, 0.7 and 0.9. The symbols ($\diamond$, $\triangle$ and $\square$) represent the positions of the bright points (on the trajectories) at particular positions (3, 4.5 and 6 $\times10^3$ km) of the negative ephemeral region fragment (along the x-axis). (b) Lifetimes of the bright point (solid), coalescence phase (dotted) and cancelling phase (dashed) against the width ratio k for this ephemeral region scenario.

Here, when the height and position of the bright point are plotted, their trajectory looks quite different from the ones seen previously (Figure 6.16a). Firstly, the point at which the fragments stops moving away from the network with which it finally cancels produces the distinctive sharp bend in the curves.

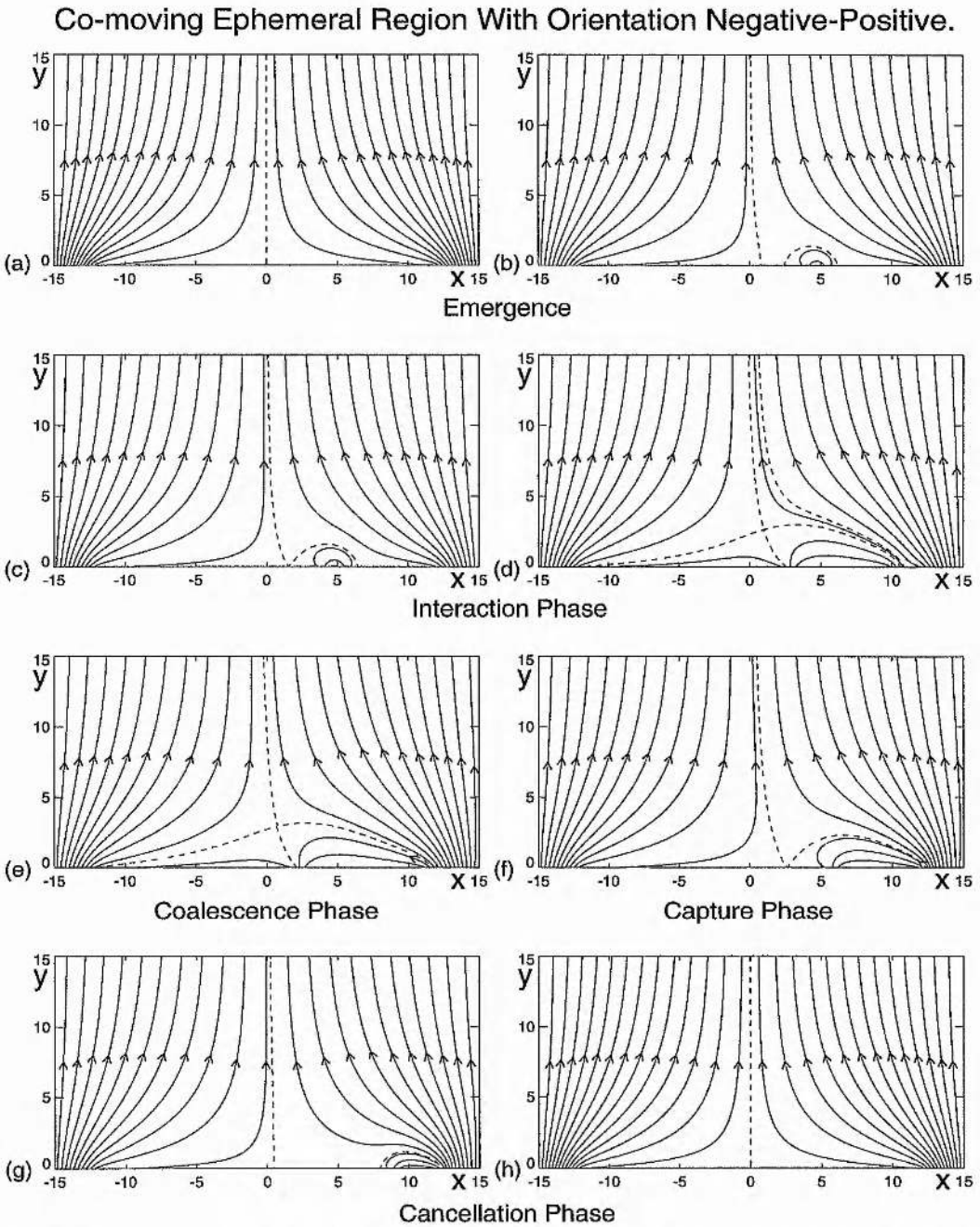

Figure 6.17: The magnetic field configurations through which a negative-positive co-moving ephemeral region evolves as it interacts in a quiet-region supergranule cell where $k = 0.3$. (a) The background field in the supergranule. (b) A pre-interaction phase occurs when the ephemeral region appears ($a_1 = 3.8 \times 10^3$ km, $a_2 = 4.7 \times 10^3$ km). (c) The interaction phase starts ($a_1 = 3.8 \times 10^3$ km, $a_2 = 4.7 \times 10^3$ km). (d) As the ephemeral region grows the bright point moves to the left ($a_1 = 3.0 \times 10^3$ km, $a_2 = 8.0 \times 10^3$ km). (e) Coalescence of the positive ephemeral region fragment takes place ($a_1 = 1.6 \times 10^3$ km, $a_2 = 11.6 \times 10^3$ km). (f) The bright point fades ($a_1 = 5.5 \times 10^3$ km, $a_2 = 12.5 \times 10^3$ km). (g) The negative fragment starts cancelling ($a_1 = 9.0 \times 10^3$ km, $a_2 = 12.5 \times 10^3$ km). (h) After cancellation the cell is restored to it's original strength.

Also, some of the symbols, indicating the position of the bright point when the negative ephemeral region is at certain points, appear twice on the bright point trajectories: they first appear when the negative fragment is moving away from the network field during the divergence stage; and for a second time the negative fragment is moving towards the network boundary as it is being pulled by the plasma motions in the cell. The ephemeral region appears at 4×10^3 km from the cell centre, therefore this diagram shows for the $k = 0.1$ and 0.3 cases, there is quite a long pre-interaction phase before the bright point appears and that the bright point only lasts for a short time. In the $k > 0.5$ cases the pre-interaction phase is not so definite and the bright point reaches a reasonable height in the corona. It is interesting to see that the bright point actually occurs fairly near the centre of the cell in this case whereas, in the previous case, it was nearer the edge of the cell.

In the lifetime plot for this scenario (Figure 6.16b) the interaction phase is clearly seen showing that for very small k there is no bright point produced and that the lifetimes of the bright points are still fairly short, reaching a maximum of only six hours. In all cases the bright point occurs well before the cancelling magnetic feature which starts, at the earliest, 4 hrs later. In this situation it is therefore likely that the bright point would be associated with the coalescing ephemeral region and not with the cancelling magnetic feature.

6.9 Discussion

From these results it may be inferred that the ratio of the fluxes of the cancelling fragments (k) is important for determining the height and lifetime of the bright point, whilst the actual size and strength of the cancelling fragment fluxes is important in determining the lifetime of the cancelling magnetic feature. It is also very likely that the sizes and strengths of the fragments that form the cancelling magnetic feature will be important in determining how much energy is released during the bright point. Obviously, if more flux is reconnected, as must be happening in the active-region $k = 0.3$ case compared to the quiet-region $k = 0.3$ case over an equivalent period of time, then the bright point will release more heat energy and appear brighter. Thus it is possible that this sort of event may explain the occurrence of transient brightenings in active regions recently seen by Yohkoh (Shimizu *et al.*, 1992). In fact bright point flares and active-region transient brightenings could be similar phenomena formed by the same mechanism. This suggestion is not unreasonable since their structure and lifetimes are similar (see Section 1.2.3 on x-ray bright points and active regions). Also from a study using Yohkoh data, Kawai *et al.*, 1992 found an example of an active-region transient brightening overlying an emerging bipolar flux region.

The energy released from a typical active-region magnetic interaction such as the one described above may be estimated using Equation (3.55). It is assumed that the opposite polarity magnetic fragments interacting are of the same strength and are converging in an overlying field of strength 0.01 T (100 G): thus if they have strengths of 10^{12} Wb (10^{20} Mx - the total flux in an active region is approximately 10^{14} Wb (10^{22} Mx), thus a hundred such sources would be present at any one time) implying an interaction distance of 6 Mm, the total free energy released from the reconnection of the fragments is 4×10^{22} J (4×10^{29} ergs). This is sufficient to provide energy at a rate of 1.4×10^{18} W (1.4×10^{25} ergs s^{-1}) to the active region for an 8 hr period, or produce 13.5×10^{17} W (13.5×10^{24} ergs s^{-1}) (equivalent to the power of nanoflares) for 7 hrs 55 mins and a further injection of energy at a rate of 10^{20} W (10^{27} ergs s^{-1}) for 5 mins (equivalent to the observed active-region transient brightening output). Thus it is speculated that normal active region heating is produced by the same mechanism as bright points, namely, multiple reconnection interactions of magnetic fragments. It is possible that these events may be part of a wide

spectrum of such events.

The total energy needed to heat an active region is approximately 1.5×10^{21} W (1.5×10^{28} ergs s^{-1}) (Shimizu, 1994) whereas the power lost from active-region transient brightenings is observed to be of the order of 10^{20} W (10^{27} ergs s^{-1}) (as produced by our model). Shimizu (1994) pointed out that this energy supplied by the transient brightenings was a factor of 10 too small to explain the heating of an active region. If, however, active-region transient brightenings are the flaring features at the end of a long lived reconnection event (similar to bright point flares that occur from 10% of bright points) then this discrepancy may be explained. For example, the typical lifetime of an active region is 2 days; therefore assuming a power of 1.5×10^{21} W (1.5×10^{28} ergs s^{-1}) the total energy released from the active region is 2×10^{26} J (2×10^{33} ergs). Active-region transient brightenings appear at a rate of one per hour in 'quiet' active regions and occur at a rate of 20 per hour in 'active' active regions, therefore suggesting that between 48 and 960 active-region transient brightenings would occur throughout the 2 days the active region lives. If it is assumed that 500 appear in total then using the same scaling for active-region transient brightenings to active-region reconnection events as that for bright point flares and bright points, namely, a ratio of 1 to 10, then a total of 5000 active-region reconnection events would occur over the life of the active region (approximately one hundred per hour). The total sum of all their energies (4×10^{22} J (4×10^{29} ergs) per event) would give 2×10^{26} J (2×10^{33} ergs) which is sufficient to heat the active region. Alternatively active-region transient brightenings may be the large end of a spectrum of reconnection events that heat the normal active region extending down to nanoflares and microflares which have energies of 10^{17} J (10^{24} ergs).

6.10 Conclusion

A model has been proposed for the interaction of an ephemeral region within a supergranule cell. The model follows the emergence of the ephemeral region right up to and, in some cases, beyond the creation of a cancelling magnetic feature between one of the ephemeral region fragments and a network region at the boundary of the supergranule cell. It is found that there are five possible scenarios for the evolution of the ephemeral region. Each case has been modelled, revealing that they all produce a bright point and cancelling feature with a network field, in a similar manner to the converging flux model of Chapters 2 - 4: thus the previous models may be created using an overlying field other than that of a horizontal one and the use of line sources although simple is not too bad. In the first situation, called the *diverging ephemeral region* case, a small bipolar pair emerges in the centre of the supergranule cell; as the ephemeral region develops and separates, its fragments are pushed to either side of the cell by convection and a bright point rises up into the corona. As the ephemeral region continues to diverge, the negative fragment becomes captured by the network boundary field and then forms a cancelling magnetic feature. Simultaneously, the positive ephemeral fragment merges with the opposite network boundary field, distorting the supergranule field and leaving one network boundary fragment much larger than the other.

If an ephemeral region emerges offset from the centre of the supergranule cell with fragments diverging at a sufficient rate, then the second and third scenarios (called *asymmetric diverging ephemeral regions*) may be observed. The ephemeral region diverges as it emerges, creating a bright point with its fragments initially in one half of the supergranule cell. Then the separation of these fragments continues and one may cross over into the other half of the supergranule cell; the bright point rises, as before, moving to the side where the cancellation will take place. The fragments maintain their divergence and the bright point descends back down to the base of the supergranule cell. In the first asymmetric case (positive-negative), cancellation of the negative ephemeral region fragment takes place before the coalescence of the positive

ephemeral region fragment, which follows a short time later and leads to a relatively short bright point lifetime, whereas a longer bright point lifetime may be seen if the negative fragment has further to move before cancellation, as seen in the negative-positive asymmetric case. Both cases leave the supergranule cell with a distorted field, as in the first scenario.

The fourth and fifth scenarios also involve an ephemeral region emerging in one side of a supergranule cell. Here, however, even though the fragments diverge as they emerge, the right-hand fragment is cancelled (coalesced) whilst the left-hand fragment is still in the right half of the supergranule. Thus this fragment, no longer driven by the separation in the supergranule cell, is pulled along by the plasma to the cell boundary where it coalesces (cancels). These scenarios are known as *co-moving ephemeral regions*; the fourth situation (positive-negative) is where cancellation occurs before coalescence, and the fifth (negative-positive) where the cancellation follows on after coalescence. In the negative-positive co-moving scenario a distinctive pre-interaction phase is seen for the first time before the bright point appears.

All of these situations were modelled for various ratios of the ephemeral region to network boundary fragment widths (k), revealing that the lifetime of the bright point is dependent on the ratio of the fragment widths rather than the actual strength of the fragments themselves, as discovered in Chapters 3 and 4. This implies that an ephemeral region with fragment width and strength equal to the width and strength of the boundary network field (i.e. a ratio $k = 1$) would produce a bright point that would last longer and be higher in the corona than a bright point produced by an ephemeral region with fragments much smaller in width than the network regions (i.e. a ratio of $k \ll 1$). Also the results reaffirmed that the lifetime of the bright point is also dependent on the distance that the two cancelling fragments move before cancellation (and hence depends upon where the ephemeral region emerges in the cell and its orientation) and their rate of convergence. In an active-region supergranule cell, the lifetime and trajectory of the bright point are similar to those in a quiet-region supergranule, so despite there being much more flux to cancel in the ephemeral region and network fragment, this does not affect the bright point lifetime. In the negative-positive asymmetric diverging case, the negative source moves over $13{\times}10^3$ km during the bright point; thus the bright point lasts up to 13 hrs whereas in the positive-negative co-moving case, the cancelling fragment moves only 8 Mm during the interaction phase producing a bright point that lasts only 4.5 hrs. Also, the distance the bright point actually moves in the corona is dependent on the interaction distance, the width ratio and the velocity of the fragments, though in all cases the rate of movement of the bright point is approximately 0.2 km s^{-1}. The height of the bright point is similarly dependent on d_i, k and v.

The comparison between a quiet-region and active-region supergranule cell revealed no major changes in the pattern of events for the interaction of the ephemeral region and production of the bright point. For similar k ratios, similar maximum heights and lifetimes for the bright points are found, though the cancelling magnetic feature lifetime is longer in the active-region case. Assuming that the speed of divergence of the ephemeral region fragments is the same in both cases, this implies that more magnetic energy is released in the active-region situation than in the quiet-region case, so the active-region reconnection event would be brighter (more intense) than one in a quiet-region cell. From a simple calculation, using the equation derived in Chapter 3 for the energy released from two unequally sized cancelling fragments it is found that an active region reconnection event could produce sufficient energy to cause a brightening that would show up against the normal active-region brightness. It is therefore possible that this may also be a model for transient brightenings seen in active regions and that transient brightenings and bright point flares could essentially be caused by the same mechanism.

The lifetime of the cancelling magnetic feature, however, is directly related to the size of the cancelling

magnetic fragments. Active-region fragments with the largest widths (strengths) take the longest to cancel whereas quiet-region fragments of width ratio $k \ll 1$ are cancelled quickly, providing cancellation takes place at the same rate in all cases. Here, it does not matter how far the fragments have travelled if it is assumed cancellation takes place only when the fragments are touching; their size and speed are what is important for cancellation.

The capture phase is obviously dependent on all of the above. A long-lived bright point and lengthy cancelling magnetic feature (as in an active-region supergranule cell situation with interaction of a $k \approx 1$ ephemeral region) will produce no capture phase, whereas a short-lived bright point and cancelling magnetic feature give rise to a capture phase of several hours, as seen in the negative-positive co-moving case with $k \approx 1$. In fact it is possible that in some cases (because the onset of cancellation takes place up to 6 hrs after the demise of the bright point), that the bright point would be considered unlinked to the cancelling magnetic feature; furthermore the bright point would more likely be associated with the emergence of the ephemeral region which is occurring almost simultaneously with the bright point. This may be an explanation as to why one-third of dark points (proxies to the thirty percent largest bright points) were linked with ephemeral regions and two-thirds with cancelling magnetic features.

In the future it would be very interesting to have more coordinated observations of bright points and cancelling magnetic features in soft x-rays, Hα, and magnetograms to discover which types of cancelling magnetic feature produce the brightest and longest-lived bright points. Also, it is suggested that having high-resolution magnetograms of the photosphere below active regions simultaneously with studies of transient brightenings may verify whether active-region transient brightenings really are the active-region sisters of bright points.

Chapter 7

Summary and Further Work

7.1 Summary

Throughout this thesis theoretical models have been set up to model x-ray bright points and cancelling magnetic features. Chapters 2 - 4 describe two-dimensional potential models where the magnetic fragments, modelled as line sources lying in a background horizontal field, move slower than the Alfvén speed so that the magnetic field evolves through a series of quasi-static states. The magnetic configurations that arise may be split into four phases: the *pre-interaction phase* in which the magnetic fragments are sufficiently far apart that they are unconnected magnetically; the *interaction phase* where an X-type neutral point (at which energy is released due to reconnection) forms a bright point that rises above the photosphere into the corona; the *capture phase* in which the bright point has faded and the two originally unconnected fragments are fully connected magnetically; and the *cancellation phase* where the two opposite polarity magnetic fragments cancel due to reconnection in the photosphere. These phases agree well with the observations in which: initially there are no chromospheric fibrils linking the magnetic fragments (pre-interaction phase); a bright point appears in the corona before the cancelling magnetic feature (interaction phase); and the two fragments mutually lose flux and form a cancelling magnetic feature (cancellation phase). In many cases a capture phase does not occur since the cancelling magnetic feature starts before the demise of the bright point, however, 72% of bright points appear above cancelling magnetic features and 88% above converging flux regions (Webb *et al.*, 1993); this suggests that 16% of bright point-cancelling magnetic feature events have a capture phase. The models also predict the typical lifetime and total energy release from a bright point. For example, from observations, the mean lifetime of a bright point is 8 hrs and the typical total energy release is 3×10^{20} - 3×10^{21} J (3×10^{27} - 3×10^{28} ergs). This may be produced from a cancelling magnetic feature with two poles of equal strength and with an interaction distance of 8.5 Mm (and so a flux per pole of 2.3×10^{11} Wb (2.3×10^{19} Mx)) in a quiet region with overlying field strength 10^{-3} T (10 G). In fact, from the models, the characteristics for bright points produced by different types of cancelling magnetic features are predicted (Table 7.1). It is hoped that by bearing these predictions in mind an observational investigation may in future be carried out comparing the different types of cancelling magnetic features and their related bright points.

In Chapter 5 the actual complex structure of bright points seen in high-resolution soft x-ray images is modelled for two observed bright points. Using the ideas from the previous models, it is assumed that the bright points arise from the cancellation of flux and that heat or plasma is injected along newly reconnected field lines, thus causing them to brighten. The structure of the magnetic field in the region of the bright point is first calculated from a study of the magnetograms; then assuming a suitable movement

CMF	k	d_i (Mm)	v (km s^{-1})	t_{bpt} (hrs)	t_{cmf} (Obs, hrs)	Capture Phase?	y_{nmax} (Mm)	x_n (Mm)	W_F (J) [ergs]
N-N	1	5-15	0.1-0.3	5-40	1-36	Never	2.5-7.5	0-0.5	5×10^{19}-10^{22} [5×10^{26}-10^{29}]
ER-N ER-I	5	2-15	0.1-0.3	2-36	1-36	Rarely	0.5-6.5	0.5-5	10^{19}-5×10^{21} [10^{26}-5×10^{28}]
I-N I-I	10	2-10	0.1-0.3	1-7	1-5	Occasionally	0.5-4.0	0.5-4	10^{19}-10^{21} [10^{26}-10^{28}]

key: N - network fragment, I - intracell fragment and ER - ephemeral region,
k - ratio of the pole strengths, d_i - the interaction distance (proportional to the flux per pole),
v - speed of convergence of the fragments, t_{bpt} - lifetime of the bright point,
t_{cmf} - the observed lifetime of the cancelling magnetic feature,
y_{nmax} - maximum height of the bright point above the photosphere,
x_n - position of the bright point relative to the mid point of the cancelling magnetic feature,
W_F - the total energy released from the bright point.

Table 7.1: Predictions of bright point characteristics for different cancelling magnetic features.

of a magnetic fragment the new field lines created are drawn. These models, in both the cases studied, compare well with the observed brightenings.

Finally, a more realistic interaction of the magnetic fragments is modelled in Chapter 6, where a bipolar pair of magnetic fragments emerges and interacts in an overlying supergranule cell field. Here again the bright point and associated cancelling magnetic feature evolve through the same phases as those in the converging flux models of Chapters 2 - 4: however this time further predictions may be made about the relation between the bright point and cancelling magnetic feature. The lifetime of the bright point depends on: the distance the magnetic fragments move from the point at which they first interact magnetically to the final complete magnetic 'capture' of the weaker fragment; the speed at which these fragment are moving together; and the ratio of their fluxes. The lifetime of the cancelling magnetic feature, however, is dependent on the total amount of flux that is cancelled and the speed of convergence of the fragments. Obviously the relation between the bright point and cancelling magnetic feature depends on all of the above factors: in fact the onset of cancellation may occur up to 3 hrs before, to 6 hrs after the demise of the bright point, such that it is possible that a bright point may be associated with the ephemeral region that has emerged, as opposed to the cancelling magnetic feature that occurs much later. From these results, it is therefore suggested that this may explain why ephemeral regions have been associated with cancelling magnetic features in the past. It is also suggested that active-region transient brightenings may be produced by the same mechanism as bright point flares, since in an active-region cell much more flux may be reconnected than in a quiet-region cell over the same time period: therefore more energy is released in an active-region interaction, which is sufficient to cause a transient brightening. It is also speculated that there may be many active-region reconnection events similar to bright points that provide the basic heat needed for normal active-region heating.

This thesis therefore contains models for bright points and associated cancelling magnetic features that satisfy many of the key observations: however, from this work it is found that coordinated observations in soft x-rays, Hα, He 10830 and vector magnetograms are very important, not only to further our knowledge of bright points and cancelling magnetic features, but also to understand more about the heating of the corona, the creation of x-ray jets, bright point flares and active-region transient brightenings.

7.2 Further Work

The models discussed here are really just a first step in the understanding of bright points, their link with coronal heating and other coronal features. They provide an important insight into the basic behaviour of a bright point and associated cancelling magnetic feature which is necessary before more realistic and therefore more complicated models may be created.

One of the first obvious extensions to this work is to carry out a comparison of bright points and their related cancelling magnetic features. This would not only show whether the models proposed in this thesis are viable, but would also provide important information that hopefully will be beneficial for further bright point and cancelling magnetic feature models. Also, in conjunction with a study of bright point flares, a more complete study of active-region transient brightenings and their corresponding magnetogram and Hα counterparts is needed to confirm whether transient brightenings and bright point flares really are related.

All the models presented in this thesis are quasi-static. It would therefore be natural to extend this work to produce time-dependent models. Already, one such model has stemmed from this work, in which two magnetic arcades interact forming a neutral point in the corona (Rickard and Priest, 1994). In this numerical simulation the reconnection is driven by the motions of the magnetic fragments in the photosphere. One of the parameters investigated is the current density which has a maximum at the neutral point and is enhanced along the separatrices: this indicates that a bright point would be associated with the central current sheet and that there would be significant heating along the separatrices (newly reconnected field lines). This model, however, was limited to studying the interaction of the fluxes for only a short period of time and therefore it would be interesting to develop a model that could study the interaction of the fluxes from the pre-interaction phase through to the cancellation phase.

Another important extension to this work would be to try and include a tiny filament which could give rise to an erupting bright point and to create a model for an x-ray jet. It has been suggested that the jet may be produced by the injection of heat or plasma along a long field line connected to a far-off source, so it would be interesting to see if this could be included in a two-dimensional time-dependent model given a suitable reconnection mechanism. Possibilities for the formation for a filament were suggested by Priest *et al.* (1994), but these require a lot of further work before they can attempt to explain the eruption of a bright point properly.

In the three-dimensional models there are still lots of open questions which will require a lot of work. Firstly, how do the field lines reconnect in three dimensions? In this thesis reconnection along a separator has been discussed briefly, but reconnection in three dimensions without a separator is not properly understood. Consider, for example, a positive source A that is stronger than a negative sink B. In two dimensions there will be one neutral point in the field from which two separatrices will extend back to A, forming a lobe enclosing B, and two others that will extend out from the neutral point forming a *spine* from B to a far-off negative sink (at infinity in this case). Now, if B is assumed to be moving to the right, field lines outside the lobe on the right-hand side will reconnect with a field line inside the lobe (Figure 7.1a) to create a new field line connected to B and a field line off to the left of the

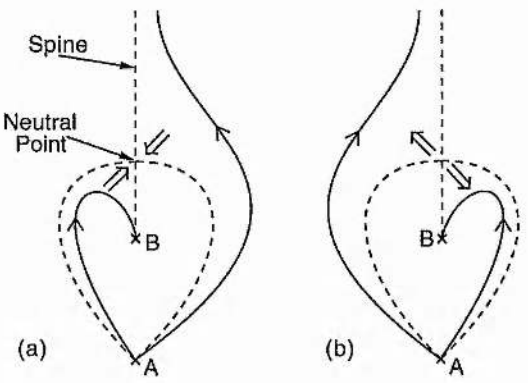

Figure 7.1: Reconnection in two dimensions as the weaker negative pole B moves to the right.

lobe (Figure 7.1b). However, what happens in three dimensions? The lobe enclosing B will extend to form a dome (a separatrix surface), but it is not clear how this divides into an 'inward' surface and an 'outward' surface through which the field lines flow in, reconnecting to form lines to B and flow outwards, reconnecting to form lines to the far off negative source, respectively. This question has been approached by Priest and Titov (1995) who point out that it is naturally dependent on the flow of the plasma. In fact they find that there can be two different types of reconnection: one in which all the field lines in the separatrix surface (called the *fan*) reconnect; and another where the field lines along the *spine* reconnect.

Another question arising from the three-dimensional work is how much energy is released through the reconnection and where is it released? Again, either a three-dimensional current sheet could be introduced to calculate the total energy released, or a time-dependent simulation could be carried out to estimate where and how much energy was being released and approximately the rate and location of the reconnection. Both of these investigations would require much thought as to how to proceed and as to the best way to achieve meaningful results. A useful addition to help with the construction of the theoretical model would be a study of the observations revealing where the heat is being released in the corona or transition region and how this heat or plasma is distributed. The rate of cooling of the plasma is discussed briefly in Chapter 5, but a more complete investigation is essential to understand fully the complex structure of the bright point and possibly help in the understanding of how active regions are heated.

From all these suggestions there is obviously a lot more work that can be done to fully explain bright points, but I hope that from the work presented in this thesis a better understanding of bright points and cancelling magnetic features has been gained.

Appendix A

Calculation of the Flux Function $A(x,y)$

The flux function $A(x,y)$ is such that

$$\mathbf{B}_p = \nabla \times A_p \, \hat{\mathbf{e}}_z \,, \tag{A.1}$$

that is to say,

$$B_{px} = \frac{\partial A_p}{\partial y} \,, \qquad B_{py} = -\frac{\partial A_p}{\partial x} \,.$$

So solving for A_p given $\mathbf{B}_p$ one finds

$$A_p = -\int_o^x B_{py} \, \mathrm{d}x \,, \tag{A.2}$$

which, since $z = x + \mathrm{i}y$ and $\mathcal{B}_p(z) = B_{py} + \mathrm{i}B_{px}$, equals

$$A_p(x,y) = -\mathcal{R}e \int_0^{x+\mathrm{i}y} \mathcal{B}_p(z) \, \mathrm{d}z \,. \tag{A.3}$$

Now, from Chapter 2 one finds the integral for A_p is of the form

$$\begin{aligned}
A_p(x,y) &= -\mathcal{R}e \int_0^{x+\mathrm{i}y} \frac{\mathrm{i}B_o\left(z^2 - s\right)}{z^2 - a^2} \, \mathrm{d}z \\
&= -\mathcal{R}e \int_0^{x+\mathrm{i}y} \mathrm{i}B_o + \frac{\mathrm{i}B_o\left(a^2 - s\right)}{2a} \left(\frac{1}{z-a} - \frac{1}{z+a}\right) \, \mathrm{d}z \\
&= -\mathcal{R}e \left[\mathrm{i}B_o z + \frac{\mathrm{i}B_o\left(a^2 - s\right)}{2a} \left(\log(z-a) - \log(z+a)\right)\right]_0^{x+\mathrm{i}y} \\
&= B_o y + \frac{B_o\left(a^2 - s\right)}{2a} \left(\mathrm{Arg}\left(\frac{z-a}{-a}\right) - \mathrm{Arg}\left(\frac{z+a}{a}\right)\right)
\end{aligned}$$

$$= B_o y + \frac{B_o\left(a^2 - s\right)}{2a}\mathrm{Arg}\left(\frac{a-z}{a+z}\right) + C\,, \tag{A.4}$$

where C is a constant and care must be taken in choosing the correct value for the $\mathrm{Arg}(z)$. So in Equation (2.1)

$$s = x_n^2 \implies A_p(x,y) = B_o\left[y + \frac{\left(a^2 - x_n^2\right)}{2a}\mathrm{Arg}\left(\frac{a-z}{a+z}\right)\right], \tag{A.5}$$

in Equation (2.7)

$$s = 0 \implies A_p(x,y) = B_o\left[y + \frac{a}{2}\mathrm{Arg}\left(\frac{a-z}{a+z}\right)\right], \tag{A.6}$$

and in Equation (2.9)

$$s = -y_n^2 \implies A_p(x,y) = B_o\left[y + \frac{\left(a^2 + y_n^2\right)}{2a}\mathrm{Arg}\left(\frac{a-z}{a+z}\right)\right]. \tag{A.7}$$

Appendix B

Solution of the Indefinite Integrals in Equations (3.48), (3.49) and (3.50)

The Solution to Equation (3.48)

Equation (3.48) contains the integral

$$\int \frac{dx}{Q(x)},$$

where $Q(x) = \left((x-x_2)^2 + y_2^2\right)^{\frac{1}{2}}$. This may be solved by using the substitution $(x-x_2)/y_2 = \sinh y$, so that

$$\begin{aligned}
\int \frac{dx}{Q(x)} &= \int dy \\
&= y + C \\
&= \sinh^{-1}\frac{x-x_2}{y_2} + C \\
&= \log\left[Q(x) + x - x_2\right] + D, \qquad \text{(B.1)}
\end{aligned}$$

where C and D are constants.

The Solution to Equation (3.49) and (3.50)

Equation (3.49) involves an integral of the form

$$\int \frac{dx}{(x-a)\,Q(x)},$$

where one can write $Q(x) = \left((x-a)^2 + 2(a-x_2)(x-a) + Q^2(a)\right)^{\frac{1}{2}}$ from Equation (3.43). Thus this integral may be written as

$$\int \frac{dx}{(x-a)\,Q(x)} = \int \frac{dx}{(x-a)\left((x-a)^2 + 2(a-x_2)(x-a) + Q^2(a)\right)^{\frac{1}{2}}}, \tag{B.2}$$

which using the substitution $y = 1/(x-a)$, becomes

$$\int \frac{dx}{(x-a)\left((x-a)^2 + 2(a-x_2)(x-a) + Q^2(a)\right)^{\frac{1}{2}}} = -\int \frac{dy}{(1 + 2(a-x_2)y + Q^2(a)y^2)^{\frac{1}{2}}}. \tag{B.3}$$

On completing the square and applying the substitution $u = \mid Q(a) \mid y + (a-x_2) / \mid Q(a) \mid$, one finds

$$\begin{aligned} -\int \frac{dy}{(1 + 2(a-x_2)y + Q^2(a)y^2)^{\frac{1}{2}}} &= -\int \frac{dy}{\left(\left(\mid Q(a) \mid y + \frac{a-x_2}{|Q(a)|}\right)^2 + \left(1 - \frac{(a-x_2)^2}{Q^2(a)}\right)\right)^{\frac{1}{2}}} \\ &= \frac{-1}{\mid Q(a) \mid} \int \frac{du}{\left(u^2 + \left(1 - \frac{(a-x_2)^2}{Q^2(a)}\right)\right)^{\frac{1}{2}}}. \end{aligned} \tag{B.4}$$

This integral is simply that solved in Equation (B.1) and therefore

$$\begin{aligned} \int \frac{dx}{(x-a)\,Q(x)} &= \frac{-1}{\mid Q(a) \mid} \log\left[\frac{\mid Q(a) \mid}{x-a} + \frac{(a-x_2)}{\mid Q(a) \mid} + \frac{Q(x)}{x-a}\right] - C \\ &= \frac{-1}{\mid Q(a) \mid} \log\left[\frac{Q^2(a) + (a-x_2)(x-a) + \mid Q(a) \mid Q(x)}{x-a}\right] - D, \end{aligned} \tag{B.5}$$

where C and D are constants.

Similarly by substituting $a = -a$ into the above equation the solution to Equation (3.50) becomes

$$\int \frac{dx}{(x+a)\,Q(x)} = \frac{-1}{\mid Q(-a) \mid} \log\left[\frac{Q^2(-a) - (a+x_2)(x+a) + \mid Q(-a) \mid Q(x)}{x+a}\right] - D. \tag{B.6}$$

Appendix C

Solution of the Definite Integrals in Equations (3.53) and (3.54)

The Evaluation of Equation (3.53)

The left-hand side of Equation (3.53) is a definite integral:

$$\int_{-\infty}^{-a} \left[B_x - B_{px}\right]_{y=0} dx \ ,$$

which has been solved indefinitely in Equation (3.52); care is however needed in applying the limits of integration.

First it is noted that in the interval $(-\infty, -a]$, $Q(x) = -\mid Q(x) \mid$, since the side of the current sheet being considered is critical. The lower limit of integration is applied by substituting $x = -R$ and taking the limit as $R \to \infty$: thus the first term on the right-hand side of the Equation (3.52) becomes

$$\begin{aligned}
\lim_{x \to -\infty} Q(x) &= \lim_{R \to \infty} -\mid Q(-R) \mid \\
&= \lim_{R \to \infty} \left[-R \left(1 + \frac{2x_2}{R} + \frac{x_2^2 + y_2^2}{R^2} \right)^{\frac{1}{2}} \right] \\
&= \lim_{R \to \infty} \left[-R - x_2 - \frac{y_2^2}{2R} + \mathrm{O}\left(\frac{1}{R^2} \right) \right] . \qquad \text{(C.1)}
\end{aligned}$$

This may be used in evaluating the following three terms in the equation:

$$\begin{aligned}
\lim_{x \to -\infty} \log \left[Q(x) + x - x_2 \right] &= \lim_{R \to \infty} \log \left[-R - x_2 - \frac{y_2^2}{2R} - R - x_2 \right] \\
&= \lim_{R \to \infty} \log \left[-2R \right] \ ; \qquad \text{(C.2)}
\end{aligned}$$

$$\lim_{x \to -\infty} \log \left[Q^2(a) + (a - x_2)(x - a) + \mid Q(a) \mid Q(x) \right]$$

$$= \lim_{R\to\infty} \log\left[Q^2(a) + (a-x_2)(-R-a) + \mid Q(a) \mid \left(-R - x_2 - \frac{y_2^2}{2R}\right)\right]$$

$$= \lim_{R\to\infty} \log[R + \mathrm{O}(1)] + \log[\mid Q(a) \mid + (a-x_2)] \; ; \tag{C.3}$$

$$\lim_{x\to-\infty} \log\left[\frac{Q^2(-a) - (a+x_2)(x+a) + \mid Q(-a) \mid Q(x)}{(x+a)^2}\right]$$

$$= \lim_{R\to\infty} \log\left[\frac{Q^2(-a) - (a+x_2)(-R+a) + \mid Q(-a) \mid \left(-R - x_2 - \frac{y_2^2}{2R}\right)}{(-R+a)^2}\right]$$

$$= \lim_{R\to\infty} -\log[-R + \mathrm{O}(1)] + \log[\mid Q(-a) \mid -(a+x_2)] \; . \tag{C.4}$$

The integral (3.52) is the sum of the above terms plus R in the limit $x \to -\infty$: thus the lower limit of Equation (3.53) equals

$$\int_{-\infty} [B_x - B_{px}]_{y=0}\, dx = B_o \{-x_2 + (f' - g')\log 2 - f' \log[\mid Q(a) \mid + (a-x_2)]$$

$$- g' \log[\mid Q(-a) \mid -(a+x_2)]\} \; . \tag{C.5}$$

The upper limit of $x = -a$ is solved by substituting in $x = -a - \delta$ and taking the limit as $\delta \to 0$. Initially $Q(x)$ is considered at $x = -a - \delta$,

$$-\mid Q(-a-\delta) \mid = -\left((a+x_2)^2 + y_2^2 + 2(a+x_2)\delta + \delta^2\right)^{\frac{1}{2}}$$

$$= -\mid Q(-a) \mid \left(1 + \frac{2(a+x_2)\delta + \delta^2}{Q^2(-a)}\right)^{\frac{1}{2}}$$

$$= -\mid Q(-a) \mid -\frac{(a+x_2)\delta}{\mid Q(-a) \mid} - \frac{\delta^2}{2 \mid Q(-a) \mid} + \frac{(a+x_2)^2 \delta^2}{2Q^2(-a) \mid Q(-a) \mid} + \mathrm{O}(\delta^3) \; . \tag{C.6}$$

This may now be used to solve all the remaining terms in Equation (3.52):

$$\lim_{x\to-a} \log[Q(x) + x - x_2] = \log[-\mid Q(-a) \mid -a - x_2] \; ; \tag{C.7}$$

$$\lim_{x\to-a} \log\left[Q^2(a) + (a-x_2)(x-a) + \mid Q(a) \mid Q(x)\right]$$

$$= \log\left[Q^2(a) - 2a(a-x_2) - \mid Q(a) \mid Q(-a)\right] \; ; \tag{C.8}$$

$$\lim_{x\to -a}\log\left[\frac{Q^2(-a)-(a+x_2)(x+a)+\mid Q(-a)\mid Q(x)}{(x+a)^2}\right]$$

$$= \lim_{\delta\to 0}\log\left[\frac{Q^2(-a)-(a+x_2)(-a-\delta+a)}{(-a-\delta+a)}\right.$$

$$\left.+\frac{\mid Q(-a)\mid\left(-\mid Q(-a)\mid-\frac{(a+x_2)\delta}{\mid Q(-a)\mid}-\frac{\delta^2}{2\mid Q(-a)\mid}+\frac{(a+x_2)^2\delta^2}{2Q^2(-a)\mid Q(-a)\mid}\right)}{(-a-\delta+a)^2}\right]$$

$$= \log\left[\left(-\frac{1}{2}+\frac{(a+x_2)^2}{2Q^2(-a)}\right)\right]. \tag{C.9}$$

The upper limit is then found to be

$$\int^{-a}[B_x-B_{px}]_{y=0}\,dx = B_o\left\{-\mid Q(-a)\mid+a+(f'-g')\log[\mid Q(-a)\mid+(a+x_2)]\right.$$

$$\left.-f'\log[\mid Q(a)\mid\mid Q(-a)\mid+2a(a-x_2)-Q^2(a)]-g'\log\left[\frac{1}{2}-\frac{(a+x_2)^2}{2Q^2(-a)}\right]\right\}. \tag{C.10}$$

Now by subtracting Equation (C.5) from Equation (C.10), the definite integral in Equation (3.53) is solved,

$$\int_{-\infty}^{-a}[B_x-B_{px}]_{y=0}\,dx = B_o\left\{a+x_2-\mid Q(-a)\mid-g'\log\left[\frac{(\mid Q(-a)\mid+a+x_2)^2}{4Q^2(-a)}\right]\right.$$

$$\left.-f'\log\left[\frac{2(\mid Q(a)\mid\mid Q(-a)\mid+2a(a-x_2)-Q^2(a))}{(\mid Q(-a)\mid+a+x_2)(\mid Q(a)\mid+a-x_2)}\right]\right\}. \tag{C.11}$$

The Evaluation of Equation (3.54)

The definite integral of Equation (3.54) is

$$\int_a^{\infty}[B_x-B_{px}]_{y=0}\,dx\,.$$

As in the first section of this appendix the limits of integration merely need to be applied since the integral has been solved analytically as an indefinite integral, with its solution given in Equations (3.52).

Here $Q(x) = \mid Q(x)\mid$, since in the interval $[a,\infty)$ one remains on the same side of the current sheet. By substituting $x = a+\delta$, and taking the limit as $\delta\to 0$, the lower limit of the integral may be evaluated. Firstly $Q(x)$ is considered at $x = a+\delta$,

$$\mid Q(a+\delta)\mid = \left((a-x_2)^2+y_2^2+2(a-x_2)\delta+\delta^2\right)^{\frac{1}{2}}$$

$$= \mid Q(a)\mid\left(1+\frac{2(a-x_2)\delta+\delta^2}{Q^2(a)}\right)^{\frac{1}{2}}$$

$$= \mid Q(a) \mid + \frac{(a-x_2)\,\delta}{\mid Q(a) \mid} + \frac{\delta^2}{2 \mid Q(a) \mid} - \frac{(a-x_2)^2\,\delta^2}{2Q^2(a) \mid Q(a) \mid} + \mathrm{O}\left(\delta^3\right) . \tag{C.12}$$

Then it is easy to calculate the remaining terms:

$$\lim_{x \to a} \log \left[Q(x) + (x - x_2)\right] = \log \left[\mid Q(a) \mid + (a - x_2)\right] ; \tag{C.13}$$

$$\lim_{x \to a} \log \left[Q^2(a) + (a - x_2)(x - a) + \mid Q(a) \mid Q(x)\right]$$

$$= \log \left[2Q^2(a)\right] ; \tag{C.14}$$

$$\lim_{x \to a} \log \left[\frac{Q^2(-a) - (a + x_2)(x + a) + \mid Q(-a) \mid Q(x)}{(x+a)^2}\right]$$

$$= \log \left[Q^2(-a) - 2a(a + x_2) + \mid Q(-a) \mid\mid Q(a) \mid\right] - \log 4a^2 . \tag{C.15}$$

Thus, in the limit $x \to a$, the lower limit is found to be

$$\int_a \left[B_x - B_{px}\right]_{y=0} dx = B_o \left\{\mid Q(a) \mid -a + (f' - g') \log \left[\mid Q(a) \mid + (a - x_2)\right]\right.$$

$$\left. - f' \log \left[2Q^2(a)\right] - g' \log \left[Q^2(-a) - 2a(a + x_2) + \mid Q(a) \mid\mid Q(-a) \mid\right] + g' \log 4a^2 \right\} . \tag{C.16}$$

The upper limit of integration is solved by letting $x = R$ in the limit as $R \to \infty$. First $Q(x)$ is considered

$$\lim_{x \to \infty} Q(x) = \lim_{R \to \infty} \mid Q(R) \mid$$

$$= \lim_{R \to \infty} \left[R \left(1 - \frac{2x_2}{R} + \frac{x_2^2 + y_2^2}{R^2}\right)^{\frac{1}{2}}\right]$$

$$= \lim_{R \to \infty} \left[R - x_2 + \frac{y_2^2}{2R} + \mathrm{O}\left(\frac{1}{R^2}\right)\right] . \tag{C.17}$$

The remaining terms in Equation (3.52) become:

$$\lim_{x \to \infty} \log \left[Q(x) + x - x_2\right] = \lim_{R \to \infty} \log \left[R - x_2 + \frac{y_2^2}{2R} + R - x_2\right]$$

$$= \lim_{R \to \infty} \log \left[2R\right] ; \tag{C.18}$$

$$\lim_{x\to\infty} \log\left[Q^2(a) + (a - x_2)(x - a) + |\, Q(a)\,|\, Q(x)\right]$$

$$= \lim_{R\to\infty} \log\left[Q^2(a) + (a - x_2)(R - a) + |\, Q(a)\,|\left(R - x_2 + \frac{y_2^2}{2R}\right)\right]$$

$$= \lim_{R\to\infty} \log[R + \mathrm{O}(1)] + \log[|\, Q(a)\,| + (a - x_2)]\ ; \tag{C.19}$$

$$\lim_{x\to\infty} \log\left[\frac{Q^2(-a) - (a + x_2)(x + a) + |\, Q(-a)\,|\, Q(x)}{(x + a)^2}\right]$$

$$= \lim_{R\to\infty} \log\left[\frac{Q^2(-a) - (a + x_2)(R + a) + |\, Q(-a)\,|\left(R - x_2 + \frac{y_2^2}{2R}\right)}{(R + a)^2}\right]$$

$$= \lim_{R\to\infty} -\log[R + \mathrm{O}(1)] + \log[|\, Q(-a)\,| - (a + x_2)]\ . \tag{C.20}$$

Thus, the upper limit of integration becomes

$$\int^{\infty} [B_x - B_{px}]_{y=0}\, dx = B_o\{-x_2 + (f' - g')\log 2 - f' \log[|\, Q(a)\,| + (a - x_2)]$$

$$- g' \log[|\, Q(-a)\,| - (a + x_2)]\}\ . \tag{C.21}$$

Equation (C.16) may now be subtracted from Equation (C.21) to give the answer in Equation (3.54)

$$\int_a^{\infty} [B_x - B_{px}]_{y=0}\, dx = B_o\left\{a - x_2 - |\, Q(a)\,| - f' \log\left[\frac{(|\, Q(a)\,| + a - x_2)^2}{4Q^2(a)}\right]\right.$$

$$\left. - g' \log\left[\frac{8a^2(|\, Q(-a)\,| - a - x_2)}{(Q^2(-a) - 2a(a + x_2) + |\, Q(a)\,||\, Q(-a)\,|)(|\, Q(a)\,| + a - x_2)}\right]\right\}\ . \tag{C.22}$$

Appendix D

Solution of the Definite Integrals in Equations (4.51) and (4.52)

The Solution of Equation (4.51)

The integral in Equation (4.51) is

$$\int_{-a}^{0} \left[B_x - B_{px}\right]_{y=0} \mathrm{d}x \,,$$

and has been solved as an indefinite integral (Equation (4.50)). The lower limit of integration is applied by letting $x = -a + \delta$ and taking the limit as δ tends to zero. Note that, since the interval $[-a, 0]$ lies to the left of the current sheet, $Q(x) = -\mid Q(x) \mid$, thus

$$\begin{aligned}
-\mid Q(-a+\delta) \mid &= -\left((a+x_2)^2 + y_2^2 - 2(a+x_2)\delta + \delta^2\right)^{\frac{1}{2}} \\
&= -\mid Q(-a) \mid \left(1 - \frac{2(a+x_2)\delta - \delta^2}{Q^2(-a)}\right)^{\frac{1}{2}} \\
&= -\mid Q(-a) \mid + \frac{(a+x_2)\delta}{\mid Q(-a) \mid} - \frac{\delta^2}{2 \mid Q(-a) \mid} + \frac{(a+x_2)^2 \delta^2}{2Q^2(-a) \mid Q(-a) \mid} + \mathrm{O}\left(\delta^3\right) . \qquad \text{(D.1)}
\end{aligned}$$

All the terms in Equation (4.50) may now be evaluated simply, except for the third term which equals

$$\begin{aligned}
&\lim_{x \to -a} \log \left[\frac{\left(Q^2(-a) - (a+x_2)(x+a) + \mid Q(-a) \mid Q(x)\right) x^2}{\left(Q^2(0) - x_2 x + \mid Q(0) \mid Q(x)\right)(x+a)^2} \right] \\
&= \lim_{\delta \to 0} \log \left[\frac{\left(Q^2(-a) - (a+x_2)\delta - \mid Q(-a) \mid^2 + (a+x_2)\delta - \frac{\delta}{2} + \frac{(a+x_2)^2\delta^2}{2Q^2(-a)} + \mathrm{O}\left(\delta^3\right)\right)(a-\delta)^2}{\left(Q^2(0) + x_2 a - \mid Q(0) \mid\mid Q(-a) \mid + \mathrm{O}(\delta)\right)\delta^2} \right] \\
&= \log \left[\frac{\left(-\frac{1}{2} + \frac{(a+x_2)^2}{2Q^2(-a)}\right) a^2}{Q^2(0) + x_2 a - \mid Q(0) \mid\mid Q(-a) \mid} \right]
\end{aligned}$$

$$= \log\left[\frac{-y_2^2a^2}{2\left(Q^2\left(0\right)+x_2a-\mid Q\left(0\right)\mid\mid Q\left(-a\right)\mid\right)Q^2\left(-a\right)}\right]$$

$$= \log\left[\frac{\left(Q^2\left(-a\right)-\left(a+x_2\right)a+\mid Q\left(0\right)\mid\mid Q\left(-a\right)\mid\right)}{2Q^2\left(-a\right)}\right] . \tag{D.2}$$

The lower limit, therefore, becomes

$$\int_{-a}\left[B_x-B_{px}\right]_{y=0}dx = B_o\left\{-\mid Q\left(-a\right)\mid+a+g'\log\left[\frac{\left(Q^2\left(-a\right)-\left(a+x_2\right)a+\mid Q\left(0\right)\mid\mid Q\left(-a\right)\mid\right)}{2Q^2\left(-a\right)}\right]\right.$$

$$\left.+f'\log\left[\frac{-\mid Q\left(-a\right)\mid-\left(a+x_2\right)}{Q^2\left(b\right)-\left(b-x_2\right)\left(a+b\right)-\mid Q\left(b\right)\mid\mid Q\left(-a\right)\mid}\right]\right\} . \tag{D.3}$$

Similarly in the upper limit $Q\left(x\right)$ must be evaluated first

$$-\mid Q\left(-\delta\right)\mid = -\left(x_2^2+y_2^2+2x_2\delta+\delta^2\right)^{\frac{1}{2}}$$

$$= -\mid Q\left(0\right)\mid\left(1+\frac{2x_2\delta+\delta^2}{Q^2\left(0\right)}\right)^{\frac{1}{2}}$$

$$= -\mid Q\left(0\right)\mid-\frac{x_2\delta}{\mid Q\left(0\right)\mid}-\frac{\delta^2}{2\mid Q\left(0\right)\mid}+\frac{x_2^2\delta^2}{2Q^2\left(0\right)\mid Q\left(0\right)\mid}+\mathrm{O}\left(\delta^3\right) , \tag{D.4}$$

and the third term of Equation (4.50) becomes

$$\lim_{x\to0}\log\left[\frac{\left(Q^2\left(-a\right)-\left(a+x_2\right)\left(x+a\right)+\mid Q\left(-a\right)\mid Q\left(x\right)\right)x^2}{\left(Q^2\left(0\right)-x_2x+\mid Q\left(0\right)\mid Q\left(x\right)\right)\left(x+a\right)^2}\right]$$

$$= \lim_{\delta\to0}\log\left[\frac{\left(Q^2\left(-a\right)-\left(a+x_2\right)a-\mid Q\left(-a\right)\mid\mid Q\left(0\right)\mid+\mathrm{O}\left(\delta\right)\right)\delta^2}{\left(Q^2\left(0\right)+x_2\delta-\mid Q\left(0\right)\mid^2-x_2\delta-\frac{\delta}{2}+\frac{x_2^2\delta^2}{2Q^2(0)}+\mathrm{O}\left(\delta^3\right)\right)\left(a-\delta\right)^2}\right]$$

$$= \log\left[\frac{Q^2\left(-a\right)-\left(a+x_2\right)a-\mid Q\left(-a\right)\mid\mid Q\left(0\right)\mid}{\left(-\frac{1}{2}+\frac{x_2^2}{2Q^2(0)}\right)a^2}\right]$$

$$= \log\left[\frac{2\left(Q^2\left(-a\right)-\left(a+x_2\right)a-\mid Q\left(-a\right)\mid\mid Q\left(0\right)\mid\right)Q^2\left(0\right)}{-y_2^2a^2}\right]$$

$$= \log\left[\frac{2Q^2\left(0\right)}{\left(Q^2\left(0\right)+ax_2+\mid Q\left(0\right)\mid\mid Q\left(-a\right)\mid\right)}\right] . \tag{D.5}$$

Thus, the upper limit of integration equals

$$\int^0\left[B_x-B_{px}\right]_{y=0}dx = B_o\left\{-\mid Q\left(0\right)\mid+f'\log\left[\frac{-\mid Q\left(0\right)\mid-x_2}{Q^2\left(b\right)-\left(b-x_2\right)b-\mid Q\left(b\right)\mid\mid Q\left(0\right)\mid}\right]\right.$$

$$\left.+g'\log\left[\frac{2Q^2\left(0\right)}{\left(Q^2\left(0\right)+ax_2+\mid Q\left(0\right)\mid\mid Q\left(-a\right)\mid\right)}\right]\right\} . \tag{D.6}$$

Subtracting the lower limit from the upper limit completes the evaluation of the definite integral in Equation (4.51)

$$\int_{-a}^{0} [B_x - B_{px}]_{y=0}\, dx = B_o \left\{ \mid Q(-a) \mid - \mid Q(0) \mid -a \right.$$
$$+ f' \log \left[\frac{(\mid Q(0) \mid + x_2)\left(Q^2(b) - (b - x_2)(a+b) - \mid Q(b) \parallel Q(-a) \mid\right)}{(\mid Q(-a) \mid + (a + x_2))\left(Q^2(b) - (b - x_2)\, b - \mid Q(b) \parallel Q(0) \mid\right)} \right]$$
$$\left. + g' \log \left[\frac{4Q^2(0)\, Q^2(-a)}{(Q^2(0) + x_2 a + \mid Q(0) \parallel Q(-a) \mid)\left(Q^2(-a) - a(a + x_2) + \mid Q(0) \parallel Q(-a) \mid\right)} \right] \right\} . \quad \text{(D.7)}$$

The Solution of Equation (4.52)

Equation (4.52) contains the integral

$$\int_{b}^{\infty} [B_x - B_{px}]_{y=0}\, \mathrm{d}x ,$$

whose indefinite solution appears in Equation (4.50). Here the interval of integration $[b, \infty)$ lies to the right of the current sheet. Therefore $Q(x) = \mid Q(x) \mid$ and, so in the lower limit of integration, where $x = b + \delta$ and the limit as δ tends to zero is taken, $Q(x)$ becomes

$$\mid Q(b+\delta) \mid = \left((b - x_2)^2 + y_2^2 + 2(b - x_2)\,\delta + \delta^2 \right)^{\frac{1}{2}}$$
$$= \mid Q(b) \mid \left(1 + \frac{2(b - x_2)\,\delta + \delta^2}{Q^2(b)} \right)^{\frac{1}{2}}$$
$$= \mid Q(b) \mid + \frac{(b - x_2)\,\delta}{\mid Q(b) \mid} + \frac{\delta^2}{2 \mid Q(b) \mid} - \frac{(b - x_2)^2\, \delta^2}{2Q^2(b) \mid Q(b) \mid} + \mathrm{O}\left(\delta^3\right) . \quad \text{(D.8)}$$

This time all the terms in Equation (4.50) are easily solved by substituting in $x = b + \delta$ and neglecting the terms of order δ and higher and so the lower limit equals

$$\int_{b} [B_x - B_{px}]_{y=0}\, dx = B_o \left\{ \mid Q(b) \mid - b + f' \log \left[\frac{\mid Q(b) \mid + b - x_2}{2Q^2(b)} \right] \right.$$
$$\left. + g' \log \left[\frac{\left(Q^2(-a) - (a + x_2)(a+b) + \mid Q(-a) \parallel Q(b) \mid\right) b^2}{\left(Q^2(0) - b x_2 + \mid Q(b) \parallel Q(0) \mid\right)(a+b)^2} \right] \right\} . \quad \text{(D.9)}$$

The upper limit is evaluated by letting $x = R$ in the limit R tends to infinity, such that

$$\lim_{x \to \infty} Q(x) = \lim_{R \to \infty} \mid Q(R) \mid$$
$$= \lim_{R \to \infty} \left[R \left(1 - \frac{2x_2}{R} + \frac{x_2^2 + y_2^2}{R^2} \right)^{\frac{1}{2}} \right]$$
$$= \lim_{R \to \infty} \left[R - x_2 + \frac{y_2^2}{2R} + \mathrm{O}\left(\frac{1}{R^2} \right) \right] . \quad \text{(D.10)}$$

The terms on the right-hand side of Equation (4.50) become, respectively:

$$\lim_{x\to\infty} Q(x) - x \;=\; -x_2 \;; \tag{D.11}$$

$$\begin{aligned}
&\lim_{x\to\infty} \log\left[\frac{Q(x)+x-x_2}{Q^2(b)+(b-x_2)(x-b)+\mid Q(b)\mid Q(x)}\right] \\
&\quad= \lim_{R\to\infty} \log\left[\frac{R-x_2+R-x_2+\mathrm{O}\left(\frac{1}{R}\right)}{Q^2(b)+(b-x_2)(R-b)+\mid Q(b)\mid (R-x_2)+\mathrm{O}\left(\frac{1}{R}\right)}\right] \\
&\quad= \log\left[\frac{2}{\mid Q(b)\mid +b-x_2}\right] \;;
\end{aligned} \tag{D.12}$$

$$\begin{aligned}
&\lim_{x\to\infty} \log\left[\frac{\left(Q^2(-a)-(a+x_2)(x+a)+\mid Q(-a)\mid Q(x)\right)x^2}{\left(Q^2(0)-x_2x+\mid Q(0)\mid Q(x)\right)(x+a)^2}\right] \\
&\quad= \lim_{R\to\infty} \log\left[\frac{\left(Q^2(-a)-(a+x_2)(R+a)+\mid Q(-a)\mid (R-x_2)+\mathrm{O}\left(\frac{1}{R}\right)\right)R^2}{\left(Q^2(0)-Rx_2+\mid Q(0)\mid (R-x_2)+\mathrm{O}\left(\frac{1}{R}\right)\right)(R+a)^2}\right] \\
&\quad= \log\left[\frac{\mid Q(-a)\mid -(a+x_2)}{\mid Q(0)\mid -x_2}\right] \;.
\end{aligned} \tag{D.13}$$

Thus, the upper limit of integration becomes

$$\begin{aligned}
\int^{\infty} [B_x - B_{px}]_{y=0}\, dx \;=\; B_o \Bigg\{ &-x_2 + f' \log\left[\frac{2}{\mid Q(b)\mid +b-x_2}\right] \\
&+\; g' \log\left[\frac{\mid Q(-a)\mid -(a+x_2)}{\mid Q(0)\mid -x_2}\right]\Bigg\} \;.
\end{aligned} \tag{D.14}$$

If the solution to the lower limit is subtracted from that for the upper limit, then Equation (4.52) is derived

$$\begin{aligned}
\int_b^{\infty} [B_x - B_{px}]_{y=0}\, dx \;=\; B_o \Bigg\{ &-\mid Q(b)\mid +b-x_2 + f' \log\left[\frac{4Q^2(b)}{(\mid Q(b)\mid +b-x_2)^2}\right] \\
&+\; g' \log\left[\frac{(a+b)^2(\mid Q(-a)\mid -(a+x_2))\left(Q^2(0)-bx_2+\mid Q(b)\mid\mid Q(0)\mid\right)}{b^2(\mid Q(0)\mid -x_2)\left(Q^2(-a)-(a+b)(a+x_2)+\mid Q(b)\mid\mid Q(-a)\mid\right)}\right]\Bigg\} \;.
\end{aligned} \tag{D.15}$$

Appendix E

Table of Munro Ascents

20/10/91	**Beinn Narnain, Beinn Ime**: my first university club trip (StAUMC), also ascended the Cobbler, visibility poor.
27/10/91	**Ben Cruachan, Stob Diamh**: StAUMC; again poor visibility.
1/11-3/11/91	**Carn a'Mhaim, Ben Macdui, Derry Cairngorm**: StAUMC; saw fantastic aurora on the walk in, weather gradually improved over the weekend. **Beinn a'Chaorainn**: interesting tors on top, weather remained reasonable.
16/11/91	**Stuc a'Chroin**: StAUMC; very frustrating day! Started off over Beinn Each and failed to reach Ben Vorlich because various members of the party were slow.
29/10-2/12/91	**Slioch**: StAUMC; poor weather. **Beinn Eighe**: excellent, even though I fell in a river!
12/01/92	**Beinn Ghlas, Beinn Lawers, Meall Garbh, Meall Greigh**: StAUMC; snowy, fun day sliding on our bivi bags.
17/01-19/01/92	**Aonach Eagach - Meall Dearg, Sgorr nam Fiannaidh**: StAUMC; excellent day on Saturday despite the weather which deteriorated on the Sunday.
26/01/92	**Beinn Dorain, Beinn an Dothaidh**: StAUMC; very early start after a noisy Burn's night in the flat below, but good day after all. Fantastically clear views.
31/01-2/02/92	**Ben Nevis**: StAUMC; Adam fell in river, so we aborted our attempt on an ice route. Sunday was a washed out, so went to Fort Bill climbing wall.
7/02-11/02/92	**Sgurr na Banachdich**: StAUMC; the weather suddenly became perfect on the Monday after two terrible days. Ascended the An Stac screes and traversed along the ridge over Sgurr Dearg, lots of snow.
16/02/92	**Cairn Gorm**: StAUMC; very cold and snowy, visibility very poor, so again no

ice route.

21/02-23/02/92 **An Teallach - Bidein a'Ghlas Thuill, Sgurr Fiona**: StAUMC; Sunday was great, fantastic views, fantastic mountain!

1/03/92 **Creag Meagaidh - Carn Liath, Stob Poite Coire Ardair, Creag Meagaidh**: StAUMC; weather deteriorated, so accurate map reading was called for.

28/03/92 **Creag Mhor, Carn Mairg, Meall Garbh, Carn Gorm**: Ian; four easy mountains, weather okayish.

4/04/92 **Ben Vorlich**: Graham; finally I succeed in good weather!

24/05/92 **Ben Chonzie**: Graham; (my return after injury) pleasant mountain on a beautiful day.

30/05/92 **Schiehallion**: Graham; a scientist's mountain (used by Maskelyne for his experiment to determine the mass of the earth), good weather.

6/06/92 **Drumochter - Sgairneach Mhor, Beinn Udlamain, A'Mharconaich**: Dave and Melissa; amazing day, swam in river afterwards.

7/06/92 **Tarmachan Ridge - Meall nan Tarmachan**: Alone; I just could not resist the excellent weather!

13/06/92 **Beinn a'Chroin, An Caisteal**: Graham; rain, rain and more rain!

28/06/92 **Bidean nam Bian, Buachaille Etive Beag**: Simon; lovely day, wonderful long walk.

3/07-5/07/92 **The Devils Point, Cairn Toul, Braeriach**: Simon; again great weather and a great long walk. Sunday also spent on a long walk, but no tops included.

10/07-12/07/92 **Torridon - Beinn Alligin**: Simon; average weather deteriorated on Sunday to terrible weather.

26/07/92 **Broad Cairn, Cairn Bannoch, Tolmount, Tom Buidhe**: Graham; reasonable weather, pleasant walk.

31/07-2/08/92 **Carn an t-Sagairt Mor, The White Mounth, Lochnagar**: Simon; intended to rock climb, but weather dreadful in the morning, the afternoon just got better and better (camped on Broad Cairn).
Driesh, Mayar

7/08-9/08/92 **Fisherfield Forest - Beinn a'Chlaidheimh, Sgurr Ban, Mullach**

Coire Mhic Fhearchair, Beinn Tarsuinn, A'Mhaighdean, Ruadh Stac Mor: Simon and Colin; one of the most amazing days on the hills I have ever had. Beautiful weather, fantastic views (11.5 hrs, 23 miles, 7000ft of ascent). The next day was a wash out.

21/08-23/08/92 **Meall a'Bhuiridh, Creise**: Simon; another failed rock climbing trip due to rain; very windy got blown off my feet! (learnt of Matthew's death).

16/10-18/10/92 **Stob Coir'an Albannaich, Meall nan Eun**: StAUMC; quite a lot of snow on the tops.
Buachaille Etive Mor: Had a great day ascending via curved ridge.

13/11-15/11/92 **The Saddle**: Simon; loads of snow, blue sky and spin drift on Saturday forced us to retreat. On Sunday the winds dropped enough to let us climb, lovely winter ridge ascent.

20/11-21/11/92 **Beinn a'Chlachair, Geal Charn, Creag Pitridh**: Alone; very very cold night, again loads of snow making the going tough. Navigation interesting at points and driving awful on the icy roads.

28/11/92 **Ben More, Stob Binnein**: Vinnie, Lucy and John; fun day though the others had problems without ice axe or crampons.

4/12-6/12/92 **Mullach Clach a'Bhlair**: Simon; we spent the weekend in a nice house with Phil Gribbon. Visibility poor both days - still loads of snow.
Bynack More: very little visibility

23/01/93 **An Gearanach, Stob Coire a'Chairn**: Simon; dire conditions with a white out along the ridge, scarey!

29/01-31/01/93 **Cruach Ardrain, Beinn Tulaichean**: Simon; icy underfoot on Saturday whilst it rained and snowed.
Meall Glas, Sgiath Chuil: Sunday was an unbelievably clear day.

12/02-15/02/93 **Sgurr Alasdair**: StAUMC; visibility poor, but excellent fun; snowy ascent of west ridge.

6/03/93 **Beinn Dubhchraig, Ben Oss, Beinn Laoigh (Ben Lui), Beinn a'Chleibh**: Simon; long day with amazing cloud inversion, still a fair bit of snow.

12/03-14/03/93 **Carn Bhac, Beinn Iutharn Mhor, Carn an Righ, An Socach**: Simon; rain, more rain and a stream to wade.

21/03/93 **Beinn a'Ghlo - Carn Liath, Braigh Coire Chruinn-bhalgain, Carn nan Gabhar**: Simon; surprisingly short day in lovely weather.

26/03-28/03/93 **Beinn Bhreac, Beinn a'Chaorainn**: Simon; failed on Beinn a'Bhuird the day before owing to a white out. Next day navigated carefully and completed the tops.

18/04/93 **Beinn Mhanach, Beinn Achaladair, Beinn a'Chreachain**: Simon; very cloudy day, but still got sun burn from the reflection off the snow.

24/04/93 **Carn an Tuirc, Cairn of Claise, Glas Maol, Creag Leacach, The Cairnwell, Carn a'Gheoidh, Carn Aosda**: Alone; good to stretch my legs in fine weather once more.

15/05-16/05/93 **Stuchd an Lochain, Meall Buidhe**: Simon; started off late, but still managed it (loads of snow high winds - still winter).
Meall Ghaordaidh: poor visibility, very cold.

21/05-23/05/93 **The Mamores - Sgurr Eilde Mor, Binnein Beag. Binnein Mor, Na Gruagaichean, Am Bodach, Sgor an Iubhair, Sgur a'Mhaim**: Simon; great long walk in good weather - super ridge.
Stob Ban, Mullach nan Coirean: another long, but fun walk from our tent.

28/05/93 **Ballachulish Horseshoe - Sgorr Dhearg, Sgorr Dhonuill**: Simon and Philip; beautiful day, so could see for miles.

6/06/93 **Glen Shee - Glas Tulaichean**: Simon; kept Simon company as he ascended the Cairnwell, etc, nice weather.

18/06-20/06/93 **Knoydart - Gairich, Sgurr Mor, Sgurr nan Coireachan**: Simon; my first visit to one of the wildest places I have ever been. Epic walk in, bothy roofless, rain torrential!

27/06/93 **Beinn a'Chochuill, Beinn Eunaich**: Simon; beautiful weather, enjoyable trip, swam in river afterwards!

3/07/93 **Beinn Chabhair**: Simon; terrible day - rain, rain and more rain.

10/07/93 **Monadh Liath - Carn Dearg, Carn Sgulain, A'Chailleach**: Simon; very flat mountains - surprisingly short day.

11/07/93 **Meall Chuaich, Carn na Caim, A'Bhuidheanach Bheag**: Simon; a long, long day (lost my watch).

17/07/93 **Ben Vorlich**: Simon; little visibility and lots of rain!

19/07/93 **Toll Creagach, Tom a'Choinich, Carn Eighe, Beinn**

	Fhionnlaidh, Mam Sodhail: Simon; the start of our weeks holiday in and around Affric, beautiful day and a lovely walk.
20/07/93	**An Socach, Sgurr nan Ceathreamhnan, Mullach na Dheiragain**: Simon; walked into Altbeithe YH, then ascended the mountains in pouring rain, not pleasant though satisfying to complete the tops.
21/07/93	**Ciste Dhubh, Aonach Meadhoin, Sgurr a'Bhealaich Dheirg, Saileag, Sgurr na Ciste Dhubh, Sgurr Fhuaran**: Simon; a long day (13 hrs) in rain and little visibility, but one of the best ridges in Scotland.
24/07/93	**A'Ghlas-bheinn, Beinn Fhada**: Simon; Simon injured after our long day, so recovered for the next few days. Weather reasonable.
30/07-1/08/93	**An Coileachan, Meall Gorm, Sgurr Mor, Beinn Liath Mhor Fannaich**: Simon; never seen so many midges before! Part of the day was sunny, but it turned very cloudy and misty in the end. **Sgurr nan Each, Sgurr nan Clach Geala, Meall a'Chrasgaidh**: torrential rain, but great mountains.
6/08/93	**Meall Corranaich, Meall a'Choire Leith**: Alone; cloudy, but fun to be let loose.
7/08/93	**Beinn Dearg, Carn a'Chlamain**: Simon; a long, but satisfying day.
14/08-15/08/93	**Sron a'Choire Ghairbh, Meall na Teanga**: Simon; torrential rain all day. Stayed in Ratagan YH that evening and dried off ready for the next day. **Creag a'Mhaim, Druim Shionnach, Aonach air Chrith, Maol Chinn-dearg, Sgurr an Doire Leathain, Sgurr an Lochain, Creag nan Damh, Sgurr na Sgine**: not quite blue sky, excellent long walk, but a tiring drive back.
22/08/93	**Drumochter - Geal Charn**; Simon; another day of repeats. Not great weather.
28/08-29/08/93	**Beinn a'Chaorainn, Beinn Teallach**: Simon; two easy little mountains. **Aonach Mor, Aonach Beag, Sgurr Choinnich Mor, Stob Coire an Laoigh, Stob Coire Claurigh, Stob Ban**: weather fairly good, one of our long days, very satisfying despite a swollen knee.
3/09-5/09/93	**Liathach - Spidean a'Choire Leith, Mullach an Rathain**: Simon; perfect day on a superb mountain. **Sgorr Ruadh, Beinn Liath Mhor**: another wonderful day on two good mountains.

26/10-27/10/93 **Ben Starav, Beinn nan Aighenan, Glas Bheinn Mhor**: Alone; Simon away on a conference, so decided to make use of the good weather.

3/10/93 **Stob Ghabhar, Stob a'Choire Odhair**: Simon; not amazing weather, okay mountains.

10/10/93 **Ben Lomond**: Simon; Simon's parents up, pleasant day's ascent from the east (excellent way to avoid the crowds).

16/10-17/10/93 **Beinn Bhuidhe**: Simon; unbelievably cold night (-9 C). Goodish day on the mountains.
Ben Vane: we made it along day by including Ben Narnain and Ben Ime for Simon's benefit.

22/10-24/10/93 **A'Chralaig, Mullach Fraoch-choire**: Simon; rainy on Saturday though interesting mountains.
Carn Ghluasaid, Sgurr nan Conbhairean, Sail Chaorainn: Cloud inversion over Knoydart and Nevis range, looked impressive, lovely weather.

14/11/93 **Mount Keen**: Simon; not brilliant weather, but a pleasant day even so.

19/11-21/11/93 **Bidean a'Choire Sheasgaich, Lurg Mhor**: Simon; long walk, but lovely weather.
Sgurr Choinnich, Sgurr a'Chaorachain, Maoile Lunndaidh: weather still reasonable, so a fun day, but the drive back took one and a half times as long due to snow on the roads and bad weather.

27/11/93 **Fersit - Stob a'Choire Mheadhoin, Stob Coire Easain**: Simon; lots of snow and no sun, started and finished late.

4/12/93 **Monadh Liath - Geal Charn**: Simon; not much visibility, but quite a bit of snow.

11/02-13/02/94 **Ben Wyvis**: Simon; so good to get out again after the long and bad winter (previously we had tried and failed on a few things). Difficult to find the cairn since it was under 5 ft of snow, very windy!
Moruisg, Sgurr nan Ceannaichean: beautiful day though still windy, great views.

18/03-20/03/94 **Carn Dearg, Sgor Gaibhre**: Simon; great to get out again to a wild place, took train to Corrour on Saturday and back on Sunday.
Beinn na Lap: loads of snow and fairly good weather.

25/03-26/03/94 **Gleouraich, Spidean Mialach, Sgurr a'Mhaoraich**: Simon; day good, going fast despite snow, so did them all in one day!

11/04/94	**Sgurr Breac, A'Chailleach**: Simon; start of our Easter trip North. Dire weather, white out on top.
12/04/94	**Conival, Ben More Assynt**: Simon; much better day with some good views and nice walking in snow.
13/04/94	**Ben Hope, Ben Klibreck**: Simon; two fairly easy hills, therefore managed to do them in one day, so we could have the next day off. Stayed in Tongue YH that night, lovely place.
15/04/94	**Seana Bhraigh, Eididh nan Clach Geala, Meall nan Ceapraichean**: Simon; day improved to give good weather, very long walk in fairly deep snow.
16/04/94	**Fionn Bheinn**: Simon; my car exhaust went, but after the AA man patched it up we ascended the mountain before heading home, poor weather.
6/05-8/05/94	**Carn an Fhidhleir, An Sgarsoch**: Simon; long walk in uninspiring weather. **Beinn Bhrotain, Monadh Mor**: also a long walk that ended in rain.
13/05-15/05/94	**Sgurr na Ruaidhe, Carn nan Gobhar, Sgurr a'Choire Ghlais, Sgurr Fhuar-thuill**: Simon; beautiful day, not a cloud in the sky, still snow on the tops. **An Socach, An Riabhachan, Sgurr na Lapaich, Carn nan Gobhar**: started off wet due to rain and falling in a river, turned out lovely, good ridge walk along tops - long, but fun.
20/05-22/05/94	**Beinn Dearg, Cona'Mheall, Am Faochagach**: Simon; more good weather though loads of snow on the tops still, Simon's boots almost collapsed. **Maol Chean-dearg**: gorgeous day, lovely bothy seen on walk in.
27/05-29/05/94	**Beinn Bheoil, Ben Alder, Beinn Eibhinn, Aonach Beag, Geal-Charn, Carn Dearg**: Simon; started off walk with Simon, but did the last four on my own. Still in my plastic boots because some large areas of compact snow remaining.
4/06/94	**Beinn Sgritheall**: Simon; start of our weeks trip to Skye, weather reasonable lots of orchids on hill side.
5/06/94	**Sgurr nan Gillean, Am Basteir, Bruach na Frithe**: Simon; staying in a cottage with Reg, Anna, Alasdair and Sheena, weather fairly good, fun day on the ridge.
6/06/94	**Bla Bheinn (Blaven)**: Simon; torrential rain leading to swollen rivers and diversions on the return, horrible loose ascent and descent.

7/06/94	**Sgurr nan Eag, Sgurr Dubh Mor**: Simon; okayish day, cloud lifted once revealing a great view, good scrambling.
8/07/94	**Sgurr a'Mhadaidh, Sgurr a'Ghreadaidh**: Simon; horrible weather, bleak on tops (even snowed on us!).
10/07/94	**Sgurr Mhic Choinnich, Inaccessible Pinnacle**: Simon; not pleasant, wet rock, no visibility, but we made it!
29/06-1/07/94	**Meall Buidhe, Luinne Bhein, Ladhar Bheinn**: Simon; stayed with Philip in a bunk house in Inverie, weather okayish. We may have seen an Eagle!
3/07/94	**Ben Challum, Creag Mhor, Beinn Heasgarnich**: Simon; low cloud, very wet and a long day.
9/07/94	**Beinn a'Bhuird, Ben Avon**: Simon; ascended surprisingly fast so beat the worst of the weather, very windy in the col.
16/07-17/07/94	**Garbh Choich Mhor, Sgurr na Ciche**: Simon; fairly good weather, nice mountains, a beautiful area. **Sgurr Thuilm, Sgurr nan Coireachan**: lovely day, fun mountains. Walked through a field of orchids at the bottom.
30/07/94	**Fersit - Stob Coire Sgriodain, Chno Deag**: Simon; finally achieved these two! Beautiful day, pleasant walk.
6/08-7/08/94	**Carn Mor Dearg**: Simon; traversed the Carn Mor Dearg arête on to Ben Nevis as well (fast!), nice walk in pretty good weather. **Gulvain**: again good weather and a satisfying ascent.
13/08-14/08/94	**Beinn Sgulaird**: Simon; nice little mountain, lovely weather giving great views. **Sgor na h-Ulaidh, Beinn Fhionnlaidh**: weather not so good, not many views and some rain (left tent in Glen Etive by accident!).
11/09/94	**Sgor Gaoith**: Alone; low cloud, rain and a small amount of sunshine as I descended off Geal Charn. A long drive.
17/09/94	**Isle of Mull - Ben More**: Simon; we woke to a beautiful sunrise and got the first ferry over to Mull. Unfortunately the cloud remained low all day on Ben More, however, it was a fun day on another super mountain.

It has been a great pleasure to me to not only complete my PhD thesis in three years, but also to complete all 277 of the Munros. Without the PhD in St Andrews I would never have had the opportunity to climb all these mountains and without the mountains my PhD may not have been achieved!

References

Athay, R.G. (1976) "The Solar Chromosphere and Corona: Quiet Sun" D. Reidel, Dordrecht, Holland.

Davis, J., Golub, L. and Krieger, A.S. (1977) "Solar Cycle Variation of Magnetic Flux Emergence" *Astrophys. J.* **214**, L141.

Dere, K.P. (1993) "Solar Mass Flow in Fine-scale Structures" *Proc. 2nd SOHO Workshop* (Dordrecht: Kluwer) in press.

Dungey, J.W. (1953) "Conditions for the Occurrence of Electrical Discharges in Astrophysical Systems" *Phil. Mag. Ser. 7* **44**, 725.

Forbes, T.G. and Priest, E.R. (1984) "Numerical Simulation of Reconnection in an Emerging Magnetic Flux Region" *Solar Phys.* **94**, 315.

Gabriel, A.H. (1976) "A Magnetic Model of the Solar Transition Region" *Phil. Trans. R. Soc. London.* A. **281**, 339.

Golub, L., Davis, J. and Krieger, A.S. (1979) "Anti-correlation of X-ray Bright Points with Sunspot Number" *Astrophys. J.* **229**, L145.

Golub, L., Krieger, A.S., Harvey, J.W. and Vaiana, G.S. (1977) "Magnetic Properties of X-ray Bright Points" *Solar Phys.* **53**, 111.

Golub, L., Krieger, A.S., Silk, J.K., Timothy, A.F. and Vaiana, G.S. (1974) "Solar X-ray Bright Points" *Astrophys. J.* **189**, L93.

Golub, L., Krieger, A.S., and Vaiana, G.S. (1976a) "Distribution of Lifetimes for Coronal Soft X-ray Bright Points" *Solar Phys.* **49**, 79.

Golub, L., Krieger, A.S., and Vaiana, G.S. (1976b) "Observation of Spatial and Temporal Variation in X-ray Bright Point Emergence Patterns" *Solar Phys.* **50**, 311.

Green, R.M. (1965) "Modes of Annihilation and Reconnection of Magnetic Fields" *I.A.U. Symp.* **22**, 398.

Habbal, S.R., Dowdy, J.F., Jr. and Withbroe, G.L. (1990) "A Comparison between Bright Points in a Coronal Hole and a Quiet-Sun Region" *Astrophys. J.* **352** 333.

Harvey, K.L. (1984) "Solar Cycle Variation of Ephemeral Active Regions" *Proc. 4th European Meeting on Solar Phys.* ESA SP 220, 235.

Harvey, K.L. (1985) "The Relation Between Coronal Bright Points as seen in He 10830 and the Evolution of Photospheric Magnetic Network Fields" *Aust. J. Phys.* **38**, 875.

Harvey, K.L., Harvey J.W. and Martin, S.F. (1975) "Ephemeral Active Regions in 1970 and 1973" *Solar Phys* **40**, 87.

Harvey, K.L. and Martin, S.F. (1973) "Ephemeral Active Regions" *Solar Phys* **32**, 389.

Harvey, K.L., Strong, K.T., Nitta, N. and Tsuneta, T. (1992) "Lifetimes and Distribution of Coronal Bright Points Observed with Yohkoh" *Adv. Space. Res.* **13** 27.

Hermans, L.M. and Martin, S.F. (1986) "Small-scale Eruptive Filaments on the Quiet Sun" *Coronal and Prominence Plasmas* (ed. A. Poland) NASA CP 2442, p369.

Heyvaerts, J. and Priest, E.R. (1984) "Coronal Heating by Reconnection in DC Current Systems. A Theory Based on Taylor's Hypothesis" *Astron. Astrophys.* **137**, 63.

Heyvaerts, J., Priest, E.R. and Rust, D.M. (1977) "An Emerging Flux Model for the Solar Flare Phenomenon" *Astrophys. J.* **216**, 123.

Kawai, G., Kurokawa, H., Tsuneta, S., Shimizu, T., Shibata, K., Acton, L.W., Strong, K.T. and Nitta, N. (1992) "Comparison Between Hα and Yohkoh Soft X-ray Images of Emerging Flux Regions" *Pub. Astron. Soc. Japan.* **44**, L193.

Leighton, R.B., Noyes, R.W. and Simon, G.W. (1962) "Velocity Fields in the Solar Atmosphere. 1. Preliminary Report" *Astrophys. J.* **135**, 474.

Livi, S.H.B., Wang, J. and Martin, S.F. (1985) "The Cancellation of Magnetic Flux. *I.* On The Quiet Sun" *Aust. J. Phys.* **38**, 855.

Low, B.C. and Hu, Y.Q. (1983) "The Energy of Electric Current Sheets. II. The Magnetic Free Energy and the Photospheric Magnetic Flux" *Solar Phys.* **84**, 83.

Martin, S.F. (1984) "Dynamic Signatures of Quiet Sun Magnetic Fields" in *Small-scale Dynamical Processes in Stellar Quiet Atmospheres* (ed. S. Keil) Sac. Peak Observatory, **30.**

Martin, S.F. (1986) "Recent Observations of the Formation of Filaments" *Coronal and Prominence Plasmas* (ed. A. Poland) NASA CP 2442 p431.

Martin, S.F. (1988) "The Identification and Interaction of Network, Intranetwork and Ephemeral Region Magnetic Fields" *Solar Phys.* **117**, 243.

Martin, S.F. and Harvey, K.L. (1979) "Ephemeral Active Regions During Solar Minimum" *Solar Phys.* **64**, 93.

Martin, S.F., Livi, S.H.B. and Wang, J. (1985) "The Cancellation of Magnetic Flux II. In a Decaying Active Region" *Australian J. Phys.* **39**, 929.

Martin, S.F., Livi, S.H.B., Wang, J. and Shi Z. (1984) "Ephemeral Regions V.S. Pseudo Ephemeral Regions" *Measurements of Solar Vector Magnetic Fields* (ed. M. Hagyard) **NASA CP 2374**, 403.

Parker, E.N. (1957) "Sweet's Mechanism for Merging Magnetic Fields in Conducting Fluids" *J. Geophys. Res.* **62**, 509.

Parnell, C.E. and Priest, E.R. (1994) " A Converging Flux Model for the Formation of an X-ray Bright Point above a Supergranule Cell" *Geophys. Astrophys. Fluid Dynamics* submitted.

Parnell, C.E., Priest, E.R. and Golub, L. (1994) "The Three Dimensional Structures of X-ray Bright Points" *Solar Phys.* **151**, 57.

Parnell, C.E., Priest, E.R. and Titov, V.S. (1994) "A Model for X-Ray Bright Points due to Unequal Cancelling Flux Sources" *Solar Phys.* **153**, 217.

Petschek, H.E. (1964) "Magnetic Field Annihilation" AAS-NASA *Symp. on Phys. of Solar Flares* NASA SP **50**, 425.

Priest, E.R. (1982) "Solar Magneto-hydrodynamics" *Geophysics and Astrophysics Monographs* D. Reidel, Dordrecht, Holland.

Priest, E.R. (1986) "Magnetic Reconnection on the Sun" *Mitt. Astron. Ges.* **65**, 41.

Priest, E.R. and Forbes, T.G. (1986) "New Models for Fast Steady State Reconnection" *J. Geophys. Res.* **91**, 5579.

Priest, E.R. and Forbes, T.G. (1992) "Magnetic Flipping: Reconnection in Three Dimensions Without Null Points" *J. Geophys. Res.* **97**, 1521.

Priest, E.R. and Lee, L.C. (1990) "Nonlinear Magnetic Reconnection Models with Separatrix Jets" *J. Plasma Physics* **44**, 337.

Priest, E.R., Parnell, C.E., and Martin, S.F. (1994) "A Converging Flux Model of an X-Ray Bright Point and an Associated Cancelling Magnetic Feature" *Astrophys. J.* **427**, 459.

Priest, E.R. and Titov, V.S. (1995) "Magnetic Reconnection at Three-Dimensional Null Points" preprint.

Rickard, G.J. and Priest, E.R. (1994) "The Dynamics of Driven Reconnection in Coronal Arcades" *Solar Phys.* **151** 107.

Rosner, R., Tucker, W.H. and Vaiana, G.S. (1978) "Dynamics of the Quiescent Solar Corona" *Astrophys. J.* **220** 643.

Schmieder, B., Golub, L. and Antiochos, S.K. (1993) "Comparison Between Cool and Hot Plasma Behaviours of Surges" preprint.

Sheeley, N.R., Jr. and Golub, L. (1979) "Rapid Changes in Fine Scale Structure of a Coronal 'Bright Point' and a Small Coronal 'Active Region"' *Solar Phys.* **63** 119.

Shibata, K., Ishido, Y., Acton, L., Strong, K., Hirayama, T., Uchida, Y., McAllister, A., Matsumoto, R., Tsuneta, S., Shimizu, T., Hara, H., Sakurai, T., Ichitmoto, K., Nishino, Y. and Ogawara, Y. (1992a) "Observations of X-Ray Jets with the Yohkoh Soft X-Ray Telescope" *Pub. Astron. Soc. Japan.* **44**, L173.

Shibata, K., Nozawa, S. and Matsumoto, R. (1992b) "Magnetic Reconnection Associated with Emerging Magnetic Flux" *Pub. Astron. Soc. Japan.* **44**, 265.

Shimizu, T. "Active-region Transient Brightenings and the Heating of Active Region Corona" (1994) *Proc. Symp. on the New Look at the Sun with Emphasis on Advanced Observations of Coronal Dynamics and Flares* (ed. S. Enome *et al.*) in press.

Shimizu, T., Tsuneta, S., Acton, L.W., Lemen, J.R., Ogawara, Y. and Uchida, Y. (1994) "Morphology of Active Region Transient Brightenings with the *Yohkoh* Soft X-Ray Telescope" *Astrophys. J.* **422**, 906.

Shimizu, T., Tsuneta, S., Acton, L.W., Lemen, J.R. and Uchida, Y. (1992) "Transient Brightenings in Active Regions Observed by the Soft X-Ray Telescope On Yohkoh" *Pub. Astron. Soc. Japan.* **44**, L147.

Spiller, E.,McCorkle, R.A., Wilczynski, J.S., Golub, L., Nystrom, G., Takacs, P.Z. and Welch, C. "Normal Incidence Soft X-ray Telescopes" (1991) *Optical Engineering* **30**, 1109.

Stenflo, J.O. (1973) "Magnetic-Field Structure of the Photospheric Network" *Solar Phys.* **32**, 41.

Strachan, N.R. and Priest, E.R. (1994) "A General Family of Nonuniform Reconnection Models with Separatrix Jets" *Geophys. Astrophys. Fluid Dynamics* **74**, 245.

Strong, K., Harvey, K., Hirayama, T., Nitta, N., Shimizu, T. and Tsuneta, S. (1992) "Observations of the Variability of Coronal Bright Points by the Soft X-ray Telescope on Yohkoh" *Pub. Astron. Soc. Japan.* **44**, L161.

Sweet, P.A. (1958) "The Neutral Point Theory of Solar Flares" *IAU Symp.* **6**, 123.

Syrovatsky, S.I. (1971) "Formation of Current Sheets in a Plasma with a Frozen-in Strong Magnetic Field" *Soviet Phys. JETP* **33**, 933.

Titov, V.S. (1992) "On the Method of Calculating Two-dimensional Potential Magnetic Fields with Current Sheets" *Solar Phys.* **139**, 401.

Tsuneta, S. (1993) "Dynamics of the Solar Corona Observed with the YOHKOH Soft X-ray Telescope" in *Physics of Solar and Stellar Coronae* (ed. J.K. Linsky and S. Serio) Dordrecht: Kluwer, 113.

Uchida, Y. (1993) "New Aspects of Solar Coronal Physics Revealed by YOHKOH" in *Physics of Solar and Stellar Coronae* (ed J.K. Linsky and S. Serio) Dordrecht: Kluwer, 97.

Vaiana, G.S., Krieger, A.S., Van Speybroeck, L.P. and Zehnpfennig, T. (1970) "The Structure of the X-ray Corona and its Relation to Photospheric and Chromospheric Features" *Bull. Am. Phys. Soc.* **15**, 611.

Wang, J., Shi, Z., Martin, S.F. and Livi, S.H.B. (1988) "The Cancellation of Magnetic Flux on the Quiet Sun" *Vistas in Astronomy.* **31**, 79.

Webb, D.F., Martin, S.F., Moses, D., and Harvey, J.W. (1993) "The Correspondence Between X-Ray Bright Points and Evolving Magnetic Features in the Quiet Sun" *Solar Phys.* **144**, 15.

Withbroe, G.L. and Noyes, R.W. (1977) "Mass and Energy Flow in the Solar Chromosphere and Corona" *Ann. Rev. Astron. Astrophys.* **15**, 363.

Yan, Y., Lee, L.C. and Priest, E.R. (1992) "Fast Magnetic Reconnection with Small Shock Angles" *J. Geophys. Res.* **97**, 8277.

Yan, Y., Lee, L.C. and Priest, E.R. (1993) "Magnetic Reconnection with Large Separatrix Angles" *J. Geophys. Res.* **98**, 7593.